Assessment of Mechanical and Tribological Properties of Alginate-Polyacrylamide Hydrogel Matrix Composites as Minimally Invasive Cartilage Implants

Mohammadreza Arjmandi

A thesis submitted to Auckland University of Technology

In fulfilment of the requirements of the degree

Doctor of Philosophy (PhD)

2019

School of Engineering, Computer and Mathematical Sciences

Auckland University of Technology

I hereby declare that this submission is my own work and that, to the best of my knowledge and belief, it contains no material previously published or written by another person (except where explicitly defined in the acknowledgements), nor material which to a substantial extent has been submitted for award of any other degree or diploma of a university or other institution of higher learning.

Signed Date 26 September 2018

ABSTRACT

The advent of orthopaedic prostheses and their widespread applications have helped millions of patients worldwide to be relieved from pain and gain their mobility. However, they are still not suitable for young or middle-aged patients suffering from localised cartilage damage, due to the limited life span of these load-bearing devices. All available remedies for those patients are temporary and some of them might result in regeneration of tissues with different properties to the existing one, and hence limited functionality and durability. Therefore, an alternative way should be investigated to prevent further tissue degeneration through replacing damaged regions of the tissue and preserving the remaining healthy portion. This will result in prolonging the tissue functionality, and further postponing the total joint replacement.

Different hydrogels have been studied extensively as potential cartilage replacement candidates, as they are biocompatible and can mimic the lubrication mechanisms found in cartilage tissue. As for the mechanical properties, there is still room for improvement. Alginate-Polyacrylamide (ALG-PAAm) hybrid hydrogel was suggested as an orthopaedic prosthesis due to their biocompatibility and promising properties. However, their friction and wear performances remained under-explored. Thus, the current study focused on ALG-PAAm and in an attempt to improve its mechanical performance, silica nanoparticles (Si-NPs) were introduced to the interpenetrating polymer network (IPN) hydrogel matrix as a reinforcement and the mechanical and tribological characteristics of the resultant nanocomposite were investigated. Furthermore, two different weave patterns were developed and produced as three-dimensional woven form, out of biocompatible polymers, to reinforce the hydrogel matrix. Inspired by the articular cartilage tissue, the woven preforms featured a through-the-thickness stiffness gradient and could resist delamination.

Beside experimental approach, wear simulation was performed by employing Archard's wear law in finite element (FE) models. Wear in a unit cell of 3D woven fabrics as well as hydrogel composites were simulated using a user-defined subroutine, UMESHMOTION, linked with ABAQUS CAE package and the model was validated with experimental results. FE simulations were further employed for parametric studies to attain information that could not be obtained directly from the experiments.

It was found that ultra-low coefficient of friction coupled with high wear-resistance and tuneable elastic and viscoelastic characteristics observed in the manufactured samples, were mainly due to the strong interfacial bonding between the nanoparticles and the polymer matrix, allowing effective stress transfer between the two main constituents. Moreover, the infiltration of hydrogel into the woven fabric led to a decrease in surface roughness and an increase in load-to-failure capacity. The wear rate and friction coefficient of the reinforced hydrogel matrix were greatly reduced under the range of applied loads and sliding velocities. These promising results are attributed to the synergistic interaction between the fibre phase and the hydrogel matrix.

The findings of this research give an insight into the tribology of hydrogel matrix composites for use as load-bearing biomedical components.

LIST OF PUBLICATIONS FROM THIS RESEARCH

- Arjmandi, M., & Ramezani, M. (2019). Finite element modelling of sliding wear in three-dimensional textile hydrogel composites. Tribology International 133: 88-100. (IF: 3.246)

- Arjmandi, M., Ramezani, M., Bolle. T., Köppe, G., Gries, T., & Neitzert, T. (2018). Mechanical and tribological properties of a novel hydrogel composite reinforced by three-dimensional woven textiles as a functional synthetic cartilage. Composites Part A: Applied Science and Manufacturing 115: 123-133. (IF: 4.514)

- Arjmandi, M., Ramezani, M., Nand, A., & Neitzert, T. (2018). Experimental study on friction and wear properties of interpenetrating polymer network alginate-polyacrylamide hydrogels for use in minimally-invasive joint implants. Wear, 406, 194-204. (IF: 2.96)

- Arjmandi, M., Ramezani, M., Giordano, M., & Schmid, S. (2017). Finite element modelling of sliding wear in three-dimensional woven textiles. Tribology International, 115, 452-460. (IF: 3.246)

- Arjmandi, M., Ramezani, M., Nand, A., & Neitzert, T. R. (2018). Tribological Characterization of Polyacrylamide-Alginate Hybrid Hydrogels as a Potential Candidate for Cartilage Replacement. Key Engineering Materials (Vol. 775, pp. 109-114). Trans Tech Publications.

- Arjmandi, M., & Ramezani, M., Mechanical and tribological assessment of silica nanoparticle- alginate-polyacrylamide nanocomposite hydrogels as a cartilage replacement. Submitted to Journal of the mechanical behaviour of biomedical materials.

Oral Presentations

- **Arjmandi, M.**, Ramezani, M., Nand, A., & Neitzert, T. "Tribological Characterization of Polyacrylamide-Alginate Hybrid Hydrogels as a Potential Candidate for Cartilage Replacement". *The 8th International Conference on Key Engineering Materials*, March 16-18 2018, Osaka, Japan.

- **Arjmandi, M.**, & Ramezani, M. "Finite Element Modelling of Sliding Wear in Biomedical Textiles" *The 2nd International Conference on Materials Science and Nanotechnology*, April 19-22 2017, Auckland, New Zealand.

- Arjmandi, M. & **Ramezani, M.** "Effect of Silica Nanoparticles on Wear Mechanism of Alginate-Polyacrylamide Hydrogel Matrix as a Load-bearing Biomaterial" *International Conference on Engineering Tribology and Applied Technology* (ICETAT 2018), November 16-18 2018, Taipei, Taiwan.

TABLE OF CONTENTS

ACKNOWLEDGEMENTS

I would like to express my sincere gratitude to my supervisors, Dr Maziar Ramezani and Professor Thomas Neitzert for their professional advice and assistance throughout my research. Maziar was always ready to help me resolving issues, and I am indebted to his comments and his recommendations.

I would also like to thank the research team at the Institute für Textiltechnik, RWTH Aachen University, Germany for their kind cooperation, led to the design and fabrication of novel 3D textiles, used in this study.

My thanks also extend to Dr Ashveen Nand, a senior technician at School of Science, AUT, who has been always ready to help me. Ashveen has significantly guided me throughout the hydrogel synthesis process, providing technical support and advice.

Thanks are due to the staff at engineering workshop of AUT, for the fabrication of the parts that I designed and used for the experiments, and their technical support.

I am grateful to my lovely wife, Sara, my dear Dad, my dear Mom and my brothers who have supported me unconditionally during this chapter of my life and have always encouraged me in demanding stages. Without your invaluable love and support, I could have never accomplished this task. Thank you God almighty.

LIST OF FIGURES

LIST OF TABLES

NOMENCLATURE

a	Apparent contact radius [mm]
A	Cross-sectional area function
A_p	Projected contact area [mm^2]
C	Material constant in Prony series for creep compliance
$C'_{i,j}$	Elastic stiffness matrix
$C'_{i,j,global}$	Global stiffness matrix
D	Material constant in Prony series for stress relaxation
$\boldsymbol{D}$	Global stiffness matrix vector
E	Young's modulus of elasticity [Pa]
E_i	Young's modulus of indenter [Pa]
f	Fibre ratio
F	Reaction force acting on the unit cell face [N]
F	Normal load vector
G	Shear modulus [Pa]
G'	Stress relaxation as a function of time
h	Wear depth [μm]
h_c	Contact depth [μm]
h_{max}	Indentation depth [μm]
H	Vickers Hardness [Pa]
H_s	Hersey Number
J	Creep compliance [Pa^{-1}]
k_D	Dimensional wear coefficient [$mm^3/N.mm$]
K	Wear coefficient
L	Unit cell dimensions [mm]
N	Entrainment speed of fluid [mm/s]
p	Pressure [Pa]
P	Normal Load [N]
P_{max}	Maximum applied load [N]
Q	Stiffness matrix for the textile composite unit cell
r	Radius of indenter [mm]
R	Surface roughness
s	Sliding distance [m]
S	Contact Stiffness [Pa]
t	Time [s]
u	Nodal displacement vector
V	Volume fraction
W	Wear volume [mm^3]

Greek Symbols:

ε	Normal strain component
$\overline{\varepsilon}$	Average strain value
η	Dynamic viscosity [$Pa.s$]
η_{warp}	Knock-down factor
ν	Poisson`s ratio
ν_i	Poisson`s ratio of indenter
σ	Normal stress [Pa]
σ_0	Initial stress value during stress relaxation [Pa]
σ_c	Contact Stress [Pa]
σ_f	Final stress value during stress relaxation [Pa]
σ_ξ	Width of distribution with respect to misalignment angle [Ra]
τ	Time constant [s]

Subscripts:

0	Initial value
a	Arithmetic
c	Composite
f	Fibre
k	Matrix
m	Effective medium
q	Root mean square
re	Resin
r	Reduced
s	Consolidated warp
t	Tow
$warp$	Wavy warp tow
x	Parallel to x-axis
y	Parallel to y-axis
z	Parallel to z-axis

List of Abbreviations:

3D	Three-Dimensional
AC	Articular Cartilage
AFM	Atomic Force Microscopy
ALE	Arbitrary Lagrangian Eulerian

ALG-PAAm	Alginate-Polyacrylamide
APS	Ammonium Persulfate
CAE	Computer Aided Engineering
CoF	Coefficient of Friction
FEA	Finite Element Analysis
FEM	Finite Element Method
HC	Hydrogel Composite
IPN	Interpenetrating Polymer Network
MBAA	Methylene-bis-acrylamide
NCH	Nanocomposite Hydrogel
OA	Osteoarthritis
PCL	Poly-capro-lactone
PEEK	Poly-ether-ether-ketone
PEG	Poly-ethylene-glycol
PET	Poly-ethylene-terephthalate
polyHEMA	Poly-(2-hydroxylethyl)-methacrylate
PLAGA	Poly-lactide-co-glycolide
PP	Poly-propylene
PVA	Poly-vinyl alcohol
PVDF	Poly-vinylidene fluoride
RVE	Representative Volume Element
SEM	Scanning Electron Microscopy
Si-NPs	Silica Nanoparticles
TEMED	Tetra-methyl-ethylene-diamine
THR	Total Hip Replacement
TJR	Total Joint Replacement
TKR	Total Knee Replacement
UHMWPE	Ultra High Molecular Weight Poly-ethylene
USP	United States Pharmacopeia

Chapter 1

INTRODUCTION

1.1 Background

In the past decades, the advent and the prevalence of orthopaedic prostheses have significantly helped millions of patients worldwide to relieve from the pain associated with joint diseases that destroy the articular cartilage (AC) tissue such as osteoarthritis (OA), and gain their mobility. In addition to great advancements in surgical procedures, design and manufacturing technologies of various joint prostheses have been evolved to achieve higher longevity, beside causing less inflammatory side effects, once it is implanted inside patient's body [1, 2]. However, total knee replacement (TKR) and total hip replacement (THR) are still exclusive to the elderly and not recommended for the young to middle-aged patients suffering from joint disease and localised articular cartilage (AC) lesions. This is mainly due to the limited lifespan they offer, as the failed prosthesis might lead to a more invasive revision surgery, which is usually carried out only once in the patient's lifetime. Current remedies for such young patients, including medication, marrow stimulation [3] and cartilage transplantation [4] are all considered as temporary treatments, which in some cases might lead to regenerated AC tissue with inferior properties to the existing one, with limited durability [5, 6]. On the other hand, total joint replacement, is known as an invasive surgery, through which the entire AC tissue covering the end of bones, together with the neighbouring portion of bone are

removed and replaced by a prosthesis made of metallic, ceramic and polymer components. There is always chance of complications and implant failure post-surgery, such as aseptic loosening and infection. According to previous studies, the average lifespan of TKA and THA are 15 and 10 years, respectively [7, 8]. Osteolysis, the destruction of bone tissues occurs in the vicinity of total joint prosthesis mainly due to the inflammatory response of bone tissues to wear debris released from metallic (due to fretting corrosion [9]), and polymer components, is known as a major reason for TKA and THA implant loosening, leading to implant failure and the need for a further revision surgery [10]. Lastly, the significant stiffness difference between the prosthesis and the bone causes remodelling and resorption of neighbouring bone cells, as less load is transferred and applied to them, known as stress shielding [11].

To this end, an alternative synthetic cartilage replacement (hereafter, "the implant") should be investigated and be developed for the young patients with localised damaged AC, to prevent further tissue degeneration by removing the AC lesions, and replacing them with the minimally-invasive implant, hence preserving the healthy tissue, and prolonging the tissue functionality. Moreover, the implant could greatly contribute in postponing the joint replacement, if not totally eliminating the need for such surgical operation altogether. Due to its minimally-invasive feature, it is expected that the implantation could be performed on the patient's joints multiple times to replace damaged tissues until joint arthroplasty becomes inevitable. In the following section, the design and structural materials for the implant will be proposed.

1.2 Conceptual Design of a Minimally Invasive Joint Implant

Concerning the gap exists in the treatment of young patients suffering from localised cartilage lesion, an innovative cartilage replacement is described in this section

(initially proposed by Schmid [12]) that is supposed to replace the damaged regions and serve as a local correction, keeping the healthy tissue intact. A schematic of knee joint is shown in Fig.1.1 (a) with the implant, together with the sectional view as shown in Fig.1.1 (b). With regard to its dimension, it could be envisioned as a plug, with the size flexible to the area of damaged tissue, and 2.5-4.5 mm in thickness close to the thickness of the AC tissue and subchondral bone combined. The implant would be surrounded and partially anchored by the neighbouring AC tissue. As for the implant fixation, the subchondral bone is to be removed during operation, exposing the trabecular bone to the base of the implant, in which some metal fibres, would grab onto and affix to the porous trabecular bone. The metal fibres are attached to a metal weave with 50% -70% porosity and pore size of approximately 0.5 mm that could facilitate bone ingrowth, also known as osseointegration [13]. Medical-grade titanium alloy (Ti4Al6V) is commonly used in orthopaedic prostheses, as promoting osseointegration, and could be considered as a potential candidate for the metallic layer of the implant. The material then transitions into structural polymer weave, with through-the-thickness gradient in fibre size, offering a combination of strength and compliance. This layer would be further infiltrated by a hydrogel to provide a lubrication mechanism similar to natural AC, a significant advantage over the dense polymer used in total joint replacement.

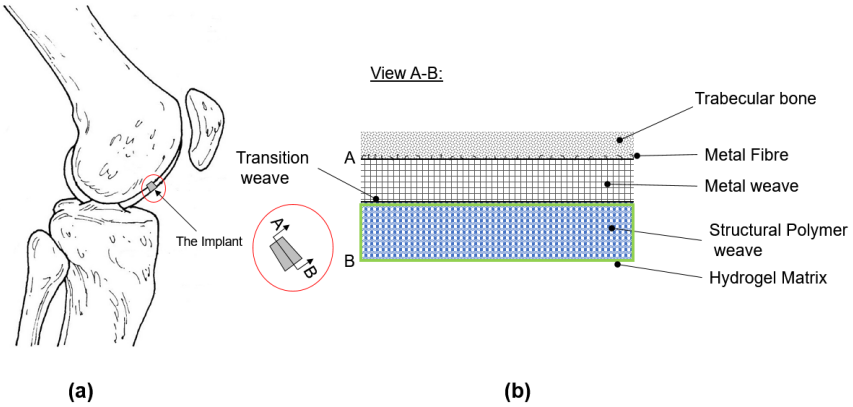

Figure 1.1 *(a) Schematic of a knee joint with the implant replacing the AC lesions [14], (b) the conceptual cross-sectional view of the implant as described in this study*

The implant would have the benefits of providing robust bone-implant integration without significant bone loss, structural strength and acceptable resilience due to the presence of the polymer weave and the hydrogel matrix. Based on this concept, a three-dimensional (3D) woven textile, produced by interweaving of metallic and polymer weaves, is suggested for the main structure of the implant. The rationale behind selection of woven textile and hydrogel matrix as the main components of the implant would be highlighted in the following sections. As a load-bearing component, the implants are subjected to different levels of compressive, tensile and shear stresses during their service life. Friction and wear not only affect their lifespan, but also might influence the countersurface, i.e. opposing cartilage tissue, and wear debris could be detrimental once it is released in the biological environment, in addition to causing "third-body" wear [15]. For the success of proposed implant, it is therefore imperative to assess their mechanical and tribological performance to achieve a desirable structure, prior to implantation and further clinical studies. Study on the mechanical and tribological performance of hydrogel matrix composites are therefore the main focus of current research.

1.3 Three-Dimensional Woven Textiles

3D woven textiles are produced by adding up the binder yarns that pass through the thickness of the 3D fabric, comprising multiple layers of longitudinal warp yarns, interlaced by the transverse weft yarns. The binder yarns are used to reinforce the entire 3D woven structure to provide strong out-of-plane properties, of which the conventional 2D woven textile would lack [16]. Once being used as a reinforcing constituent of a matrix in a 3D woven composite, they provide delamination resistance and damage tolerance, resulting in much superior properties, as compared to 2D woven composites. Moreover, near-net-shape manufacturing method is possible with 3D woven textile,

leading to a higher efficiency and lower cost of the final product. Different sizes of warp and weft yarns could be implemented through the thickness of the fabric during weaving process, allowing gradient in stiffness and porosity, which can be tailored to mimic the stiffness gradient observed in AC tissue [17]. Interestingly, the AC tissue would benefit from a collagen fibre-reinforced structure, with denser fibres adjacent to the articulating surface [17]. Interweaving polymer and metallic weave is also feasible by 3D weaving. Depending on the weaving path of the binder yarn, different 3D woven architectures could be fabricated, as shown schematically in Fig. 1.2, namely, orthogonal, angle-interlock, and layer to layer. The warp yarns lie parallel to the direction of weaving process (x-axis in Fig.1.2), while weft yarns are oriented orthogonal to warp tows and in y-direction.

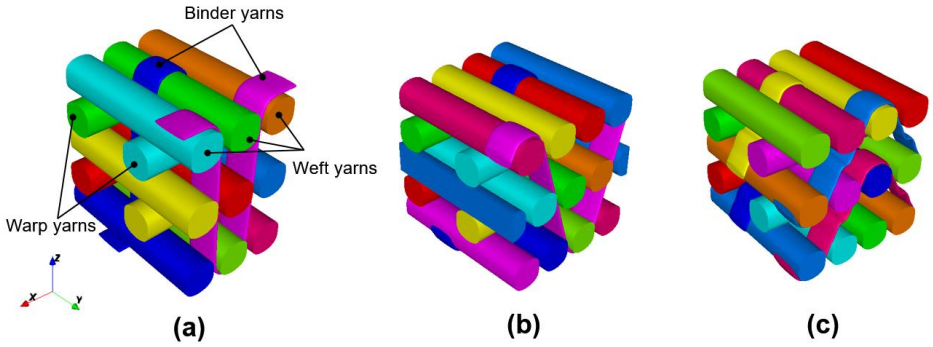

Figure 1.2 Typical woven architectures used in 3D woven textiles: (a) orthogonal, (b) angle-interlock, (c) layer to layer

1.4 Hydrogels as a Potential Candidate for Cartilage Replacement

Hydrogels comprise 3D network of crosslinked hydrophilic polymers that can absorb water or other solvents, once being held in aqueous environment, and swell without being dissolved. Hydrogels are widely used in numerous biomedical applications, such as regenerative medicine [18, 19], drug delivery [20-22], wound dressing [23], tissue engineering [24-26], etc. As hydrogels were found to be biocompatible, offer low protein

absorption rate, and can generate a lubrication mechanism similar to cartilage, they are suggested as a promising candidate for cartilage replacement [27]. The most common hydrogels studied for such application include polyvinyl alcohol (PVA) [28] , poly (2-hydroxylethyl) methacrylate (polyHEMA) [29] , and poly-(2Acrylamido-2methypropane sulonic acid)/ poly (N, N'-dimethyl acrylamide) (PAMPS/PDMAAm) [30]. However, hydrogels exhibit poor mechanical performance, such as low strength and low toughness, as compared to cartilage tissue, which restricts their use in load-bearing applications. Relatively low elastic moduli of the hydrogels indicate they cannot bear the load levels that are usually experienced by cartilage tissue, as they would undergo large deformations. To overcome this issue, various methods were investigated, including developing entangled multiple polymer networks, known as interpenetrating polymer network (IPN) hydrogels [31, 32], fibre-reinforced hydrogel composites [33], and nanoparticle-reinforced hydrogel nanocomposites [34-36]. Each method is depicted schematically in Fig.1.3. It is expected that with improvements in mechanical and tribological properties, hydrogels could be considered as a promising candidate for cartilage replacement.

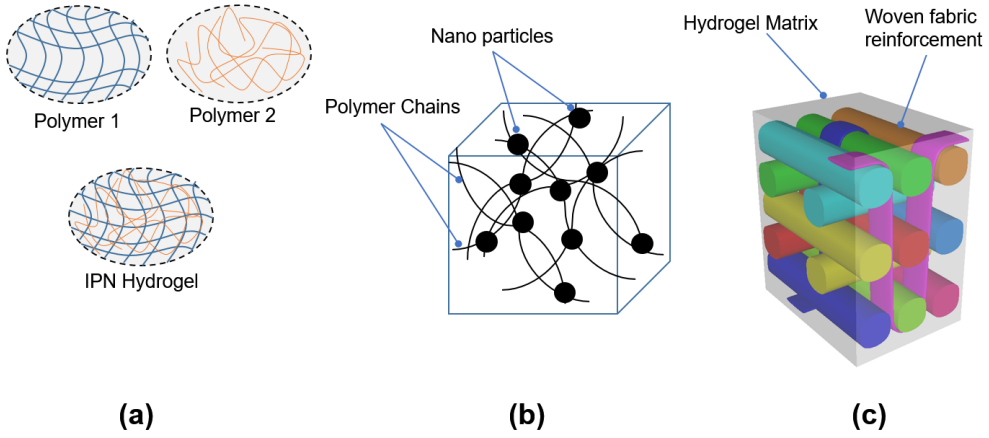

Figure 1.3 Schematic illustration of various concepts for improving the mechanical response of hydrogels: (a) entanglement of polymer networks [37], (b) incorporation of nanoparticles [38], (c) fibre reinforcement

1.5 Aims of the Study

This research aims to investigate a number of mechanical assessment methods for new class of orthopaedic implants, ideally suited for the currently unaddressed ailments associated with young patients. Due to increasing trends in research and development of hydrogels for use as synthetic cartilage, the investigations are expanded to IPN hydrogels as well as nanoparticle-reinforced hydrogels, in addition to the 3D woven hydrogel composite highlighted in section 1.2. The mechanical and tribological responses of all three types of potential candidates for synthetic cartilage will be investigated in this study through experimental approach as well as finite element simulations. The aims of the current study are as follows:

- Design and development of 3D woven textiles with desired properties suitable for cartilage replacement.
- Selection of proper materials based on literature review with the focus on those less explored potential candidates for the application.
- Synthesis of aforementioned hydrogels and composites for the proposed implant.
- Design of suitable experiments to effectively assess each candidate for the desired application and study the parameters that could affect their mechanical and tribological responses.
- Development of finite element models to simulate sliding wear for the neat 3D woven textiles, as well as the textile-embedded hydrogel composites and parametric studies after FE models validations.

1.6 Significance of the Study

A survey conducted in 2011 on the prevalence of total knee replacement and revision surgeries across 18 countries with the total population of 755 million, revealed approximately 1,324,000 TKR and revision surgeries were performed annually [39]. The figures showed an average of 10% annual growth in TKR procedure between 1997 and 2008 in western countries including USA, Canada, Australia and some European countries. According to a recent study, between 2006-2011, a total number of 31260 and 31958 operations performed in New Zealand for THR and TKR, respectively, while by 2026, the demand for those surgeries will be increased by 84% and 183% for THR and TKR, respectively [40]. The study conducted by the World Health Organization (WHO) indicates OA is ranked 18th among all injuries/disease in the pacific region, imposing heavy costs on healthcare section [41]. Traumatic joint injuries are known as a major cause for early-onset OA, and for the majority of patients who are within the 17-30 years age group, the signs of OA, might appear on average fifteen years after the injury [42]. This suggests that for such patients, the age for diagnosable OA, is 35 to 40 years of age, at which TKR is too early to be implemented. Persistent joint or spine pain might lead to less mobility, which in turn gives rise to risk of developing other conditions such as cardiovascular disease and diabetes. According to a survey, nearly 17% of New Zealanders reported chronic pain in joints [43]. Ministry of Social Development data indicate that in 2009, over one fifth of all sickness and benefit payments are provided for bone and joint disorders costing $320 million for NZ companies [44]. An analysis of eight-year injury claims data of the Accident Compensation Corporation (ACC) for rugby league injury in NZ showed the knee-related injuries were the most prevalent ones [45]. These data suggest there is a real need for investigations on an alternative implant that could prevent the progression of OA in young patients, hence postponing joint replacement, in addition to providing pain relief and mobility recovery.

Friction and wear behaviours together with the mechanical response of such implant govern its reliability and effectiveness. Therefore, it is important to allocate some research resources for the characterisation of mechanical and tribological properties under realistic situations, which helps in design, development and optimisation, prior to implantation inside living organism (also called *in vivo*).

1.7 Overview of the Research

In this research, only the load-bearing region of the implant described in section 1.2, including polymer weave infiltrated with a hydrogel, will be evaluated by various mechanical and tribological experiments, and compared with ALG- PAAm IPN hydrogel, as well as silica-nanoparticle-reinforced ALG-PAAM hydrogel nanocomposite as other potential candidates. Moreover, the numerical models of neat 3D textiles and 3D woven hydrogel composites will be developed and being studied under similar sliding wear conditions. The thesis outline is briefly as follows:

In chapter 2, a comprehensive literature survey is conducted to elucidate the various aspects of characterisation methods being implemented previously for hydrogel composites with respect to elastic deformation, and time-dependent response. The focus will be on the tribology of hydrogel matrix composites. Furthermore, potential research gap and research questions will be identified.

Chapter 3 describes the materials and methods, implemented in this study for the experiments, as well as the finite element model development.

The experimental results and findings for the studied IPN hydrogel, hydrogel nanocomposite, and 3D woven hydrogel composite are gathered in chapters 4, 5 and 6, respectively.

Chapter 7 presents finite element analysis (FEA) of sliding wear, and model validation. Parametric studies are also conducted to study the effect of main parameters on the wear rate of textiles.

Finally, the conclusions and recommendations for future studies are highlighted in chapter 8.

The thesis includes information already published in [46-49].

Chapter 2

LITERATURE REVIEW

2.1 Articular Cartilage

2.1.1 The Structure of Articular Cartilage

Articular cartilage, a smooth tissue covering the epiphysis of long bones in diarthrodial joints, plays a crucial role in load distribution and almost frictionless movement, once the bones articulate. Unique biomechanical characteristics and multiphasic fibre-reinforced structure with anisotropic, viscoelastic, nonlinear and inhomogeneous material properties, are known to provide an ultra-high wear resistance and damage tolerance that would lead to several decades of service life [50, 51]. Articular cartilage comprises mainly of type-II collagen fibres, cartilage cells (chondrocytes), proteoglycan molecules, and water [52]. The structure of cartilage was found as a solid matrix containing interstitial fluid, accounts for 70%- 80% of tissue mass [53]. As illustrated schematically in Fig. 2.1, there exist three distinct zones, namely, superficial, middle and deep zones. It was found that the orientations of collagen fibres are zone-dependent and they are arranged parallel to the articulating surface in the superficial zone, with the highest level of density and water content [52]. Underneath, there is a middle zone with a lower collagen fibre density, and randomly oriented fibres transition to a deep zone, characterised by relatively larger fibre size, arranged perpendicular to the tide mark. Throughout the thickness of the cartilage, the number of chondrocytes dwindle, while they become larger in size [53]. The articular cartilage can be embodied as a fibre-

reinforced hydrogel composite material. It is believed the composite structure of the cartilage would contribute to withstanding compressive and tensile loads. The orientation of collagen fibres within the matrix and load transfer from the low stiffness matrix to the fibres affect the mechanical behaviour of cartilage. For an effective fibre-matrix load transfer, a strong interfacial bonding is essential. Interestingly, the surface of Type II collagen fibres are equipped with Type IX collagen, which facilitates the interaction between fibre and matrix phases in cartilage [54].

Moreover, articular cartilage is avascular and aneural, implying limited healing capacity of damaged regions due to the lack of blood vessels and nerves, which are typically found in the majority of living tissues. The most prevalent causes of cartilage damage include osteoarthritis (OA) and trauma. OA is a progressive, degenerative disease that affects the performance of cartilage by initially restricting the swelling ability of the tissue, which in turn reduces the overall compressive stiffness and causes mechanical failure and tissue deterioration. This might lead to bone-to-bone contact, joint inflammation, and joint stiffness, resulting in pain, and lack of mobility for the patient.

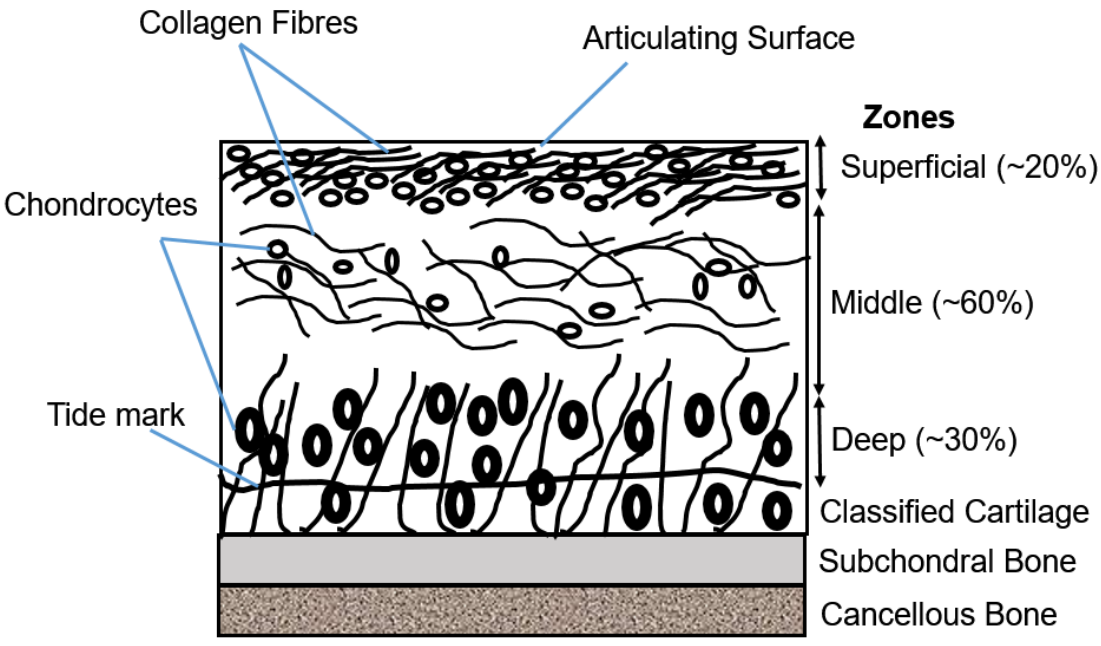

Figure 2.1 Schematic structure of the articular cartilage [53]

2.1.2 Treatment Methods for the Damaged Cartilage

A recent study indicated that over 27 million people struggle with damaged cartilage, with several million patients are added each year, while the knee joint was found to be affected the most [55]. To prevent the OA progression, the surgeons implemented a number of less invasive surgical procedures, for instance arthroscopic lavage, which can relief the pain, but not repairing the damaged cartilage. To date, the most effective reparative techniques, commonly applied for small lesions, are based on marrow-stimulating approach. One of these reparative techniques is microfracturing [56], which involves drilling several holes in the subchondral bone, allowing the marrow components containing mesenchymal stem cells to reach the damaged regions, encouraging the repair process. However, the regenerated tissue, called fibrocartilage, was found to offer inferior mechanical properties as compared to the healthy cartilage, and although helping the patient to recover from joint pain, it might degenerate approximately a year after regeneration [57, 58]. Another surgical method is cartilage grafting either from the patient or from a cadaveric source, which according to the articles published in recent years, provides mediocre and temporary results in the best-case scenario [56, 59, 60]. Eventually, the OA might progress to the severe level, at which the cartilage resurfacing is not feasible and Total Joint Replacement (TJR) is inevitable, which is restricted to the elderly, as mentioned earlier.

Alternatively, cartilage regeneration through the methods associated with tissue engineering, was reported in the literature [61]. The rationale is to form new tissues using chondrocytes or stem cells, either with or without biodegradable synthetic scaffold, acting as a support medium during the formation of tissue and withstanding loads. Despite the great efforts and advancements made, the regenerated tissues cannot be considered as a long-term solution, as they are still struggling with the limited lifespan and inferior

mechanical properties [62]. The most promising results were reported once the tissue was developed from cultured juvenile chondrocytes, as more extracellular matrix (ECM) was produced in comparison to adult chondrocytes, resulting in an enhanced mechanical stability and better maintenance [63, 64]. However, donor availability is a major issue restricting the widespread application of juvenile chondrocytes. To this end, a long-term cartilage treatment method does not currently exist.

2.1.3 Biomechanical Characteristics of Articular Cartilage

The articular cartilage benefits from a biphasic permeable structure with anisotropic, viscoelastic and inhomogeneous material characteristics [51, 65]. These properties are known to provide the load-bearing capacity for the tissue, in addition to energy dissipation and lubrication during joint movement. Under tensile loading situation, the collagen fibres embedded within the ECM are rearranged parallel to the loading direction. As the tensile load increases, crosslinked collagen fibres are further stretched, giving rise to the elastic modulus of the cartilage. Previous experiments has revealed the Young's modulus of healthy cartilage is in the range of 0.4-10 MPa [66].

As mentioned previously, there exists an uneven distribution of collagen fibres within ECM of cartilage tissue, suggesting depth-dependent and direction-dependent materials properties [67, 68]. Therefore, the elastic modulus was found significantly larger for the superficial region, as compared to the other zones [69]. Moreover, the fibres arranged in parallel to the articulating surface, lead to different tissue responses in tension and compression. It was observed that the tissue stiffness is remarkably higher in tension than in compression, approximately two-orders of magnitude, contributing to the unique biomechanical properties of cartilage [70]. Under compressive load, the reinforcing collagen fibres hamper the radial stretch of the cartilage, resulting in a more effective

pressurisation of the interstitial fluid [71]. This pressurisation contributes both in load-bearing capacity and ultra-low friction levels observed in cartilage [72]. The cartilage tissue also exhibits time-dependent mechanical response, known as viscoelasticity, such as creep and stress relaxation, mainly attributed to the flow of interstitial fluid within the permeable structure of the matrix, and the viscoelastic properties of other constituents such as collagen fibres [73].

2.1.4 Friction and Wear Properties of Articular Cartilage

Wear is the gradual removal of material at an interface due to the shear and normal forces and/or sliding motion, and is usually measured by gravimetric or volumetric methods. However, wear quantification of articular cartilage is a complex issue, due to difficulties in measuring extremely small wear volume of soft tissues. Wear can be intensified by factors such as injuries, abnormal loading, physiological change of tissue matrix, absence of lubrication, etc. It was found the wear of articular cartilage is area-dependent and for instance in the knee joint, the medial compartment of the cartilage is normally more prone to wear, due to the uneven load distribution of the knee joint [74]. Magnetic resonance imaging (MRI) and radiographic studies are usually utilised for the screening of cartilage morphology and tracking of degeneration [75, 76]. Cartilage wear was investigated in a research with the aid of knee simulator, using ovine cartilage [77]. Surface morphology as well as wear debris were used in wear assessment. Scanning electron microscopy (SEM) examination showed visible pitting and accumulation of wear debris on the worn surface, specifically after 7000 cycles with severe deformation, and surface cracks at 18000 cycles. As the wear process continued, wear particle size decreased, with more irregularly shaped debris. In a living cartilage, superficial damages will heal, whereas for the cartilage specimens studied in joint simulators, the damage

occurred to the cartilage surface, resulting in visible lesions and accumulated damage to ECM. It was suggested in another study that there exists a phospholipid layer on the outer surface of articular cartilage, preventing direct contact between opposing cartilage surfaces, and contributing in wear-resistance of articular cartilage [78]. Without synovial fluid lubrication, this phospholipid layer governs the friction and wear of articular cartilage and with the removal of lipid layer, accelerated cartilage wear occurred. In the presence of synovial fluid, interstitial fluid pressurisation of cartilage contributed significantly to the ultra-low CoF observed during joint articulation. In a study conducted on bovine femoral-tibial joints, it was revealed that friction was lowered down by a factor of 1.5 in the presence of synovial fluid, compared to saline solution. This factor was reached to almost 60, when the pressurised intestinal fluid was compared to its equilibrium, zero-pressure state [79].

The existing classical lubrication theories were utilised to describe the lubrication process observed in synovial joints and it was realised that no individual theory would be able to describe the entire tribological characteristics, suggesting multiple mechanisms would be present in synovial joints [80]. Mow et al. [50] developed the biphasic constitutive equations initially to elucidate the compressive behaviour of articular cartilage, indicating the fluid phase is pressurised under the load, and weeps out of porous, deformable solid matrix, contributing in lubrication. Load-bearing and friction characteristics of cartilage arise from its biphasic nature, high porosity of the matrix (75%-80%), effective pore size (2-6.5 nm), and the presence of charged proteoglycan groups, all leading to low permeability (10^{-15} to 10^{-16} $m^4/N\ s$) [81]. Therefore, fluid flow within the matrix causes robust drag forces, producing pressure gradients. The pressurised fluid carries the majority of the applied load until it eventually exudes from the matrix into the regions with less pressure. Eventually, the load is transferred to and carried by the solid phase. As the coefficient of friction of mating cartilage surfaces is mainly

controlled by the solid matrix, and the shearing between the two surfaces, it will be maintained relatively low, as long as most of the load is carried by the fluid phase [82]. This phenomenon is explained by “biphasic lubrication” as theoretically suggested by Mow et al. [50], and experimentally demonstrated by Forster and Fisher [82]. Followed by decrease in fluid load support, the lubrication regime will transition to boundary lubrication, and the morphology of cartilage surface would affect the friction coefficient. Under boundary lubrication, the surface-to-surface contact can be prevented, as the synovial fluid could be adsorbed by the cartilage surface, resulting in minimising friction and wear.

2.2 Three-Dimensional Woven Composites

2.2.1 Applications and Benefits over Conventional Laminated Composites

3D woven preforms were initially used as a reinforcement of carbon-carbon composites for aircraft breaks in 1972, as an alternative to the expensive metallic alloys for high temperature applications [83]. A decade later, 3D woven composites were also used as structural materials for the combustion compartment of hypersonic missiles [84]. In general, these structures have been used as a reinforcing phase in aerospace and marine components, such as stringers and stiffeners, where the cost or the performance of traditional laminated composites has restricted their applications. In recent years, 3D woven preforms have found new applications such as tissue engineering of biodegradable scaffolds for cartilage reconstruction [51, 85] in biomedical industry, as well as structural materials for industrial components such as pressure vessels, and wind turbine blades, where the out-of-plane loading is present. In construction industry, lightweight I-beams made from 3D woven composites has been implemented in the roof section of ski chair-lift buildings as an alternative to heavy steel beams to save costs, and to acquire better

mechanical performance [86]. These materials were also used as H-joint connectors to join honeycomb sandwich wing panels of Beechcraft Star ship, leading to an effective improvement in stress transfer at the joint, and a reduction of the peeling stress [87]. With regards to weaving pattern, layer-to-layer and angle interlock types were implemented in applications such as brackets, t-shaped profiles, and curved beams, where the load is supposed to be transferred through a bend, as they can exhibit better performance against interlaminar shear and radial stress experienced in those structures [88]. Orthogonal weave type composites were successfully utilised in the manufacturing of fan blades, engine casing of Airbus A320 Neo, and barrel stringers of the aircrafts [89]. Hemrick et al. [90] reported the application of orthogonal woven composites in low-weight heat exchangers for automotive radiators, due to the high thermal conductivity of orthogonal architecture.

Compared to laminated composites, 3D woven composites offer improved out-of-plane properties, owing to the binding yarns introduced in the normal direction to weft and warp yarns, resulting in an enhanced delamination resistance. Furthermore, the fabric architecture can be altered by the designer through parameters such as weave pattern, tow size, fibre type, tow count, etc., to meet desired requirements [91]. It was revealed in a past study that 3D woven preforms were able to absorb twice as much as the impact energy absorbed by 2D woven constructs, without any sign of fibre damage, suggesting their potential capacity for load-bearing applications [92]. The compression after impact test, showing damage initiation and further propagation, was performed and 3D woven textiles showed up to 79% higher performance compared to 2D woven fabrics [93]. Other properties observed in these materials, including high interlaminar toughness [93], and high strain to failure, an indication of damage-tolerance [94, 95], suggest 3D woven preforms as an efficient structural component for load-bearing applications.

2.2.2 Manufacturing Methods

3D textiles can be woven by the conventional weaving instrument, although Jacquard looms are commonly used as they offer high level of automation, and extensive control over the weave structure, resulting in less manufacturing costs and enhanced quality [96]. Compared to conventional methods used for manufacturing of laminated composites, near-net-shape production is feasible with 3D textile composites, suggesting reductions in material waste, production time, bonding, and labour costs, as no ply layup is required. A typical weaving process is schematically illustrated in Fig. 2.2. Prior to the initiation of weaving process, the warp yarns are passed through a comb-like device followed by winding onto cylindrical beams (*warp beam winding*).

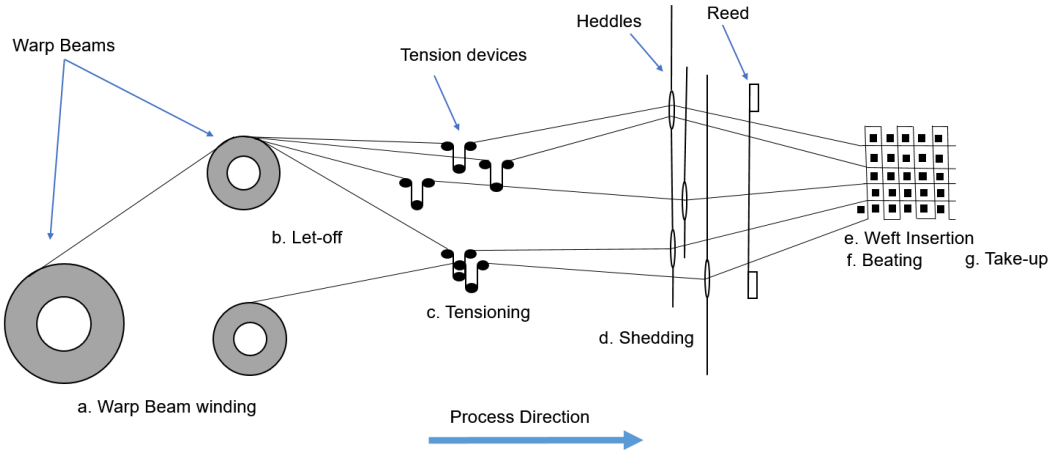

Figure 2.2 Schematic illustration of the process for weaving 3D textiles [97]

Then, the warp yarns are drawn off towards the tensioning devices (*let off*), where the yarns are stretched to ensure no slack and simultaneously prevent yarn over-tensioning (shown as *tensioning* in Fig. 2.2). Therefore, this stage prevents yarn slack, which might lead to yarn entanglements during next weaving stages, as well as over-tensioning, resulting in fibre damage. Yarn tensioning is achieved by suspended-weight loaded yarn guides of tensioning devices, followed by the tension generated during shedding, and fabric take-up. In case of a tension rise, the suspended weights move up,

breaking an infra-red (IR) beam, which in turn activating the warp beam controller to let-off more warp yarns, and this process is paused again once the weights passed through the lower limit IR beam, hence the yarn tension can be controlled.

Next, the yarns travel through the heddles' "*eyes*", which determine the vertical translation of yarns during the process. Every individual layer is moved up and down in turn to form a gap, called *shed*, and the weft yarns are passed through these gaps, a process called *shedding*. Another set of heddles is used to weave binder yarns perpendicular to warp layers. *Weft insertion* is done using a rapier device, which pulls the weft yarns to pass through warp sheds, followed by the operation of comb-like device, called *reed*, which firmly packs the weft yarns into the textile (*beating*). Finally, the produced textile is pulled along the weaving machine for the weaving process to continue (*take-up*). The 3D textile is now ready for the production of 3D woven composite.

In order to produce composite structures, there exist few methods such as vacuum-assisted resin infusion, and resin transfer moulding (RTM). Under resin infusion process, the 3D woven textile, under a vacuum seal is exposed to a resin flow, infiltrating the preform from inlet pipe, which fills all the internal voids of the fabric while flowing through it to reach the outlet pipe. In RTM, a pre-fabricated mould is used, and the reinforcing textile is initially placed into the mould. It is manually conformed to the mould's shape before sealing the mould and applying vacuum. Next, the resin is injected usually from the centre of the mould, until the excess amounts exit from edges of the mould, ensuring the whole fabric is infiltrated with resin. In both methods, sufficient time must be given to the fluid form resin to be cured and consolidated. Then, the composite material can be removed from the production platform. In this regard, it is imperative to ensure the resin is able to reach all empty spaces inside the woven structures, as the formation of voids might compromise the mechanical performance of the material. Other manufacturing defects include fibre damage, weave distortion and unevenly distributed

resin pockets [98]. These issues might restrict the widespread application of 3D woven composites, implying enough attention should be paid in the manufacturing and characterisation methods, to ensure robust and reliable composites.

2.2.3 Characterisation of Mechanical Performance for the 3D Woven Composites

Due to the enhanced out-of-plane properties of 3D composites as compared to laminated type, some studies investigated such materials subjected to impact loading situations, under low (<10 m/s), high (20-50 m/s) and ballistic (900 m/s) impact velocities [99-101]. The purpose was to investigate the effect of binder yarn architecture on impact damage behaviour of the composites. It was found that orthogonal composites demonstrated higher impact damage resistance in comparison to angle-interlock and layer-to-layer types. Another study revealed energy absorption increases with higher impact velocities. Fibre pull-out, matrix fracture, and fibre breakage were observed as the dominant failure modes of 3D woven composites under impact loading. Delamination on the other hand, was minimised, which is an advantage over laminated composites.

The flexural stiffness and shear strength of 3D woven composites were investigated previously, using a 3-point bend test configuration [100, 102]. As the volume fraction of z-binder increased in the woven structure, the interlaminar shear strength tended to decrease, mainly due to a larger fibre crimp, and the stress concentration caused by introduction of binder yarns, leading to an earlier occurrence of damage and load drop. However, due to the presence of binders, fairly shorter cracks were found in the 3D woven test specimens with a uniform distribution throughout the structure. In contrast, macro cracks were found in the laminated composite, indicating higher strain-to-failure capacity of 3D woven composites under flexural loading. Under such loading condition, the failure

mode was found to be similar to that of uniaxial tensile loading, combined with compression mode. In an attempt to improve the mechanical properties of conventional 3D woven composites, the biased layers were introduced to the weave pattern followed by epoxy resin impregnation, and the mechanical response was assessed using tensile and short beam shear experiments [103]. The results confirmed the specimens with biased yarns outperformed the 3D woven composite, and it contributed in delamination resistance of the structure.

The in-plane properties of 3D woven composites were explored by in-plane tension [104], compression and bending tests [105]. Dominant failure mechanisms include tow breakage and delamination under tensile and compressive loadings, respectively, while a combination of both failure modes was observed under bending scenario. Another study [106] revealed z-binder yarns could slightly enhance the in-plane properties of woven fabrics, attributed to an increase in the planar fibre volume fraction as a result of compaction caused by the binder yarns, regardless of their tow size. Thus, the mechanical properties of the composites are influenced by a combination of factors such as yarn size, fibre orientation, yarn spacing, fibre volume fraction and stacking sequence [107].

2.2.4 Constitutive Material Models Available for 3D Woven Composites

Mathematical models have been extensively developed in previous studies to describe the mechanical behaviour of orthogonal woven composites [108-111]. Briefly, these models can be categorised as analytical and computational material models. Basically, the analytical approach involves some assumptions associated with stress and strain fields, and might lead to immediate results, whereas the numerical models are usually based on finite element discretisation of a continuum medium and free from those

assumptions. In terms of modelling scale, they can be classified as micro-, meso-, and macromechanical models. In the micromechanical approach, the properties of yarn fibres are studied, while the mechanical characteristics of fabric unit cell and the textile fabric as a continuum medium are explored in mesomechanical, and macromechanical approaches, respectively. A fabric unit cell, also known as representative volume element (RVE), is defined as the smallest building block of the textile, as an assembly of repeated unit cells can form the textile.

Hage et al. [110] proposed a unit-cell-based analytical model for a 3D woven composite made of epoxy resin and 3D orthogonal weave of T300J carbon fibres. The global stiffness matrix ($C_{ij,Global}$) could be expressed using:

$$C_{ij,Global} = \frac{1}{V_t} \sum_{k=1}^{n} V_k . C'_{ij,k} \qquad i = 1-6\,,\ j = 1-6 \tag{2.1}$$

where $C'_{ij,k}$ is the elastic stiffness matrix for each constituents of the unit cell, containing their elastic properties, while V_k and V_t are the volume fraction of unit cell components, and total volume of unit cell, respectively. As the whole composite can be built based on the unit cell duplication in space, the mechanical response of the composite under loading can be determined by studying the unit cell, comprising of warp tows, weft tows, binder yarns and matrix. The elastic properties of the unit cell were computed from calculation of mechanical properties of the yarns, obtaining the local stiffness matrices based on homogenization method and computation of total stiffness matrix, taking into account the volume of each component (resin and yarns).

The Young's moduli of 3D woven orthogonal composite can be obtained based on a model developed by Kou and Pon [112]. It was assumed the yarns within the unit cell were undulated, and treated as spatially oriented solid bodies. Furthermore, normal strain components in each x,y,z directions were assumed as one dimensional (i.e.

$\varepsilon_i\,(i), i = x, y, z)$, due to the uniaxial deformation assumption made. The stress-strain relations were expressed as:

$$\sigma_{xx}^{k} = \overline{Q}_{11}^{(k)} \varepsilon_x(x) + \overline{Q}_{12}^{(k)} \overline{\varepsilon}_{\,y} + \overline{Q}_{13}^{(k)} \overline{\varepsilon}_{\,z} \tag{2.2}$$

$$\sigma_{yy}^{k} = \overline{Q}_{12}^{(k)} \overline{\varepsilon}_{\,x} + \overline{Q}_{22}^{(k)} \varepsilon_y(y) + \overline{Q}_{23}^{(k)} \overline{\varepsilon}_{\,z} \tag{2.3}$$

$$\sigma_{zz}^{k} = \overline{Q}_{13}^{(k)} \overline{\varepsilon}_{\,x} + \overline{Q}_{23}^{(k)} \overline{\varepsilon}_{\,y} + \overline{Q}_{33}^{(k)} \varepsilon_z(z) \tag{2.4}$$

where Q denotes the stiffness matrix, k denotes unit cell components (tows in x, y, z, directions and the matrix), and $\overline{\varepsilon}_{\,i}$ are the average strain values obtained from:

$$\overline{\varepsilon}_i = \frac{1}{L_i} \int_0^{L_i} \varepsilon_i(i) di \;, i = x, y, z \tag{2.5}$$

where L_x, L_y, and L_z are the unit cell dimensions in x, y, and z directions, respectively. This simply implies, the global strain function, $\overline{\varepsilon_i}$(i), was determined by averaging the normal strains over the unit cell dimensions.

By using the geometric and stiffness data for tows as well as force equilibrium, the normal strain functions, $\varepsilon_i(i\,)$, were determined with respect to the applied stress field.

$$F_{ii} = \sum_k A_i^{(k)}(i)\, \sigma_{ii}^{(k)}\,(i)\,, i = x, y, z \tag{2.6}$$

Here, F_{ii} denotes the reaction force acting on the unit cell face normal to i-axis and in the direction of i-axis ($i = x, y, z$), and $A_i^{(k)}$ are the cross-sectional area functions of k^{th} constituents normal to i-axis. Substitution of (2.2-2.4) into (2.6) yields to:

$$\varepsilon_x(x\,) = \frac{F_{xx} - \sum_k A_x^{(k)}(x)[\overline{Q}_{12}^{(k)} \overline{\varepsilon}_{\,y} - \overline{Q}_{13}^{(k)} \overline{\varepsilon}_{\,z}]}{\sum_k A_i^{(k)} \overline{Q}_{11}^{(k)}} \tag{2.7}$$

The other two normal strain functions $\varepsilon_y(y)$ and $\varepsilon_z(z)$ could be obtained likewise. The external applied stress at a far distance, σ_{ii}^{∞}, must be in equilibrium with the corresponding reaction force. For instance, for *x* direction:

$$F_{xx} = L_y L_z \sigma_{xx}^{\infty} \tag{2.8}$$

Similarly, σ_{yy}^{∞} and σ_{zz}^{∞} could be computed. Next, the stiffness matrix for the unit cell of the woven composite was computed using stress and strain vectors:

$$\begin{bmatrix} \sigma_{xx}^{\infty} \\ \sigma_{yy}^{\infty} \\ \sigma_{zz}^{\infty} \end{bmatrix} = \begin{bmatrix} Q_{11}^{c} & Q_{12}^{c} & Q_{13}^{c} \\ Q_{21}^{c} & Q_{22}^{c} & Q_{23}^{c} \\ Q_{31}^{c} & Q_{32}^{c} & Q_{33}^{c} \end{bmatrix} \begin{bmatrix} \overline{\varepsilon}_x \\ \overline{\varepsilon}_y \\ \overline{\varepsilon}_z \end{bmatrix} \tag{2.9}$$

Here the superscript *c* indicates the array values are related to the composite. The expressions for Q_{ij}^{c} are listed in [112]. Finally, the Young's moduli was obtained from the inverse of stiffness matrices, called compliance matrix, [$\mathbf{S}^{c}$].

$$E_x = \frac{1}{S_{11}^{c}} \tag{2.10}$$

$$E_y = \frac{1}{S_{22}^{c}} \tag{2.11}$$

$$E_z = \frac{1}{S_{33}^{c}} \tag{2.12}$$

In comparison with the experimental results, analytical Young's moduli predicted larger values, which according to the authors, was attributed to manufacturing defects of tested materials.

Another approach implemented previously for the prediction of mechanical response of 3D woven composites was based on orientation averaging (OA) method, also known as homogenization method [113, 114]. According to this method, the composite is discretised into volume elements, where all constituent tows are aligned in the same

direction. Thus, each element could be treated as a single laminate with isotropic properties in transverse direction. By averaging all constituent elements and assuming either iso-stress or iso-strain situations, the properties of the woven composite was characterised. The in-plane properties of 3D woven angle-interlock composites under tensile loading was predicted using an orientation averaging model, and the classical laminate theory [115]. The unit cell was initially discretised into several subsections, as supposed to have unidirectional lamina configuration, and the predicted properties for the plain weave were in good correlation with experimental findings. It should be noted that structural defects such as yarn waviness, are not considered in OA approach, which was addressed in a developed OA-based model by Cox and Dadkhah [94]. A stiffness degradation parameter, known as *knock-down factor*, η, was introduced to take into account out-of-plane waviness, whereas in-plane waviness was found insignificant and therefore was neglected. A loaded wavy tow was assumed as a sequence of unidirectional distorted segments, carrying out the equal amount of stress in the load direction. The knock-down factor can be approximated expressed as:

$$\eta_{warp} \approx \left\{1 + \sigma_{\xi}^{2}\left[\frac{E_{x}^{(UD)}}{G_{xy}^{(UD)}} - 2\left(1 + \nu_{xy}^{(UD)}\right)\right]\right\}^{-1} \tag{2.13}$$

where η_{warp} denotes the knock-down factor for the wavy warp tows, and σ_{ξ} denotes the width of distribution corresponding to the misalignment angle, obtained based on maximum likelihood estimators of normal distribution. $E_{x}^{(UD)}$, $G_{xy}^{(UD)}$ and $\nu_{xy}^{(UD)}$ are engineering constants for a unidirectional composite, subjected to a load with an angle ξ to the fibre direction.

The Young's modulus of the 3D woven composite was obtained using OA. Provided a relatively small misalignment angle, low binder yarn density, and application of modifying knock-down factor mentioned above, the application of OA method leads

to high accuracy in Young's modulus determination. The Young's modulus of consolidated warp, E_s, can be expressed as [116]:

$$E_s \approx \frac{f_s V}{A_s} E_f + \left(1 - \frac{f_s V}{A_s}\right) E_{re} \tag{2.14}$$

where f_s is the ratio of fibres in warp direction, V and A_s are total volume fraction and areal warp fraction, respectively. E_f and E_{re} are the elastic modulus corresponding to the individual fibres and the resin, respectively. The Young's modulus of the effective medium, E_m , incorporating weft and the matrix material elements can now be obtained from (2.15), by assuming weft and matrix as spring elements in series:

$$E_m = \left[\frac{(1 - f_s)V}{1 - A_s} \frac{1}{E_f} + \left(1 - \frac{(1 - f_s)V}{1 - A_s}\right)\frac{1}{E_{re}}\right]^{-1} \tag{2.15}$$

Finally, the Young's modulus of the unit cell could be obtained from rule of mixture:

$$E_1 \approx \ A_s E_s + \ (1 - A_s) E_m \tag{2.16}$$

2.2.5 Investigation of Candidate Materials for the Polymer Layer of the Proposed Implant

Generally, design process of a medical device to be implanted inside human body must involve a systematic sequence. It involves a comprehensive analysis of required functions of the biomaterial, its localisation within the living environment, properties of the surrounding tissues, interaction with the biological fluids, material and manufacturing techniques selections, prototype fabrication and testing of physical and chemical properties, realistic examination of the prototype *in vitro* and *in vivo* (within animal bodies), and finally testing inside human bodies to explore the long-term effects [117].

Therefore, a close multi-disciplinary collaboration is imperative to achieve the desired outcomes.

In recent years, various polymeric materials have been suggested for use in vivo, with a wide range of biomedical applications, such as implantable devices, drug delivery, tissue engineering, etc. [118]. The key factors determining their application as a biomaterial include the following:

- Biocompatibility
- Promoting a desired cellular response
- Mechanical performance

The candidate material must be biocompatible, meaning it should achieve the desired functions within the living environment, without evoking any undesirable effects in the host. The biomaterials must adhere well to the soft tissues or bones, and exert minimal stress on the neighbouring tissues, meaning minimal damage and/or loss of surrounding tissues must be achieved. Furthermore, the candidates must be capable of encouraging desired cellular response, through an active interaction with the host, leading to an effective treatment. Lastly, mechanical and tribological responses determine the reliability and service life of biomedical devices, especially in load-bearing applications, such as joints prostheses. A brief review of the most common polymeric materials suggested for orthopaedic implants is summarised in Table 2.1. These materials could be produced in fibre form, through methods such as electrospinning, allowing the weaving process to be feasible. In general, the selection is based on how well the biomaterial matches with the mechanical properties of the region it is going to be implanted, in addition to the level of bioactivity and integration to neighbouring tissues.

Table 2.1 Summary of common polymeric materials used as artificial organs

Material	Ref.	Key Features	Findings
Ultra High Molecular Weight Poly-ethylene (UHMWPE) (cross-linked)	[119, 120]	- Non-biodegradable - Bearing material in hip and knee implants - High corrosive resistance - Ultra-low moisture absorption - Ultra-low friction coefficient - Characteristic of self-lubrication - High abrasion resistance - Highly cross-linked type was developed to address osteolysis	- Showed similar mechanical behaviour to cartilage and intervertebral discs in compression, torsion and tension, - Bonding to bone with hydroxyapatite coating - Wear Particles of this material can cause inflammatory response of living tissues
Poly-ether-ether-ketone (PEEK)	[121]	- Remarkable chemical resistance - Excellent mechanical properties - Resistance to hydrolysis - High wear resistance - Remarkable thermal properties - Excellent dielectric strength, volume resistivity, tracking resistance - High resistance to radiation	Knitted carbon fibre reinforced PEEK structures were suggested for bone plates due to their strength and potential for bone ingrowth
Polyvinylidene fluoride (PVDF)	[122]	- Non-biodegradable - Excellent biocompatibility - High chemical resistance	An artificial cornea made from multifilament PVDF yarns as scaffold was tested and implanted successfully
Polylactide-co-glycolide (PLAGA)	[123]	- Biodegradable - Excellent biocompatibility - Widespread applications in sutures and fixations devices	A 3D braided PLAGA was produced and evaluated as a bioresorbable tissue-engineered scaffold for Anterior Cruciate Ligament reconstruction
Poly-ethylene-terephthalate (PET)	[124]	- Non-biodegradable - Biostable - Tissue ingrowth encouragement - Well-characterised fibrotic response - Background as orthopaedic implants	polyethylene terephthalate (PET) fabrics were used as a tissue engineering scaffold for tendon replacement

Material	Ref.	Key Features	Findings
Poly-urethane	[125]	- Non-biodegradable - Flexibility in physical and mechanical properties - Application in soft tissue, cartilage reconstruction and bone regeneration - High elasticity	A knee implant made from PU and reinforced by bioactive glass was produced through compression moulding and once implanted on rabbits showed non-toxicity and The tribological surface showed a fibrocartilaginous tissue

2.3 Hydrogel Materials

2.3.1 Biomedical Applications of Hydrogels

Hydrogels benefit from a three-dimensional crosslinked network of hydrophilic polymers, and once being kept in an aqueous medium, can absorb large proportions of water, and retain it within their macromolecular structure, changing in volume (swelling). The hydrogel is water-insoluble, due to the strong physically or chemically crosslinked chains present in its network, while the water content significantly affects the physical and chemical characteristics of the hydrogels. Basically, hydrogels offer desired properties such as biocompatibility, tuneable mechanical properties, and the feasibility of being produced in an injectable form, all of which have made them suitable to be used in different biomedical and pharmaceutical applications. Furthermore, they can be formed or casted into different shapes. Hydrogels are known as a potential candidate that can mimic the chemical, mechanical, and biological features found in living tissues [35]. Hydrogels have found applications in tissue engineering [24-26], regenerative medicine [18, 19], drug delivery [20-22], and biosensing. Historically, the hydrogel network of poly (hydroxy-ethyl-methacrylate), poly HEMA, was the first of its kind discovered as biocompatible and suggested for use in contact lenses [126]. It was then found

applications in drug delivery, skin dressing and as scaffold for tissue engineering of spine and cartilage [29, 127]. Alginate, a natural polymer mainly extracted from brown seaweed that can easily be formed as a hydrogel in the presence of a divalent cation such as Ca^{2+}, has found applications in wound-healing, drug delivery, and cell transplantation [128]. Poly acrylamide (PAAm), in the hydrogel form, is generally used as enzyme immobilizer, and as a carrier for bioactive compounds [129]. Other applications mentioned for PAAm, include the use in plastic surgery, and soft tissue filling [130]. For the wound dressing applications, hydrogels can be applied in the forms of emulsions, sprays, ointments and creams, while containing drug compounds, that can be released gradually, contributing to an efficient healing process [117].

The choice of hydrogels for specific biomedical applications mainly depends on the bulk structure of hydrogel. The key factors determining the hydrogel properties include the polymer volume fraction of hydrogel in fully hydrated state, controlling the level of water uptake capacity, molecular weight between two adjacent cross-linked chains, determining the cross-linking density, and the polymer network mesh size, giving information on the space available chains [18].

2.3.2 Synthesis of Hydrogels

Depending on the chemical constituents, various approaches exist for the hydrogel preparation, such as physical, chemical and radiation cross-linking methods. With physical cross-linking, there is no need to use the cross-linking agent, which could also eliminate the process of unreacted agent substance removal. The common physical procedures involve:

- Cooling/heating a pre-gel solution; such as polyethylene glycol (PEG) [131]
- Ionic interaction; such as Alginate crosslinked with Ca^{2+}
- Hydrogen bonding; such as poly methacrylic acid and PEG [131]
- Freeze-thawing cycle; such as poly vinyl alcohol (PVA) [132]

Physical cross-linking causes weak bonding between polymer chains, and the hydrogels formed by this method are usually dissolved at elevated temperatures, owing to the rupture of cross-links.

The most common cross-linking method for alginate is by ionic reaction, initiating through bonding between the guluronate blocks (G blocks) of alginate chains, and a divalent cation, Ca^{2+}, owing to the high degree of flexibly of G blocks. Next, the G blocks of adjacent chains are joint in a so-called *egg-box* cross-linking model, resulting in the hydrogel formation. Calcium chloride ($CaCl_2$), is the most common chemical used for cross-linking of alginate, although it causes rapid cross-linking which is not desirable for some applications, and instead calcium sulphate ($CaSO_4$) and calcium carbonate ($CaCO_3$) might be utilised to achieve a more gradual process [128].

The reaction between polymer functional groups such as OH, COOH, and NH_2 with the cross-linking agent might cause chemical cross-linking. Radical polymerization of a monomer in the presence of an agent might lead to chemical cross-linking. For instance, poly HEMA can be crosslinked if it is combined with ethylene glycol dimethacrylate. PVA is another common synthetic polymer that can be cross-linked by either physical or chemical methods [133]. The amount of cross-linking agent affects the properties of the chemically-crosslinked hydrogel, such as swelling ratio. Other methods, such as crosslinking by addition reactions, condensation reactions, high energy irradiation, and by enzymes were discussed in [131].

Polyacrylamide (PAAm) hydrogel is formed by dissolving acrylamide (AAm) monomer in deionized water, followed by dissolving N,N′-methylenebisacrylamide (MBAA) in the solution, acting as cross-linking agent. Additional chemicals in certain ratios, are required for the cross-linking to be occurred, including ammonium persulfate (APS), acting as free radical initiator, and N,N,N′,N′-tetra-methyl-ethylene-diamine (TEMED) acting as process catalyst. The existence of oxygen is known to restrain acrylamide polymerization, due to absorption of free radicals. Therefore, the solution containing AAm and MBAA must be degassed prior to addition of APS and TEMED [134].

Cross-linking by radiation is another common method used for the synthesis of hydrogels. Unlike chemical method, the presence of chemical additives is not required in radiation type. Moreover, the modification and sterilization would be conducted in a single step, leading to more cost-effective solutions, especially in biomedical applications [135]. Initially, free radicals are produced in the pre-gel solution, followed by exposure to a high-energy source, such as X-ray, gamma, or electron beam. The macromolecules present in the hydrogels formed by radiation, are covalently bonded to each other, suggesting resistance to dissolution, even at high temperatures, unlike those formed by physical cross-linking. Covalent bonds can be broken only by chemical reactions, or by stress induced by an external force, in an irreversible process. Hydrogels synthesised with this method, were first introduced as a novel wound dressing material [117]. The applied hydrogel, with a commercial name: AQUA-GEL, prevented wound contamination by external substances, barricaded loss of biological fluids, and brought oxygen to the wound, accelerating the healing process [117].

2.3.3 Methods to Enhance Mechanical Properties of Hydrogels

As previously mentioned, despite their desired properties, poor mechanical performance of the single-network hydrogels hinders their use in load-bearing applications. To date, three major methods have been introduced and explored to enhance the mechanical strength of compliant hydrogels:

- Multi-network polymer entanglement through development of IPN networks
- Reinforcement by nano-particle (NP) incorporation
- Structural reinforcement by embedding woven textiles or 3D-printed scaffolds

In the following sections, each method will be further discussed.

2.3.3.1 Interpenetrating Polymer Network Hydrogels

A multi-network IPN hydrogel is created when the networks of at least one of the polymer constituents is cross-linked in the presence of other polymer networks [136]. Many IPNs form multiple separate, yet continuous phases within the IPN. Depending on the synthesis method, there are simultaneous and sequential IPNs, where the present networks are cross-linked at the same time in the former type (Fig. 2.3 (a)), whereas for the latter one, the crosslinking of the remaining networks are done following the cross-linking and gelation of the first cross-linked network. Next, the hydrogel must be kept in a solution, containing the activator and cross-linking agents for the other chains to be crosslinked (Fig.2.3 (b)). If one polymer component is crosslinked, and the other one remains un-crosslinked, semi-IPN hydrogel is created [137]. A special case of IPN hydrogels, known as *double-network,* was developed by Gong et al. [138, 139], and suggested as a cartilage replacement. It was synthesised by a polymer network featuring high ionic cross-linking density, coupled with a neutral loose cross-linked network of

second polymer. Promising wear resistance and mechanical strength were resulted from assessment of double-network hydrogels.

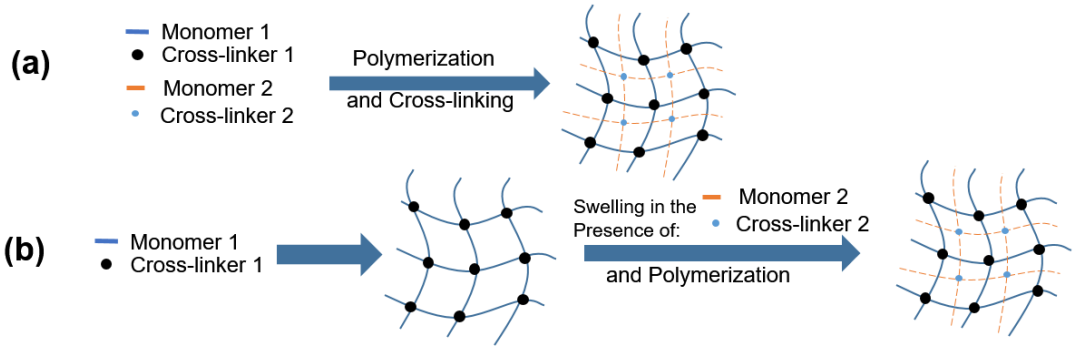

Figure 2.3 Schematic representation of IPN hydrogel formation: (a) simultaneous approach, (b) sequential method [137]

Another study revealed the enhanced mechanical and frictional properties of Alginate-Polyacrylamide (ALG-PAAm) IPN hydrogel compared to the individual constituents and other studied hydrogels, therefore suggested it as a scaffold for tissue engineering of cartilage [51]. Moreover, ALG-PAAm IPN hydrogel was suggested as a structural material for an orthopaedic prosthesis, due to the outstanding fracture toughness it offers (up to 9 kJ/m^2) and insensitivity to notch, making the hydrogel a potential patch for suturing [32]. However, friction and wear behaviours of these hydrogels have not been explored in depth, suggesting a research gap.

The ALG-PAAm hydrogel is formed as an interpenetrating polymer network where methylenebis-acrylamide (MBAA) acts as a crosslinking agent for covalently crosslinking of PAAm, and calcium cations (Ca^{2+}) help ionic crosslinking of ALG. As schematically illustrated in Fig. 2.4, in the IPN hydrogel, there exists covalent crosslinks between two entangled polymer chains, between amine and carboxyl groups of PAAm and ALG, respectively [32], implying the load sharing of both networks. Alginate forms a short chain that can dissipate strain energy via recoverable breaking of ionic crosslinks, meaning after the unloading, the ionic crosslinking can be re-formed, thus healing the

damage, while long-chained polyacrylamide network remains intact, contributing to stabilisation of structural deformation. The mechanical characteristics of ALG-PAAm IPN hydrogel were investigated previously and were found promising [32].

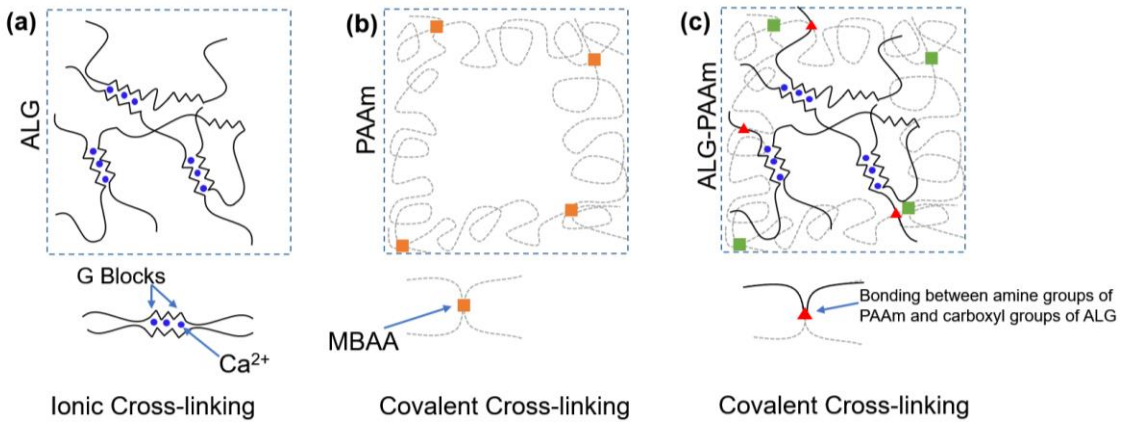

Figure 2.4 Schematic representations of three hydrogels. (a) ionic cross-linking of G blocks of alginate chains with Ca^{2+} as cross-linker, (b) covalent cross-linking of PAAm chains with MBAA as cross-linking agent, (c) in an intertwined ALG-PAAm, there are cross-links between carboxyl groups of ALG and amine groups of PAAm [32]

2.3.3.2 Nanocomposite Hydrogels

Recently, a growing trend has been emerged in nanocomposite hydrogels (NCH) development for a wide range of biomedical applications. In a NCH, the polymer networks are physically and/or chemically cross-linked and bonded to each other, and to the nano-particles (NPs) or nano-structures. This category of biomaterials have found numerous applications in biosensors, bioactuators, drug delivery, and regenerative medicine [35]. To date, different materials in nano scale, have been utilised for development of NHCs, including carbon nanotubes (CNT), graphene, polyester NPs, silica, hydroxyapatite, and metallic NPs such as gold, silver and iron-oxide [35]. The covalent bonds between the hydrogel network and the NPs is a key factor in fulfilment of load-transfer between two phases, leading to an increase in mechanical strength and toughness. Incorporation of inorganic NPs was found to have additional advantage of promoting desired biological responses [140]. For instance, incorporation of silicon-

based NPs in the biomaterial, would add the bioactive properties to it, as silicon is known to contribute significantly in osteogenic differentiation of stem cells, as well as encouraging collagen type I production [141]. A previous study showed the introduction of nano particle hydroxyapatite into PEG matrix, improved the mechanical properties and structural stability to endure physiological environment, in addition to an increase of cell adhesion [141]. Further, PEG matrix was reinforced with silica-NPs, and the result was promising as an improvement in mechanical strength and cell adhesion were observed. The authors suggested the PEG hydrogel modified by either nHA, or silica-NP in an injectable form, for orthopaedic applications [142, 143].

Biocompatible silica nanoparticles were previously demonstrated to enhance not only the mechanical properties of hydrogels when added to them, but also encouraging the cell proliferation of hydrogel scaffolds used for tissue engineering applications [144, 145]. Silica was proven to be stable in the most biological environments [146, 147], as well as easy to fabricate, thus it was employed in bone scaffolds to improve bioactivity of those structures and stimulation of apatite formation, in addition to improving the tissue adhesion and mechanical stiffness [144]. Silica NPs benefit from silanol functional groups on the surface that can be released, and form negatively charged groups in water [148]. Once embedded in PAAm, Silica NPs form covalent/hydrogen bond with polymer chain. It was also shown if there is insufficient amount of crosslinking agent, they contribute in formation of crosslinked polymer network by adsorbing to polymer chains and improving network connectivity, leading to an increase in storage and loss moduli [149]. It was recently revealed that the thermal properties of polyacrylamide hydrogels could be optimised when silica nanoparticles were added to the polymer matrix, due to the robust interaction between additive particles and PAAm network [150]. Thoniyot et al. [38] reviewed the available methods to incorporate NPs into bulk hydrogel matrix, including gelation in the presence of NP suspension, and physical addition of NPs into

matrix after gelation. These methods are schematically illustrated in Fig. 2.5. The first method was also employed by Sershen et al. [151] for the synthesis of polyacrylamide-based NCH with gold NPs embedded as filler. It was also adopted as an efficient way to prevent inhomogeneity, due to NPs aggregation in a previous study [152].

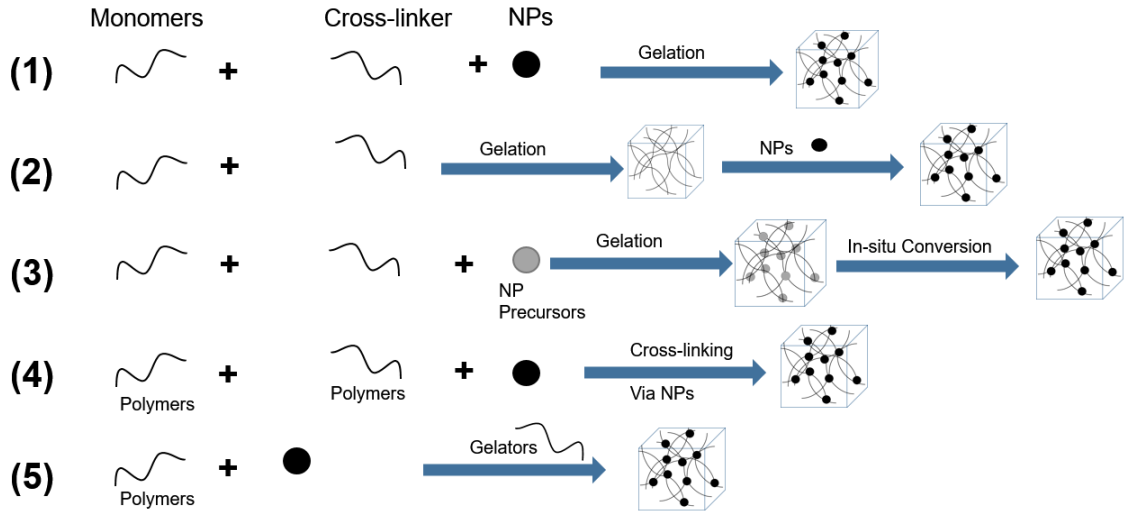

Figure 2.5 *Available methods to synthesise hydrogel nanocomposites with uniform NP dispersion: 1) formation in a NP suspension, 2) physical integration of NP into hydrogel after gelation, 3) NP formation within prefabricated hydrogel through chemical reaction, 4) use of NP as a cross-linker to form the hydrogel, 5) use of gelator molecules to form hydrogel nanocomposites [38]*

Another silicon-based NP, called silicate, also known as nanoclay, was explored as a reinforcing agent of hydrogels [153, 154]. The improvement observed in the mechanical performance was attributed to plate-like, anisotropic morphology of the NPs, leading to relatively high matrix-NP surface interaction. Limited information is available on the application of nanoclay-embedded hydrogels for biomedical purposes, although nanoclay offers bioactive properties, which makes it an attractive candidate for use in tissue repair, especially for bone-related applications [155]. To this end, the incorporation of ceramic NPs, have been found to enhance the mechanical properties of hydrogel matrix, as a result of high mechanical strength of ceramics, and the release of these particles in the biological environment might lead to a favourable response, contributing to treatment process.

2.3.3.3 Three-Dimensional Woven Hydrogels Composites

As mentioned previously, any improvements in the mechanical properties of the hydrogels are favourable, hence fibre-reinforcement was suggested recently [33, 156]. However, only tough hydrogels could be considered as the matrix for such composite materials, as those with low toughness could not sustain the fibre-matrix interaction once being loaded, and the composite fails as soon as fibres cut through the hydrogel matrix [157]. Interestingly, a similar form of composition is found in the articular cartilage itself, where proteoglycan matrix gel is reinforced by collagen fibres, and although containing over 70 wt % water, the tissue is stiff and tough [158, 159]. IPN hydrogels, developed by covalent crosslinking of polyacrylamide (PAAm) and ionic crosslinking of alginate (ALG), were turned out to exhibit significantly higher stiffness and toughness values compared to the single networks [32]. Therefore, fibre-reinforcement is feasible due to sufficient matrix toughness of the IPN hydrogels, and hydrogel composites benefit from even more robust mechanical performance, becoming eligible for use in structural components. In this regard, the PAAm-ALG hydrogel was reinforced by steel wool and the mechanical properties were investigated, in addition to a failure mechanism characterisation [33]. It was shown that under tension, the hydrogel matrix was capable of maintaining the steel fibres in place, preventing their original entanglement to be disrupted, and hence the composite could sustain large deformation to the point where fibres eventually turned towards the loading direction, and the composite failed due to fibre-matrix debonding. Moreover, the amount of dissipated strain energy could be engineered by changing the reinforcement concentration, suggesting an additional design parameter compared to unreinforced hydrogels.

To date, various methods were used for the fabrication of woven hydrogel composites; Liao et al. [51] utilised vacuum-assisted infusion method to inject pre-gel solution into a 3D woven textile out of Polycaprolactone (PCL), followed by holding the negative pressure during gelation. However in another study, the pre-gel solution was manually casted into a mould containing the reinforcing constituent, without applying vacuum condition and the mould was covered until a consolidate material was achieved [33]. Bubble formation was avoided by thoroughly wetting the fabric with precursor monomer solution, prior to casting. Similar fabrication method was implemented by Huang et al. [157], and King et al. [156] for the preparation of hydrogel composites with a polyampholyte matrix and glass fabric reinforcement. The pre-gel was injected into a mould produced by placing the fabric between two glass plates and a spacer, to control the thickness. The relatively high wettability of glass fibres were known to provide a good penetration of pre-gel solution into the fabric, owing to the existing capillary forces.

2.3.4 Characterisation of Mechanical Properties of Hydrogels

Due to the growing trend of hydrogels being utilised in various applications, understanding the mechanical response of hydrogels is imperative as a mean of applicability assessment. Hydrogels represent a biphasic medium with polymer network as a solid phase and interstitial solvent phase, which is water. Therefore, a more sophisticated analysis should be conducted for mechanical characterisation of hydrogels compared to single-phase polymeric materials. Comprehensive reviews of the methods implemented for the evaluation of the mechanical properties of hydrogels were published by Oyen [160] and Anseth et al. [161]. An overview of the relevant methods focused in the current study will be outlined here.

Uniaxial tensile tests, confined and unconfined compression tests, indentation, creep and stress relaxation tests are among the most common mechanical experiments that are performed on hydrogel materials. Indentation tests, where a probe with a particular shape is brought into contact with hydrogel surface has been adapted from the tests originally conducted for measurement of metals' hardness. Sample preparation process could be minimised for the indentation tests, which is beneficial, especially for the soft hydrogels which are difficult to machine, as well as designing special jig and fixture for their clamping. The resultant loading-unloading forces are recorded versus time and used to determine their elastic modulus and hardness. Indentation can be performed in both macro (mm) [162], and micro (nm to μm) [163] scales.

Because of time-dependent properties observed in polymeric materials attributed to their molecular size, molecular arrangement, and intermolecular bonds, hydrogels exhibit viscoelasticity, which is characterised by performing stress relaxation, and creep tests. Viscoelastic response of hydrogels comprises time-dependent response of polymer chains, and flow of interstitial fluid, which adds to the complexity of the problem. The strain level is remained constant and change in resultant force is monitored during stress relaxation. In general, the induced stress due to strained polymer network decreases with time, or "relaxed". For the creep tests, a particular load is applied and is kept constant for the test duration, leading to an increase in deformation with time. Creep compliance is denoted as the ratio of creep stress to the strain, which was found to be time-independent over short, and long test time periods [161]. Hydrogel response can be also evaluated under dynamic loading scenario, using a rheometer, in which storage and viscous moduli can be characterised.

The mechanical behaviour of hydrogels are described by theory of rubber elasticity [164], and viscoelastic models such as standard linear solid model [165, 166], for the prediction of time-independent and time-dependent responses, respectively.

Alternatively, the viscoelastic response of hydrogels can be treated using empirical Prony series, expressed as 2.17 and 2.18 for stress relaxation and creep, respectively [160]:

$$G'(t) = \frac{\sigma\,(t)}{\varepsilon_0} = D_0 + \sum D_k \exp\left(-\frac{t}{\tau_k}\right) \tag{2.17}$$

$$J(t) = \frac{\varepsilon\,(t)}{\sigma_0} = C_0 - \sum C_k \exp\left(-\frac{t}{\tau_k}\right) \tag{2.18}$$

which give the stress relaxation modulus, G', and creep compliance, J, as a function of time, *t*, based on stress and strain functions ($\sigma\,(t)$ and $\varepsilon\,(t)$), under fixed stress and strain (σ_0 and ε_0) for each case. Other terms are material constants, obtained by curve fitting to the experimental data. Based on these models, transient and equilibrium data could be determined for the moduli, as well as time constant, τ_k.

2.4 A Brief Overview of Tribology

Tribology is a branch of science that explores wear, friction, and lubrication of interacting surfaces in relative motion. This includes the study of contact between solid surfaces or between a solid surface and liquids/gases. The task is to determine which process causes complex phenomena such as friction and wear, which involves an investigation at a microscopic scale. The advent of sophisticated instruments such as scanning electron microscopy (SEM), and atomic force microscopy (AFM) in the late 20th century, has paved the path towards a true understanding of such phenomena, indicating the tribology as a relatively new field of science [167]. In tribology, an operational analysis is carried out to assess reliability, maintenance and wear resistance of a wide range of equipment components, resulting in significant economic impacts as well as safety-related benefits. It is worth mentioning that surface interaction governs the operation of almost all man-made equipment. Wear is one major cause of failure of

interacting moving components such as bearings, brake pads, cams, couplings, gears, etc., leading to machine break-down. Any improvements in wear resistance and reliability of materials might lead to significant savings [167]. Tribology has been also expanded to the study of interacting surfaces inside biological media, including synovial joints, subjected to lubrication and wear. In the next sections, the fundamentals of tribology are briefly highlighted.

2.4.1 Friction

Friction is the force that resists the sliding or rolling motion of a solid object over another. It can also be considered as energy dissipation between sliding bodies. Friction enables us to walk and run, and provides traction force for the wheels of transportation systems, in addition to other beneficial applications. However, in most cases friction is responsible for energy loss and machine component degradations; thus, it should be minimised.

Due to the distortions and defects present on the surface of solids, a parameter called surface roughness was defined, measured by the vertical deviation from the mean line. Arithmetic roughness, R_a, and root mean square roughness, R_q, are common methods of surface roughness quantification. The former is defined as the mean height deviation of finite number of points on the surface profile with respect to the mean line, while the latter expresses the root mean square of height deviation of points on the surface profile. Surface roughness value gives an estimation on the magnitude of peaks and valleys on the surface, also known as asperities. The true area of contact between interacting solid surfaces is controlled by these asperities, also affecting friction, lubrication and wear. The well-known Coulomb friction law [168], which states the proportionality exists between normal load and frictional force, known as coefficient of

friction (CoF), fails to predict friction force at the length scale of surface asperities. Surface roughness also restricts the area of contact between two surfaces to the peaks of surface asperities, also known as true area of contact, and load support is carried out through the deformation of asperities. During the relative sliding of interacting solid bodies, the asperities are continuously deformed and new morphologies are formed. At macro-scale, two key factors affect the friction, namely adhesion and deformation of surface asperities [169].

To assess a candidate material for specific application, or to simulate a contact setup observed in an application, standard friction tests are carried out. The friction level is usually assessed by the measurement of coefficient of friction (CoF), using instruments known as tribometers. These instruments can provide a range of relative motions between contact pairs, in both unidirectional and multidirectional manners, and measure the frictional force and CoF, while controlling the pre-set parameters, such as normal load, operational speed, temperature, environmental conditions, and number of cycles. Schematics of the most common configurations used for friction and wear studies are illustrated in Fig. 2.6.

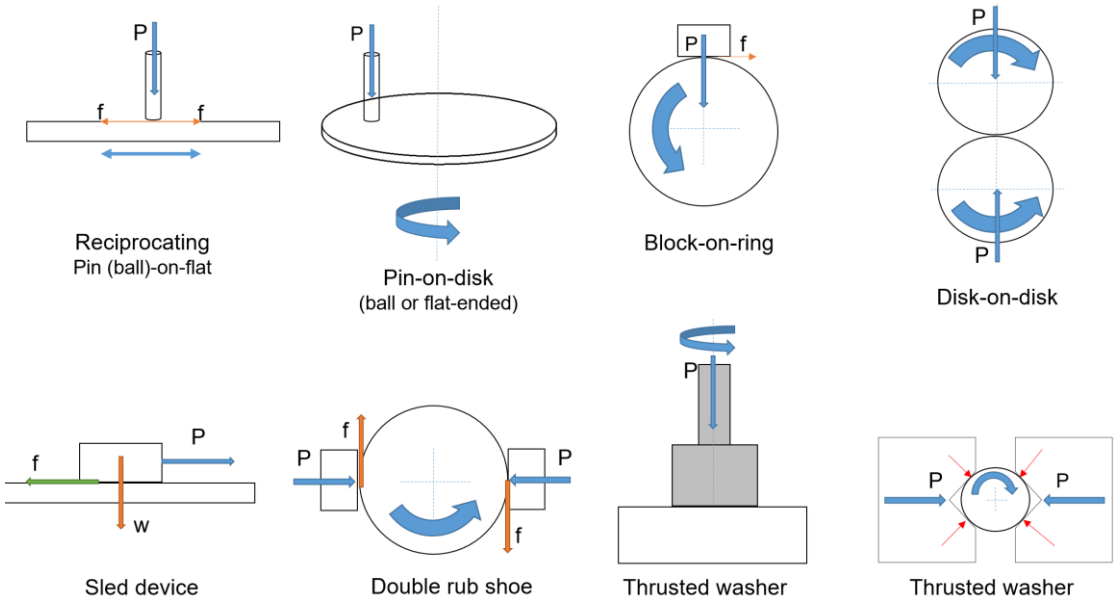

Figure 2.6 Conventional test setups used in tribometers [170]

The CoF varies with respect to sliding distance or time, and this variation depends on types of materials, interfacial conditions and surrounding medium. Before CoF reaches a steady-state value, there is a run-in phase where the surface asperities of softer material are constantly deformed by the harder counter-surface. Depending on the above-mentioned factors, there might be multiple transitions and steady-state stages during sliding motion between solid bodies.

2.4.2 Wear

As a continuous damage process, wear is the material loss occurring on the surface of mating components in relative motion [171]. This description expresses the influence (damage), the advent (material loss), the location (on the surface) and the requirement for the wear process to occur. In most cases, wear is an undesirable phenomenon, leading to surface deterioration, an increase in friction, a negative influence on the mechanical performance, and combined with failure modes such as fatigue and creep would give rise to the possibility of component failure. The particles removed from the surface are called *wear debris*, which can be transferred to the counterface or remain on the worn surface, known as *wear scar*. Wear rate of materials is not an intrinsic property, but depending on the external factors, such as lubrication, temperature, type of motion (sliding, rolling, etc.), sliding distance, slip rate, applied load, counter-surface material, surface roughness, manufacturing defects, etc. Wear quantification was initially formulated in the works of Archard et al. [172], and Holm [173] on the sliding wear of metal solids. Total volumetric material loss, W [mm^3], was determined using (2.19), also known as Archard's wear law:

$$W = K\frac{P}{H}\,s \tag{2.19}$$

where P is the applied normal load [N], s is sliding distance [m], H is the Vickers hardness of softer material [Pa], and K is a dimensionless constant, called wear coefficient, obtained from wear experiments and indicates wear severity. In general, K is a small value, suggesting wear is caused by a limited number of asperity contacts. From (2.19), it can be concluded that wear is a function of applied load, and independent of contact area. As mentioned above, wear is significantly dependent on the mating materials and other external factors, and these factors should be considered when applying Archard's law. Depending on the contact geometries and type of relative motion, different types of wear occurs at the interface, classified into: sliding, rolling, abrasive, and fretting wear.

In general, three distinct phases are observed during wear testing of various materials:

- Run-in stage: denotes initial phase when mating surface adaption occurs with fluctuations in the value of wear rate.
- Steady-state stage: wear rate is reaching a relatively constant quantity, owing to the asperity softening as a result of steady-state ablation. It involves the majority of the lifespan of most components [174].
- Final stage: is distinguished with high wear rate occurring abruptly, as a result of microscopic crack initiation and propagation, and surface fatigue, leading to failure of component [175].

Wear tests can be carried out using tribometers with the configurations highlighted in Fig. 2.6. Gravimetric measurements of test samples before and after the test would indicate the material loss, although it is not the most accurate method for all test materials such as hydrated hydrogels, or when comparing wear resistance of materials with large differences in density. Moreover, wear volume can be obtained from mass loss determination, if the value for material density is known. Alternatively, an optical

profilometer can capture the surface profile of a wear track and compute the overall wear volume by identifying the reference surface, and the indent region generated as a result of material loss. In the following section, the typical mechanisms causing wear of materials will be discussed briefly.

2.4.3 Wear Mechanisms

Wear can be caused by different mechanisms. Bhushan [176] has classified all these mechanisms into six categories, namely, abrasive, adhesive, fatigue, impact, chemical, and electrical wear mechanisms. Determination of existing wear mechanisms require microscopic examination of wear track. The relevant mechanisms to the current study will be briefly explained in the following paragraphs.

Abrasive wear refers to the plastic deformation of asperities occurring at the surface of softer material due to the sliding of a hard, rough counterface [167]. The loss of material occurs because of asperities of softer material is forced, and pushed by the hard asperities of counterface. Abrasive wear is characterised by deformation processes known as ploughing, microcutting, and fragmentation on the worn surface. In general, the presence of severe grooves on the worn surface might be an indication of abrasive wear. Hard asperities carve into the opposing surface, removing a thin layer of material, generating a groove in the microcutting process, contributing the most to the abrasive mechanism. With the ploughing mode, the material is displaced away from the contact region, forming grooves without separating from the surface, and the rise of wedges at the edges of the wear scar is usually observed. The ridges formed parallel to the sliding direction are eventually removed by subsequent sliding motion. Abrasion can also be caused by the loose solid particles on the surface as they might contribute to surface cracks and localised fracture, known as abrasive fragmentation, which can accelerate the

wear rate. Application of hard coating on the surface, and high viscosity lubricants, could prevent abrasive wear.

Adhesive wear occurs between two surfaces in contact, due to the formation of atomic bonds between their contact asperities. When one surface is made to slide against the other, these junctions start shearing. In the case where the interfacial bonds are stronger than the cohesive force in the softer material, wear particles would detach from the surface of the softer material, being transferred to the counterface, known as adhesive wear. CoF usually exhibits some level of instabilities under adhesive wear mode. Usually, when two surfaces sliding against each other are pressed together with an external load, this would facilitate material transfer, and therefore adhesive wear takes place. Increasing surface energy promotes surface adhesion. In contrast, the establishment of oxidation layer, lubrication and external surface contamination suppress adhesion. Adhesive wear is responsible for considerable increase in CoF at the interface, which according to the theory of asperity junction growth, is attributed to plastic deformation of asperities [177].

Fatigue wear occurs when in the absence of considerable surface adhesion, contact asperities are subjected to high stress amplitudes, caused by repetitive loading-unloading cycles, during sliding or rolling motions. This might cause the onset of cracks and their propagation, happening either at the interface or the subsurface, as a result of plastic deformation of contact asperities. Wear debris is produced as a result of consecutive steps: First a crack is initiated on the weak points of surface, which propagates along the slip planes. Next, secondary cracks originate from initial cracks and growing in various directions, or several cracks simply join each other. Finally, the subsurface cracks might reach the surface, at which point a chunk of material detaches from the surface in the form of a debris. Reciprocating sliding is a common test setup where fatigue wear could occur due to the propagation of surface generated cracks [178]. As mentioned above, fatigue wear occurs due to the surface cracks, as well as subsurface cracks. The latter case usually

happens when the surface asperities are worn off swiftly, resulting in no surface cracks. In this case, certain regions at the subsurface, with voids have been already developed due to the aggregate dislocations, or material's imperfection are believed as crack nucleation sites, and as the loading-unloading cycles continue, cracks propagate without being observable on the surface. Once the cracks reach surface, a long strip of material is released from the surface as a result. Subsurface fatigue wear is also known as *delamination wear*. The presence of small holes on the worn surface, as a result of fatigue wear is known as micro-pitting. In metals, corrosion is also responsible for generation of surface pits, and fatigue-originated pits are usually distinguished from corrosive ones with respect to depth (10-20 μm) and colour (grey) [179]. Selection of right viscosity for the lubricant with respect to loading level, increasing the speed and lowering operation temperature all affect lubricant film thickness, which in turn would control micro-pitting and surface fatigue.

Other wear mechanisms including erosive, fretting, corrosive, and oxidation wear have been deeply reviewed by Bhushan [176].

2.4.4 Lubrication

To reduce friction and wear of interacting surfaces, substances in fluid, solid or gaseous forms are introduced at the interface, known as lubricants, to separate the asperities of opposing surfaces during their relative motion. Furthermore, lubrication contributes to heat distribution, transfer of wear debris from the interface, and the reduction of third-body wear, all resulting in efficiency and service-life improvements. Depending on the lubrication level, either full or partial surface separation would take place. Load-transfer between mating surfaces is feasible through pressurisation of

lubricant fluid. Hersey Number, H_s, a dimensionless parameter that could be correlated to film thickness (h), is defined by:

$$H_s = \frac{\eta . N}{P} \tag{2.20}$$

where η is lubricant viscosity, N is entrainment speed of fluid, and P is applied normal load. Based on H_s values, three main lubrication regimes were identified by Stribeck [180, 181], as schematically represented in Fig. 2.7. In the case of fluid film lubrication, H_s is greater than 10, and a thick fluid film completely separates the mating surfaces. Under such conditions, the majority of load is transferred through the pressurised fluid, hence friction and wear are minimised. A slight increase in CoF is observed with the increase in film thickness, which is attributed to the induced motion resistance, caused by the thick film. With H_s in the range of 3 to 10, a thin film of lubricant is present between the two surfaces, and a full surface separation is still feasible. The combination of thin and thick film lubrication is called hydrodynamic lubrication, contributing to low friction and wear at the interface. A special case of fluid-film lubrication is known as elasto-hydrodynamic lubrication (EHL), whereby the film formation mechanism is improved by elastic deformation of surfaces at the interface, as well as an increase in the viscosity of the lubricant, as a result of high pressure. Soft EHL is observed in synovial joints, unlike the lubrication mechanism observed in artificial joint replacements.

With lower film thickness, H_s would lie in the range of 1 to 3, and the lubrication is shifted into mixed-mode mechanism, where the separation would occur by pockets of pressurised fluid that are stuck between asperities in contact. Load transfer is carried out by a combination of asperity contact and pressurised lubricant. Higher friction and wear is observed in the mixed-mode, compared to the fluid-film mode. As H_s approaches unity, the CoF increases significantly. If H_s is found less than 1, boundary lubrication is

occurring, through which the majority of load is transferred across surface asperities, also characterised by high friction level due to the partial contact of interacting asperities.

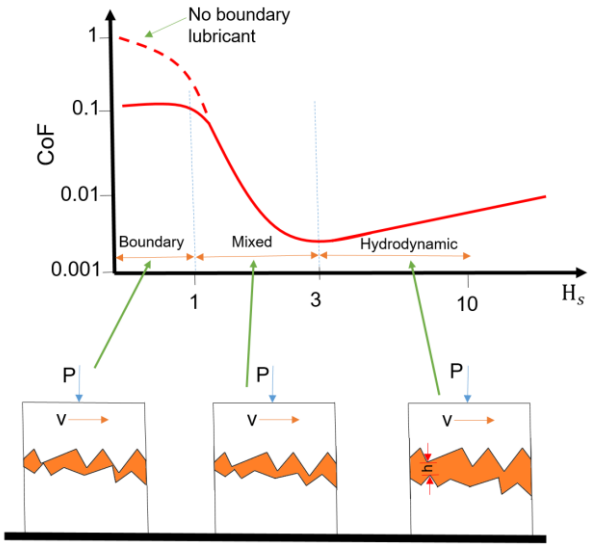

Figure 2.7 The Stribeck curve represents the effect of lubrication regime on CoF [181]

According to the Stribeck graph (Fig. 2.7), a slight increase in film thickness might lead to significant decrease in friction and wear, which is more considerable under boundary and mixed lubrication modes. Therefore, orthopaedic implants can be designed such that maximum fluid film thickness can be achieved in order to minimise friction and wear. This is a major rationale behind considering a woven polymer layer in the design of the implant proposed in Fig. 1.2.

2.4.5 Tribology of 3D Woven Materials

Most of the works done in the literature is related to tribological investigation of consolidated composites, and less information is available on the neat woven textiles and fibre interaction once the fabric is subjected to sliding motion. In this regard, Giordano [182], conducted several dedicated wear studies on polymeric woven materials, also found in [183, 184]. The microscale fibre scratch tests were utilised with AFM, while

fibre-on-fibre friction was simulated using a custom-designed setup, in addition to the sliding wear testing of bulk 3D woven fabrics with a tribometer. Parameters such as load, type of material, and number of cycles were found to impact the scratch and indentation responses, with the indenter speed having a negligible effect. The polymer yarns in mono/multifilament condition were found to benefit from higher hardness compared to their bulk types. Moreover, multifilament ultra-high-molecular-weight-polyethylene (UHMWPE) fibres were reported as the most wear-resistant material among others (PEEK, PET, Polypropylene (PP)), based on fibre-on-fibre wear tests results. For all tested materials, the value of wear coefficient drastically fell from the initial cycle to the second one. Pin-on-disk test of samples soaked in DI water revealed the 3D orthogonal woven PEEK, with a two-layer UHMWPE satin weave on the top surface, demonstrated the least wear rate for the duration of 3 million cycles test, in contrast to those made completely out of multifilament PET, that failed due to severe wear after approximately 1 million cycles. However, it was unclear whether the 3D woven architecture was responsible for the outstanding wear resistance of the candidate fabric, or it was due to the wear resistance of the bearing surface material itself.

Fibre indentation and scratching was also affected by environmental parameters such as moisture. In general, moisture plasticizes polymeric fibres, leading to the material recovery improvement, and reduction in hardness. The moisture was found to reduce surface hardness of PET and PP, while increasing that of PEEK and nylon [184].

In order to reduce fibre mobility on the bearing surface, and thus decreasing inter-fibre friction and wear, fibre welding of bearing surface for 3D woven textiles were suggested in a previous study and it was experimentally assessed [185, 186]. Concerning the process, a consistent laser welding was achieved for the orthogonal weaves. As for the satin-topped fabrics, inconsistent welding and some levels of fibre damage was observed, attributed to the loose nature of satin pattern, preventing sufficient contact

between yarns. This issue was also reflected in the wear rate, as the 3D woven PET with UHMWPE weave on top layer demonstrated higher wear resistance as compared to the top-layer welded sample. Wear debris analysis with the SEM, revealed plate-like morphology, an indication of fatigue wear mechanism. As the number of cycles approached 2 million cycles, the size of wear debris was increased, and micro-cutting was determined as the transient wear mechanism. Therefore, welding was suggested for the substrate orthogonal weave to improve damage resistance, with the non-welded satin weave pattern made of UHMWPE on top for the optimal tribological performance.

Experimental friction and wear studies were carried out on 2D woven polyester composites with reciprocating sliding motion, to investigate the effect of fabric orientation with respect to sliding direction. Highest and lowest wear rates were observed along warp direction (90º), and 45º respectively, due to different mechanical properties in warp and weft directions [187]. It was shown in recent studies that adding reinforcement to 3D textiles will improve their wear resistance and reduce their wear rates [188-190]. Rattan et al. [191] observed that weave patterns will affect tribological performance, and among different patterns of plain, satin, and twill weaves, the latter offers the best strength and wear resistance, while satin showed the worst performance. Weave density was also found to be the other important factor as wear rate increases at higher densities, while coefficient of friction is inversely proportional to weave density [192]. In general, conventional pin-on-disk, reciprocating pin-on-plate and block-on-ring tribometers were used in the past to investigate the wear characteristic of textiles [185, 193]. Wear can be quantified by mass loss measurement, or change in the geometry of contact surfaces.

Although wear characterisation of 3D woven textiles was performed in several studies before, however, the friction and wear behaviours of 3D woven textiles infused by hydrogels, have never been explored in the past. 3D woven hydrogel composites were

introduced as a potential synthetic cartilage candidate [51], with the focus on mechanical properties, although the same yarn size was utilised for weaving the whole fabric and the stiffness gradient found in cartilage was not considered in the weave.

2.4.6 Tribology of Hydrogels

To serve as a load-bearing component, efficient assessment of tribological properties of a potential cartilage replacement candidate seems inevitable for a long-lasting implant. Some studies were conducted to study the effect of parameters such as load, sliding speed, lubrication, and crosslinking density on friction and wear behaviour of hydrogels, such as PVA and poly-HEMA [28, 29, 194-196]. Wear was quantified by dried polymer mass loss. It was concluded that applied load, degree of polymer crosslinking and amount of water content are crucial factors for assessing wear resistance of hydrogels. To improve tribological performance, PVA hydrogel was developed with a boundary lubricant on the surface, and it was found that lower hydrocarbon chain length of the lubricant has more promising effect in friction and wear reduction [197]. Lin et al. [198] developed a bilayer hydrogel structure, inspired by natural cartilage with low-friction porous layer on top, and a more crosslinked and tough substrate as load-bearing layer, followed by the evaluation of tribological properties of the material as an artificial cartilage. The reported friction coefficient was in the range of 0.01 to 0.05, increased rapidly after 12000 cycles due to critical wear of top layer, resulting in less lubrication. Influence of contact geometry on lubricity of hydrogels was also studied in the past, and it was associated with speed-dependent and time-dependent friction coefficients, once the hydrogel sample is moving and once it is in stationary contact, respectively [199]. On the other hand, hydrogel on hydrogel sliding motion, which resulted in low friction coefficient (0.058), was found to be neither speed, nor time dependent, and not following

classic Stribeck curve, as their permeability would prevent lubricant pressurisation in between the counterfaces. It was discovered that polymer network mesh size plays the most crucial role in controlling both elastic modulus and permeability of gel, thus determining the lubrication regime at the interface [200]. The PAAm hydrogels with the biggest mesh size (9.4 nm), meaning the least polymer concentration, showed the lowest friction coefficient (0.005), over the range of sliding distance of 30-1000 μm/s, and 2mN normal load, using a pin-on-disk microtribometer [201]. Friction was found to be speed-independent at very low speeds, but there also exists a transition speed, of which friction would increase with the speed, attributed to polymer network relaxation time and mesh size.

It is widely accepted that any biomaterial suggested as cartilage replacement, should tolerate the critical loading experienced in knee and hip joints, with minimal wear, non-toxic wear debris, and low friction coefficient during millions of cycles life span, with respect to an average of one million steps that a normal person takes per year [202]. Friction and wear characteristics of a silk fibroin hydrogel were studied in an attempt to find an appropriate candidate for cartilage repair [203]. Reciprocating sliding tests revealed CoF was generally higher compared to that of cartilage. An increase in silk concentration led to higher stiffness, due to smaller structural pores, and improved fluid load support, positively affecting frictional response. However, reduced pore size might negatively influence the cell-culture, and this restriction must be considered if using the particular hydrogel as a scaffold for tissue regeneration.

Nanoparticle-reinforced hydrogels were also assessed against tribological criteria in the past. In this regard, Korres et al. [204] synthesised PAAm-p-Acrylate hydrogel nanocomposite with 4 wt % clay NPs for friction and wear studies, using a shaft on plate setup. With constant water lubrication, a very low CoF was obtained (0.003), while the wear rate was relatively high (0.05 mm^3/N m), although it was found markedly lower

when compared to the reference hydrogel without NP reinforcement. Relatively low friction level was attributed to the strong repulsive forces present on the surface of the studied hydrogel nanocomposite, due to their negative surface charge. Based on another study, the wear resistance of PVA hydrogel was improved, when hydroxyapatite NP were introduced to the matrix [205]. The composite was slid against stainless steel disk under water lubrication condition. Applied load was found as a key parameter on wear rate, while hydrogel preparation method influenced both wear rate and wear mechanism.

2.5 Computational Modelling of Sliding Wear

2.5.1 An Overview of Hertzian Contact Stress

When two solid bodies are in contact with each other, contact stress and elastic deformation at the contact area occur, which are described using the concepts of contact mechanics. Contact stress formulations were initially introduced by Hertz in 1882 for a non-adhesive elastic contact between two solid bodies [206]. The theory of Hertzian contact stress was proposed based on some assumptions, such as frictionless contact, non-conforming property of surfaces, and elastic deformation of surfaces in contact region. Hertzian theory was further improved by other scientists, such as Johnson [207] in 1970, when it was expanded to describe adhesive contacts, as well. The contact area between two spheres is a point, implying the contact stress must be infinite, but in practice, an extremely small contact area exists when the two spheres are in contact, due to the elastic deformation of their surface in contact region. According to Hertzian theory, the contact stress σ_c [MPa] between a sphere with radius r, and a flat half-space (with the radius of ∞), is determined as [206]:

$$\sigma_c \cong \frac{3}{2}\frac{P}{\pi a^2} = 0.4\left(\frac{E_*^2 P}{r^2}\right)^{\frac{1}{3}} \tag{2.21}$$

where P [N] is the applied force, and a [mm] denotes the radius of contact area, and E_* [Pa] is the composite elastic modules obtained from:

$$\frac{1}{E_*} = \frac{1}{2}\left(\frac{1-\nu_1^2}{E_1} + \frac{1-\nu_2^2}{E_2}\right) \tag{2.22}$$

where E_1 , E_2 are elastic moduli of the sphere and the flat half-space, and ν_1 , ν_2 are Poisson's ratios of the sphere and the flat half-space, respectively (see Fig. 2.8).

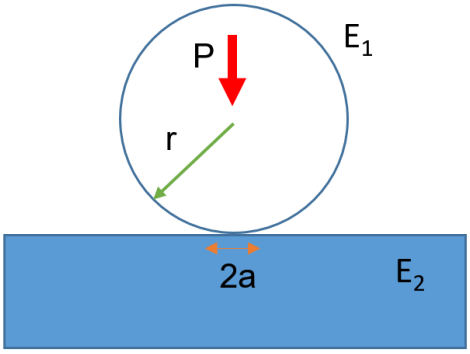

Figure 2.8 Contact between a sphere and elastic flat half-space

Contact stress and surface displacement, also known as indentation depth, were formulated for other forms of contacts, such as contact between two cylinders, two spheres, conical indenter on flat half-space, etc. These values are frequently utilised in indentation, hardness testing, wear, and impact analysis for a wide range of engineering applications. Material properties such as hardness, and elastic modulus could be obtained from hardness test, as the indentation depth is known, and the applied force could be measured by testing machine's sensors.

2.5.2 Finite Element Simulation of Sliding Wear

Numerical methods such as Finite Element Analysis (FEA) are powerful tools for wear prediction and parametric studies, and when compared to physical experiments, they would offer a cost-effective solution for optimisation of tribosystems for wear reduction. FEA can compute the stress and strain fields by discretisation of a continuum medium of an arbitrary shape, into finite number of elements assembled at nodes. To calculate wear, the model must initially determine the contact stress, by computation of nodal displacements using:

$$[\boldsymbol{D}]\,\{\boldsymbol{u}\} = \{\boldsymbol{F}\} \tag{2.23}$$

where $\{\boldsymbol{u}\}$ is the nodal displacement vector, $\{\boldsymbol{F}\}$ is nodal loads vector, and $[\boldsymbol{D}]$ is called global stiffness matrix [208]. The nodal stress values would then be utilised to obtain nodal displacement due to the surface ablation, and wear is therefore predicted based on implemented wear law. Archard's wear equation could be simply implemented in a FE model, as the output variables are readily available from solution of contact problem by the FE solver. Most of wear simulations conducted in the literature were based on Archard's wear law, although other wear models were developed based on frictional force [209], and energy methods [210, 211]. While these models provide additional considerations of the contact conditions, such as the effect of lubrication, they would need CoF to be known. Moreover, the introduced wear factors by these models are static, meaning that any change in tribosystem would require a new wear factor to be determined. Tribosystem is defined as a system of mating surfaces, and any factor affecting their interaction. The most conventional methods implemented in the literature for wear prediction are highlighted in the following sections.

2.5.2.1 Wear Simulation by Shifting Surface Nodes

The key tasks in wear simulation include determination of wear volume, material removed from the surface due to relative sliding, and updating surface geometry due to wear incident. The latter one would affect nodal stress quantities for the further wear cycles, which in turn affects wear computation. Previously a method was developed and implemented to shift the vertical coordinate of surface nodes based on the contact pressure quantities that are calculated by the FEA.

Podra and Andersson [208] performed a series of pin-on-disk tests and compared the experimental findings with a computational 2D wear model under dry sliding condition. The general contact problem was solved, followed by updating the coordinate of the contact nodes and generating wear depth with the aid of a postprocessor based on Archard's wear law. However, only a constant wear coefficient was considered for the Archard's equation during the entire wear simulation. Therefore, wear depth computed from FEA, was in large deviation, 40% to 60%, from experimental results. In reality, during the test, there exist one or two periods when the wear rate and wear coefficient varies from a steady value. Therefore, more detailed tests are required to find the evolution of wear coefficient with respect to test duration or more sophisticated analytical models should be implemented in the wear modelling procedure to achieve more accurate results.

Similar method was implemented on the numerical study of brake pad wear against a rigid rotor, turning at constant speed [212]. It was assumed the opposing surfaces conform to each other and wear depth of the pad is very small compared to its dimensions. Thus, a uniform wear profile was considered over the entire surface of brake pad and therefore, wear was simulated by moving the surface nodes in the direction normal to the contact surface. However, in reality more severe wear occurs at the regions farther away

from the centre of rotor, due to the longer sliding distance experienced. The authors found that if local normal vector of each surface node was obtained and implemented in the wear model, more accurate predictions could be achieved. However, this would significantly complicate the programming of wear processor, particularly in 3D models.

The drawback of the above method is that it requires relatively large surface elements if considerable change in geometry occurs due to substantial wear. This is to prevent element distortion or complete element removal because of node shift. Larger surface elements would result in less accuracy in contact pressure computation of surface nodes, or even divergent contact errors [213].

2.5.2.2 Wear Simulation by Part Re-meshing

Due to the issues mentioned above, re-meshing the part would seem necessary in case a specific wear depth was reached, to avoid instabilities in contact solution. In this regard, Hegadekatte et al. [175] developed a global incremental wear model based on Archard's wear law that updates the geometry based on average contact pressure, and sliding distance at defined intervals. The part is re-meshed when the wear depth is reached to a pre-set ratio of element height, while the previous wear depth acts as displacement boundary condition. Their model was able to measure materials removal and wear for 2D and 3D geometries. However, the smaller the contact elements are, the more frequent remeshing is required, and more contact problems are to be solved. It is in fact computationally expensive and difficult to implement.

2.5.2.3 Adaptive Meshing and UMESHMOTION

Adaptive meshing method has been introduced into CAE packages such as ABAQUS to enhance the mesh quality when the elements are subjected to large

deformations, such as material forming and impact, as well as simulation of steady-state processes such as rolling and extrusion. The mesh smoothing is based on Arbitrary Lagrangian Eulerian (ALE) approach, where a combination of both Lagrangian and Eulerian methods would be applied. According to the Lagrangian method, the nodes follow the material points, whereas in Eulerian approach the nodes are fixed, while the material flows through the mesh. In ALE, node movements only rely on material motion at free boundaries, and these are independent elsewhere. Most CAE packages support user-defined programming, called *subroutine*, to implement wear models into adaptive meshing for wear simulation. In ABAQUS, the dedicated wear subroutine is UMESHMOTION [214]. The user can prescribe surface nodes displacement based on the wear model defined in the subroutine, and the adaptive meshing will retain the mesh quality in the rest of the part by adjusting the nodes.

Bortoleto et al. [215] used ABAQUS user subroutine, UMESHMOTION with ALE adaptive meshing technique to simulate surface ablation. A pin-on-flat dry sliding motion was simulated to predict wear depth. The subroutine updated contact nodes successfully, and changes in surface topology could be achieved using Archard's model. Wear coefficient was measured experimentally for three normal loads and implemented into the model. However, computed wear volume still didn't match the experimental results very well, which was due to inaccurate estimation of wear coefficient without considering running-in period.

Martinez et al. [216] conducted FE simulation of thermoplastic polyurethane sliding on a metal block, using ALE adaptive meshing. An elastic material model was assigned to the polymer material due to the issues arise with adaptive meshing of a viscoelastic material model. A relatively good mesh quality was maintained during the simulation, thanks to adaptive meshing technique applied. They showed that the accuracy of numerical method depends on how precise the primary stage (running-in period [174])

is reflected in modelling. Therefore, it was suggested to perform more simulation steps in the running-in stage to better characterise wear coefficient at that period.

2.5.3 Unit Cell Modelling of 3D Woven Textile Composites

To date, the modelling of textiles and textile composites have been performed in various length scales, namely micro-, meso-, and macro-level models. In micro-level, the fibres within yarns are focused and analysed. The mechanical properties of yarns are determined based on fibre orientation, fibre fraction volume, and fibre properties using homogenization technique. Meso-scale analyses the interlaced yarn interactions, and can be utilised for mechanical property determination of textiles at macro-level, while the deformation and stress analyses of a textile constituent as a continuous medium, within a part is under the scope of Macro-level analysis. Unlike conventional bulk materials, fabrics are heterogeneous, consisting of fibre bundles, which would slide against each other, and therefore their mechanical analysis requires constitutive models and computational procedure to study yarns deformations [217-219].

FE modelling of woven textiles and textile composites were carried out in the past, mostly at mesoscopic scale [220-222]. In general, only smallest possible building block of the textile structure, known as unit cell, is usually considered for FE modelling to achieve less computational costs without accuracy compromise [223, 224]. However, as a reliable representative of the whole textile, the effect of adjacent cells is to be considered in unit cell modelling, meaning proper boundary conditions must be applied to the unit cell, wherever it is attached to the neighbouring cells. Therefore, *periodic boundary conditions* (see [225, 226]) are assigned to unit cells in order to simulate the actual deformation of infinite textile preforms. According to Peng and Cao [227], the side surface of yarns should remain normal to the unit cell once it is subjected to deformation.

Most of previous numerical studies on textiles and textile composites are allocated to the analysis of mechanical response under external loading scenarios such as tension [228], compression [229], shear [230], impact [92], and fatigue [231] simulations. A large-scale FE model was developed for the simulation of 3D angle-interlock textile composite under three-point bending fatigue test. Both of glass fibre yarns and the resin were modelled as solid elements and assembled together. Six-node linear triangular prism elements were assigned to the matrix, due to its complex structure. The FEA revealed warp yarns absorbed much of the strain energy compared to other constituents, while stress concentration was found between the fibre-matrix interface as well as the inclined portion of the warp yarns [231].

A domain superposition technique was proposed by Jiang et al. [232], to reduce computational costs of an explicit matrix model. According to this method, tows domain and a global domain (not resin pocket model) are discretised separately with solid elements, then the textile composite model would be the superposition of tow and global domains using coupling equations. The properties of the matrix material were assigned to the elements in the global domain, while modified properties based on the difference between matrix and tow materials properties were assigned to the elements of tow domain. The proposed technique correlated well with the conventional modelling of textile unit cell embedded within resin matrix, but with the ability to assign brick-shape elements, and an easier modelling procedure. The effect of yarn spacing, yarn width and fabric thickness on the mechanical properties of 2D woven composite was evaluated by modelling the fabric unit cell in TexGen, a pre-processor tool developed for textile modelling [233], and importing it into ABAQUS [234]. It was found that increasing yarn spacing would lead to a decrease in longitudinal moduli as it negatively affects the fibre volume fraction, while increasing the yarn width and yarn thickness resulted in an increase in longitudinal moduli, with no influence on transvers moduli of the textile

composite. A review on recent modelling strategies of textile composites can be found in [224].

2.6 Summary

In this chapter, a comprehensive review on literature relevant to the current research was presented. The structure of articular cartilage and the distinct zones were discussed. It was found that the unique structure of articular cartilage with the viscoelastic, anisotropic biomechanical properties and the presence of an interstitial fluid that can be pressurised during joint articulation, all contribute to ultra-low friction, and wear resistance of the cartilage. If cartilage is damaged as a result of an injury or a disease, the current treatment methods are not able to repair it and only offer transient remedies.

3D woven materials, their applications, production methods and mechanical characterisation methods were discussed, as a 3D weave made of polymer fibres is considered for the bearing layer of an implant proposed in section 1.2. The stiffness varies across the thickness of the weave, to mimic the zone-dependent and anisotropic properties of cartilage. Biocompatible hydrogels resemble cartilage, as they can retain large volume of interstitial fluid, and offer lubrication mechanism comparable to cartilage. Their poor mechanical properties would restrict their use in load-bearing applications. Three major methods were discussed in this chapter, i.e. mixing two polymer networks in molecular scale, incorporation of NPs, and fibre reinforcement. In addition to mechanical testings such as tension, compression, shear, etc., the friction and wear performance of candidate materials must be assessed. An overview of friction and wear assessment techniques for the above materials were outline in this chapter. Finally, the use of FEM in modelling sliding wear of textiles and textile composites was discussed.

Based on the literature survey, some research gaps were identified as follows:

- Tribological evaluation of ALG-PAAm hydrogel has never been carried out previously, although the hydrogel exhibits promising mechanical performance.
- The effect of NP and fibre reinforcement on mechanical and tribological responses of above-mentioned hydrogel have not been analysed, yet.
- The mechanical properties of 3D woven textiles with through-the-thickness stiffness gradient has never been assessed in the literature.
- The sliding wear simulation of textiles and textile composites have not been conducted in the previous studies.

This research tries to address above gaps. The questions associated with the research include:

- What are the design parameters for the proposed implant and how they can be optimised to achieve the best performance and durability?
- Which experiments are required to characterise wear properties of candidate materials and how environmental parameters can influence the results?
- How a user-defined subroutine can be developed to precisely predict generated wear and compute structural strength?

The methods designed to deal with the above questions will be discussed in the next chapter.

Chapter 3

MATERIALS AND METHODS

3.1 Development of 3D Woven Textiles

3.1.1 Design, Production and Analysis

The *Design and Textile Lab* of Auckland University of Technology was contacted regarding 3D weaving facilities to produce polymer weave of the proposed implant. However, it was found that no 3D weaving loom was available in the laboratory. Therefore, several overseas commercial services specialised in design and manufacturing of 3D woven textiles were approached. These include Secant Medical® (Perkasie, PA, USA), Biomedical Structures® (Warwick, RI, USA) and ATEX® technologies (Pinebluff, NC, USA). However, we could not achieve an agreement for the fabrication of desired weave patterns. The feasibility of design and manufacturing of a table-top weaving loom, similar to the one developed by Moutos et al. [235] for production of 3D orthogonal textiles, was also considered. However, it was decided that although it is feasible, but the lead time for design and manufacturing of the machine does not suit the timeframe of the current PhD project. Finally, the *Institute für Textiltechnik* (ITA), RWTH Aachen University, Germany was selected based on their widespread expertise and the mutual interest in the field. Design development phase was conducted as a mutual collaboration between ITA staff, and the researcher. Based on the two distinct designs finalized, the manufacturing process was conducted at ITA workshop as a final-year project [236], and

a brief description of loom setup is presented in the following pages. Polyvinylidene fluoride (PVDF) polymer fibre was selected as the raw material for weaving the textiles, due to their light-weight, strong chemical resistance, heat resistant, and abrasion resistant features. Medical-grade monofilament PVDF yarns were purchased in 3 different sizes, called USP-2.0 (Ø 0.315 mm), USP-3.0 (Ø 0.23 mm), and USP-5.0 (Ø 0.134 mm) from G. Krahmer GmbH, Buchholz, Germany, and used as the main polymeric material for warp and weft yarns.

Three distinct layers were incorporated into the woven preform, each having a different warp thread size as schematically shown in Fig.3.1 (a), to mimic the stiffness gradient feature of the articular cartilage. The weft threads were selected from individual monofilament size USP-3.0 and double insertion was accomplished by custom setting of the weaving loom. For the binding of the multi-layered woven structure, medical-grade polyethylene terephthalate (PET) multifilament yarns were selected, which passed through the layers (z-direction, Fig. 3.1 (b), and (c)) in a continuous fashion. As depicted in Fig. 3.1, the warp and weft yarns are drawn parallel to x and y axes, respectively.

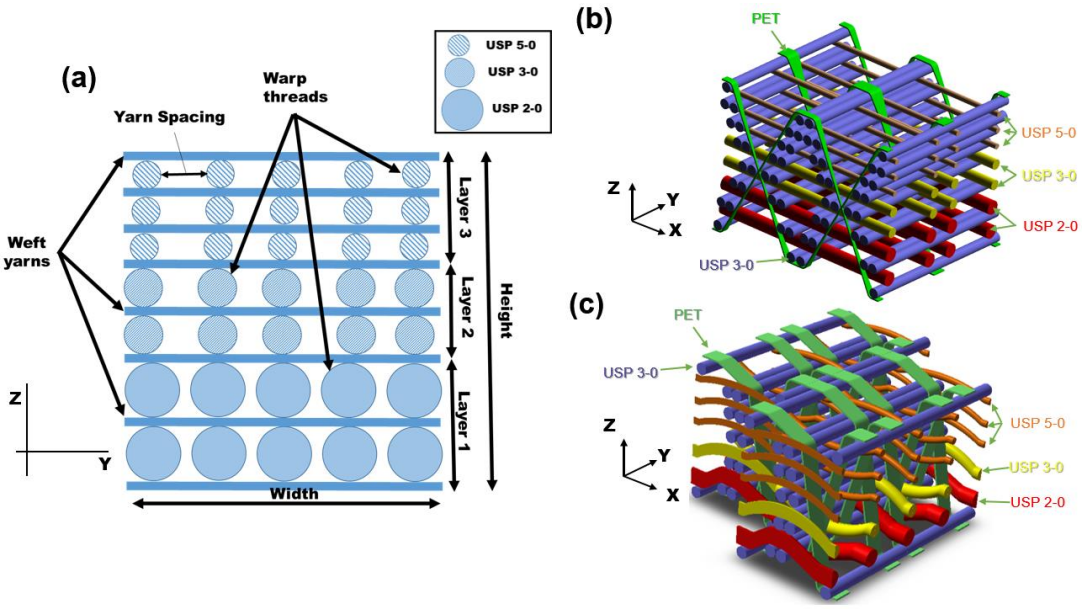

Figure 3.1 (a) Schematic configuration of the 3D woven textiles produced, (b) weave pattern of textile Type-A, (c) weave pattern of textile Type-B

Fig. 3.2 represents the needle loom utilised at ITA for the fabrication of 3D textiles. A needle loom (Type NH2, Jakob Müller AG, Frick, Switzerland) was utilised for the weaving process. The creel used for PVDF yarns comprises of a large number of bobbins, feeding the raw fibres in various sizes to the main weaving mechanism. Prior to the weaving process, the yarns were rewound from a big bobbin received from the supplier to a smaller one suitable for the loom, using a rewinding machine. In total, 250 bobbins were prepared and stored in the creel. Due to weaving a layered pattern, where warp yarns of each layer differ in tow size, the bobbins with the largest yarn size (USP 2-0) were placed at the lowest level of the creel, followed by bobbin containing USP 3-0, USP 5-0 (middle floor) and PET threads (top floor). As the bobbins were arranged in line, to collect and sort the threads, some plates containing some holes were used, through which the threads are drawn towards the weaving mechanism, and passed through a pre-reed, acting as a thread splitter. Followed by passing from some rollers, acting as yarn tensioners, and the heddle frame, the threads need to be sorted properly into the reed's gaps. Finally, the threads were wound around some other pulleys again, to complete the yarn tension through the route. A blade was placed onto each thread, to stop the weaving process in case of fibre breakage. The loom can be programmed, using a hand-held device, and the user input the weave pattern into the device to initiate the weaving process. Parameters such as weft density, and weaving speed could be configured from the hand-held device. Weft density controls the overall thickness, porosity and pore size of the fabric, and therefore, should be identified properly to achieve a desired textile.

Weaving trials revealed weft density (weft thread picks per unit length of the fabric) would affect porosity and total thickness of the 3D textile. Starting from 15 picks/cm, the thickness was found insufficient and the structure seemed unstable. With a gradual weft density increase, the combination of 55 picks/cm for every first and 15 picks/cm for the subsequent 7 weft insertion in a row seemed efficient as a uniform textile

and was produced with the thickness (2.6 cm) and a porosity close to articular cartilage [237]. The weave was called *Type-A*, as the weave architecture is schematically shown in Fig. 3.1 (b).

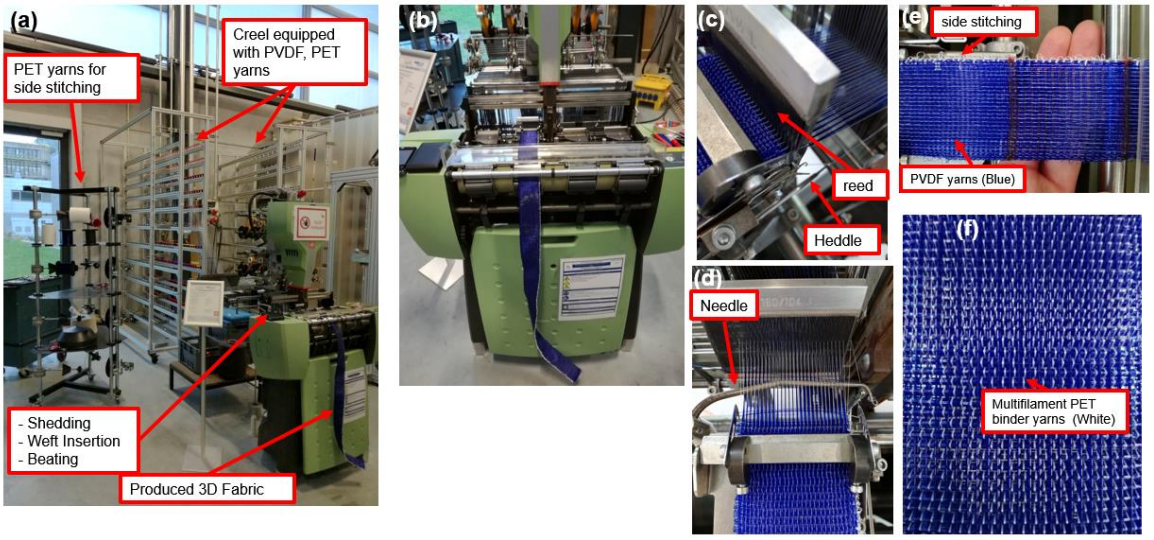

Figure 3.2 *(a),(b) Weaving loom utilised at ITA for 3D textile production, (c),(d) a closer view of weaving process, (e), (f) produced 3D textiles (Type-A)*

The second weave pattern, *Type-B*, was developed such that each single layer was interlocked with one another, as schematically shown in Fig. 3.1 (c), to achieve more flexibility in thickness and higher stability and less relative movements of fibres. A weft density of 35 picks/cm was considered proper for the second pattern. It should be noted that there was a third, multi-layered design developed, which instead of binder yarns, side stitching of weft yarns, made a multilayer fabric feasible. However, due to the flimsy nature of produced fabric, and movement of warp and weft yarns, it was not considered for the current study.

Porosity and pore size of each weave pattern were analysed using the results of micro-CT scans taken from CT-Alpha (Procon X-Ray GmbH, Sarstedt, Germany) with a post-processing software, GeoDict (Math2Market GmbH, Germany). With the aid of a porous media analysis module, the porosity and average pore size were determined for

the weave Type-A as 74% and 0.3-1.1 mm, respectively, compared to 72% porosity and a 0.2-0.8 mm pore size range for the weave Type-B [236].

The produced 3D textiles were then shipped to New Zealand. Initial investigations were conducted on gold-sputtered specimens in a Hitachi SU-70 SEM. Various view angles of each pattern are illustrated in Fig. 3.3. The accelerating voltage of 2.0 kV and average working distance of 16.0 mm were used for this study. Dissimilar fibre configurations at the top and bottom layers, and different fibre sizes implemented at each layer could be clearly distinguished from the images. Furthermore, double weft insertion could be seen from side view images, attributed to the weaving mechanism of needle loom.

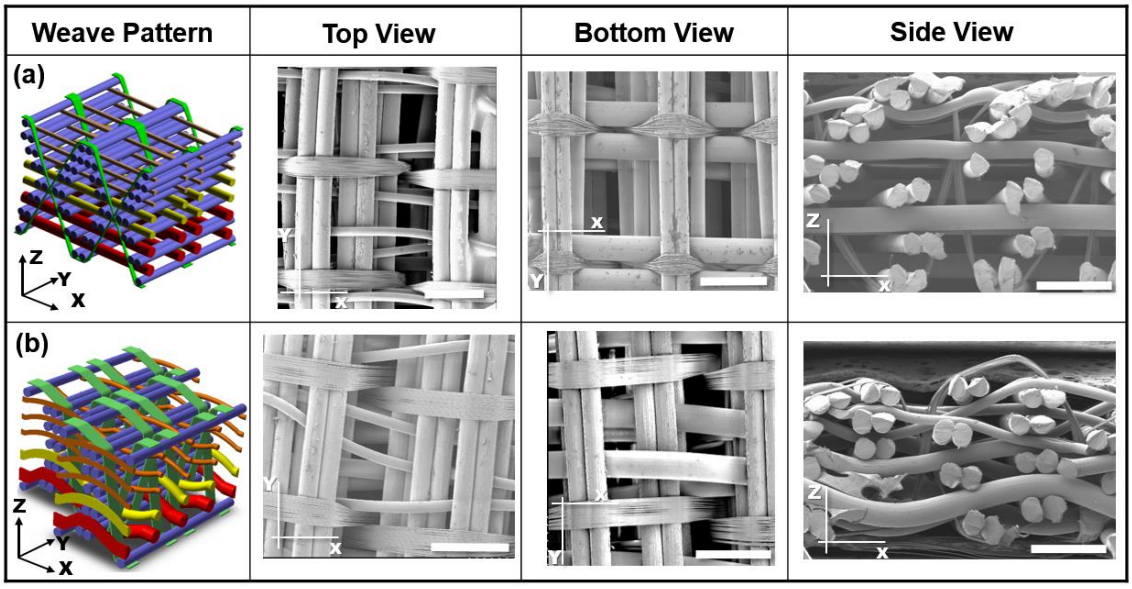

Figure 3.3 SEM images of the different woven textiles from various view angles for (a) Type-A, (b) Type-B. All scale bars shown are 1 mm

The pore size, and yarn spacing were measured from each viewing angle, as the reference dimensions for unit-cell modelling of both textile types. The textiles were also inspected using an optical microscope. The images are shown in Fig. 3.4 for Type-A and Type-B of textiles. It could be seen that warp and weft yarns were arranged differently when comparing both textile types together. Warp yarns are oriented almost straight in

textile Type-A (except for the bearing surface), unlike sinusoidal architecture of warp tows, observed in Type-B. Moreover, weft yarns are not aligned vertically when observing the sectional-view, and they were constrained by the binder yarns. Fibre damage was observed in the form of abrasion, attributed to manufacturing process and yarn rewinding. Overall, the textiles were found susceptible to cutting by a scissors or a cutter blade, and the structure might be easily distorted in that case. Therefore, glue was injected into the fabric on the perimeter of specimen, then was cured, followed by using cutter blade for textile sample preparation.

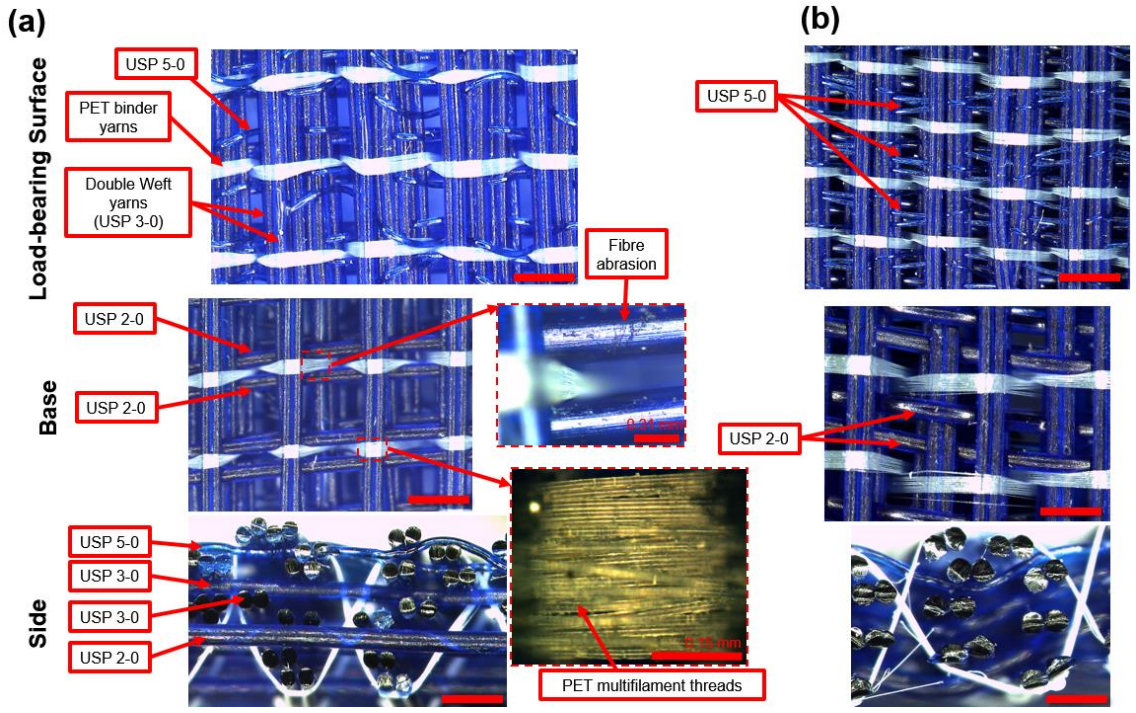

Figure 3.4 Optical images of textiles and the constituent fibres (a) Type-A, (b) Type-B. All scale bars are 1.33 mm, (except those mentioned)

3.1.2 Yarn Characterisation

In order to obtain elastic properties (such as Young's Modulus) of the yarns for FE modelling, tensile tests were conducted on the PVDF and PET yarns as received from the supplier following ASTM D 2256-02 standard [238]. The yarns were wound on

smaller bobbins by ITA staff for 3D weaving, as illustrated in Fig. 3.5. Technical specifications as measured are listed in Table 3.1.

Figure 3.5 PVDF Yarn as received from ITA, Germany

Table 3.1 Measured yarn properties for tensile tests

Yarns	Diameter [mm]	Weight of 0.3 m of Sample [g]	Linear Density [Tex]*	Linear Density [Denier]**
USP 2-0	0.327 ± 0.023	0.0473 ± 0.0014	157.7	1419
USP 3-0	0.24 ± 0.02	0.0256 ± 0.0008	85.5	769
USP 5-0	0.14 ± 0.015	0.0089 ± 0.0004	29.5	266
PET (Multifilament)	0.0137 (24 Strands)	0.0015 ± 0.0002	5.1	46

* Tex: Mass in gram per 1000 m of yarns
** Denier: Mass in grams per 9000 m of yarns

All tensile tests were conducted using TA XT Plus (Stable Micro Systems, Godalming, UK) with custom-designed jigs that could grip the yarns firmly during the tensile tests, as illustrated in Fig. 3.6 (a-d). According to the ASTM standard, a gauge length of 250 mm is required for the tensile tests. A length of 300 mm of each yarn was cut and mounted on the clamps, resulting in the initial gauge length of 256.25 mm, as shown in Fig. 3.6(b). Two washers were implemented in each clamp to provide uniform load distribution, and prevent the yarn cut by the sharp screw threads, and each end of the strand was passed through the space between flat washers, before tightening up the screws. Pre-tensioning load of 0.5 cN/Tex was applied before running each test, and few trial tests were conducted to find the optimum displacement rate to meet 20 ± 3 seconds

"time-to-break" requirement, as advised by the standard. The determined rates are presented in Table 3.2. Eight tests were conducted for each yarn type until rupture, and only those tests in which the yarn broke at least 3 mm away from clamping points were accepted for the analysis.

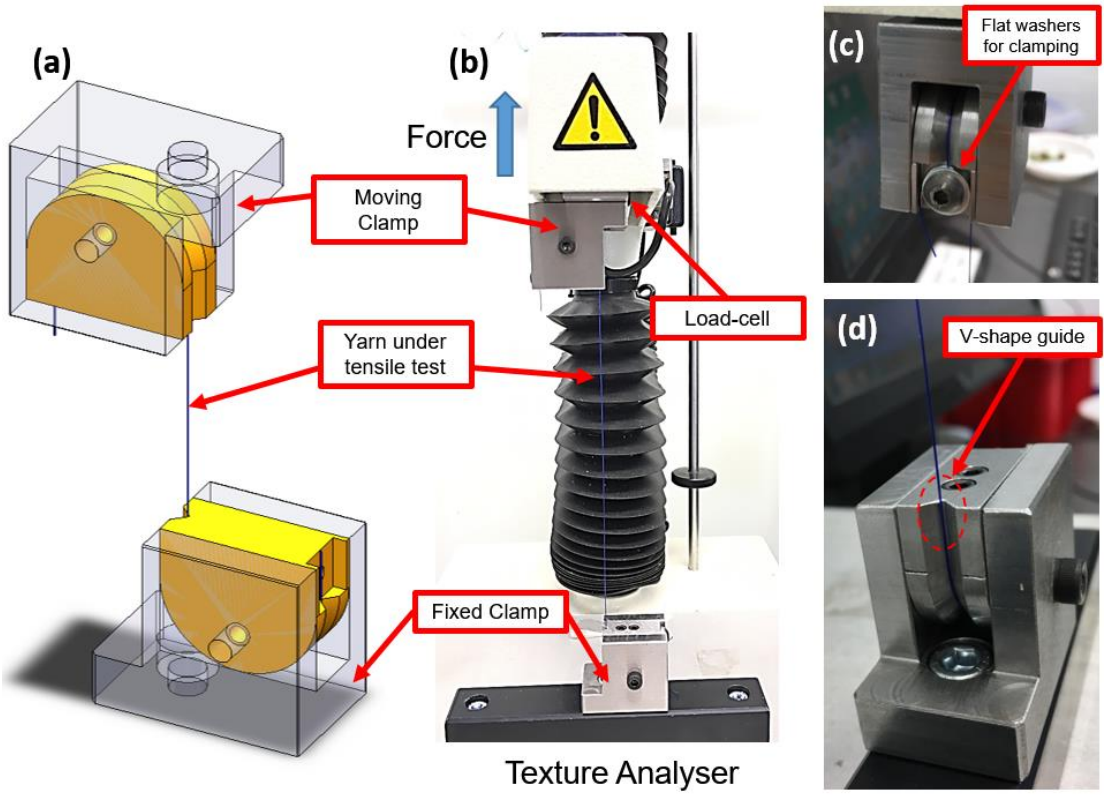

Figure 3.6 *(a) Schematic view of clamping jigs made for the tensile tests, (b) test setup, yarns were clamped by passing between two washers tighten by a screw in (c) upper clamp, (d) lower clamp*

Table 3.2 *Test displacement rate for 20 ± 3s "time-to-break"*

Yarns	Diameter [mm]	Displacement Rate [mm/sec]
USP 2-0	0.327 ± 0.023	3.5
USP 3-0	0.24 ± 0.02	3.5
USP 5-0	0.14 ± 0.015	2.5
PET	0.0137 (24 Strands)	3.0

3.2 Materials and Sample Preparation

3.2.1 Materials

Acrylamide monomer (AAm) in powder form (MW: 71.08), alginic acid sodium salt from brown algae, N,N′-Methylene-bis-acrylamide (MBAA), N,N,N′,N′-tetra-methyl-ethylene-diamine (TEMED), ammonium persulfate (APS), and calcium chloride ($CaCl_2$) were all purchased from Sigma-Aldrich (St. Louis, MO, USA), and used as received. Fresh bovine serum (contains in average 65 mg/ml albumin protein) for lubricated tests was obtained from Auckland Biosciences Ltd. (Auckland, New Zealand). Silica-NP powder (99 % purity, 20 nm NP size, hydrophilic) was purchased from NanoAmor (Houston, TX, USA).

3.2.2 ALG-PAAm IPN Hydrogel Synthesis

Using the analytical balance with 0.1 mg sensitivity, sufficient amounts of each chemical were weighted for hydrogel synthesis. First, acrylamide (AAm) monomer was dissolved in deionized (DI) water (33 w/v %), followed by adding 2 w/v % alginate, under continuous stirring at 40ºC temperature until a complete solution was achieved. Upon reaching a consistent solution, MBAA (2.5 wt % aqueous solution) was added as acrylamide crosslinker (0.06 wt% with respect to the amount of acrylamide), while 4µl of APS (10 wt % aqueous solution) as free radical initiator, and 0.22 µl of TEMED as catalyst, were added per each millilitre of pre-gel solution. To study the effect of crosslinking agent concentration (X.A%) on friction and wear behaviours of hydrogels, various ratios of MBAA (0.015%, 0.03% and 0.12%), in addition to the above-mentioned value, were added during synthesis phase. It is worth mentioning that the solution was degassed to eliminate dissolved oxygen prior to addition of TEMED, as oxygen might act as free radical sweeper and restrain acrylamide polymerization. The solution was then

immediately injected into disk-shape acrylic moulds, Ø21 mm, and 4.5 mm in thickness, confined between microscope glass slides (76.2 mm × 25.4 mm) on both sides, as illustrated in Fig. 3.7, to create flat, smooth-surfaced hydrogel samples. The polymerization and covalent crosslinking of PAAm chains were achieved by storing the moulds in an incubator room, with the constant temperature of 35ºC for six hours. In order for the alginate component to crosslink ionically, the samples were then immersed in 10 wt % $CaCl_2$ aqueous solution for 24 hours prior to washing the samples with sufficient amount of DI water for several hours to ensure removal of non-reacted particles. The samples were then dried in the incubator for several days prior to wear studies, for determining the dried mass of each sample before the tests.

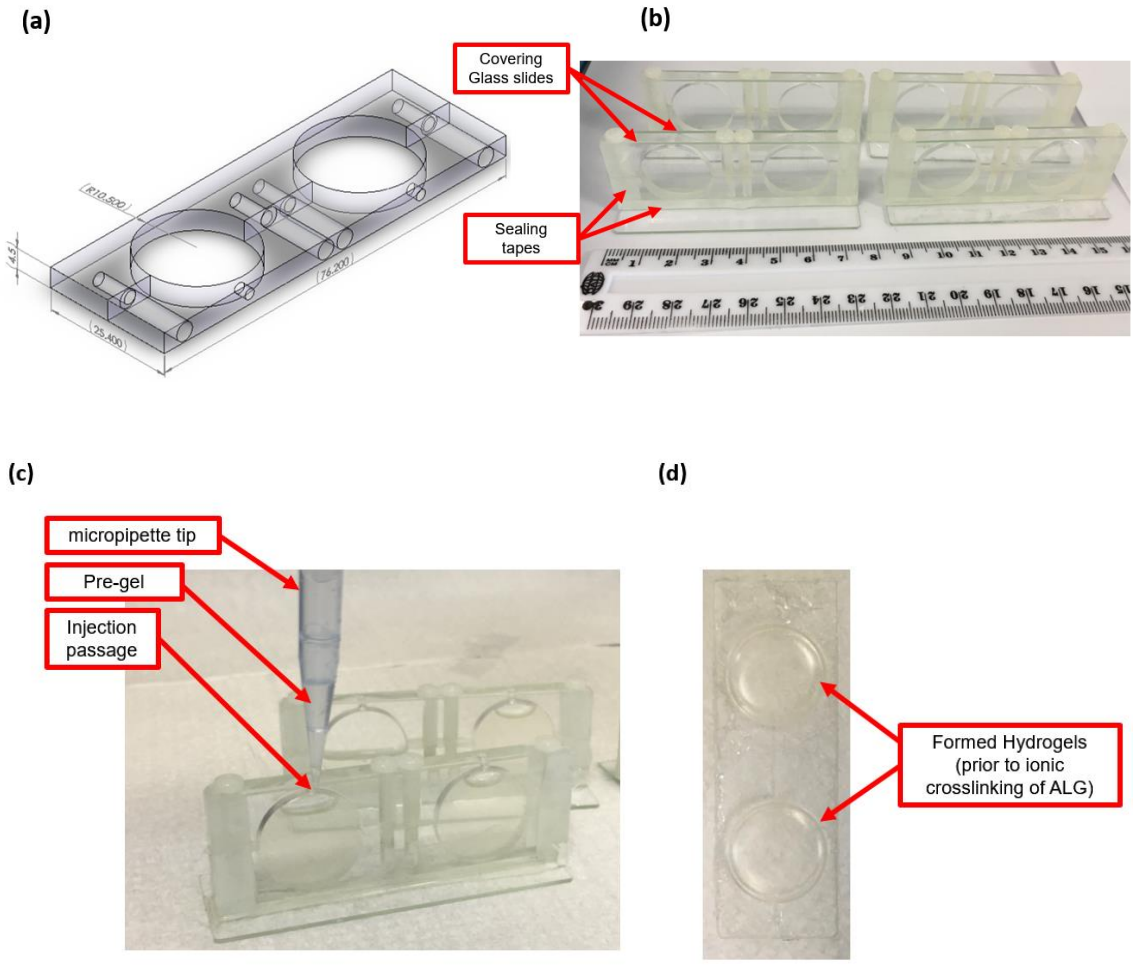

Figure 3.7 *(a) Acrylic mould made for hydrogel sample preparation, (b) assembled moulds with covering glass slides, (c) pre-gel injection process, (d) formed hydrogels*

To study the effect of crosslinked alginate on friction and wear behaviour of ALG-PAAm hydrogel, PAAm samples were created by dissolving two different concentrations of AAm monomer (33 w/v % and 50 w/v %) in DI water followed by the same above-mentioned procedure, except no alginate was added to the mixture, therefore no immersion in $CaCl_2$ was required.

3.2.3 Si-NP-ALG-PAAM Nanocomposite Hydrogel Synthesis

Silica-ALG-PAAm NCH was prepared by dissolving acrylamide monomer in deionized (DI) water (33 w/v%), followed by adding three different ratios of silica-NP powder, 1-4 wt% (based on AAm+ ALG), to the solution and uniformly dispersing the powder in the solution with vigorous stirring. The remaining procedure was the same as the method described in 3.2.2. Just one ratio of MBAA (0.06%) was added to prepare NCHs. Produced samples of NCH with various NP concentrations, along with IPN hydrogel are illustrated in Fig. 3.8, and could be distinguished from each other by the level of their transparency. Once in fully swollen state, the samples measured in average 30 mm in diameter and 7 mm in thickness.

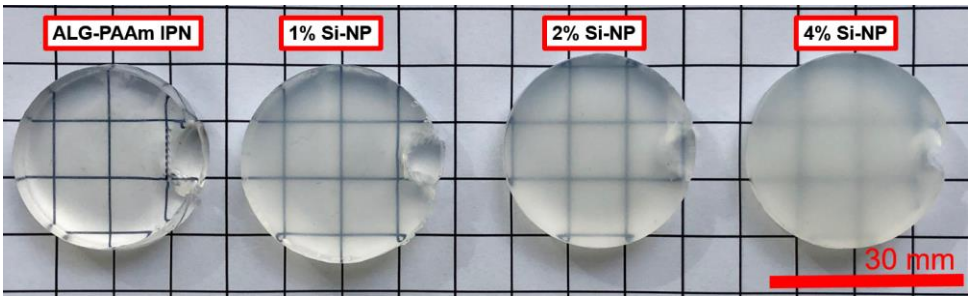

Figure 3.8 *IPN and NCH hydrogel samples prepared by covalently-crosslinked PAAm and ionically-crosslinked alginate. The silica-NPs were uniformly dispersed in the pre-gel solution. As the concentration of silica powder increased, the samples became less transparent, and more opaque*

3.2.4 3D woven Hydrogel Composite Sample Preparation

PAAm-ALG hybrid hydrogel was prepared as previously described (with 0.06% concentration of MBAA as crosslinking agent). It was planned to fabricate the HCs via vacuum-assisted infusion method, consistent with a previous study [235]. Resin infusion setup was successfully accomplished at *Centre for Advanced Composite Materials*, the University of Auckland, as shown in Fig. 3.9 (a). A 10 cm strip of textile type-A was initially cut and placed under the plastic cover followed by sealing, then the vacuum pressure was applied. A sufficient amount of the pre-gel solution was then prepared, and was made flown through the inlet pipe, then through the fabric promptly, exiting through the outlet pipe. Due to relatively low viscosity of the pre-gel, comparable to water viscosity, and the negative pressure setting (-10 mbar as minimum), resin flow rate could not be easily controlled, and a considerable bubble formation was observed throughout the textile, leading to major defects in the final cured HC. Therefore, resin infusion method was set aside, and an alternative procedure for sample fabrication was considered, i.e. resin transfer moulding.

The polystyrene-made rectangular containers were purchased and used as a mould. The inner width of the mould was measured almost the same as each textile width. Thus, a sample with the length equal to the mould's inner length was cut from the strip of each textile, and placed inside the mould, as illustrated in Fig. 3.9 (b). Bubble formation was avoided by thoroughly wetting the fabric with precursor monomer solution. The moulds were then covered, with a custom-made acrylic cover, made as slide-fit to the mould and stored in an incubator room at 35ºC temperature for six hours to ensure complete polymerization. A similar approach was used in a previous study to prepare steel-wool reinforced hydrogels [33]. The hydrogel composites (HC Type-A and HC Type-B) were then removed from the moulds and soaked in a calcium chloride bath for

24 hours for the ionic crosslinking of the alginate network to occur, followed by soaking the composites in DI water for several hours to ensure removal of unreacted chemicals from the hydrogel, as illustrated in Fig. 3.9 (c). As illustrated in Fig. 3.9 (d), the surface facing the mould's bottom surface was used for the surface analysis and tribological tests. The fibre volume fractions for the final composites were measured as 0.26 and 0.28 for HC Type-A and HC Type-B, respectively.

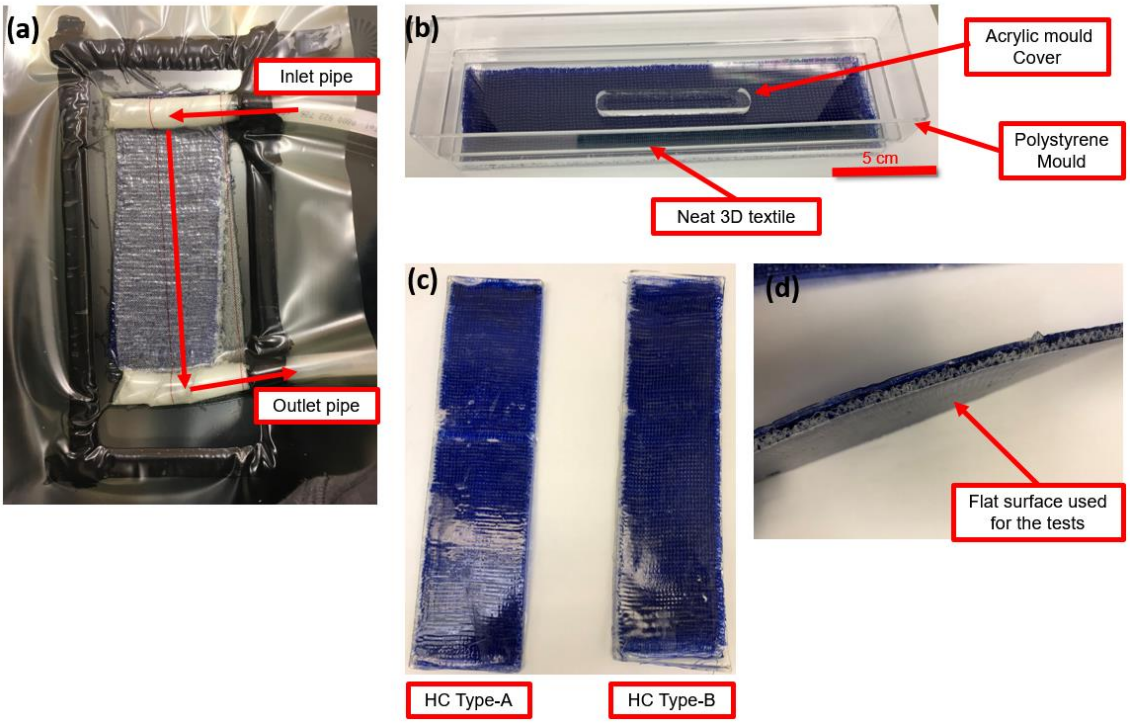

Figure 3.9 (a) Resin infusion setup, and resin flow direction, (b) alternative resin transfer moulding implemented for this study, (c) produced HCs, (d) side view of HC; the surface facing the bottom of mould was selected for the experiments

3.3 Experimental Procedure

3.3.1 Indentation Test

The localised properties of each specimen, such as elastic modulus and hardness, were determined by indentation tests. Indentation experiments were carried out using a TA XT Plus texture analyser, equipped with a 50N load-cell, and a spherical stainless

steel indenter (Ø5 mm), following ASTM E2546 [239], to measure the elastic modulus and hardness of all studied materials. The indentation depth was 1.2 mm and the cross-head speed was 1.2 mm/min. Prior to each test, samples (n=3 for each material) were allowed to reach to equilibrium state by submersion in water bath for 30 minutes. The reaction force with respect to indentation depth was recorded during loading and unloading of each sample and plotted, then the reduced elastic modulus, E_r, could be obtained from:

$$E_r = \left(\frac{S}{2}\right)\sqrt{\frac{\pi}{A_p}} \tag{3.1}$$

where S called contact stiffness, is the slope of linear fitting of the unloading curve, and A_p, the projected contact area is equal to $2\pi R h_c$ for spherical indenter. Here, R is the radius of indenter and h_c is the contact depth that can be determined as:

$$h_c = h_{max} - \frac{3P_{max}}{4\,S} \tag{3.2}$$

where h_{max} is the indentation depth and P_{max} is the maximum reaction force occurring at h_{max}. Therefore, the elastic modulus, E, and hardness, H, can be determined using:

$$\frac{1}{E_r} = \frac{1-\upsilon^2}{E} + \frac{1-{\upsilon_i}^2}{E_i} \tag{3.3}$$

$$H = \frac{P_{max}}{A_p} \tag{3.4}$$

where, υ_i and E_i are Poisson's ratio and elastic modulus of the indenter, respectively, while υ and E are the Poisson's ratio and elastic modulus of the hydrogel specimen. It is worth mentioning that due to high water content of hydrogels, their incompressibility is usually assumed, resulting in $\upsilon = 0.5$ [240, 241].

3.3.2 Unconfined Compression Test

In general, the articular cartilage tissue tolerates loading in tensile, shear and compressive modes. However, the most crucial loading, compression, was focused in this study. Uniaxial, unconfined compression experiments were performed on all samples at ambient temperature (25ºC), using TA XT Plus texture analyser equipped with a 50 N load cell (500N load cell for testing of HCs and the neat textiles). The test coupons were produced by cutting the specimen into Ø7 mm, and a thickness of 6.5mm, while HCs and 3D woven textiles were cut into strips, 55 mm long and 10 mm wide, as illustrated in Fig. 3.10. All samples were compressed to 50% of their initial thickness with the strain rates of 0.01 s^{-1}, 0.1 s^{-1}, and 1 s^{-1} to cover the entire range of strain rates that are experienced by cartilage [242]. The maximum strain was reported to be within the elastic region of each hydrogel type [34]. To ensure reproducibility of results, each measurement was performed on at least 3 samples from each material and the average values are reported here. Each specimen was allowed to equilibrate by soaking it into DI water 30 minutes before each test. A pre-load of 0.1N was applied to each sample prior to initiating each test to ensure a full contact of the specimen with the substrate and the compressing cylinder. The load-displacement data was then converted into engineering stress-engineering strain, and the curves were fitted by (3.5) for IPN hydrogel and (3.6) for NCH and HC with higher gradient [243, 244]:

$$\sigma = A + Be^{(C\varepsilon)} \tag{3.5}$$

$$\sigma = D + Ee^{(F\varepsilon)} + Ge^{(H\varepsilon)} \tag{3.6}$$

where σ is compressive stress, ε is strain and A-H are curve fitting constants. The compressive modulus was obtained as the first derivative of stress with respect to strain for each of the above equations.

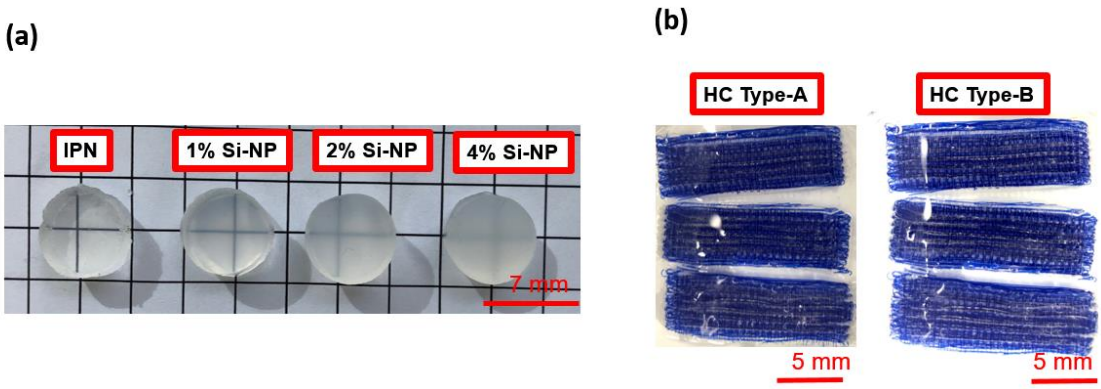

Figure 3.10 *Test coupons for compression tests: (a) IPN and NCH, (b) HC Type-A and Type-B*

3.3.3 Measurement of Viscoelastic Response

As all tested samples are made from polymeric materials, they would exhibit a time-dependent mechanical response, which could be assessed by a stress relaxation test method. Using the previously-described testing instrument, the samples (n= 3 for each material) with the same dimensions as those for compression tests, were compressed to 0.5 strain, and the strain level was held constant for a duration of 1 hour, while the variation of reaction force vs. time was recorded by the instrument. The force was then converted into stress, and the ratio of stress at time, t, to the initial peak stress ($\sigma\ (t)/\ \sigma_0$) was calculated. Stress-time data were then curve fitted into (3.7), as previously utilised for the characterisation of viscoelasticity in hydrogels [245, 246].

$$\frac{\sigma(t)}{\sigma_0} = \frac{\sigma_f}{\sigma_0} + ae^{(-bt)} + ce^{(-dt)} \tag{3.7}$$

where σ_f is the final stress value (at t=3600 s) and *a-d* are material constants, determined from curve fitting.

3.3.4 Friction and Wear Testing

Tribological tests were conducted using Rtec tribometer (Rtec-instruments, San Jose, CA, USA). The test setup for each type of sample is illustrated in Fig. 3.11. Normal load was applied on the surface of the specimens through an alumina ceramic ball (Ø3 mm, surface roughness, R_a: 0.133µm) attached to a 10N load cell. Alumina (Al_2O_3) is a common countersurface for the evaluation of orthopaedic materials [195, 247, 248].

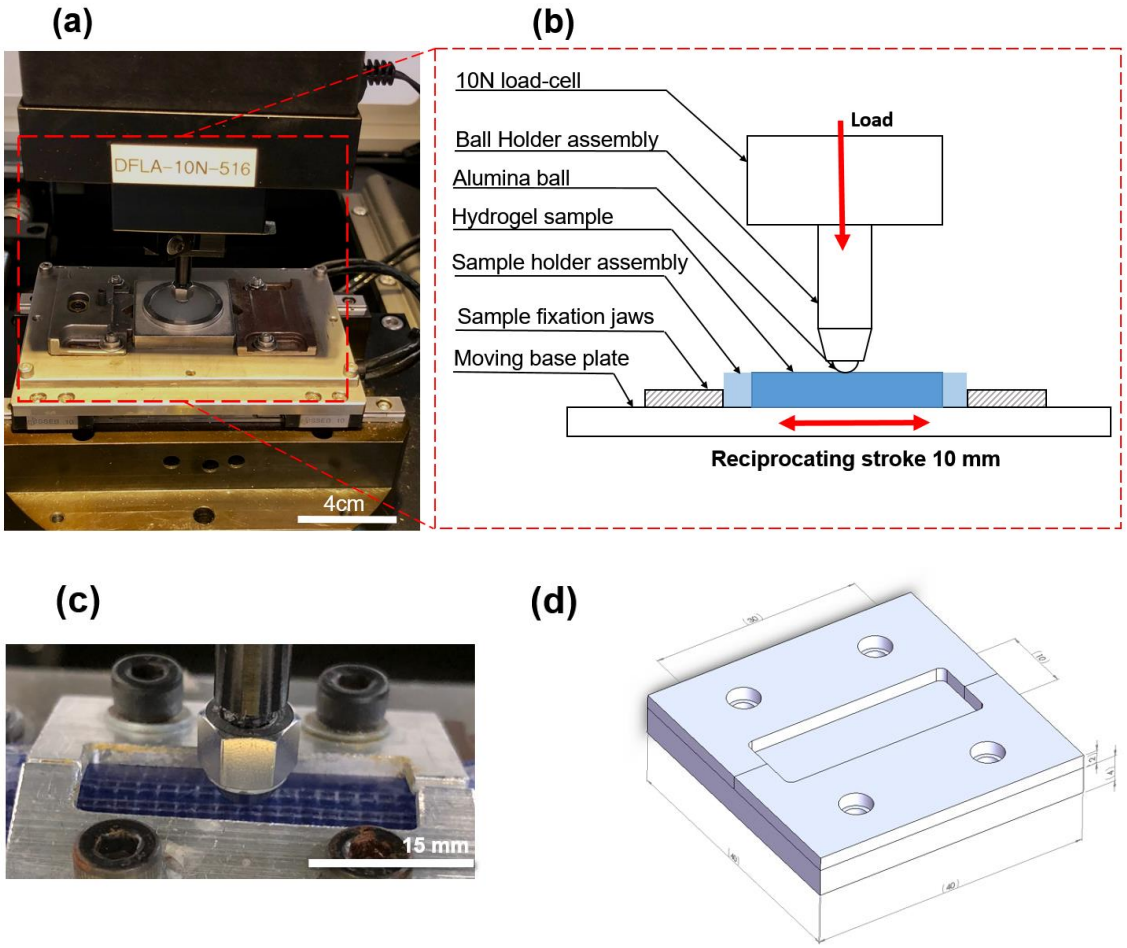

Figure 3.11 *(a) Experimental setup of wear testing instrument for hydrogels and NCHs, (b) schematic illustration of ALG-PAAm hydrogel specimen sliding against alumina ball pressed into the hydrogel, (c) setup for testing of HCs, (d) design of the clamping tool*

All tests were conducted in ambient temperature, on the samples in their equilibrium state. The purpose was to assess the friction and wear of the materials with

and without lubrication. The lubricant film was applied only on the interface and was maintained during the test by applying fresh lubricant in regular intervals.

The compliant hydrogels, as well as NCH and HC samples were found not affecting the surface roughness of alumina ball, due to the high level of hardness the ceramic offers. For achieving a consistent surface roughness of countersurface, the same alumina ball was used for the entire tribology tests. Under various normal loads, the lower platform, in which the samples were fixed, performed reciprocating motion, and the samples were slid against opposing ceramic ball. During the tests, the frictional forces were sensed and recorded by a set of beam sensors inside the load cell, while the normal load was continuously monitored and maintained at a pre-set value.

During the sliding wear tests, 0.1, 0.5 and 0.7N normal loads were applied. The resultant contact pressures were determined using pressure sensitive films (Fujifilm Prescale LLLW & LLW ranges), inserted between mating surfaces prior to a quasi-static loading. The equivalent contact pressure is a function of hydrogel's elastic modulus. Based on visual comparison of the results with the reference colour scale provided by the supplier, it was observed the load range of 0.1 – 0.7N correlated to the contact pressure of 0.248 – 2.025 MPa, and 0.267 – 2.25 MPa for hydrogels with 0.03 and 0.06% crosslinking agent (X.A %), respectively. The contact pressure was found in the range of 0.279 – 3.13 MPa for NCH with 1% – 4% NP concentrations, while it was measured as 0.45 MPa – 2.45 MPa for HC Type-A, and 0.54 MPa – 2.65 MPa for HC Type-B for the above load range. These values were found to be within the same order of magnitude mentioned in the literature regarding the average pressures tolerated by cartilage in human knee (0.1–2.0 MPa) [196, 249, 250]. Moreover, the sliding rate was selected to simulate the average sliding speed tolerated by the tissue during walking and running activities [249]. Tribosystem test parameters are summarised in Table 3.3. To ensure

reproducibility of the results, each test was conducted on 3 samples of each hydrogel system and the average values were reported.

The total sliding distance of 1000 meters was considered constant for all experiments, while boundary lubrication tests were performed using bovine serum, to evaluate the effect of proteins found in synovial fluid, on tribological performance of the materials. Wear volumes of all samples were determined by cross-sectional wear area multiplied by the length of wear track. A Taylor Hobson Form 50 surface profiler (Taylor Hobson, AMETEK, PA, USA) was utilised, equipped with diamond-tip stylus to analyse the geometrical properties of wear scar, such as the width and the wear depth. The stylus was moved across the width of generated wear scar at 3 different regions, the average cross-sectional profile was obtained, which was then used to calculate the average cross-sectional area by curve fitting. The surface roughness of each sample was also measured by a 20X confocal objective of optical profilometer module of the tribometer before each test, to study the surface properties of each kind of materials.

Table 3.3 Summary of the test parameters and levels used for wear experiments

Parameter	Level 1	Level 2	Level 3
Load, (P) [N]	0.1	0.5	0.7
Sliding rate, (v) [mm/s]	50	100	150
Materials	IPN Hydrogel (0.03, 0.06 X.A%)	NCH (1%, 2%, 4% Si-NP)	HC (Type-A, Type-B)
Lubrication	No Bovine Serum (“dry”)	Bovine Serum (“lubricated”)	-

3.3.5 SEM Investigations

In order to identify the dominant wear mechanism occurring in hydrogel samples, scanning electron microscopy (Hitachi, SU-70 SEM, Fig. 3.12 (a)), was utilised to examine the worn surface morphology. The accelerating voltage of 5.0 kV and average

working distance of 18.0 mm were used for this study. To resolve the conductivity issue, associated with samples, the worn surface was gold sputtered using ion sputter coater (Hitachi, E-1045) and the samples were mounted on a metallic support.

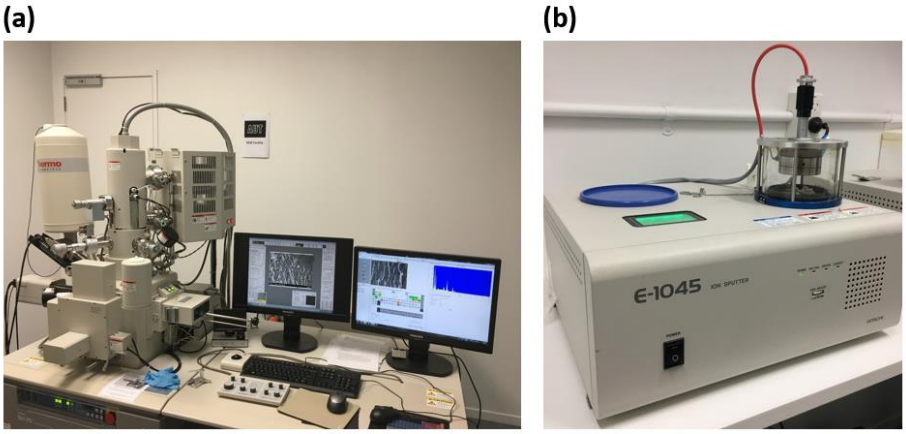

Figure 3.12 (a) Hitachi SU-70 SEM, (b) Hitachi, E-1045 ion-sputter coater

Energy-dispersive X-ray spectroscopy (EDS) module of SEM was utilised to analyse surface elemental mapping of NCH, and to investigate if Si-NP was uniformly distributed on the surface of NCHs, as implemented in a previous study [204]. Furthermore, the porous structure of IPN hydrogels and NCHs were studied under SEM, using freeze-drying method. To prepare such samples, the precursor solution was casted into multi-well plates, as can be seen in Fig. 3.13 (a), and being formed same as described in 3.2.2 and 3.2.3. Each cylindrical sample was prepared in two aspect ratios, i.e. 0.5 and 1, (aspect ratio: height/diameter). Next, the samples (Fig. 3.13 (b)) were completely frozen by either submerging into liquid nitrogen bath, or keeping in freezer (-80ºC) for two days. The frozen samples were then kept in a freeze-dryer for three days, as can be seen in Fig. 3.13 (c), prior to being prepared for SEM studies.

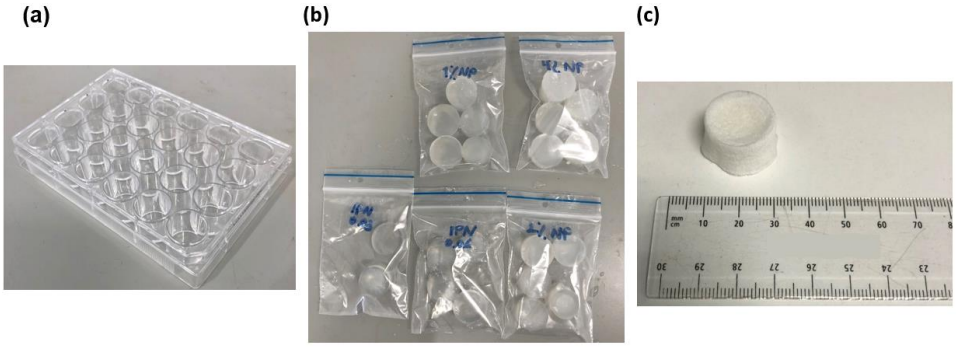

Figure 3.13 (a) A multi-well plate used for sample preparation, (b) prepared hydrogels and NCHs, (c) a freeze-dried sample

3.4 FE Modelling Procedure

In this section, FE simulation of sliding wear on woven textiles and textile composites are described. A unit cell of 3D orthogonal fabric (without matrix) is initially developed to match the experimental set-up proposed by Giordano and Schmid [182]. Their experimental set-up consisted of pin-on-disk tests using a six-station OrthoPOD (AMTI, Watertown, MA). Circular samples with 35 *mm* diameter were cut out of fabric strips and were pasted to metal puck using adhesive, allowed to dry overnight. Samples were also aligned in a direction that the lowest friction with pin movement was achieved. Cobalt-chromium (Co-Cr) pins with a diameter of 25.4 mm were used for the experiments [177]. Pin motion pattern and applied normal load shown in Fig. 3.14 (a), were acquired from literature [249, 251, 252]. A normal load equivalent to the pressure of 1 MPa was applied to mimic stance phase, and then it was reduced to 0.667 MPa during swing phase. Covert et al. [249] suggested the speeds ranging from 50 to 150 mm/s for walking and running simulations. Therefore, 50 mm/s was chosen for stance and 81.5 mm/s for swing stage, hence one cycle takes 0.785 seconds. The tests were performed in the presence of 20 ml deionized (DI) water and wear was measured using gravimetric measurement according to modified ASTM 2025-06 [253]. The intervals between gravimetric measurements were increased as testing progressed.

The FE results are to be compared with experimental data as a means of model validation. Furthermore, parametric studies are conducted to explore the effect of various parameters on the wear rate of the material. Next, the model is further extended to hydrogel composites, i.e. the custom-designed weave patterns, focused in the current study, embedded in the hydrogel matrix.

3.4.1 FE Modelling of Orthogonal 3D Textile Unit Cell

Geometric representation of the 3D fabric unit cell is shown in Fig. 3.14 (b). Commercial CAD package, SolidWorks®, was employed for tow modelling and unit cell assembly. The geometric data used in the process are summarised in Table 3.4.

Multifilament yarns were modelled as solid geometries to reduce model complexity. Tow cross-section was sketched as race-track, (Fig. 3.14 (c)) to achieve surface contact for better results [254, 255]. Other cross-sectional forms such as circular, elliptical and lenticular might result in line contact between tows and therefore, stress and contact pressure computed is not accurate enough, especially when a small amount of load is applied. To reduce computational costs, and due to symmetry in x-direction, only half of the unit cell was modelled, as shown in Fig. 3.14 (d). The final assembly was placed between two blocks for the sliding wear simulations. Due to the small size of unit cell compared to pin cross-section (Ø12.7 mm), only part of the pin in contact, in the form of a block, was considered for simulation. Finally, it was imported to ABAQUS (version 6.14), as 3D ACIS model (.sat file format).

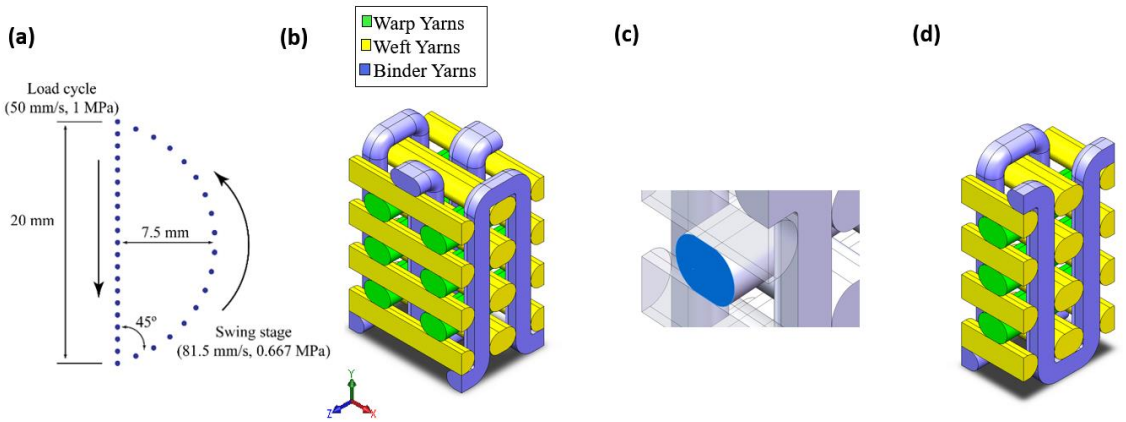

Figure 3.14 (a) Pin track and applied load for wear tests (b) fabric unit cell modelled in SolidWorks®, (c) race-track cross-section of tows, (d) half model for FE simulation

Table 3.4 Input data for geometric modelling of textile in SolidWorks

Model	No. of Warp Yarns + Binder Yarns	No. of Warp Yarns	Yarn Spacing [mm]	Yarn Width [mm]	Overall thickness [mm]	Unit cell size [L×W×D] [mm^3]
Whole unit cell	6 +2	8	0.75	0.35	2.2	1.50 ×1.10 × 2.20
Half unit cell	3+1	8	0.75	0.35	2.2	0.75 × 1.10 × 2.20

Material properties assigned to individual fabric tows as well as both blocks, are presented in Table 3.5. Only linear elastic material properties were assigned, since ALE adaptive meshing technique might lead to inaccurate results for other material models such as hyper-elastic materials [216]. Pin was made to slide 20 mm linearly against the textile specimen (p= 1MPa, v = 50 mm/s), followed by moving in a semi-circular route (p= 0.67MPa, v = 81.5 mm/s) and returning to the start point completing a cycle. Due to the model scale, the entire pin motion is not applicable in the FE simulation, and only a linear motion, in one direction on the woven fabric was simulated. Load was applied first on the upper block, leading to fabric compression, followed by its linear movement in

one direction under load. Finally, the block was unloaded, and the yarns returned to their original position and one cycle was accomplished. The block was relocated to its original position before second cycle took place. “Hard” contact was defined as normal behaviour of interaction properties between contact pairs to transmit contact pressure between surfaces without any limitations in magnitude. Tangential behaviour was also set to frictional motion with coefficient of friction (CoF) of 0.3 between contact pair (Co-Cr and PET), while CoF was considered to be 0.19 between the yarns in contact [256, 257]. This is to monitor shear forces transferred between solid bodies in contact. As shown in Fig. 3.15 (a), periodic boundary conditions were assigned to the unit cell to account for the whole fabric replication, while the lower block was constrained in all directions and upper block was restricted to move only in the *y*-direction during loading, while it moves just in *z*-direction during sliding.

Table 3.5 Material properties used in FE modelling [257, 258]

Material	Density [g/cm^3]	Young’s Modulus [MPa]	Poisson’s Ratio	Coefficient of Friction
PET	1.27	2700	0.37	0.19
Co-Cr	8.5	220,000	0.29	0.3

126,486 three-dimensional, 8-node elements with reduced integration (C3D8R, enhanced hourglass) and 217,227 nodes meshed the entire assembly. The accuracy of the FE solution was improved by applying reduced integration elements causing stiffness softening in the model. There is only one drawback: it leads to mesh instability, since zero strain energy is calculated for deformed elements, which might violates solution accuracy. Hence, enhanced hourglassing option is embedded in the FE package to solve zero-mode energy of relevant elements, which without them, adaptive meshing is not feasible. Finer mesh was created in the contact region of the binder tows and the block as shown in Fig. 3.15 (b), and mesh convergence study was performed to ensure that the

results are independent of the element size. Adaptive mesh constraint was only applied to 355 nodes in contact with sliding block. Wear was considered to happen only in fabric surface, and hence element deletion option was assigned only to binder tows' elements.

The simulation was run to replicate as much cycles of the experiment as possible, to ensure good accuracy, as well as maintaining computational expense as low as possible. Geometry update due to material removal (wear) of the fabric surface occurred only at the final step after the structure was unloaded, and the FE results were compared with the experimental study. Upon reaching good agreement between these values, the computed wear was extrapolated linearly to predict wear at a large number of wear cycles.

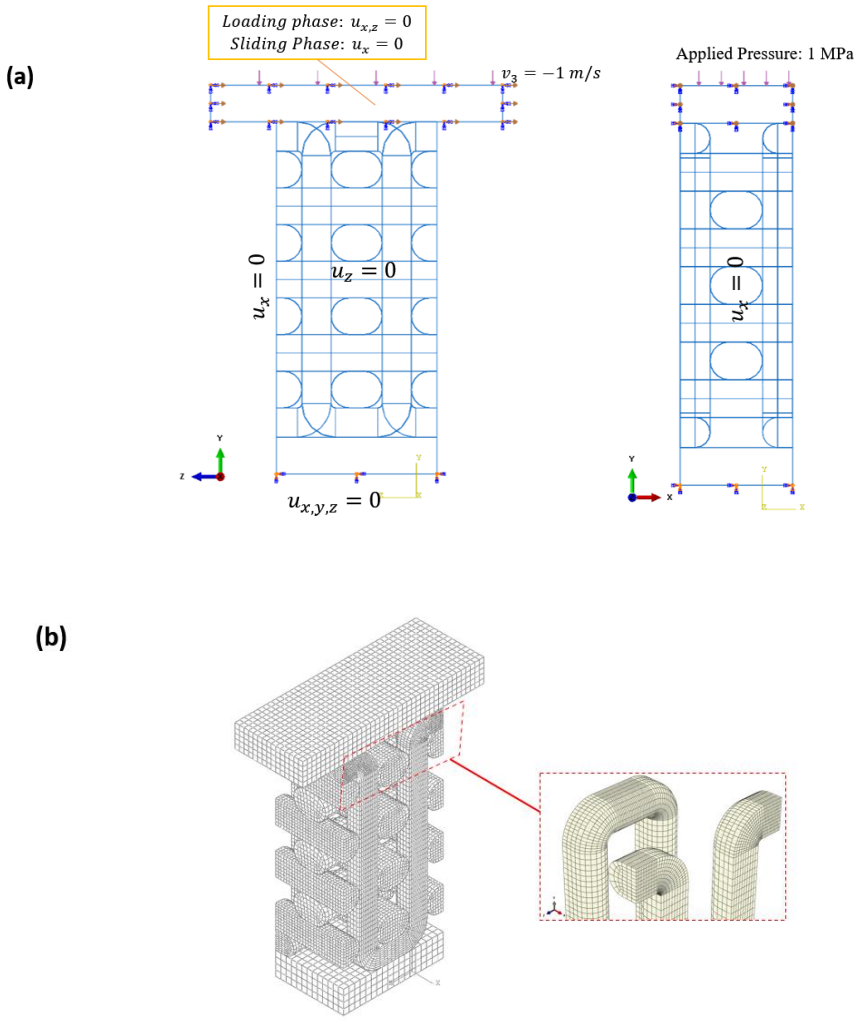

Figure 3.15 *(a) Load and boundary conditions implemented in the model, (b) FE discretisation with finer mesh in contact region (top faces of binder yarns)*

3.4.2 Description of Wear Subroutine

The general method for computational wear simulation includes two major steps: solving the non-linear contact problem and use the computed outputs such as contact pressure and sliding distance in order to compute wear. In the current study, Archard's wear law was implemented, in which wear is a function of contact pressure and sliding distance:

$$W = \frac{K}{H} . P . s \tag{3.8}$$

where W [mm^3] is the volume of material removed from softer material's surface, H [N/mm^2] is the hardness of worn surface, P [N] is the normal load applied, s [m] is the sliding, and K is the dimensionless wear coefficient. To obtain the evolution of surface profile due to wear, wear depth of each contact node should be acquired and deducted from the original vertical component of nodal coordinate. Therefore, by dividing both sides of (3.8) by incremental apparent contact area, ΔA, wear depth increment, dh, can be determined from:

$$dh = k_D . p . ds \tag{3.9}$$

where k_D [mm^3/N.mm] is dimensional wear coefficient, p [MPa] is contact pressure, and ds [mm] is sliding distance increment. The total wear depth of contact surface can be formulated as:

$$h = \int k_{\mathrm{D}} . p . ds \tag{3.10}$$

A user-defined UMESHMOTION subroutine was developed and utilised for wear computation. The overview of simulation method together with subroutine function is depicted in Fig. 3.16. Contact pressure data, tangential traction (contact slip), nodal displacement and contact area, all computed from FE solver, will be used in the

subroutine to determine wear depth. Wear coefficient must be acquired from experiments, and put into subroutine, as well. Fortran-based subroutine was linked with the FE package, hence the code was run to obtain required nodal data from FE solver at the end of each time increment. Finally, the mesh geometry was updated as a result of extrapolated wear depth occurred at the end of the analysis, when the contact pair were not in touch, due to upper block unloading, and ALE adaptive meshing method implemented in the FE package, resulted in non-distorted mesh across the domain.

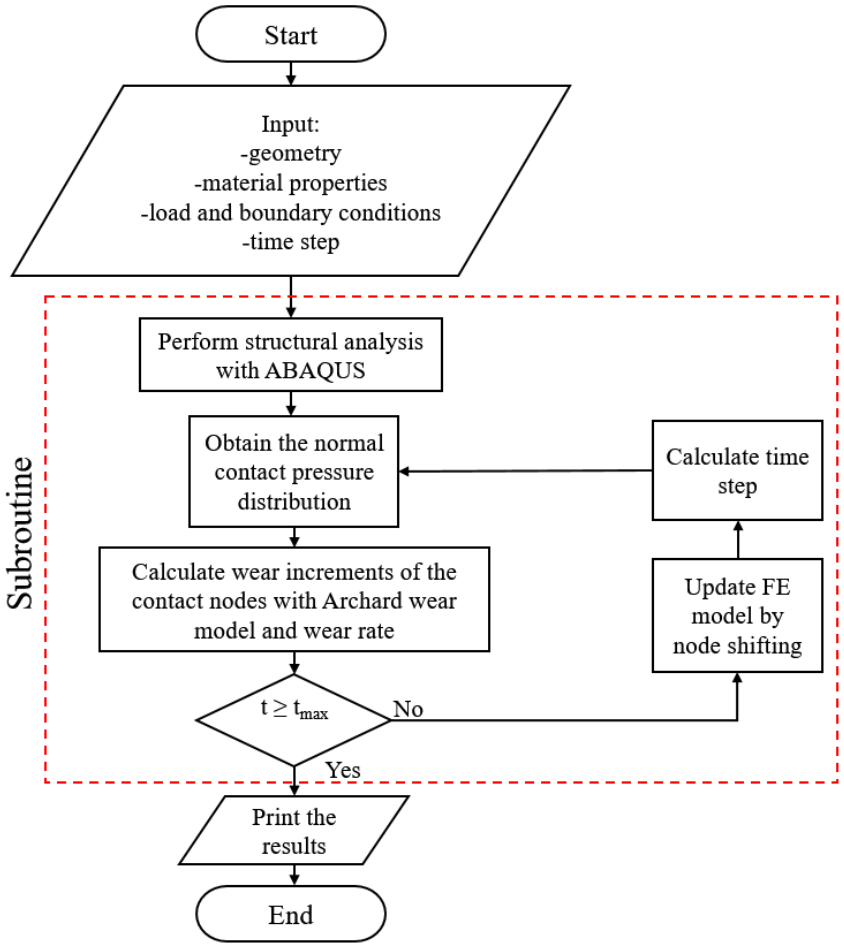

Figure 3.16 Simulation flowchart

3.4.3 FE Modelling of Hydrogel Composites

The geometric modelling of the composite unit cells were carried out in SolidWorks CAD package. The unit cells for both textiles are highlighted in Fig. 3.17.

The dimensions obtained from SEM images, were used as a reference for geometric modelling. The geometric data used in the process is summarised in Table 3.6.

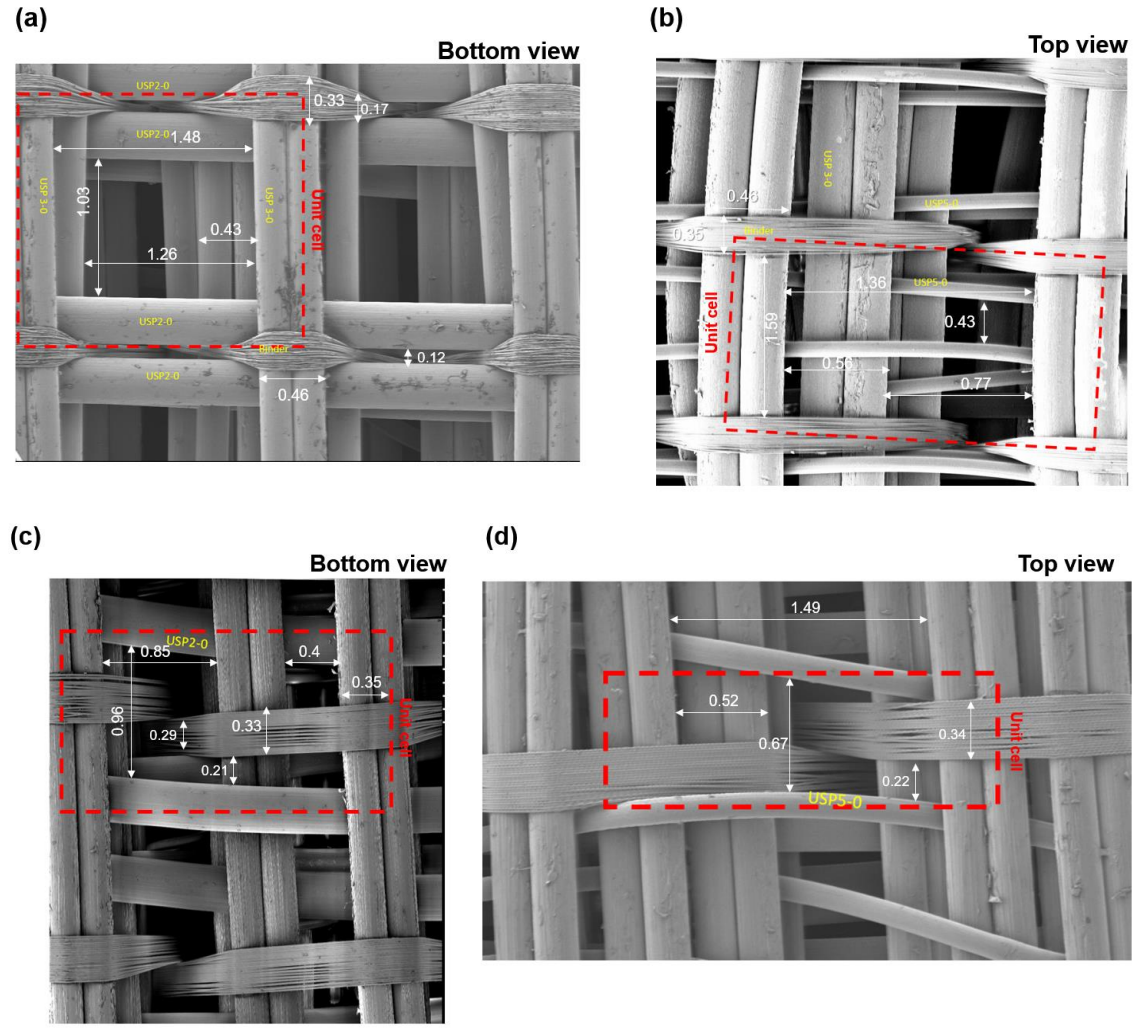

Figure 3.17 Unit cell of 3D textiles with their dimensions (indicated by a dashed box) obtained from SEM: (a), (b) textile Type-A, (c),(d) textile Type-B; (all dimensions in mm) Typical two sizes are also identified in the images.

Table 3.6 Input data for geometric modelling of textile in SolidWorks

Model	No. of Warp Yarns + Binder Yarns	No. of Weft Yarns	Warp Yarn Spacing [mm]	Yarn Width [mm]	Binder thickness [mm]	Unit cell size [L×W×H] [mm^3]
Unit Cell Type-A	14 +2	30	1.03	0.12~0.3	0.03	2.20 ×1.88 × 3.41
Unit Cell Type-B	5+2	16	0.96	0.12~0.3	0.03	1.95 × 0.98 × 2.60

As illustrated in Fig. 3.18, the HC unit cells geometries were developed by assembling the individual textile tows, and embedding them within a solid box, i.e. hydrogel matrix, followed by Boolean subtraction of the tows' volume from the matrix in the CAD package. Both mono and multifilament yarns were modelled as solid bodies to reduce model complexity and computational costs. Each unit cell type was then imported into the CAE package as a 3D ACIS model (.sat).

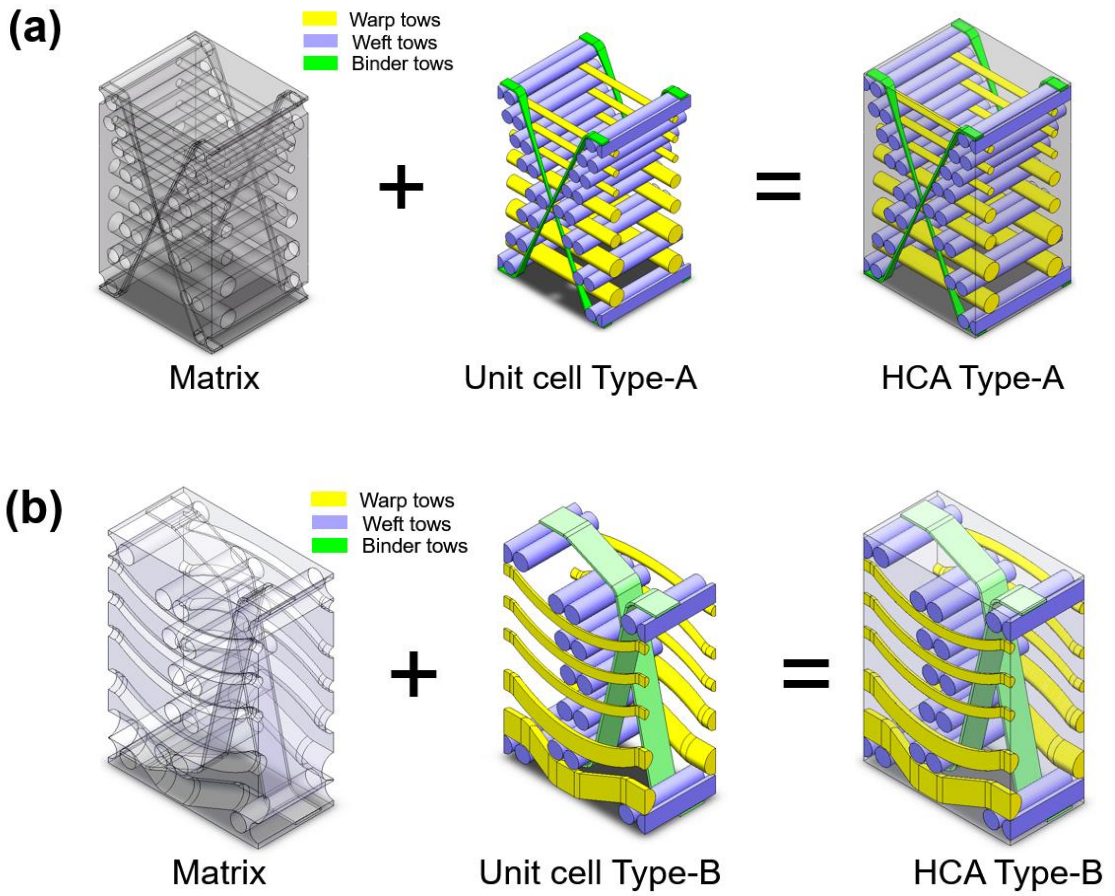

Figure 3.18 HC unit cells were modelled in SolidWorks as an assembly of textile unit cell and hydrogel matrix; (a) HC Type-A, (b) HC Type-B

Mechanical properties listed in Table 3.7 were assigned to individual tows, as well as the hydrogel matrix. Poisson's ratios of materials were obtained from previously published literature, while Young's moduli were acquired from the tensile tests for the yarns, and from the indentation tests for the hydrogel matrix. As previously mentioned,

due to the material model limitations for wear simulation, only elastic material properties were assigned to all components. Friction was only considered at hydrogel-alumina ceramic interface, and load-dependent and velocity-dependent friction coefficients were assigned based on measured mean values obtained from the friction experiments.

Table 3.7 Material properties used in FE modelling of HCs

Material	Density [g/cm^3]	Young's Modulus [MPa]	Poisson's Ratio
Alumina ceramic[259]	3.69	300000	0.21
PET[257]	1.5	13375	0.37
USP 2-0[260]	0.183	2892.5	0.38
USP 3-0	0.188	3130.1	0.38
USP 5-0	0.191	2992.7	0.38
ALG-PAAm matrix	1.05	0.122	0.49

As for the matrix-fibre interaction, tie constraints were assigned, i.e. adjacent matrix-fibre surfaces were tied together. Load and boundary conditions implemented to the unit cell Type-A model, are illustrated in Fig. 3.19, consistent with the periodic boundary conditions previously utilised for the 3D textile unit cell. In Fig. 3.19, u_x, u_y and u_z represent the displacements in the x, y and z-directions, respectively. P_y indicates pressure loads in the y-directions, while v_x represents the linear velocity on the x-direction. The bottom surface of the unit cell was constrained in all direction, while the warp and the weft tows were constrained in x and z-direction respectively (See Fig. 3.19). These boundary conditions match well with the actual textile, where the displacement of warp and weft yarns are restricted in mentioned directions due to stitching at the margins. Similar load and boundary conditions were implemented for unit cell Type-B, as well. The uniformly distributed pressure was applied through the ball, leading to composite compression, followed by a linear reciprocating motion of the ball, carried out by applying alternating velocity constraint on the ball. After a certain number of strokes, the load was removed, and 0.01 mm displacement in positive y-axis was exerted on the ball,

leading to separation of ball and composite material, before geometry was updated by the subroutine.

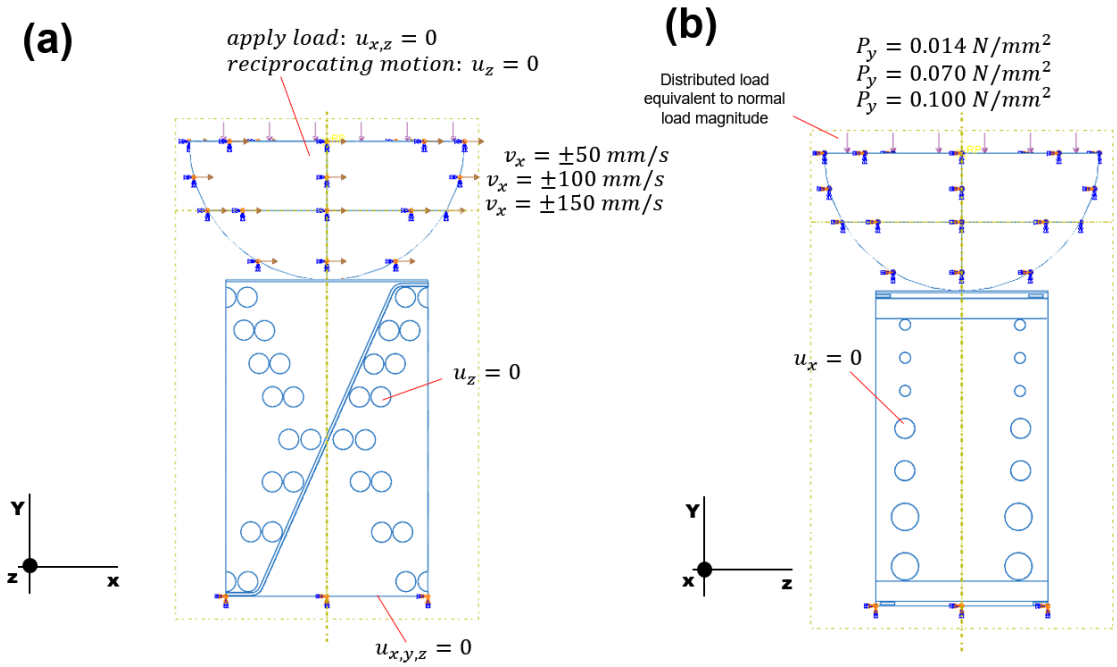

Figure 3.19 Load and boundary conditions for HC Type-A (a) front view, (b) side view. P, u and v indicate applied pressure, displacement (in either x, y, z directions) and linear velocity, respectively.

The FE models were discretised using hexahedral elements for the fibre tows, and tetrahedral elements for the matrix body, as shown in Figs. 3.20 and 3.21 for HC Type-A (107885 elements), and HC Type-B (93805 elements), respectively. These values were obtained based on mesh sensitivity studies. Meshing the matrix with hexahedral elements is desirable with respect to less computational costs they offer, compared to tetrahedral elements. Moreover, hexahedral elements result in better mesh quality and less distortion. Nevertheless, due to the complex geometry of the matrix, mainly as a result of resin-rich pockets (see Fig. 3.20 (b)), and the presence of internal swept faces, hexahedral elements could not be assigned to the matrix, as partitioning tools or bottom-up meshing technique failed once they were employed. In order to utilise wear subroutine, ALE adaptive meshing should be applied on matrix elements and a prerequisite for this is an enhanced hourglass mesh control that is only available with hexahedral element type. Thus, a

rectangular cubic partition was created on the top face of each matrix and hexahedral elements (C3D8R, An 8-node linear brick, reduced integration, hourglass control) were assigned followed by the definition of adaptive mesh region to the partition elements. Furthermore, adaptive mesh constraint was assigned to surface nodes (1295 nodes, and 722 nodes for Type-A and Type-B, respectively), so that node-shifting would become feasible via the user-defined subroutine. C3D4 (4-node linear tetrahedron) elements were assigned to the rest of each matrix. In general, for contact problems, quadratic shape functions were found problematic in establishing the contact between an element with a curved outline and a flat contact surface. Therefore, to prevent solution convergence issues, linear elements were implemented. Moreover, quadratic element type is not supported by ALE adaptive meshing method.

The subroutine was able to update the mesh after a certain number of strokes, hence improving wear computation. Wear simulations were then run on both HC models and FE results were compared with experimental results at various loads and sliding speeds.

ABAQUS 6.14 (Dassault Systèmes, Vélizy-Villacoublay, France) was employed for FE analysis. The software was installed on a workstation equipped with 8-core central processing unit (CPU) (Core-i7® 6700 at 3.4 GHz clock speed) with a nominal 32 GB of random-access memory (RAM). In terms of computational costs, based on available software tokens, six processing cores of the CPU were employed for running each individual FE analysis. Memory usage was monitored, and it was found each job usually engages 60-65% of total RAM available on the computing resource. The average computational time required for an individual wear simulation to complete was recorded as 5410±1412 sec for HC Type-A and 3279±1248 sec for HC Type-B across the range of studied loads and sliding velocities.

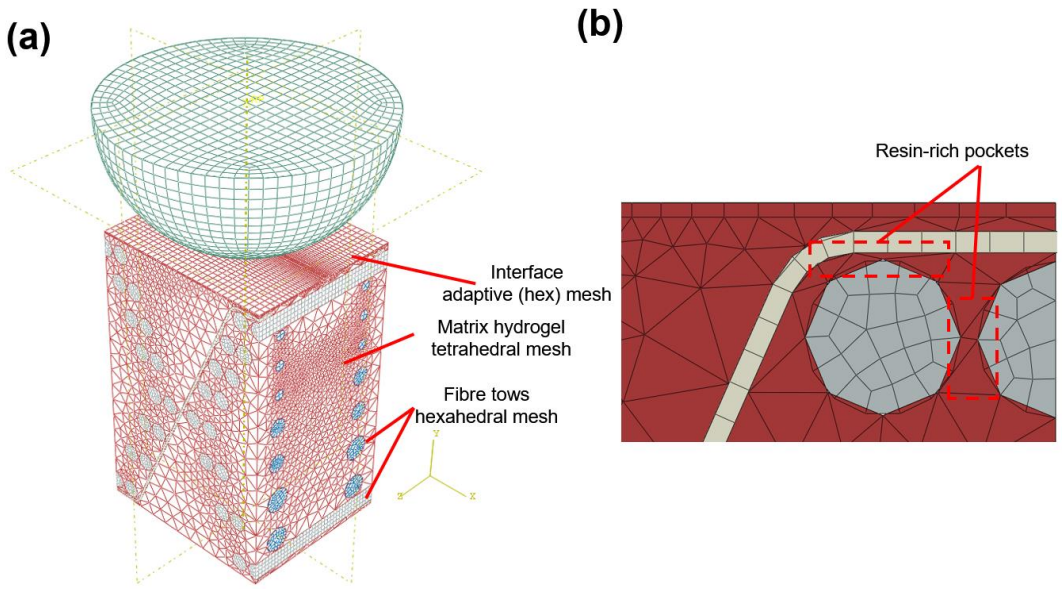

Figure 3.20 *(a) Finite element discretisation of the unit cell for HC type-A, dissimilar element types were assigned to matrix and tows, (b) typical resin-rich pockets*

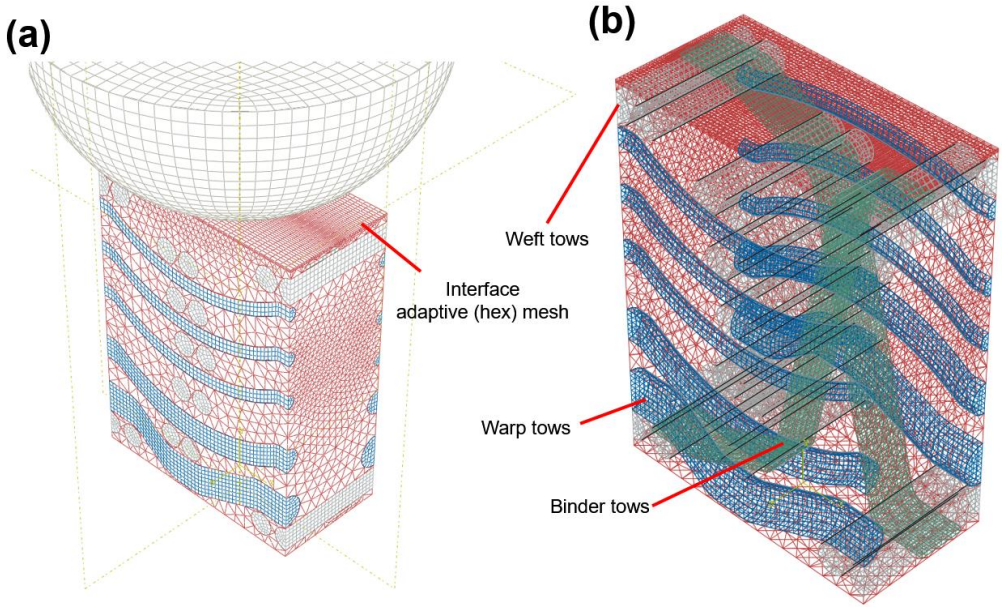

Figure 3.21 *(a) Finite element discretisation of HC Type-B unit cell, (b) internal components*

Chapter 4

ALGINATE-POLYACRYLAMIDE IPN HYDROGELS FOR USE IN MINIMALLY-INVASIVE JOINT IMPLANTS

4.1 Mechanical and Tribological Behaviour of IPN Hydrogels

Based on the experimental procedure described in chapter 3, different tests were carried out on IPN hydrogel samples and the results are presented in this chapter. The elastic characteristics of samples, prepared with different ratios of crosslinking agent, were assessed by indentation tests. Furthermore, tribological performance was evaluated under various normal loads and sliding velocities, with and without the presence of biological lubrication. Finally, the samples were completely dried and the top surfaces were coated to study the dominant wear mechanisms using SEM.

4.1.1 Indentation Test/ Surface Roughness Determination of Hydrogels

Elastic modulus and hardness of hydrogels obtained from indentation tests are illustrated in Fig. 4.1 (a). The obtained values were in good agreement with previous studies on ALG/PAAm IPN hydrogels [51, 261]. As can be observed, the increase in crosslinking agent concentration (from 0.03 to 0.06 X.A %) has had a positive impact on the mechanical properties of ALG/PAAm, contributing to more than 21% increase in elastic modulus and nearly 32% increase in hardness. Furthermore, increasing the concentration of acrylamide monomer in the hydrogel from 33 wt% to 50 wt%, resulted in much stronger hydrogel, by comparing the values of elastic modulus and hardness

obtained for two PAAm types. It was observed that PAAm hydrogel with 33 wt% monomer concentration, was fragile and therefore indentation test was assumed as a proper method in order to obtain mechanical properties. By comparing the ALG/PAAm IPN hydrogel (0.03 X.A %) with 33 wt% PAAm, with identical acrylamide concentrations, it was found that elastic modulus and hardness were almost doubled which is due to addition of alginate that formed chemical crosslinked network entangled with polyacrylamide chains. The surface roughness values of gels were determined using an optical profilometer as shown in Fig. 4.1 (b). The smoothest surface belongs to PAAm gels, compared to IPNs, and this can be attributed to additional roughness because of the introduction of alginate to PAAm. Increasing crosslinking agent concentration might also increase the roughness, as can be observed by comparing the corresponding values of R_a and R_q for 0.03 X.A% with 0.06 X.A%, which can be attributed to smaller mesh size as a result of more crosslinking. Roughness also increases with concentration of AAm, by comparing PAAm gels, indicating gels with more water content and less polymer concentration have smoother surfaces.

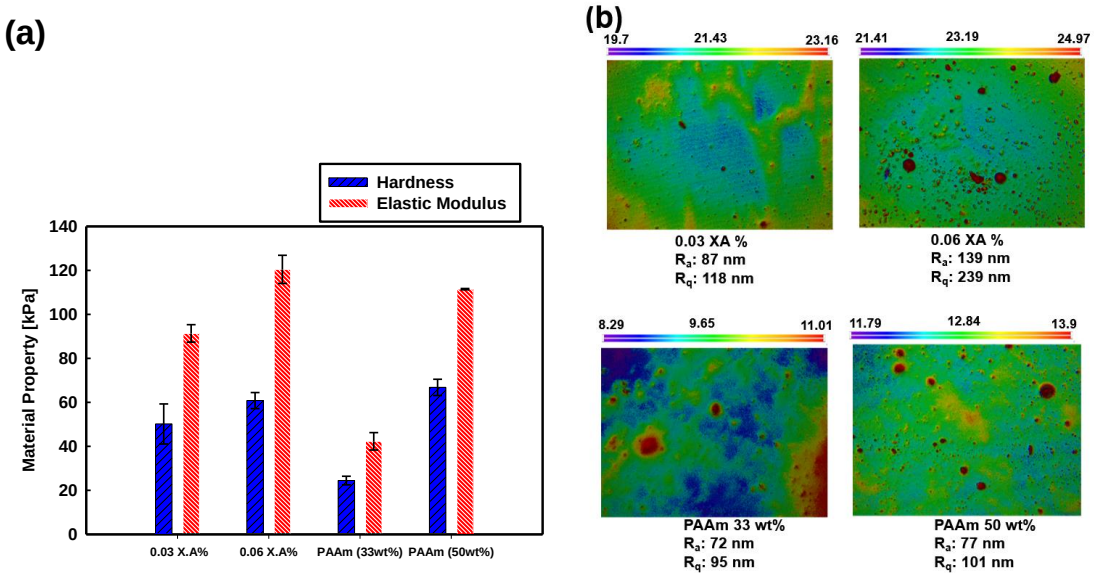

Figure 4.1 (a) Stiffness and hardness values of various hydrogels obtained from indentation tests (n=3, ±SD), and (b) surface topography contour of 566×426 μm² region of each sample with surface roughness values measured using 20X optical profilometer (values of color scale bar in μm)

4.1.2 Friction and Wear Test Results

As explained in chapter 3, a ball on plate reciprocating test setup was used for tribology tests. The ball displacement against hydrogel surface was recorded by the instrument once the 0.1-0.7N load range was statically applied, resulting in vertical displacements of 0.21-0.69 mm and 0.15-0.61 mm for 0.03 and 0.06 X.A%, respectively. Since the displacement is less than 10% of sample thickness (7 mm), the substrate does not affect the friction and wear measurement results [240]. Percentages of dry polymer mass loss for ALG-PAAm samples are listed based on percentages of crosslinking agent in Table 4.1 and Table 4.2, with varying loads and sliding speeds, respectively Gravimetric measurements were performed on dry mass of the hydrogel samples before and after the tests to prevent water content of the samples affecting the results due to sample dehydration. Each sample was weighed in dry condition, then submerged in DI water for at least 24 hours to reach equilibrium water content. The desiccation process was repeated to find out the mass loss post testing. Regarding the applied load, there is a similar trend in mass loss increase with higher loading in ALG-PAAm hydrogels regardless of crosslinker concentration. In the absence of bovine serum lubrication, the gel samples with lower crosslinking concentration were found to have better wear performance and less mass loss, although the samples with higher crosslinker density might benefit from enhanced mechanical properties. By introducing bovine serum lubrication, the mass loss dropped drastically and the samples with less crosslinking concentration showed better performance, while the samples with higher crosslinking were affected more severely from increasing of load, especially from 0.1 to 0.5N.

Table 4.1 Wear (% Dry polymer loss) of ALG/PAAm hydrogel samples with respect to applied load (constant speed v = 100 mms-1), lubrication and crosslinking density (Mean (n=3) ± SD)

Crosslinking agent [X.A%]	Without Lubrication			Bovine Serum Lubrication		
	0.1 N load	0.5 N load	0.7 N load	0.1 N load	0.5 N load	0.7 N load
0.03	7.65 ± 1.30	9.05 ± 0.65	9.36 ± 1.40	1.33 ± 0.78	2.84 ± 0.32	3.01 ± 0.43
0.06	6.95 ± 1.49	9.28 ± 1.06	10.45 ± 1.67	2.96 ± 0.88	5.60 ± 1.23	6.44 ± 0.63

Table 4.2 Wear (% Dry polymer loss) of ALG/PAAm hydrogel samples with respect to sliding speed (constant load, p = 0.5 N), lubrication and crosslinking density (Mean (n=3) ± SD)

Crosslinking agent [X.A%]	Without Lubrication			Bovine Serum Lubrication		
	50 mm/s Speed	100 mm/s Speed	150 mm/s Speed	50 mm/s Speed	100 mm/s Speed	150 mm/s Speed
0.03	11.01 ± 2.28	9.05 ± 0.65	7.77 ± 1.90	3.61 ± 1.85	2.84 ± 0.32	1.15 ± 1.01
0.06	7.66 ± 2.48	9.28 ± 1.06	6.60 ± 0.45	5.02 ± 0.20	5.60 ± 1.23	1.68 ± 0.68

Polymer mass loss was also investigated against sliding speed, as listed in Table 4.2, and it was concluded that in general, under higher sliding speed, less material was removed due to wear (this will be further discussed in details). Similar to the values reported in Table 4.1, the hydrogel samples prepared with less crosslinker, exhibited better tribological performance, which was even more enhanced in the presence of bovine serum lubrication. Before desiccation process, the wear scar of each hydrated sample was analysed using a stylus profilometer. Having obtained the cross-sectional profile of wear scar at 3 different locations, the wear volume was determined by average cross-sectional area, obtained through polynomial curve-fitting of each profile, multiplied by the length of scar and was plotted as a function of applied load and sliding speed as can be seen in Fig.4.2 (a) & (b), respectively. The minimum wear volume was obtained under lubricated conditions for the samples with 0.03 X.A% under 0.1N load (0.291 ± 0.013 mm^3), which was increased to 6.09 ± 0.53 mm^3, under 0.7N load. Comparing both graphs of Fig. 4.2, the ranking of materials in terms of generated wear volumes was as follows:

0.03 X.A%_Lubricated < 0.06 X.A%_Lubricated <0.03 X.A%< 0.06 X.A%

The wear volumes of PAAm samples are not shown in Fig. 4.2, but were recorded in the range of 3.87-28.49 mm^3 and 3.45-21.376 mm^3 for 33 wt% and 50 wt%, respectively, for the range of 0.1-0.7N load (with no lubrication). These ranges are higher than the wear volumes obtained for IPN hydrogel, implying the role of IPN in improving the tribological performance of the hydrogel.

Average cross-sectional profiles of wear tracks, depending on the type of hydrogel and the magnitude of applied load and sliding rate are illustrated in Fig. 4.3 (b-e). Similar approach was previously utilised to measure wear depth of double-network hydrogels [195]. As shown in Fig 4.3 (a), the diamond-tip stylus moves across the wear scar width, and captures the surface topography of worn area based on the height difference of the points sensed by the stylus. It was observed that the scar width and depth both increased drastically by increasing the normal load from 0.1N to 0.5 N load, while changes in sliding speed from 50 mm/s to 150 mm/s has had less effect on the geometrical shape of wear scar cross-section, especially in 0.06 X.A% samples. Comparing the two types of hydrogels, the scar width and wear depth were found to be higher in the samples prepared with 0.06 X.A%. The only exception was under 0.1N load and 50 mm/s sliding speed, where the samples with 0.03 X.A% showed greater wear volumes, hence deeper and wider wear scars were generated.

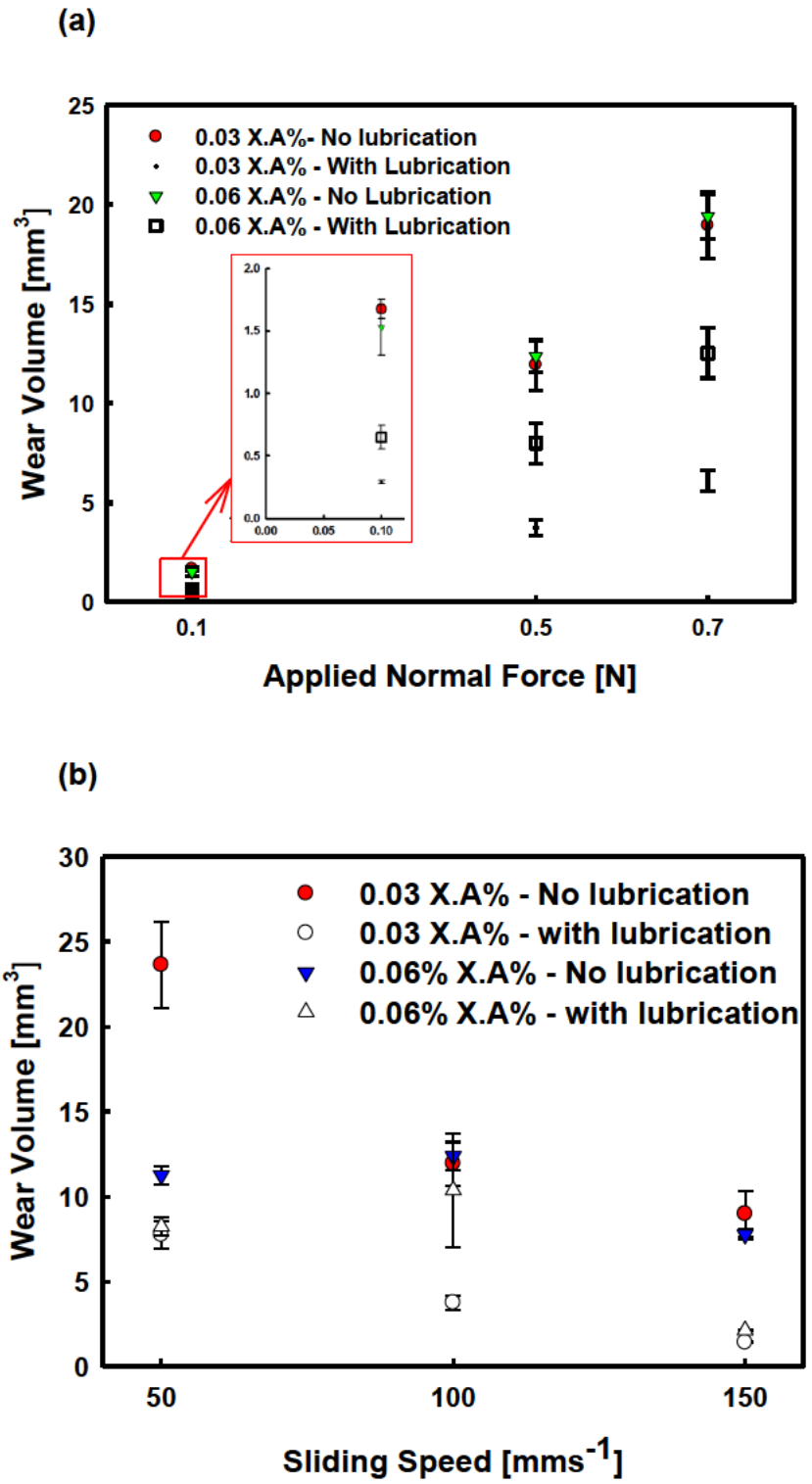

Figure 4.2 *Wear volume of all hydrated samples with respect to (a) applied loads (v = 100 mm/s), (b) sliding speeds (p = 0.5 N), (n=3, ±SD).*

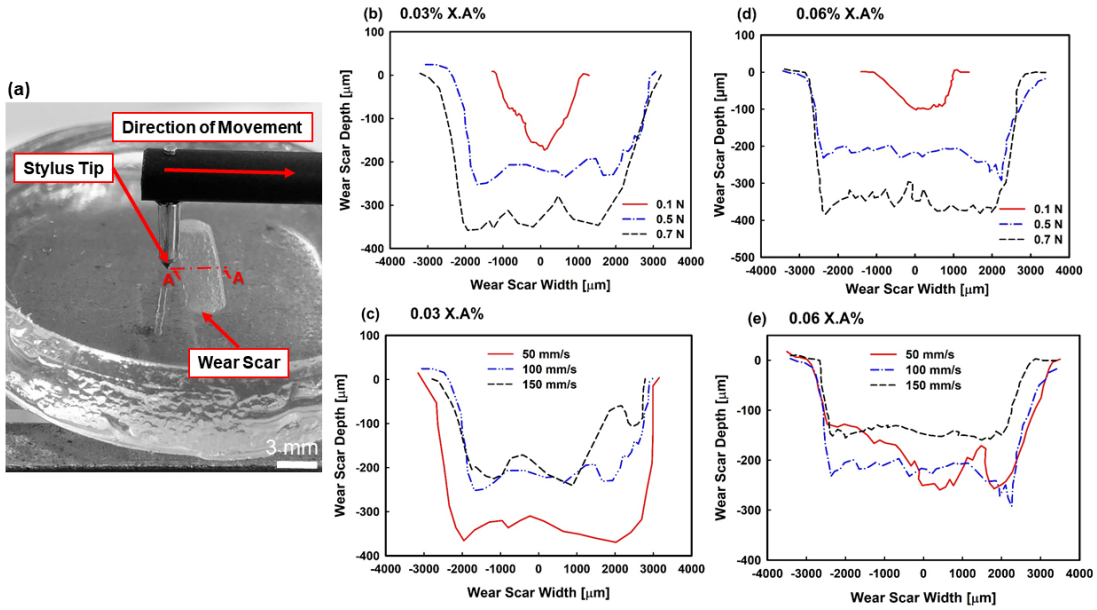

Figure 4.3 *(a) The tip of stylus profilometer moving across the wear track width (A-A), (b-e) average wear track profile of hydrogel samples based on crosslinker amount and applied load/sliding speed (under dry contact condition)*

The wear track on dried, gold-coated samples were studied using 20X confocal objective of optical profilometer. Upon desiccation, the hydrogel samples shrunk in size, therefore the wear scar's geometrical parameters would be affected, too. However, the imaging gives fairly good insight on the entire worn region and visualizes where more severe wear has occurred on the surface of each specimen. The plan view of the wear scar for 0.03 X.A% under 0.1N load, is illustrated in Fig. 4.4 (a-c), generated by consciously scanning the regions and final image stitching tool embedded in profilometer software. Due to much larger wear areas of higher loads, only the mid region was scanned orthogonal to sliding direction and being stitched as can be seen in Fig. 4.4 (d,e). By referring to each colour scale bar, it was found that deepest region (in violet colour) was placed almost in the middle of wear track, which indicates the region that was sliding against the ball more than other areas, thus has lost more material. Comparing the images (b), (d), and (e) of Fig.4.4, corresponding to 0.1, 0.5 and 0.7 N loads respectively, revealed more severe wear depth with applying higher loads. Furthermore, as the load increased,

the deepest region propagated along the scar width, resulting in a wide flat valley along the wear track.

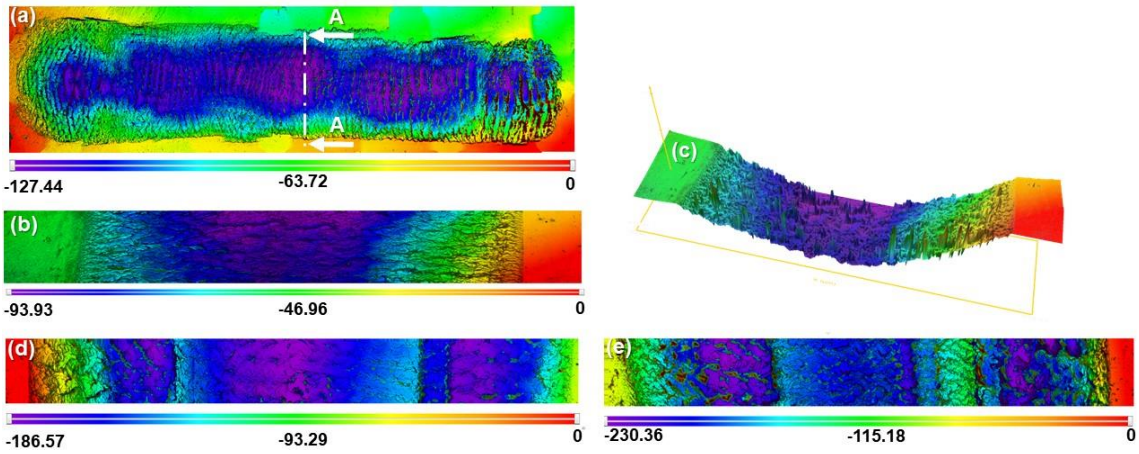

Figure 4.4 *(a),(b) 2D illustration of hydrogel wear track under 0.1N load and unlubricated conditions, generated by continuous scanning using 20X confocal objective and utilisation of software stitching tool, (c) 3D image of central scar region under 0.1N load. For other loads, only the central region of wear scar was scanned (A-A) and stitched; (d) P=0.5N (d), (e) P=0.7N*

The mean values of coefficient of friction (CoF) versus applied load, sliding speed and lubrication condition for various types of hydrogel samples are shown in Fig. 4.5. In general, friction has decreased by increasing the load, and by applying lubricant, while the changes in sliding rate did not have a remarkable effect on CoF. Bovine serum lubrication contributed to 69.4% ±19.5% and 89.4% ± 1.95% reduction in friction coefficient in hydrogels with 0.03 and 0.06 X.A%, respectively. With lubrication and under 0.7 N load, the minimum mean friction coefficient was obtained for samples with 0.06 X.A% (0.010 ± 2.6E-3) which is an order of magnitude greater than reported friction coefficient of natural cartilage (0.001) [262] and less than the values reported for PVA-alumina pair (0.04-0.1) [263]. The PAAm-only hydrogels displayed higher friction compared to IPN samples, which were more noticeable at 0.5 and 0.7N loads, while higher AAm concentration resulted in higher friction. Compared to 0.03 X.A% specimens, 0.06 X.A% hydrogel showed in average nearly 20% higher CoF in the lack of

lubrication, attributed to smaller mesh size, while the CoF value dropped by almost 60% compared to 0.03 X.A% specimens in the presence of bovine serum lubrication.

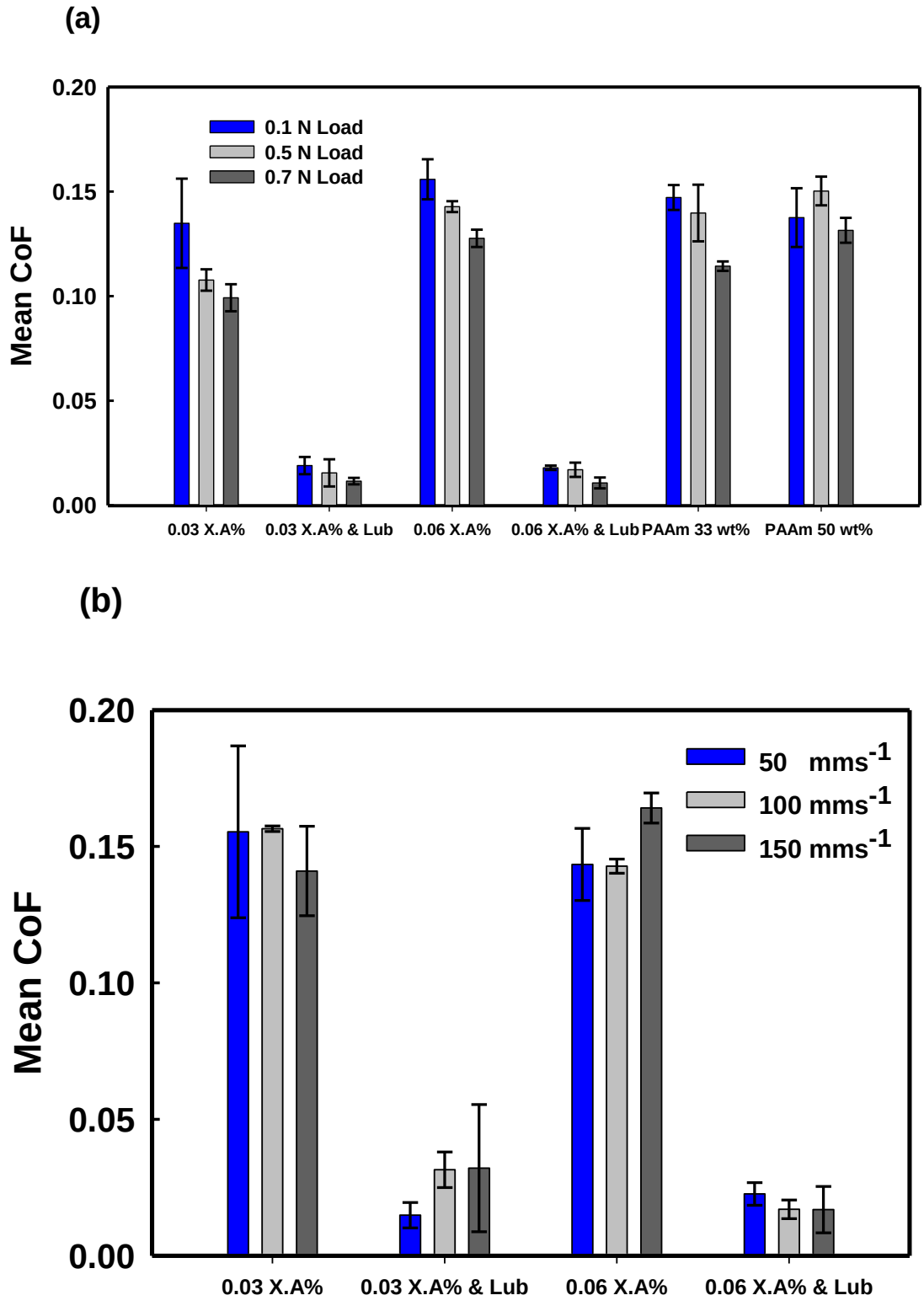

Figure 4.5 Mean friction coefficient values for various groups of ALG-PAAm hydrogels with respect to (a) applied load (v = 100 mm/s), and (b) sliding speed (P = 0.5 N), (n=3, ± SD)

The variations of CoF versus sliding distance are illustrated in Fig. 4.6 for both groups of IPN hydrogels with respect to load and sliding speed, under lubricated contact condition. By comparing the curves in Fig. 4.6 (a) & (b), it can be seen that under 0.1N load, and without lubrication, the friction coefficient tends to severely fluctuate and the values were normally greater than friction coefficients obtained for higher loads. This could be because of the lack of proper boundary lubrication that is normally developed by formation of water layer on the bearing surface, which is mainly due to the small amount of applied load. The highest friction has occurred for 0.06 X.A% specimens at 0.1N load, while at higher loads, the friction levels were reduced for both types of IPN gels. The effect of bovine serum lubrication on CoF can be clearly seen, both in massive reduction of friction coefficients, and shorter transition to steady-state condition. As can be seen in the zoomed-in section of each graph, friction coefficient is characterised by a sharp increase of CoF to reach a pick upon running the test, followed by a sudden drop and then it continues in the transition mode where CoF increases gradually to finally reach a steady-state condition. Depending on the lubrication mode, CoF might decrease or increase with the increase of sliding distance. As can be seen in Fig.4.6 (c) & (d), CoF is lower at higher sliding speeds, and more stability can be observed which is mainly due to less time available for the fluid content to diffuse away from the gel surface. This is contributing to a better lubrication, thus lowering the friction. This finding is in line with previous studies, where lower CoF were reported at higher sliding speeds for hydrogels [264, 265]. In the absence of external lubrication, friction levels for samples with 0.06 X.A% tend to fluctuate more intensively, while that of 0.03 X.A% showed smoother curves especially when tested under higher speeds.

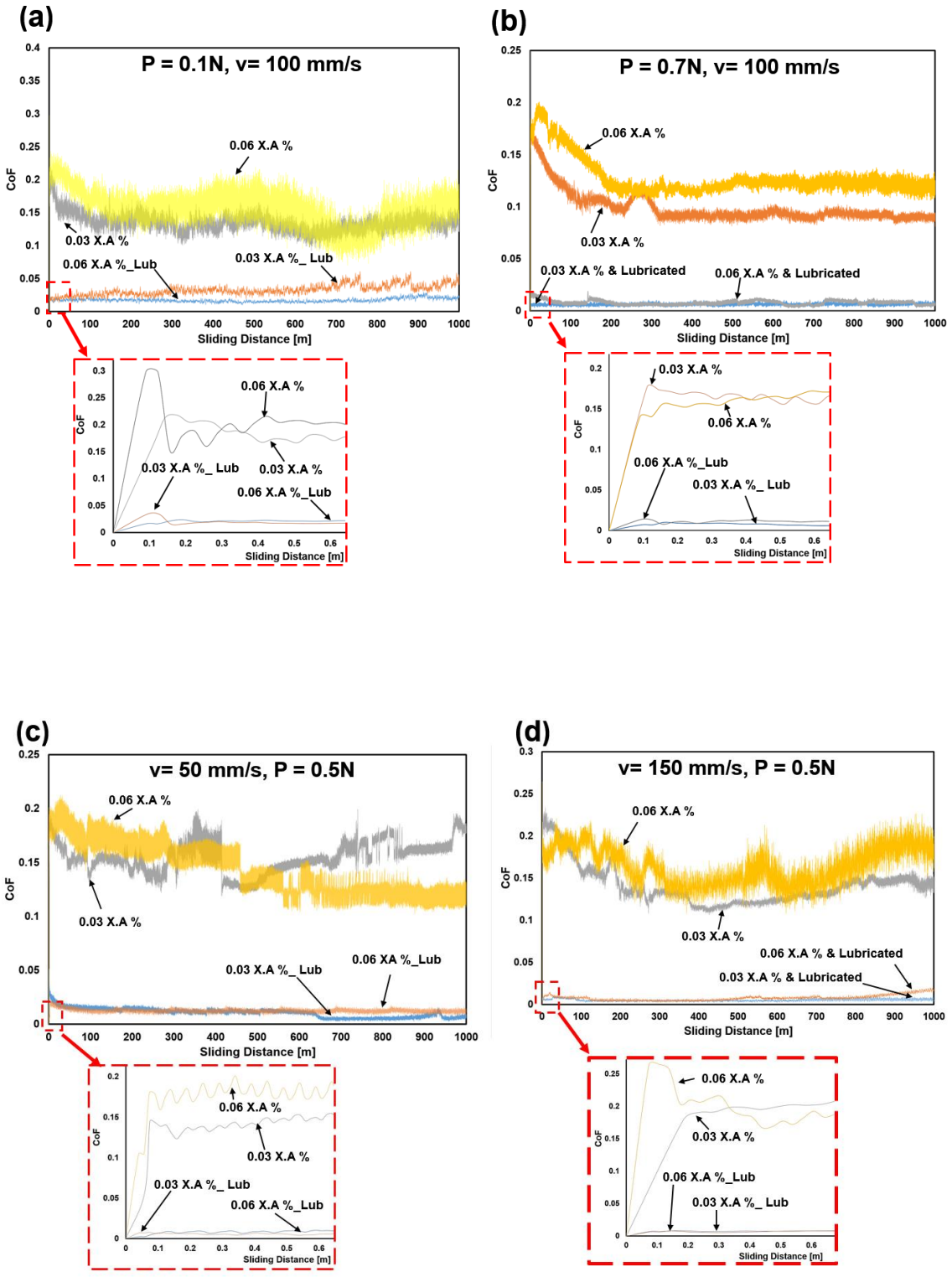

Figure 4.6 *The effect of load and speed on variation of friction coefficient with sliding distance, recorded by the tribometer during each test under lubricated condition; (a) & (c) ALG/PAAm (0.03% MBAA), (b) & (d) ALG/PAAm (0.06% MBAA)*

To further investigate the effect of X.A% on tribological behaviour of hydrogels, samples were prepared with one ratio lower (0.015%) and one ratio higher (0.12%) X.A

than previous samples and were tested under 0.1N load and 100 mm/s speed, with and without bovine serum lubrication. The load was restricted to 0.1N due to the excessive strain experienced by the samples prepared with the lowest agent concentration (0.015%). As can be seen in Fig. 4.7 (a), with increase in X.A concentration, wear rate decreased, although less significant variation was observed under lubricated condition. This suggests that initially-considered 0.03 and 0.06 X.A% values were within acceptable range for this study and an increase in X.A% won't remarkably change the state of friction and wear in this material. As illustrated in Fig. 4.7 (b), the CoF values increased with higher X.A%, under dry condition, however slight decrease was observed under bovine serum lubrication, indicating the least dependency of CoF on X.A% under lubrication.

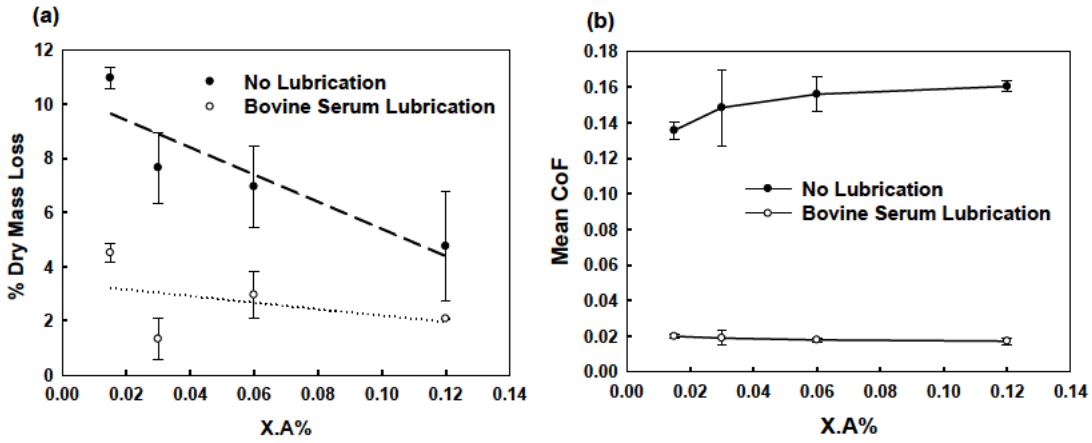

Figure 4.7 *The effect of crosslinking agent on (a) wear, (b) friction coefficient of ALG-PAAm hydrogels under 0.1N load, 100 mm/s sliding speed, with/ without bovine serum lubrication*

4.1.3 Study of Wear Mechanisms Using SEM

The topography of the worn surfaces of all dehydrated and gold-coated specimens were analysed using SEM, as shown in Fig. 4.8 and Fig. 4.9 to find out the effect of load, speed and presence of biological lubricant on surface deformation and wear mechanism. It was observed that in the absence of bovine serum, worn surface morphology was transitioned from light ploughing grooves at the lowest load to more severe deformation

along with considerable surface pitting specifically at both ends of the wear track when the load increased. The plastic deformation observed in both hydrogel groups (with 0.03 and 0.06 X.A%) was known as an indication of adhesion mechanism, while surface pitting, occurring at the highest load could be due to fatigue mechanism [29]. The cracks that can be observed in Fig. 4.8 (c) had occurred due to the coating process and not the wear test. By applying biological lubricant, due to the load carrying capacity of the bovine serum and the effective separation of asperities of the mating surfaces, friction coefficient reduced drastically, together with much less visible wear scar on the surface. As can be seen in Fig. 4.8 (b) the wear track can be distinguished by minor depression and small regional indents plus the distributed wear debris at the edge of the scar. Change in sliding speed resulted in less destructive surface deformation according to Fig. 4.9 (when compared to Fig. 4.8), and the surface was less deteriorated with lighter ploughing pattern at higher speed (Fig. 4.9 (f) & (g)) which is due to less dehydration of specimen as a result of shorter test period. Tests conducted at 50 mm/s speed, took three times longer than 150 mm/s to finish, therefore, signs of fatigue wear were found on the surface of those specimens (Fig. 4.9 (e)). However, by continuous and steady application of bovine serum, much less deformation and material loss was observed (Fig. 4.9 (b)). Overall, more considerable deformation were observed at the two ends of the scar, which was attributed to the change in direction of sliding motion.

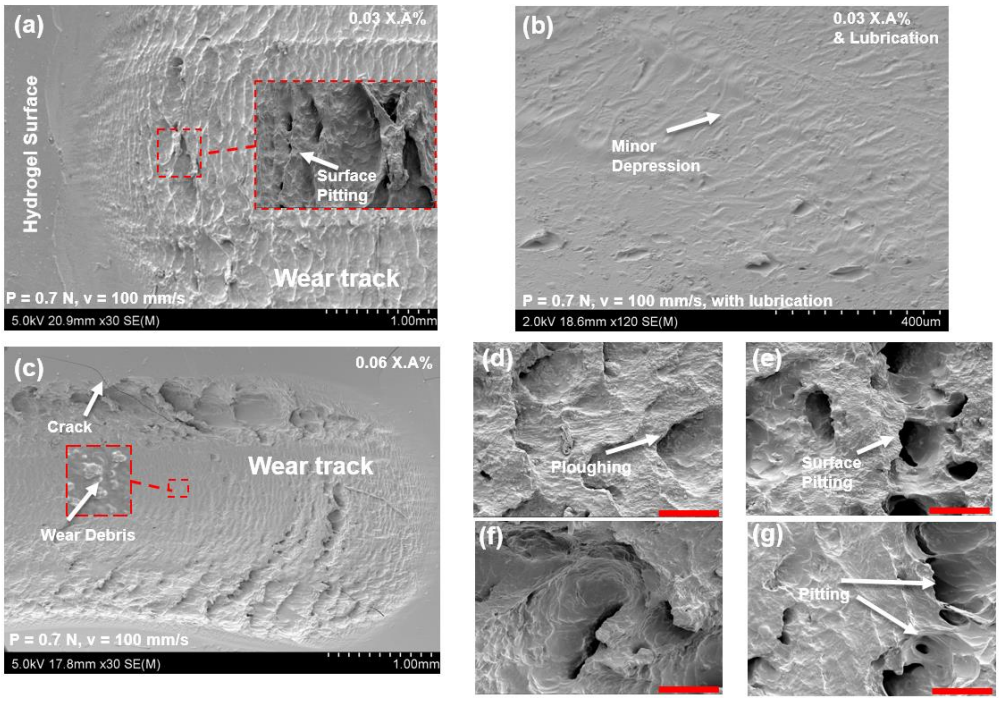

Figure 4.8 *SEM micrographs of two groups of IPN hydrogels; IPN hydrogel (0.03 X.A%) under the highest applied load: (a) without, (b) with lubrication, hydrogel (0.06 X.A%): (c) no lubrication and 0.7N load, (d-g) surface deformation. Unless mentioned, all scale bars = 100 µm*

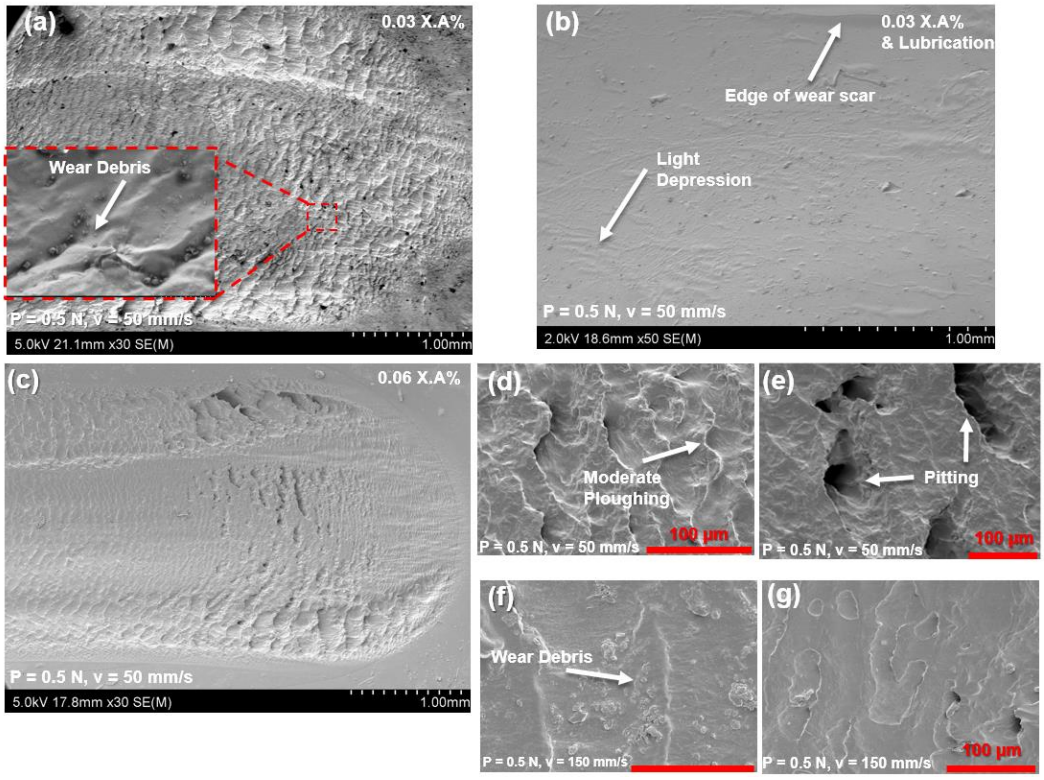

Figure 4.9 *SEM micrographs of two groups of IPN hydrogels; IPN hydrogel (0.03 X.A%) under the lowest sliding rate: (a) without, (b) with lubrication, hydrogel (0.06 X.A%): (c) no lubrication and 50 mm/s speed, (d-e) surface deformation, (f-g) hydrogel (0.06 X.A%) under highest sliding speed*

4.2 Discussion

The manufacturing method for alginate-polyacrylamide hybrid (IPN) hydrogel samples had been discussed in the previous chapter. The samples were tested for mechanical strength by indentation tests and their tribological performance were also evaluated by sliding wear tests. Test conditions were chosen to represent the actual working condition of artificial cartilage implant. With regard to indentation tests, it is worth mentioning that due to the viscoelastic nature of polymer hydrogels, the stress induced in the hydrogel as a result of external load is time-dependent and will be reduced if the amount of load is kept constant for a long period of time. Therefore, during the indentation tests, the indentation depth and cross-head speed were selected such that stress relaxation would be prevented as a result of short test period. The loading and unloading cycles were performed in two minutes in total, which was theoretically not sufficient for stress relaxation to occur and it was not observed in any tests. Overall, three factors were found to contribute to enhancing the mechanical strength and integrity of PAAm, which are AAm concentration, crosslinking density, and utilisation of IPN structure. AAm concentration was found to have the greatest impact on improving mechanical properties of hydrogels, followed by IPN. It is worth noting that there are some restrictions on the amount of AAm that can be used for gel preparation. As the weight percentage of AAm increases in the final mixture, the solubility will be adversely affected and more amount of unreacted monomers might leave the gel after gelation, affecting the biocompatibility. Furthermore, stiffer, more brittle polymer might be achieved which is undesirable in terms of mimicking mechanical behaviour of cartilage. Moreover, this will adversely affect the wear performance of the hydrogel. Therefore, IPN was shown to enhance the mechanical properties of PAAm hydrogel by introducing the second polymer network which is chemically crosslinked.

In general, wear quantification of hydrogels is complex due to biphasic nature of the material. Most of previous studies that have focused on tribological characterisation of hydrogels, maintained the sample hydrated during the test using a lubrication bath of DI water, synovial fluid or bovine serum [29, 266]. Therefore, the wear rate was not focused as the sample might swell and gain mass during the test. Therefore, only friction and lubrication were analysed. On the other hand, gravimetric measurement of the hydrated gel without lubricant bath is not accurate as the ambient temperature, together with the heat generated by friction of sliding counterface will accelerate the dehydration of sample, which leads to large errors in the final measurement. Dry mass measurement before and after the test was more reliable as adapted in previous studies [28, 197]. In the case of ALG-PAAm IPN hydrogel, the two types of polymer networks are interlocked and bonded together through covalent joints of amine groups from PAAm chain and carboxyl groups of ALG network [32]. Therefore, no considerable loss of material should occur during rehydration of samples, as the samples were kept in DI water for sufficient amount of time during sample preparation, for the unreacted particles to leave the gel. This was investigated by several control samples that were dried, rehydrated and dried again to explore any probable changes in dry mass before and after rehydration. No significant change was recorded for all of the control samples and this ensured the validity and accuracy of wear evaluation by dry mass measurement method.

Regarding the wear tests, monitoring the friction coefficient variations throughout the tests revealed that the selected sliding distance is sufficient for reaching a steady-state wear condition. Wear rates increased at higher loads, due to a larger contact area. This increase was observed in both dry and lubricated contact conditions and with different crosslinking densities, although the increase rate is higher with the lack of lubrication. However, opposite trend was observed for friction and CoF decreased at higher contact pressures, which is consistent with previous studies [267]. This can be attributed to the

formation of a charged surface of ALG/PAAm hydrogels that can retain a water layer when higher loads are exerted and this thin layer of water acts as a lubricant and decreases CoF [268]. This also explains the differences observed in the wear rates of ALG-PAAm hydrogels with 0.03 and 0.06X.A%. The water content was found to be lower with the increase in crosslinking, therefore the samples with 0.06% agent suffered from lower water content (82.1% compared to 86.7% water content of samples with 0.03% agent) and less fluid lubrication, leading to a higher wear rate. Comparing the friction coefficients also revealed that less crosslinking density led to a lower friction, which is not only due to higher water contents in the specimens, but also larger mesh sizes as a result of less crosslinking. Wear rates were also decreased at higher sliding speeds due to less surface dehydration, and less lubrication as a result of longer test duration. Once a ball slides on a surface of biphasic material such as hydrogel, friction coefficient can be correlated to the ratio of sliding rate to fluid diffusion inside the hydrogel, and if the speed overpasses the diffusion rate, which means no enough time for the fluid to move away, friction coefficient would reach its minimum value [269]. Overall, friction and wear behaviour of hydrogels are complex phenomena, due to the biphasic structure and mechanical properties of these materials. Moreover, the frictional force depends on chemical and mechanical properties of bearing interface, applied load, and sliding speed. Any change in chemical structure of the hydrogel, such as the amount of crosslinking agent, water molecules bound to the polymers and chemical properties of the mating surfaces will affect frictional force. In order to model the frictional behaviour of complaint hydrogels, fundamentals of rubber elasticity, biphasic materials theory and polymer physics should be implemented. When a solid smooth material slides on hydrogel, the friction arises from two factors: the elastic deformation of polymer chains, same as adhesive friction [270], and lubrication of hydrated layer of polymer chains. Sliding causes the polymer chains at the interface to elastically stretch due to their

tendency to adhere to the mating counterface. However, at higher speeds, less adhesion would occur and the lubrication regime approaches the hydrodynamic type, when the fluid layer shearing dominates surface adhesion [271]. It was found that biphasic and boundary lubrication plays an important role in ultra-low friction and extremely high wear-resistant of articular cartilage and PAAm hydrogels were shown recently, mimicking the cartilage attaining these lubrication modes [265]. The promising lubrication mechanism and tribological performance of ALG/PAAm IPN hydrogel make it a potential candidate for further studies to fulfill performance optimisation.

4.3 Conclusions

The tribological performance of ALG-PAAm IPN hydrogel for use as synthetic cartilage was assessed in this chapter. Effect of mixing polymer networks on friction and wear properties of IPN hydrogel, along with the impact of other chemical and environmental parameters were focused as the very first attempt to assess them as synthetic cartilage. The hydrogel's low friction coefficient was attributed to its high water retention capacity, permeability, range of stiffness, and presence of fluid film at the interface. Based on the reciprocating motion of the alumina ball as the counterface, the lowest friction coefficient obtained for ALG/PAAm hydrogel in the presence of bovine serum lubrication was 0.01, which is fairly close to that of a healthy cartilage and lower than PVA (as the most common hydrogel proposed for cartilage replacement). Hydrogel specimens with 0.03 X.A% showed better tribological performance in terms of lower wear rate and lower friction levels in the absence of bovine serum lubrication. On the other hand, gels with 0.06 X.A%, exhibited improved mechanical properties such as higher stiffness, meaning they can withstand higher loads with less deformation compared to the other types, as well as a significantly lower friction coefficient under bovine serum

lubrication. Moreover, the wear volume values showed a marginal increase compared to gels with lower crosslinking agent concentration. Therefore, the hydrogels with higher crosslinking concentration should be selected for further studies due to stronger mechanical performance and acceptable friction and wear behaviour. Microscopic analysis of worn surfaces revealed adhesion as the most prevalent wear mechanism, while surface pitting as an indication of fatigue wear was observed at higher loads and lower speeds. However, due to the efficient lubrication of bovine serum film, no such mechanisms were observed and worn surfaces could hardly be distinguished from unworn surfaces in samples tested under lubricated conditions and at lower loads. One of the limitations was that all the tests were performed at room temperature, and this can have an influence on the properties of biphasic materials. Future tests should be conducted at body temperature and for more realistic test conditions. Synovial fluid could be utilised as the lubricant, as previous studies showed that friction coefficient of hydrogels would decrease by using synovial fluid [28]. Even though ALG-PAAm IPN hydrogels showed a promising tribological performance, the improvement in mechanical and wear performance by other methods such as adding nanoparticles as a structural reinforcement could be further investigated which is the subject of the following chapters.

Chapter 5

MECHANICAL ASSESSMENT OF SILICA NANOPARTICLE-ALGINATE-POLYACRYLAMIDE NANOCOMPOSITE HYDROGELS

5.1 Mechanical and Tribological Performance of NCHs

In this chapter, the focus is mainly on the assessment of ALG-PAAm hydrogels reinforced with three different concentrations of Si-NP to be considered as a potential cartilage implant. Based on the results presented in previous chapter, a suitable crosslinking agent concertation was identified and was utilised for the preparation of NCHs. A number of different test methods were carried out to study the elastic and viscoelastic responses of NCHs as compared to original unreinforced hydrogel. Moreover, friction and wear tests were conducted consistent with the previous study (chapter 4) and the effect of NP reinforcement on the mechanical and tribological performance of the hydrogel matrix was investigated. All quantitative data were represented as average ± standard deviation. SigmaPlot 14.0 package was utilised for statistical analysis. One-way analysis of variance (ANOVA) method was implemented on data to investigate if there exists any statistically significance difference between the control group (IPN hydrogel) and the treatment groups (NCHs). In this study, if $p < 0.05$, the difference was considered as statistically significant.

5.1.1 Indentation and Surface Roughness Analysis of NCHs

The force-displacement response of NCHs, with Si-NP concentrations ranging from 1% to 4%, and the comparison with the reference IPN hydrogel are illustrated in Fig. 5.1 (a). It can be seen that by introducing the Si-NPs in the structure and increasing

the concentration, more force is required to indent the surface, which shows significant increase for 4% concentration of NPs. Elastic modulus and hardness values obtained from unloading portion of each curve are illustrated in Fig. 5.1 (b). The positive impact of adding NPs to the IPN hydrogel could also be observed by comparing the measured mechanical properties (Fig. 5.1 (b)). Compared to the control hydrogel samples, a significant difference was found for the NCH samples containing 2% and 4% Si-NP concentrations, with respect to hardness and elastic modulus (only 4% type) values ($p < 0.05$). The elastic modulus and hardness of the reference hydrogel increased by 38.6% and 39.11% respectively, when incorporating 4% Si-NP into the matrix, while no significant increases were observed for samples reinforced by 1% NPs (9.4% & 4.6% respectively). This shows the positive effect of NP concentration on the mechanical properties of NCHs.

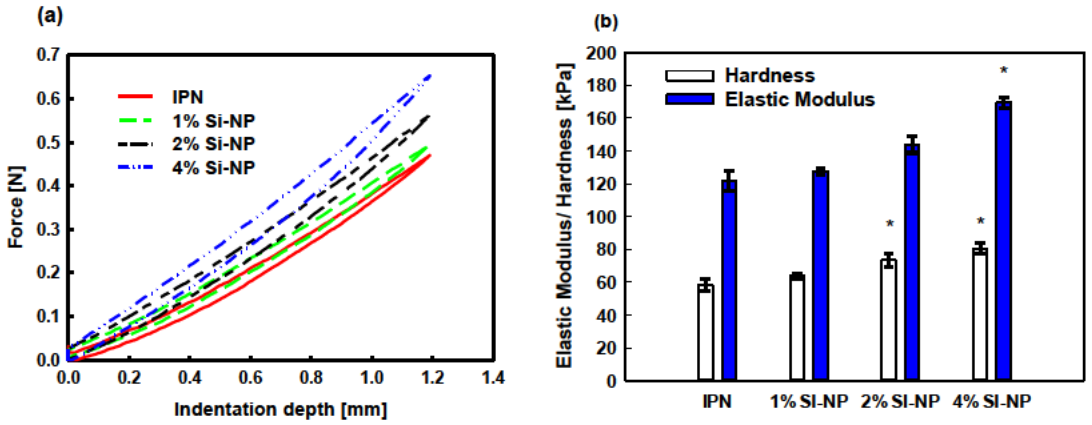

Figure 5.1 *(a) Indentation results obtained for NCH, compared to IPN samples (Mean (n=3) ± SD), (b) the calculation of hardness and elastic modulus based on the maximum reaction force, contact area, contact depth values and the slope of unloading curve, * represents $p < 0.05$.*

The surface topography of each NCH, as well as IPN hydrogel were scanned using an optical profilometer, as illustrated in Fig. 5.2, and the mean values for arithmetic surface roughness (R_a) were determined through diagonal and longitudinal lines drawn on the scanned area using software tools. In general, NCHs were found to benefit from lower R_a compared to IPN hydrogel. However, by increasing the NP concentration, R_a

increased gradually, which could be attributed to smaller pore size caused by higher crosslinking due to NP contribution in the process. It is likely that the polymer chains are brought closer together because of the higher level of crosslinking, thus producing a denser and smoother structure with finer pores. The positive impact of crosslinking on the reduction of surface roughness was reported in a previous study [272]. It has also been proven through pore size investigation of freeze-dried samples using scanning electron microscopy. Smaller pores were observed in NCHs compared to IPN hydrogel and with an increase in Si-NP concentration throughout the hydrogel matrix, finer pores were formed.

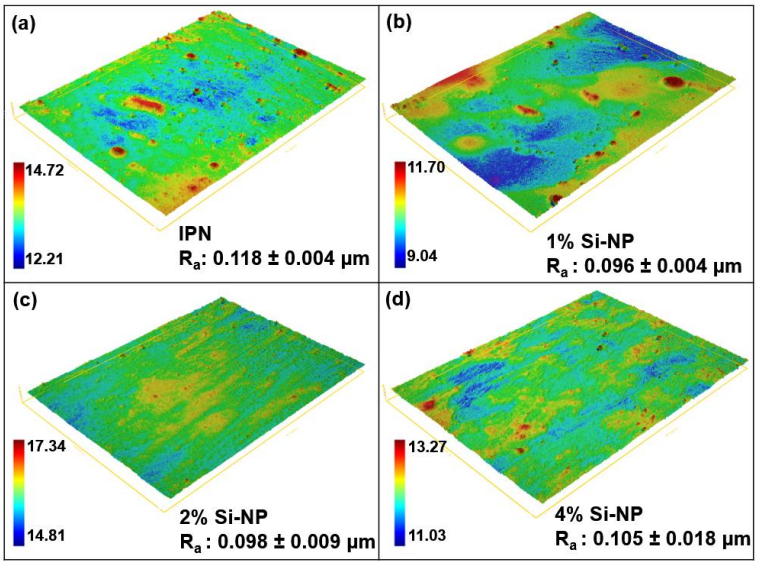

Figure 5.2 (a) Surface topography contour of 567×426 µm^2 region for reference IPN hydrogel in comparison with (b-d) each NCH with Si-NP ranging from 1% to 4%; Measurements were obtained from 20X confocal objective of the optical profilometer.

5.1.2 Compression testing

The stress-strain curves of all NCH samples along with IPN hydrogel are depicted in Fig.5.3 (a) based on unconfined compression tests conducted at 0.01 s^{-1} strain rate. The non-linear stress-strain response was observed for all hydrogel types, as previously noticed by indentation tests. According to the statistical analysis, the compressive moduli

were significantly affected by incorporation of Si-NP into the hydrogel matrix, across the range of strain rates studied ($p < 0.01$). Similar trend was observed in terms of ranking of materials with respect to structural stiffness, although the compression tests were conducted at a significantly higher strain level and with various strain rates. The compressive moduli were obtained by finding the constants in (3.5) & (3.6) for IPN and NCH respectively, through exponential fitting of the curves (Fig.5.3 (a)) and derivation with respect to the strain. Fig.5.3 (b) shows the comparison between compressive moduli of all hydrogel types at 0.5 strain. As expected from indentation test results, the stiffness values for NP-reinforced samples were significantly enhanced compared to reference IPN hydrogel and increased with higher NP concentrations. It was also found that the moduli were strain-rate dependent for the entire range of NP-reinforced samples, as well as reference IPN hydrogel, with more NPs resulted in higher strain-rate dependency. The compressive moduli were also computed for the strain level corresponding to the indentation test and it was found that the values were in good agreement, hence the model was validated for the prediction of elastic (time-independent) behaviour of various hydrogel types studied in this research.

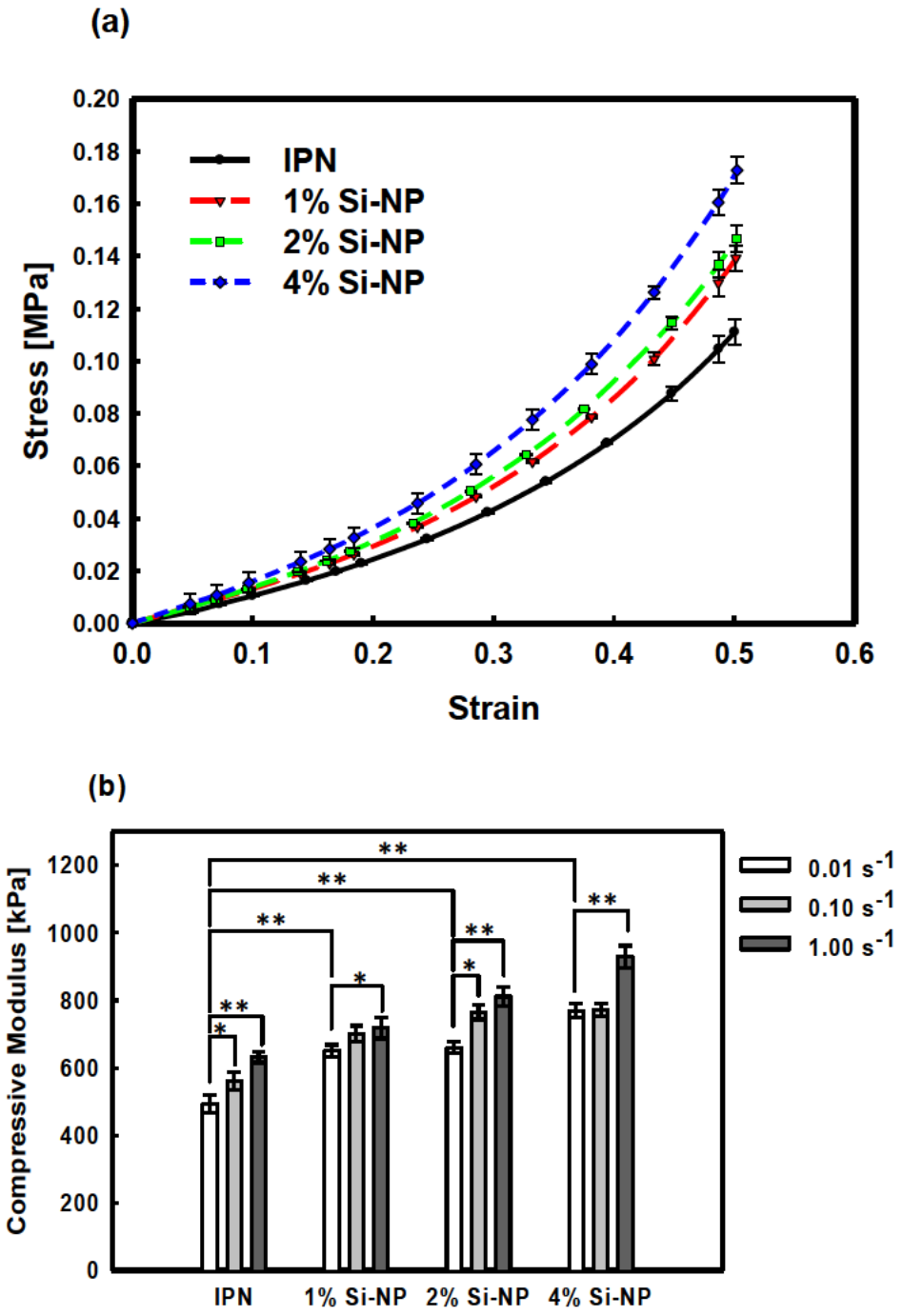

*Figure 5.3 (a) Compressive stress-strain response of NCHs and comparison with the reference IPN hydrogel at the strain rate of 1% s^{-1} (Mean (n=3) ± SD), (b) the effect of Si-NP on the compressive modulus of NCH with respect to varying strain rates at 0.5 strain, * represents p< 0.05, ** represents p< 0.01.*

5.1.3 Stress Relaxation

If the compliant hydrogels are being held under constant deformation for a period of time, this would lead to a gradual time-dependent reduction in stress, called stress

relaxation, mainly due to the movement of internal polymer chains that can adopt to the deformation level, indicating the viscoelasticity of hydrogels. The time-dependent responses of all NCHs were measured and compared to the reference IPN as illustrated in Fig. 5.4 (a), where relative stress was plotted versus test time. A trend was observed in the reduction of stress level with time for all samples, although the reduction rate was found to be material-dependent. Data analysis revealed the stress was relaxed more significantly for 2% ($p< 0.02$) and 4% ($p< 0.001$) Si-NP modified samples, while no significant difference was found between 1% NCHs and the control hydrogel samples. Thus, the incorporation of Si-NP in the hydrogel resulted in lowering the stress level, and as more NPs implemented in the hydrogels, the stress relaxation level drastically increased, which could be realised by comparing the values corresponding to 1% and 4% Si-NP in Fig. 5.4 (a) at the end of the test (t=1800s). Moreover, the stress relaxed at the highest rate for all samples shortly after the test initiated (t =60s), and again samples with higher NP concentrations showed remarkable performance with higher stress relaxations.

Two-term exponential decay curve fitting method was utilised to find the parameters of (3.7) and the results are listed in Table 5.1. The dotted lines showed in Fig. 5.4 (a), represent the fitted curve for each set of data. The viscoelastic model characterised for each hydrogel type, was utilised for the prediction of relative stress level at 1 hour test period, while stress relaxation experiments were also conducted for the same period of time and the relative stress levels at t=3600 s from experiments were compared with the values computed from the mathematical model. As can be seen from Fig. 5.4 (b), the results obtained from the model were in good agreement with the experimental data. Similar trend was observed for other hydrogel types, hence the model could be validated.

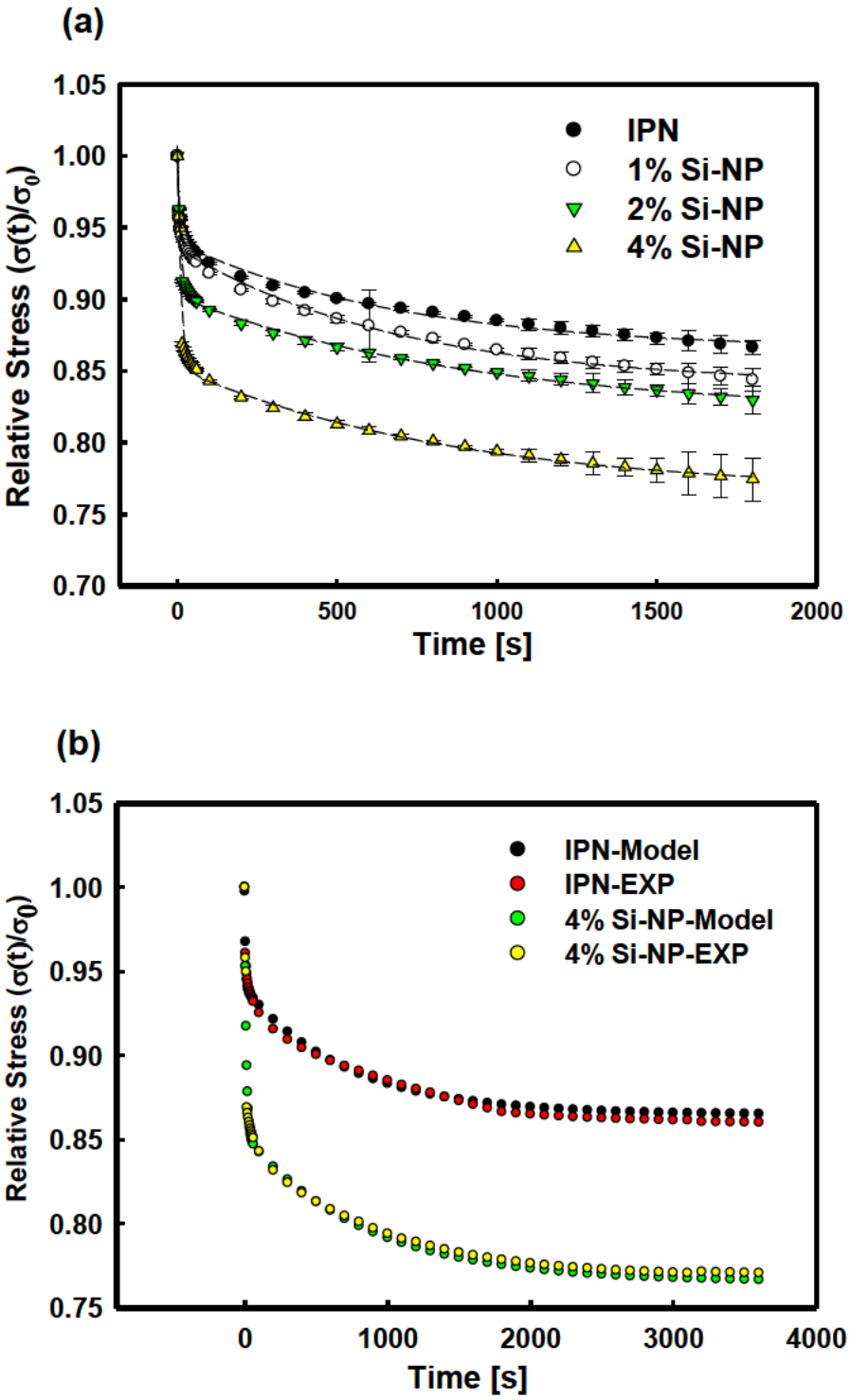

Figure 5.4 *(a) Stress relaxation response of NCHs and the comparison with the reference IPN hydrogel at 0.5 strain, (b) the validation of mathematical viscoelastic model by experimental approach*

Table 5.1 Relaxation parameters of NCHs and IPN hydrogels obtained from curve fitting (Average ± SD)

Coefficient	IPN	1% Si-NP	2% Si-NP	4% Si-NP
σ_f/σ_0	0.8647 ± 0.0029	0.8403 ± 0.0029	0.8206 ± 0.007	0.7655 ± 0.0126
a	0.0578 ± 0.0031	0.0617 ± 0.0031	0.0997 ± 0.0044	0.155 ± 0.0087
b	0.143 ± 0.0171	0.151 ± 0.0171	0.0931 ± 0.0092	0.0852 ± 0.0107
c	0.0751 ± 0.0027	0.0957 ± 0.0027	0.0813 ± 0.0063	0.0868 ± 0.0111
d	0.0014 ± 0.0001	0.0014 ± 0.0001	0.0011 ± 0.0002	0.0012 ± 0.0004

5.1.4 Friction and Wear Test Results

During the sliding wear tests, prepared samples were mounted on top of a metal substrate that might interfere with the measurements, if the total through-thickness deformation of the specimen is above 10% of sample's initial thickness [240]. This was investigated following the procedure described in section 4.1.2. It was found that under the maximum applied load, Si-NPs with 1% and 4% concentrations showed 0.58 mm and 0.44 mm through-thickness deformation, respectively. Therefore, it was concluded that the substrate had no adverse effect on tribological measurements, as the deformation did not exceed 10% of sample's initial thickness. The wear volume losses for NCH specimens in the swollen state, and in the presence of boundary bovine serum lubrication, are presented in Fig. 5.5 (a) and (b), with respect to the normal loads and sliding speeds, respectively. Increasing the normal load resulted in continuous wear volume increase for all NCH specimens, regardless of NP concentration. Similar trend was observed in the previous chapter for the reference IPN Hydrogel, as shown in Fig. 5.5 (a). ANOVA analysis showed the effect of Si-NP modification on wear properties of hydrogel matrix as statistically significant ($p< 0.001$), across the range of applied loads and sliding speeds. In addition, changes in applied normal load as well as sliding speed were found to significantly affect the wear properties of all studied materials ($p< 0.001$). Moreover, wear volume decreased by incorporating Si-NPs into the hydrogels, as shown in Fig. 5.5

(a). Specimens made by 4% Si-NP showed the lowest wear volume, just below 4 mm^3, and about 69% lower than the reference IPN hydrogel. Overall, samples prepared with 4% Si-NP showed the least wear rate across the range of studied loads. However, without lubrication, the 4% Si-NP specimens showed higher wear volume than the other NCH samples at both 0.1N (2.18 mm^3) and 0.7N (12.33 mm^3), but lower wear volume at 0.5N load (5.39 mm^3) as shown in Fig. 5.6. No significant difference was found between 1% and 2% Si-NP NCHs during "dry tests" and least amounts of wear were measured for these specimens (average range of 0.99-8.83 mm^3). At the highest normal load, bovine serum lubrication contributed to lowering the wear rate by 56.7% in average, for NCHs, and by 35.5% for IPN hydrogel samples.

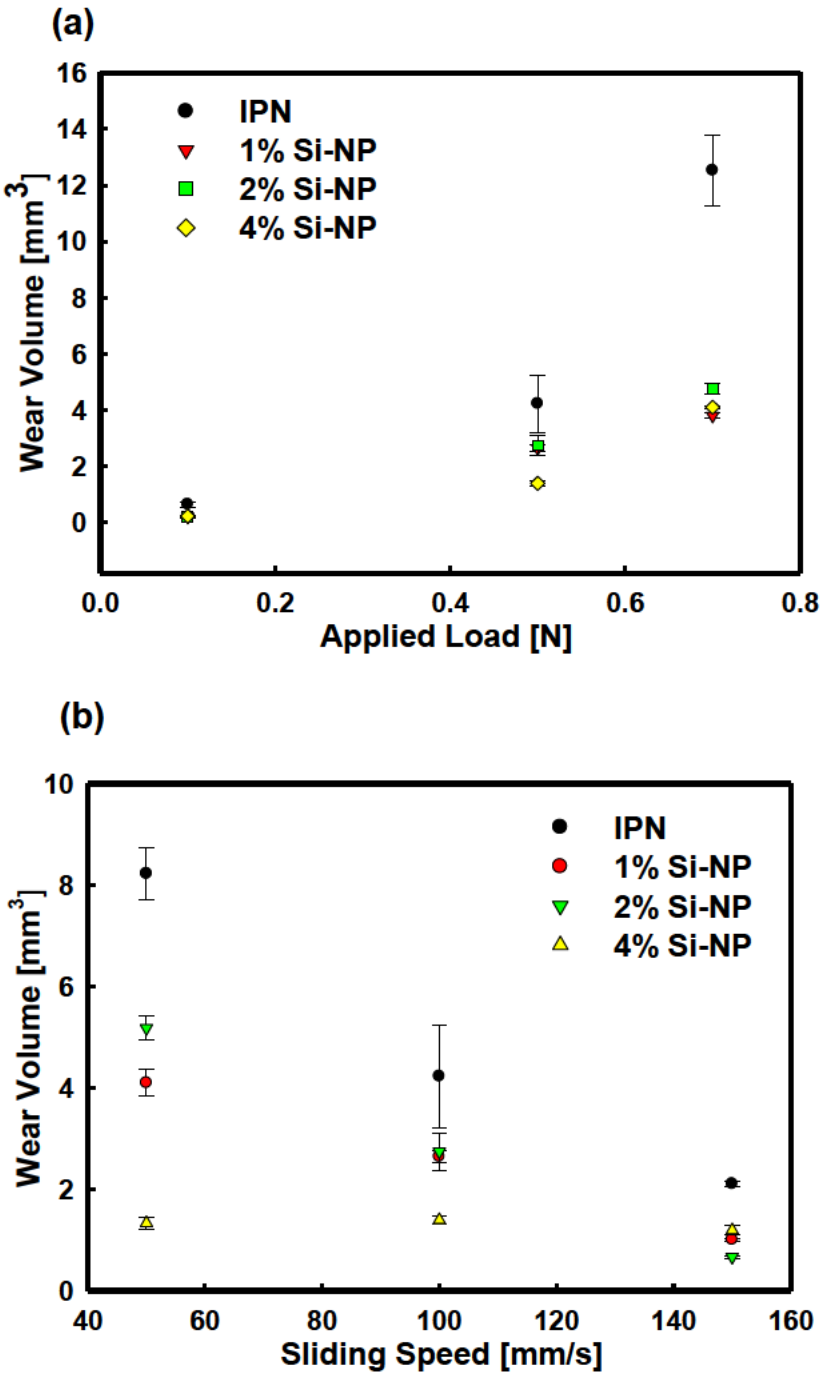

Figure 5.5 *The comparison between generated wear volume of NCHs with different Si-NP concentrations and the reference IPN hydrogel in the presence of the lubricant with respect to (a) various loads (constant speed, v= 100mm/s), (b) various sliding speed (constant load, p =0.5 N)*

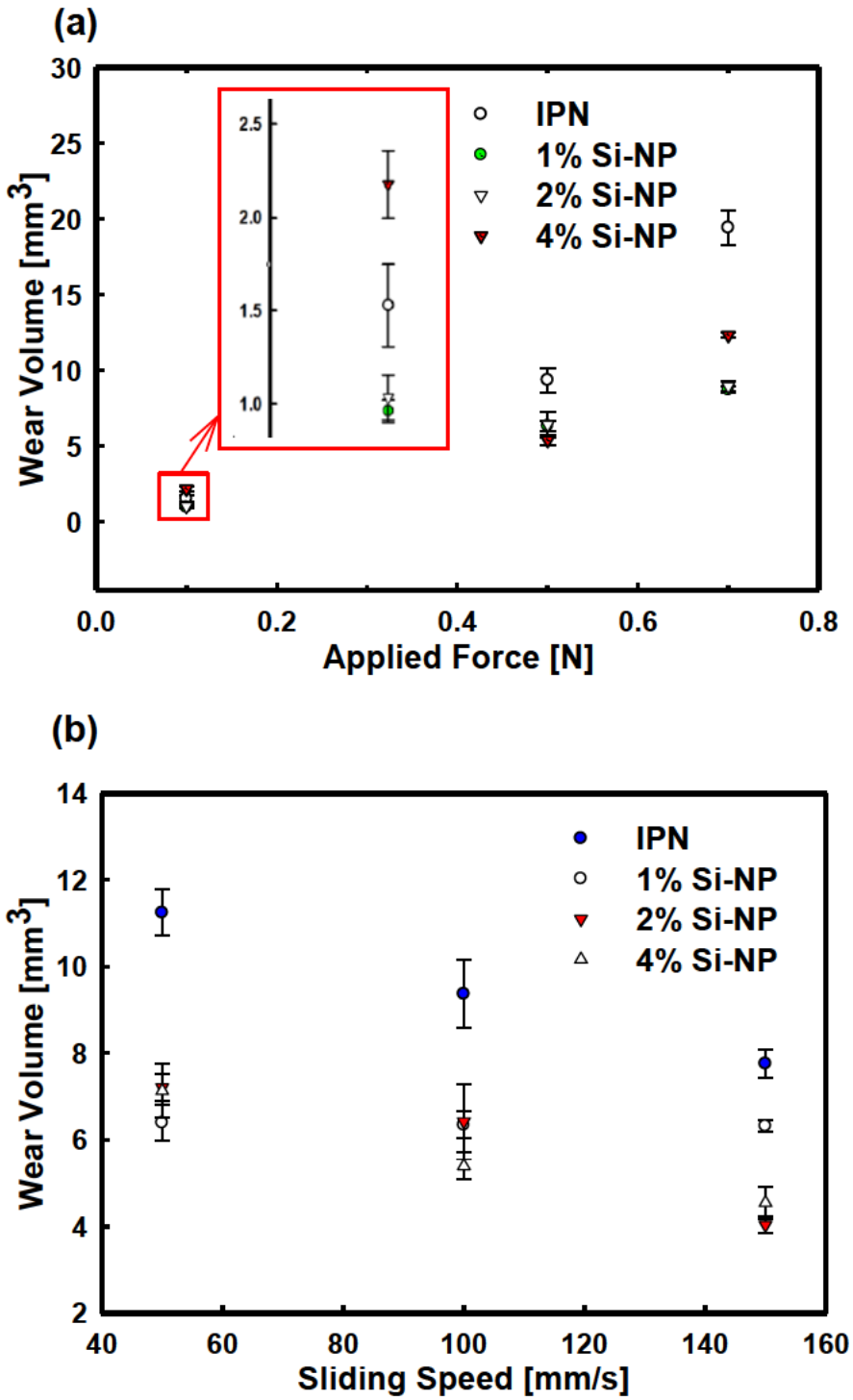

Figure 5.6 Comparison of generated wear volumes of NCHs with different Si-NP concentrations and the reference IPN hydrogel in the absence of the lubricant tested under (a) various loads (constant speed, v= 100mm/s), (b) various sliding speed (constant load, p =0.5 N)

Wear volume decreased when the sliding speed increased from 50 mm/s to 150 mm/s for all hydrogel types as illustrated in Fig. 5.5 (b). Again, 4% Si-NPs specimens showed the best wear-resistant feature, especially at the lowest sliding speed, while 1% and 2% NCHs displayed the lowest wear volume at 150 mm/s (0.66 mm^3 for 2% Si-NP).

Under dry test condition (when no external lubricant was applied), almost similar trend was observed for the wear volume with regard to the sliding speed for all tested materials, except for 1% Si-NP, where wear rate remained constant, as shown in Fig. 5.6 (b) Based on the wear volume data, samples with 2% and 4% Si-NP exhibited the best performance across the range of sliding rates. The biological lubricant was more effective at higher test speeds, especially at 150 mm/s, where wear volume dropped by 72.8% and 80.4% for IPN and NCHs, respectively.

The morphology of the worn surfaces for each tested material, with lubrication and under the highest applied load, was captured by a 20X confocal objective of the optical profilometer module, as shown in Fig. 5.7. Overall, less visible surface deformation (indicated by white arrows) was observed under lubricated tests among all test coupons, as can be seen in Fig. 5.7. It was also noticed that as the Si-NP concentration increased in the hydrogel matrix, wear-resistance improved and surface damage, as a result of sliding motion, decreased drastically.

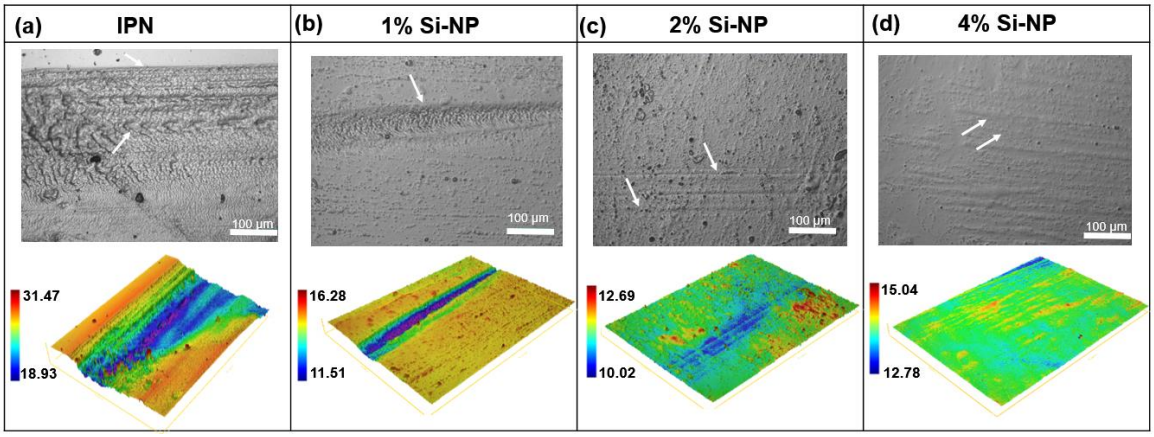

Figure 5.7 *Micrographs of the worn tracks, together with the 3D scar profiles for (a) IPN hydrogel, (b-d) NCHs with Si-NP concentration 1%-4%, under lubrication and 0.7N normal load. The unit for all colour scale bars are in µm.*

The mean CoF values for different load levels, are illustrated in Fig 5.8 (a) and (b), for dry and lubricated test conditions, respectively. No statistically significant difference was found between CoF values of Si-NP modified samples and the control IPN hydrogel in

the absence of lubrication ($p = 0.51$). Nevertheless, increasing the load and addition of NP, as well as increasing the NP concertation, have had positive effect on the reduction of CoF under lubrication, as observed in Fig. 5.8 (b) ($p < 0.01$ in most cases). Friction increased from 0.1N to 0.5N for NCHs, while it decreased from 0.5N to 0.7N for all tested materials, as revealed from Fig. 5.8 (a). With lubrication and at the highest applied load of 0.7N, the CoF values showed a significant decrease (over 67%) for the samples made with 1% Si-NPs compared to the IPN hydrogel. At 0.7N load and with the aid of lubrication, the CoF was recorded in the range of 0.0035-0.0055 for 1%-4% Si-NP samples, almost an order of magnitude lower than the value obtained for ALG-PAAm IPN hydrogel (0.01) in section 4.1.2, and close to the CoF reported for articular cartilage tissue (0.001) [249, 262].

Concerning the effect of sliding speed on friction, as shown in Fig.5.9 (a), dissimilar trends were observed between IPN and NCHs, under dry testing condition. Again, CoF values were found not statistically different between the control and the treatment groups under dry testing condition, while change in sliding speed influenced CoF for IPN and 2% Si-NP samples ($p < 0.05$). However, lower friction levels were obtained for NCHs when compared to the reference hydrogel samples at 100 mm/s and 150 mm/s sliding velocities. As for the tests conducted under lubrication, CoF decreased as the sliding speed increased among all tested samples, as illustrated in Fig. 5.9 (b). Friction levels were significantly affected by varying sliding speed across the NCHs, as can been seen in Fig. 5.9 (b). Specimens with 4% Si-NP showed the lowest CoF over the range of sliding speeds tested under lubrication. Overall, the results indicated the positive impact of incorporating Si-NP on lowering the friction experienced on the surface of the hydrogel matrix.

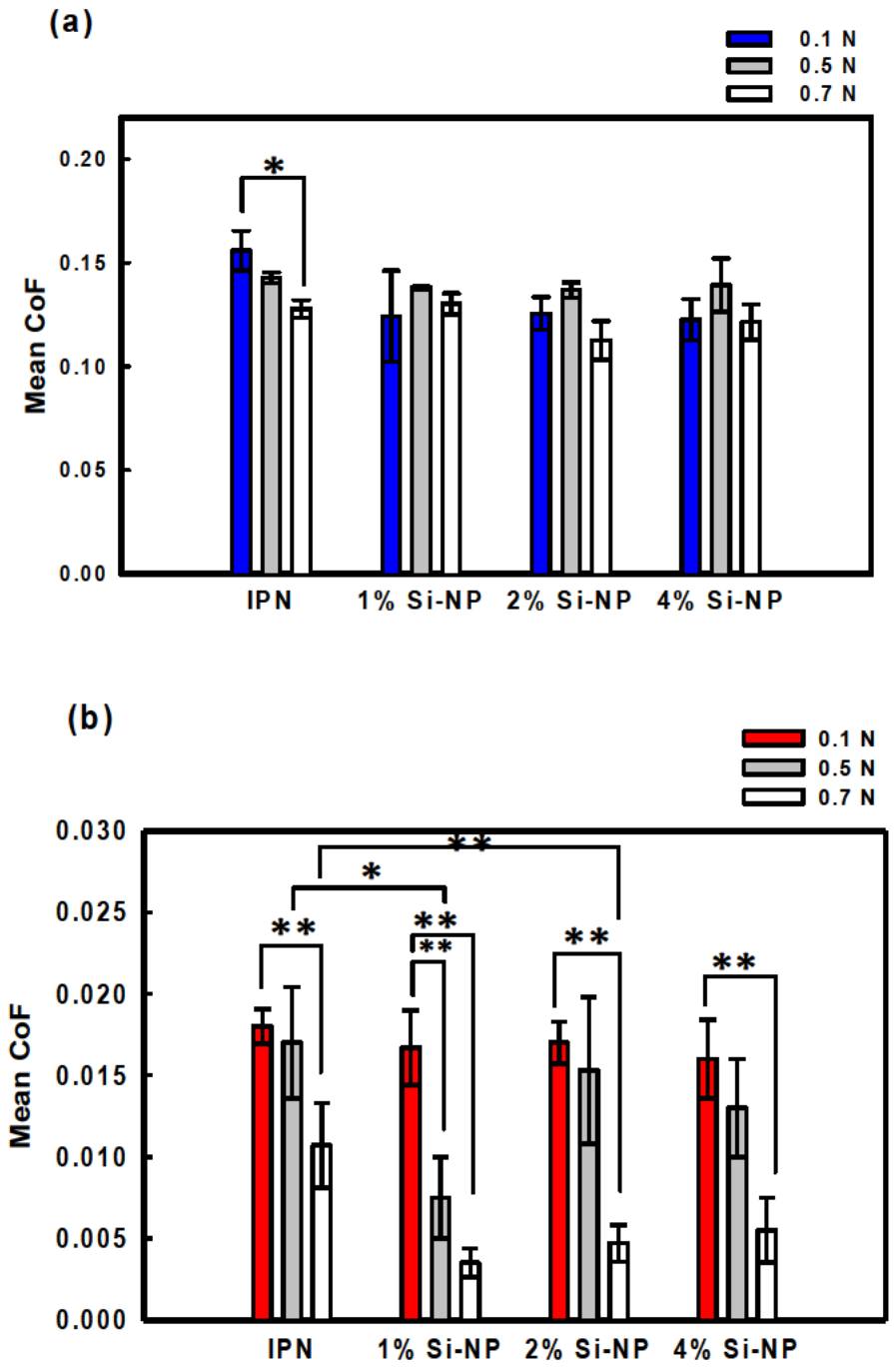

Figure 5.8 *Mean values of friction coefficient obtained from averaging the friction plots versus normal loads: (a) without lubrication and (b) with bovine serum lubrication (All tests were run at a constant sliding speed of 100 mm/s). * represents $p < 0.05$, ** represents $p < 0.01$.*

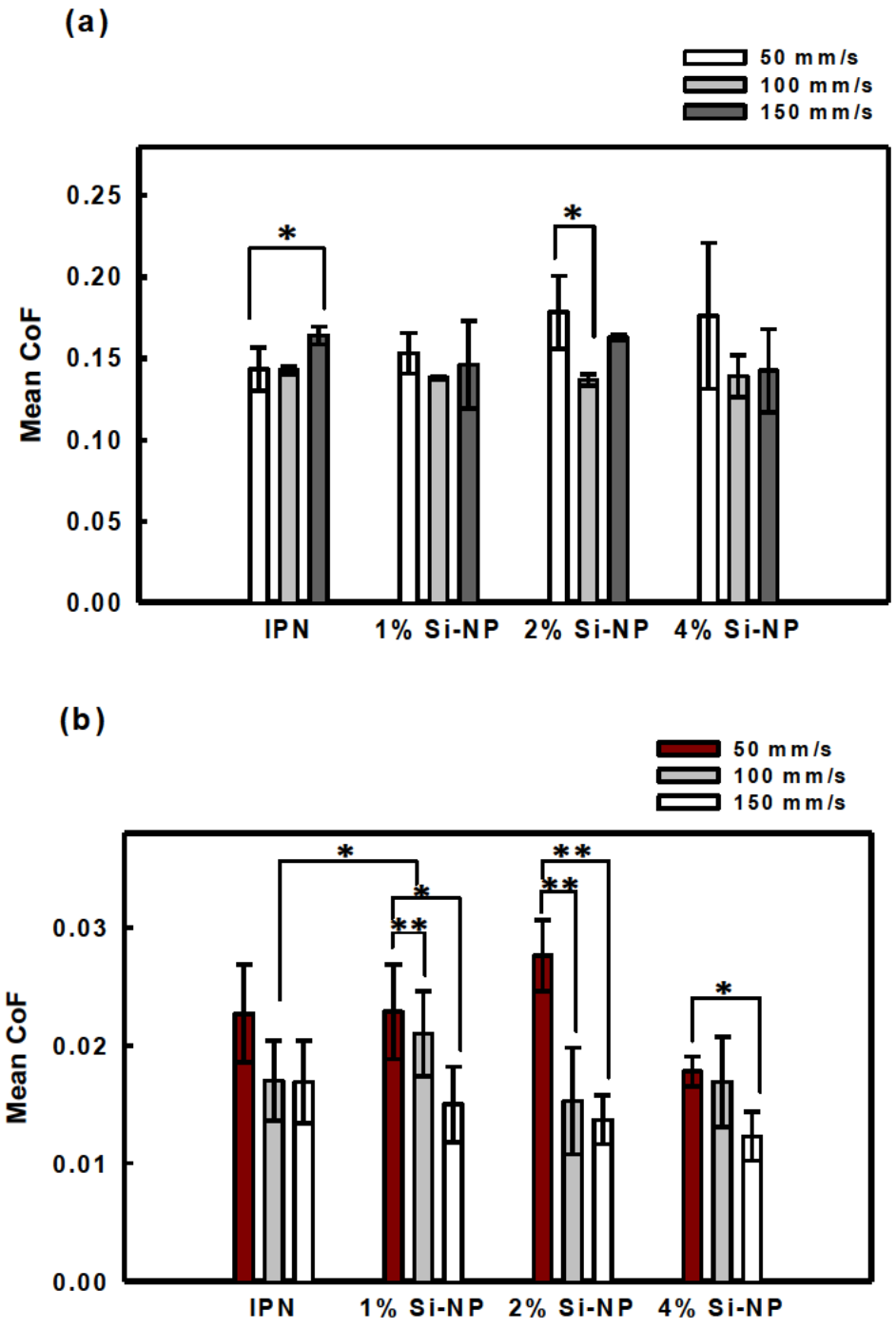

*Figure 5.9 Mean values of friction coefficient obtained from averaging the friction plots versus sliding speeds: (a) without lubrication, (b) with bovine serum lubrication (All tests were run at a constant applied load of 0.5 N. * represents p< 0.05, ** represents p< 0.01.*

5.1.5 SEM and EDS Investigations

SEM images of the freeze-dried samples are shown in Fig. 5.10. The samples were fractured, and a porous structure was observed at the cross-section, unlike the outer

surface of the intact samples (see Fig. 3.13 (c)). From Fig. 5.10, it could be clearly seen that higher NP concentration resulted in smaller pore size for the NCHs. Regarding the freezing method, it was found the samples were more sensitive to abrupt freezing by liquid nitrogen and it usually resulted in sudden cracks and fracture. This is due to the abrupt volume expansion of frozen interstitial fluid, and the brittle polymer structure that could not adopt itself to the condition. In contrast, the samples fairly maintained their shapes when being subjected to gradual freezing, in a freezer, attributed to the ability of flexible hydrogel networks to adopt to the environmental temperature.

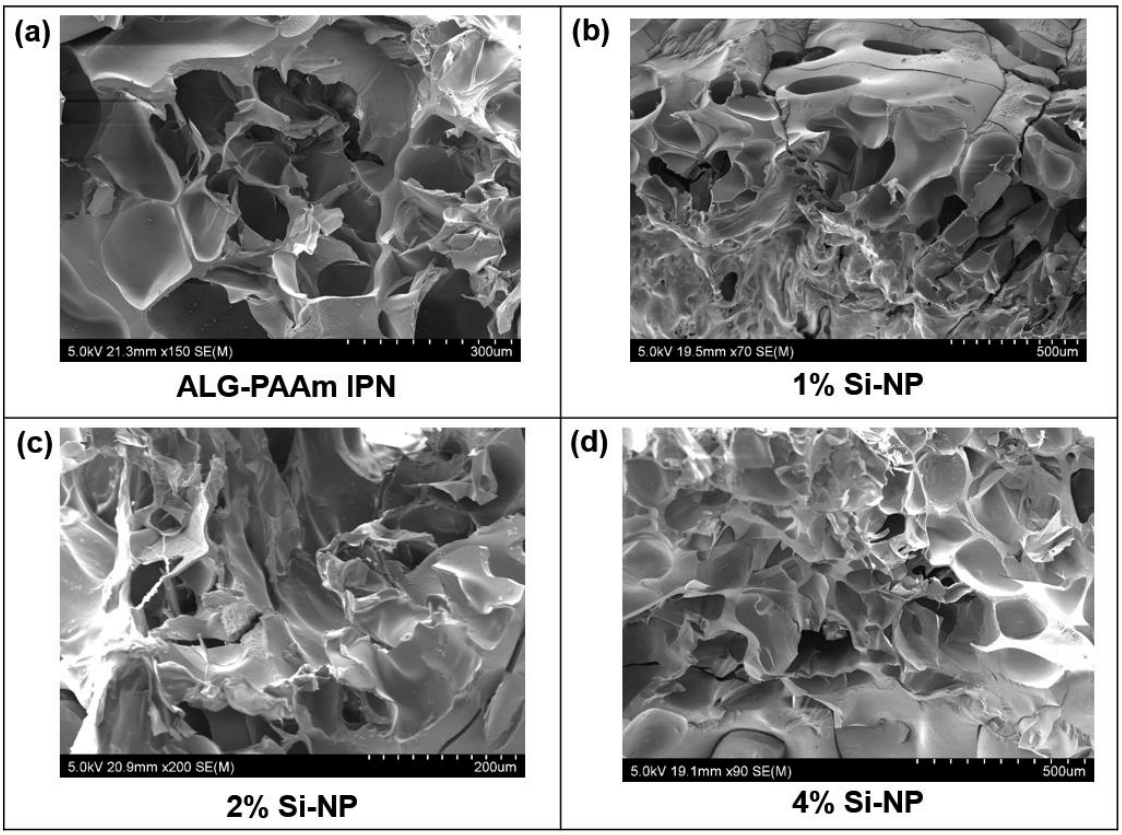

Figure 5.10 SEM images of freeze-dried samples

Moreover, it was noticed that the sample aspect ratio affects the shape of freeze-dried hydrogels, as minimum deformation was found when the aspect ratio was equal to 1. In general, samples with the aspect ratio of 0.5 were significantly distorted, leading to the collapse of the porous structure.

The Si-NP powder was also coated and studied under SEM/EDS. Agglomeration of Si-NPs were observed under SEM as illustrated in Fig. 5.11 (a), with the size in the range of 30~100 nm. Agglomeration is mainly due to the high surface energy of NPs as a result of high surface area to volume ratio and the strong van der Waals bonds between the particles. The EDS analysis results are presented in Fig. 5.11 (b) and carbon, oxygen and silicon were identified as the main elements of Si-NPs.

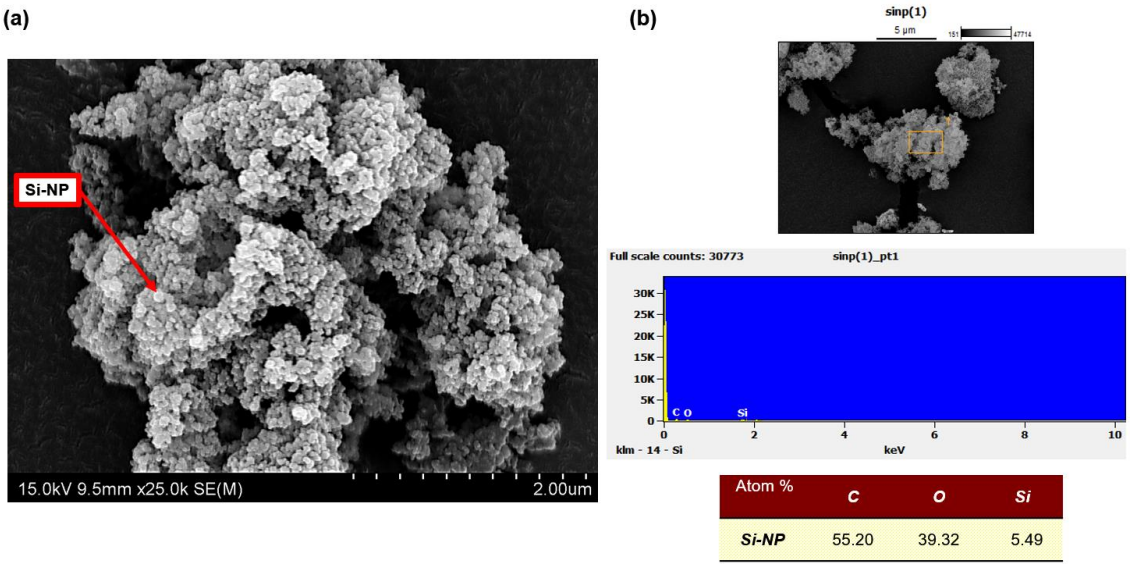

Figure 5.11 (a) Si-NP cluster, (b) EDS elemental analysis

SEM micrographs captured from the worn surfaces of NCHs with different Si-NP concentrations are presented in Fig. 5.12 (a)-(d). As can be seen, an increase in Si-NP concentration contributed to less severe surface deformation. Pitted surfaces were frequently observed across the wear track of the samples. Si-NP clusters were observed on the worn surfaces of NCHs, and relatively larger clusters were found on samples with 4% Si-NP concentration. Comparing Fig. 5.12 (a) and (b), less surface pitting was observed at lower applied load in samples made with 4% Si-NP. More uniform deformation was observed on the surface of the 1% Si-NP samples compared to that of 4% Si-NP. The presence of Si-NP clusters were frequently observed accompanied by wear debris, and as the NP concentration increased, larger areas of agglomeration were

found on the surface. To prevent agglomeration, the electrostatic repulsion must occur between NPs which can be achieved by surface modification [273]. Agglomeration was found as a function of nano particle concentration. Larger clusters were observed in samples prepared with 4% Si-NP compared to other samples. In addition, wear volume was found to be higher for 4% Si-NP without lubricant. It was concluded that the increase in nanoparticle agglomeration might adversely affect the wear resistant of NCHs. However, in the presence of bovine serum lubricant, lower wear rate was achieved for NCHs with higher NP concentrations.

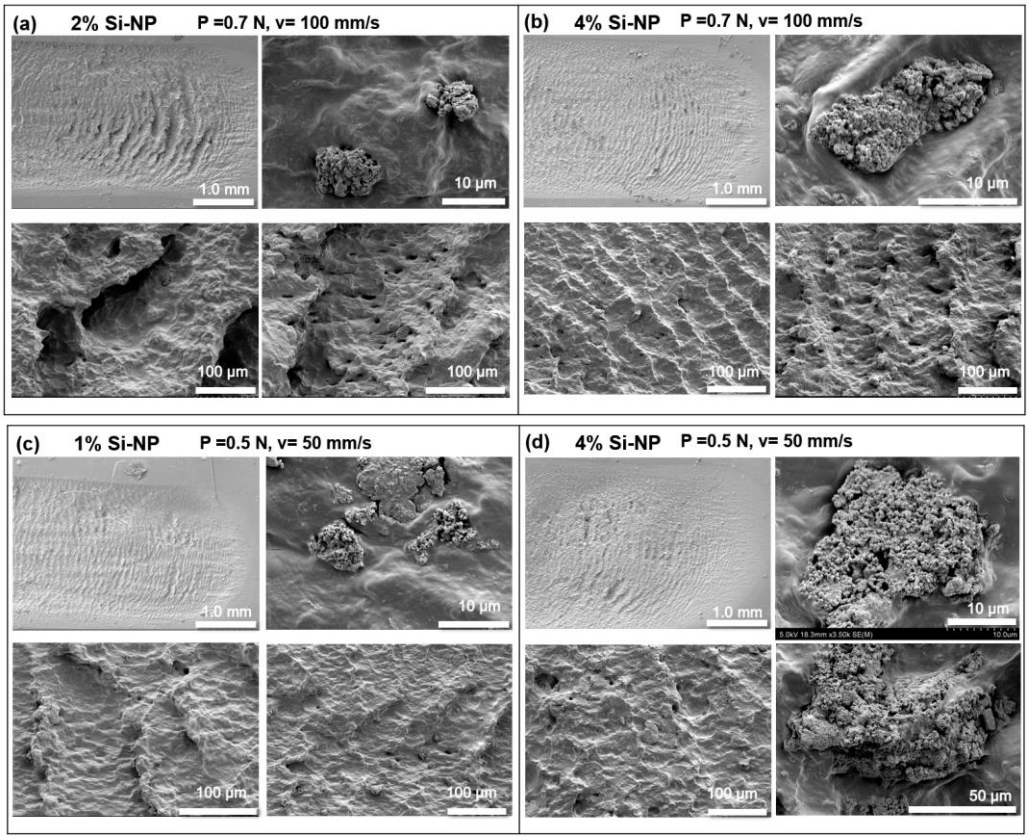

Figure 5.12 SEM images of worn surface of NCHs at (a, b) highest load, (c, d) lowest test speed

Uniform dispersion of Si-NPs was initially observed visually during sample preparation, as a homogenous solution was achieved. EDS was also employed at different regions, on the surface of three NCH samples to investigate whether or not a consistent distribution exists. The EDS results for NCH samples with 4% Si-NP are shown in Fig. 5.13. Atom percentage measurements on three different samples indicated a uniform

presence of silicon on the scanned region. Similar trend was observed for the other variants.

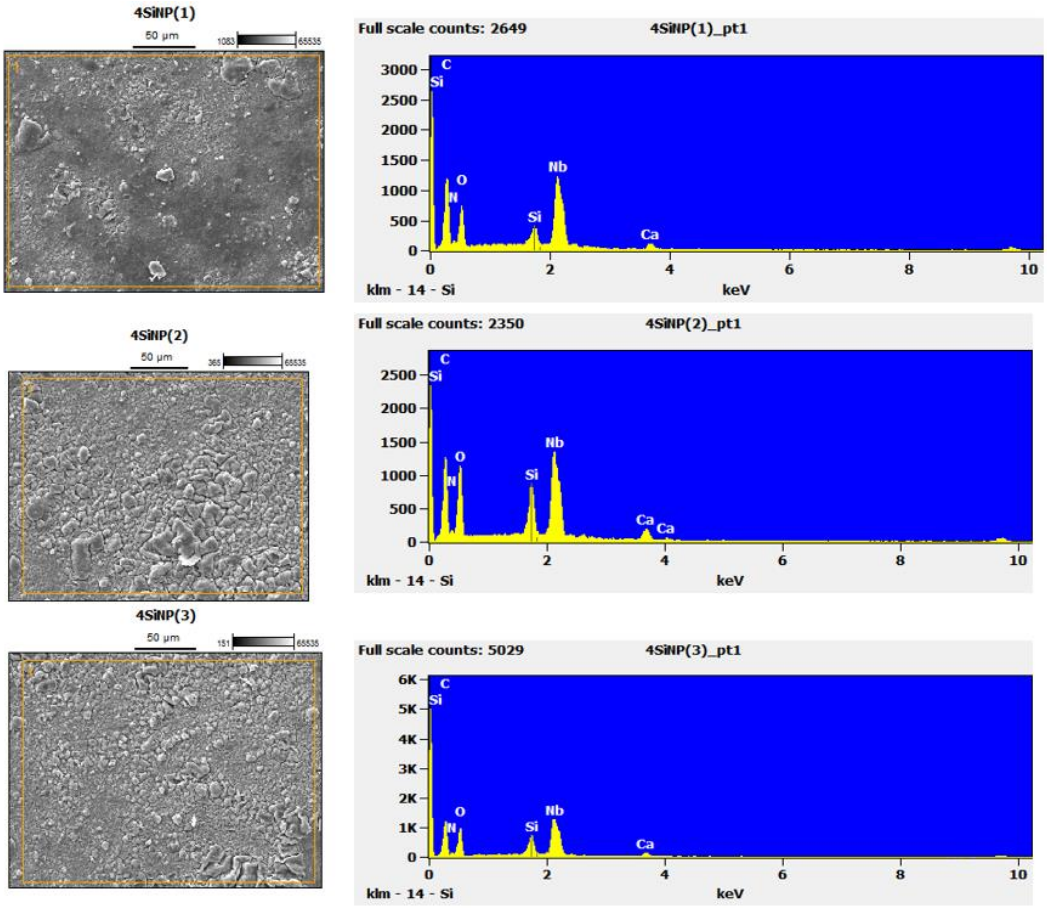

Atom %	C	N	O	Si	Ca	Nb
4% Si-NP (1)	52.39	11.19	29.97	1.67	0.59	4.19
4% Si-NP (2)	45.51	9.88	36.94	2.90	0.88	3.89
4% Si-NP (3)	48.52	9.71	33.97	2.81	0.86	4.13

Figure 5.13 EDS analysis of three different regions on the surface of 4% Si-NP samples (n =3)

As can be seen in Fig. 5.13 Nb peaks were identified in the results. The reason behind this was further investigated. It was found Nb L series overlaps Au M series. Referring to the Energy Table for EDS Analysis revealed Nb Lα is 2.166 while Au M is 2.12. The overlapping is therefore attributed to resolution of EDS instrument utilised. Therefore, the peaks basically show Au on the surface, which is due to the gold coating of the samples.

5.2 Discussion

The mechanical and tribological characteristics of nano-silica-reinforced ALG-PAAm hydrogels were focused in this chapter. Previous study has shown how the elastic and viscoelastic properties of ALG-PAAm hydrogel could be tuned by the change of constituents such as alginate and amount of crosslinking agent concertation, to mimic the mechanical response of a biological tissue, implying its potential capacity [274]. On the other hand, as a double network structure, ALG and PAAm are known to provide different mechanical responses, once the structure undergoes compression. Long-chained, covallentally-crosslinked PAAm network stretches under compressive load, while the physical bonds between ALG network break (hence dissipating strain energy), and rearrange with deformation. Therefore, the PAAm network remains intact, and can recover the structure's shape once the load is removed. The incorporation of Si-NPs into ALG-PAAm IPN hydrogel has not been attempted before. However, it was expected that Si-NPs would enhance the mechanical properties of the hydrogel, through establishment of hydrogen bond with PAAm network, and serving as a crosslinker to increase structural stiffness.

The results demonstrated that the studied NCHs benefit from enhanced mechanical properties, such as elastic modulus, hardness, compressive modulus, and stress relaxation response, compared to the reference IPN hydrogel. This is mainly due to the strong interfacial bonding between the nanoparticles and the polymer matrix, allowing effective stress transfer between the two main constituents as validated in a previous study [150]. Moreover, nano-filler size and dispersion quality affect the mechanical properties of NCHs. In general, smaller nano-particles result in more property enhancement [150]. Compressive moduli of the studied NCHs in full hydrated state was found in the range of 0.65-1 MPa at 0.5 strain which is within the reported range for articular cartilage (0.4-10

MPa) [66]. Higher values for this property might be achieved if the tests were conducted right after chemical crosslinking occurred and without subsequent water submersion, as carried out in previous studies [32, 166].

It is worth mentioning that the indentation tests were conducted in a loading rate to ensure viscoelasticity of the materials does not interfere with the results. With minimal test coupon preparation, the indentation test provides the localised material property data, which was shown appropriate for the assessment of hydrated, compliant hydrogels [160]. From Fig. 5.3 (a), all tested samples showed typical non-linear stress-strain behaviour, as a requirement for the cartilage replacement candidates [51], while for the NCHs, the stiffness and toughness were correlated to the percentage of NPs present in the hydrogel structure. The native cartilage tissue exhibits viscoelastic nature, similar to other biological soft tissues. Therefore, viscoelasticity is considered as a crucial design parameter for any potential cartilage replacement candidate. Under compression, the native cartilage exhibits approximately 50% stress relaxation capacity [68, 275]. On the other hand, the studied materials in this research showed about 25% stress relaxation, which can be considered as a limitation of these materials. As shown in Fig. 5.4 (a), NCHs were relaxed at a faster rate as the concentration of Si-NP increased from 1% to 4%. Therefore, the degree of viscoelasticity is related to the amount of incorporated NPs in the hydrogel matrix, which explains the increase in strain-rate dependency with higher NP concentrations. As this degree increases, the material would benefit from more viscous flow once being under stress, thus strain-rate dependency increases. This is a crucial factor, as higher strain-rate dependency enables the biomaterial to properly function once various levels of loads and articulation velocities are exerted on the implant during physical activities of the patient. Similar trend was reported in a previous study on PVA hydrogels, reinforced by bacterial cellulose NPs [276]. The equilibrium water content is believed to adversely affect the elastic modulus and stress relaxation behaviours

due to less mobility of stretched polymer chains once the hydrogel is in fully swollen state [274]. NCHs were analysed for this parameter and it was found that water content was lower in NCHs (75.2% - 80.1%) compared to IPN (82.1%), and less fluid would be contained with higher NP concentration. Similar finding was reported previously [150]. This could be attributed to the introduction of NPs into the hydrogel matrix which might restrict water uptake capacity of NCHs through occupying the pores and smaller mesh size as a result of polymer bridging of Si-NPs. Crosslinking agent concentration was reported in a previous study as another parameter that would affect stress relaxation response [274]. It was observed that by lowering the MBAA concentration, molecular weight between crosslinks increased, and this led to a higher relaxation response of hydrogel. However, specimens prepared with lower MBAA concentration showed inferior mechanical properties as found in the previous chapter. Thus, using the right MBAA concentration is important to benefit from both optimal stiffness and relaxation response.

Similar to cartilage, hydrogels retain a large proportion of water, which not only plays an important role in the mechanical behaviour of the structure, but also provides fluid film lubrication and decreases CoF, a feature which lacks in the conventional structural materials for the orthopaedic prosthesis such as ultra-high-molecular-weight-polyethylene [277]. Based on the tribological tests conducted, wear volume was found to be significantly lower for NCHs compared to IPN hydrogels, in most tests with various tribosystem parameters. This suggests the reinforcing impact of silica nanoparticles on the wear resistance of hydrogels, through a strong adsorption of polymer chains on the surface of nano particles. There also exists a hydrogen bond between silanol and carbonyl functional groups of Si-NP and PAAm, respectively [149], and as a result, apparent crosslink density increases compared to the non-modified hydrogel, which also leads to an improvement in wear-resistance as well as compression properties of NCHs.

As seen from Fig. 5.7 (b), CoF values recorded for Si-NP modified samples were an order of magnitude lower than other IPN specimens, and in the range of 0.003-0.005, which was very close to that of articular cartilage and almost two orders of magnitude lower than PVA hydrogels (0.04-0.1), as the most common hydrogel suggested for cartilage replacement. The presence of silica nanoparticles on the surface could affect the surface morphology and polarity, as well as surface tension, all resulted in decreasing the CoF values. Similar trend was found in a past study on nano-clay-reinforced polyacrylate hydrogels [204]. In general, for the compliant hydrogels, friction depends on the apparent contact area of mating surfaces and sliding speed, in addition to the applied load. The trend observed for variation in CoF could be explained based on the repulsion-adsorption friction model developed by Gong et al. [278] for hydrogels sliding against solid smooth counterface such as alumina ceramic ball. Due to the electrostatic repulsion exists between the hydrogel and the opposing surface at the sliding interface, a water layer is retained even at high normal loads, responsible for low friction level, observed in ALG-PAAm hydrogels, as well as NHCs [268]. Moreover, low friction level is attributed to free dangling polymer chains present at the hydrogel surface, non-adhesive to the opposing surface. This polymer brush effect was studied in the past, and it was revealed low friction could be achieved for long polymer brush only at low sliding speeds [279]. Therefore, by the pseudo crosslinking of silica nanoparticles, it is expected to achieve shorter polymer brush and therefore, low CoF is more feasible at higher sliding speed as observed in this study.

5.3 Conclusions

In summary, SiNP-ALG-PAAm nanocomposites hydrogels were synthesised and tested to characterise the mechanical and tribological behaviour against various test

parameters and compared with the reference IPN hydrogels. The results showed ultra-low CoF, coupled with high wear-resistance, and tuneable elastic and viscoelastic behaviours, suggesting these biomaterials as a promising candidate for use as a cartilage replacement. The improvements were attributed to the powerful interfacial bonding between the nano particles and polymer matrix, and it is expected to achieve even more robust nanocomposites using smaller size nano particles. Samples with 4% concentration of Si-NP, showed considerably efficient mechanical performance, high wear-resistance and fairly low CoF compared to the others. It is expected for the NCHs to achieve even better performance, once the counterface is made of cartilage tissue, rather than solid-phase alumina, with higher surface roughness. More realistic simulation is feasible with the aid of synovial fluid lubrication, running the tests at body temperature and more sophisticated butterfly sliding motion, to be implemented in future. Furthermore, to serve as synthetic cartilage, the implantation and integration with the neighbouring tissue needs to be addressed. In the following chapter, fibre-reinforced hydrogel composites will be studied.

Chapter 6

PROPERTIES OF A NOVEL HYDROGEL COMPOSITE REINFORCED BY THREE-DIMENSIONAL WOVEN TEXTILES

6.1 Mechanical and Tribological Properties of Fibre-Reinforced Hydrogel Composites

Based on the results presented in the previous chapter, introducing Si-NP into the hydrogel matrix was found to improve the mechanical and tribological responses, making the resultant NCH a promising candidate to be used as a load-bearing material. However, as mentioned previously, fibre-reinforcement of hydrogels is considered as an effective method for mechanical property enhancement. In the current chapter, consistent with the procedure implemented for hydrogels and NCHs samples, a number of tests were conducted using HCs with two different weaving patterns and they were compared with the reference unmodified ALG-PAAm hydrogel. Based on the analysis of the data presented in chapter 5 and this chapter, a comparison will be also made between two methods of reinforcement.

6.1.1 Tensile Testing of Polymer Yarns

Tensile tests were conducted on polymer yarns used in 3D textiles to find out the elastic properties as an input for the FE model. Mechanical properties of mono and multifilament yarns are presented in Table 6.1. Breaking tenacity was computed as breaking force divided by the yarn's linear density, while the toughness was computed as the area under force-elongation graph up to the fracture point.

Table 6.1 Material Properties acquired from tensile tests

Yarns	Breaking Tenacity [cN/Tex]	Tensile Strength [MPa]	Elongation [%]	Young's Modulus [MPa]	Breaking Toughness [J/mm^3]
USP 2-0	29.36 ± 1.82	551.3 ± 34.3	26.6 ± 1.12	3246.7 ± 98.1	73.28 ± 6.46
USP 3-0	25.9 ± 0.54	489.5 ± 10.2	26.3 ± 1.40	3112.1 ± 68.4	68.94 ± 6.64
USP 5-0	31.78 ± 3.32	596.3 ± 62.2	20.3 ± 2.16	1817.5 ± 32.5	55.44 ± 12.31
Multifilament PET	32.97 ± 1.10	480.4 ± 16.0	25.4 ± 0.24	13375 ± 141	93.9 ± 1.87

The engineering stress-strain response of various yarns are plotted in Fig. 6.1. In multifilament yarn, several filaments might rupture, while the remaining yarn is still bearing the tensile load, as can be seen in Fig. 6.1 (b). This can be clearly seen in the stress-strain graph as well, in which multifilament PET yarns exhibits a distinct mechanical behaviour in comparison with monofilament ones.

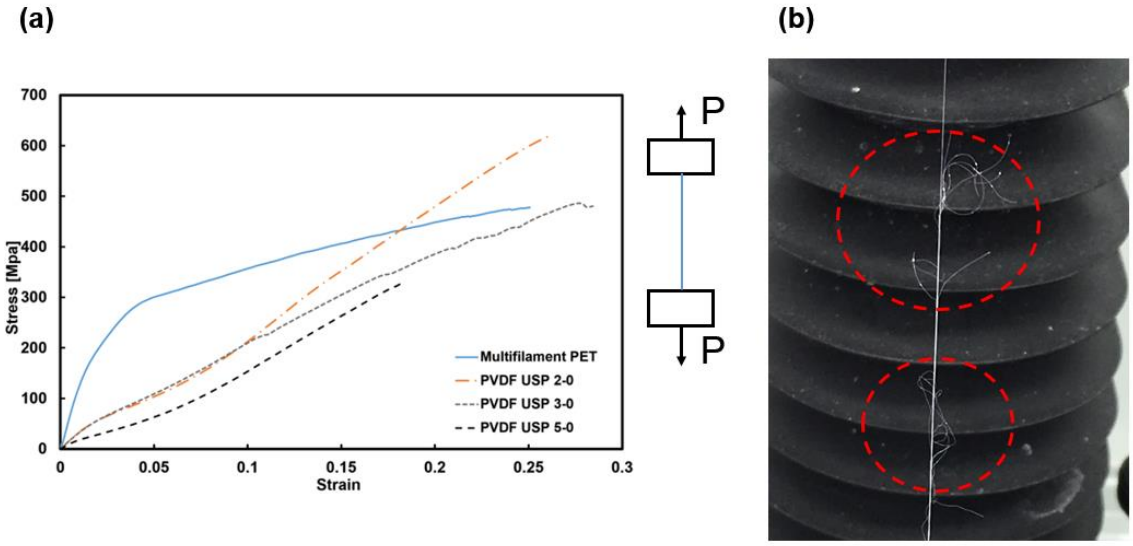

Figure 6.1 (a) Stress-strain response of polymer yarns under tensile loading, (b) filament rupture occuring prior to final failure of multifilament yarn

In summary, the stiffness gradient through the thickness of each 3D fabric was achieved by using fibres with different diameters and different stiffness. To prove this,

tensile tests were conducted to characterise material properties of each type of fibre used in fabric design. The elastic moduli of all polymer tows used in weaving process were obtained using TA XT Plus texture analyser equipped with custom-designed jigs. The Young's moduli were obtained from linear regression of stress-strain curves as summarised in Table 6.1. The stiffness values were found to be different for different types of fibres, indicating the stiffness variation through the thickness was achieved when tows with different sizes were implemented across the textile layers.

6.1.2 Indentation and Compression Tests Results

The reaction forces versus indentation depths for textile-reinforced hydrogels and IPN hydrogel are plotted in Fig. 6.2 (a). Type-A and Type-B textile designs were explained in section 3.1. The impact of reinforcing textiles on the boost to mechanical response of hydrogel could be observed in Fig. 6.2. Under the spherical indenter, HC Type-B required the largest indentation force, increased by a factor of 7.5 compared to the hybrid hydrogel. From the unloading curves, mechanical properties of HCs were obtained and compared with those of the hybrid hydrogel, as shown in Fig. 6.2 (b). As mentioned before, significant property improvements were observed, where the elastic moduli were improved by almost 7.5 and 10 times, for HC Type-A and HC Type-B, respectively, while the hardness was improved by 3.55 and 5.1 times for types A and B, respectively. Less porosity and smaller pore size observed in Type-B textile has led to larger elastic modulus, hardness and higher load-carrying capacity of the resultant hydrogel composite compared to HC Type-A.

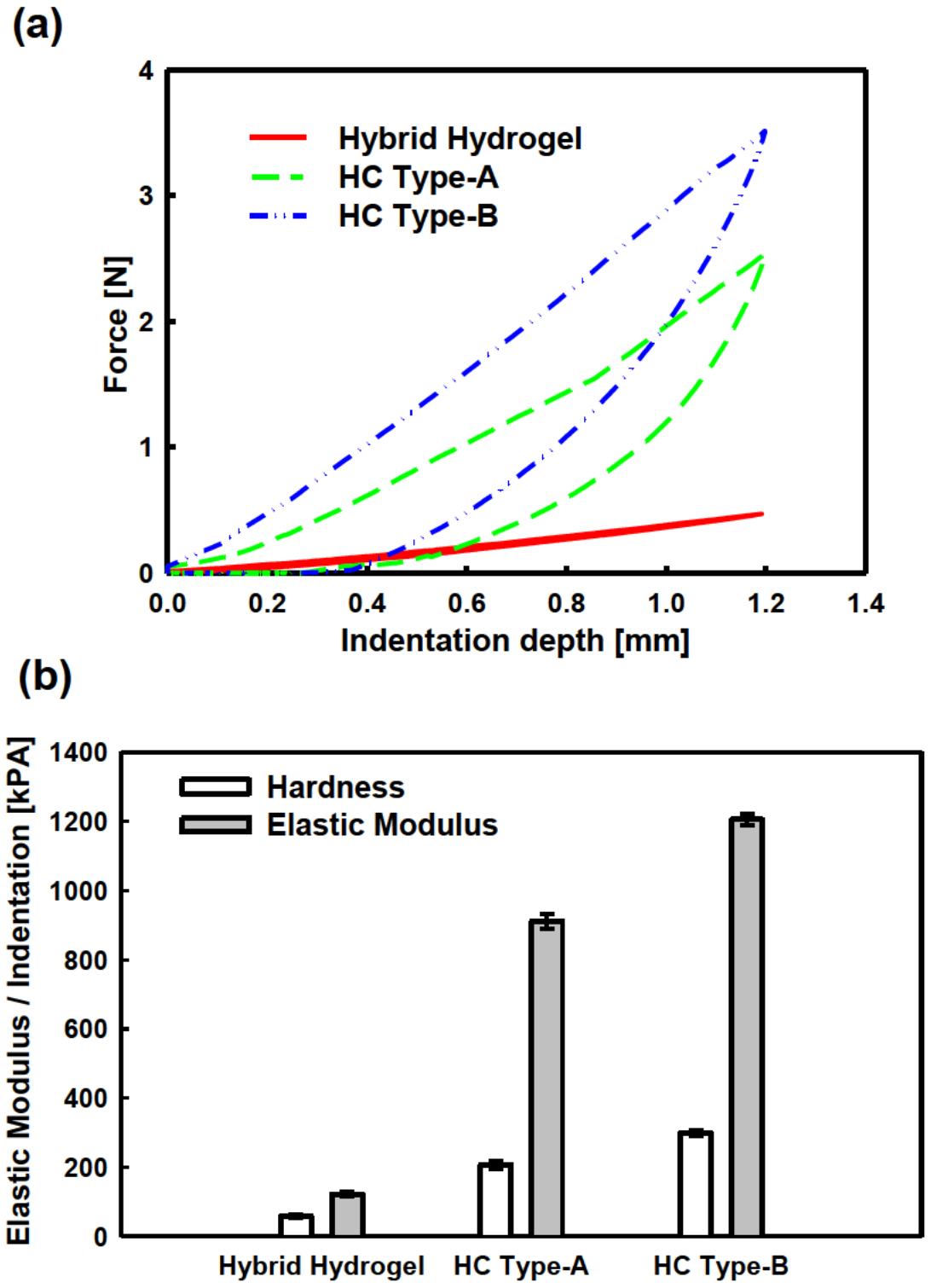

Figure 6.2 (a) The mean force-displacement responses of woven fabric hydrogel composites recorded during indentation tests and the comparison with non-reinforced hydrogel, and (b) the elastic properties obtained from the unloading portion of each graph

Fig. 6.3 (a) shows the stress-strain responses of both HCs compared to the unreinforced hybrid hydrogel, as well as 3D woven textiles, when they are all compressed

to 50% of their initial thickness with a rate of $0.1s^{-1}$. The trend observed was consistent with the results obtained from the indentation tests in terms of stiffness ranking, although the compression tests were carried out at a much higher strain level, and at different strain rates. The nonlinear compressive response of all samples was found to be affected by both strain level and strain rate. Unlike the hydrogel-based specimens, failure was observed once the strain exceeded 0.4 for both types of textiles, indicated by a drop in load-carrying capacity of the structures, as can be observed in the stress-strain curve (see Fig. 6.3 (a)). Fibre breakage was identified as the failure mode when the strain exceeded 0.4. This suggests the infusion of woven textiles with the compliant hydrogel matrix would improve the load-to-failure capacity of the textiles. Moreover, it was found that both HCs outperformed the corresponding 3D woven textile and the hydrogel matrix combined, demonstrating a strong synergistic effect.

The compressive tangent moduli were computed by finding each material constant via two-term exponential curve fitting of the stress-strain graphs, followed by differentiating (3.6) with respect to ε, and the values were plotted as a function of strain as illustrated in Fig. 6.3 (b) under a constant strain rate. The compressive tangent moduli were strain-magnitude dependent for all studied materials, while they increased for all hydrogel-based samples with increasing strain rate (results not shown). Compressive moduli for HC Type-A were found to be significantly influenced by the strain rate compared to HC Type-B, while the latter was more affected by the variation of strain level. Further data analysis for the HCs revealed the moduli were increased the most, when the strain rate was changed from 0.01 s^{-1} to 0.1 s^{-1} compared to a lower variation when the strain rate increased from 0.1 s^{-1} to 1 s^{-1} , suggesting moduli were more sensitive at relatively lower strain rates. In contrast, hybrid hydrogels exhibited a less remarkable strain-rate dependency compared to HCs, suggesting the woven reinforcement might enhance the strain-rate dependency of the hydrogel matrix.

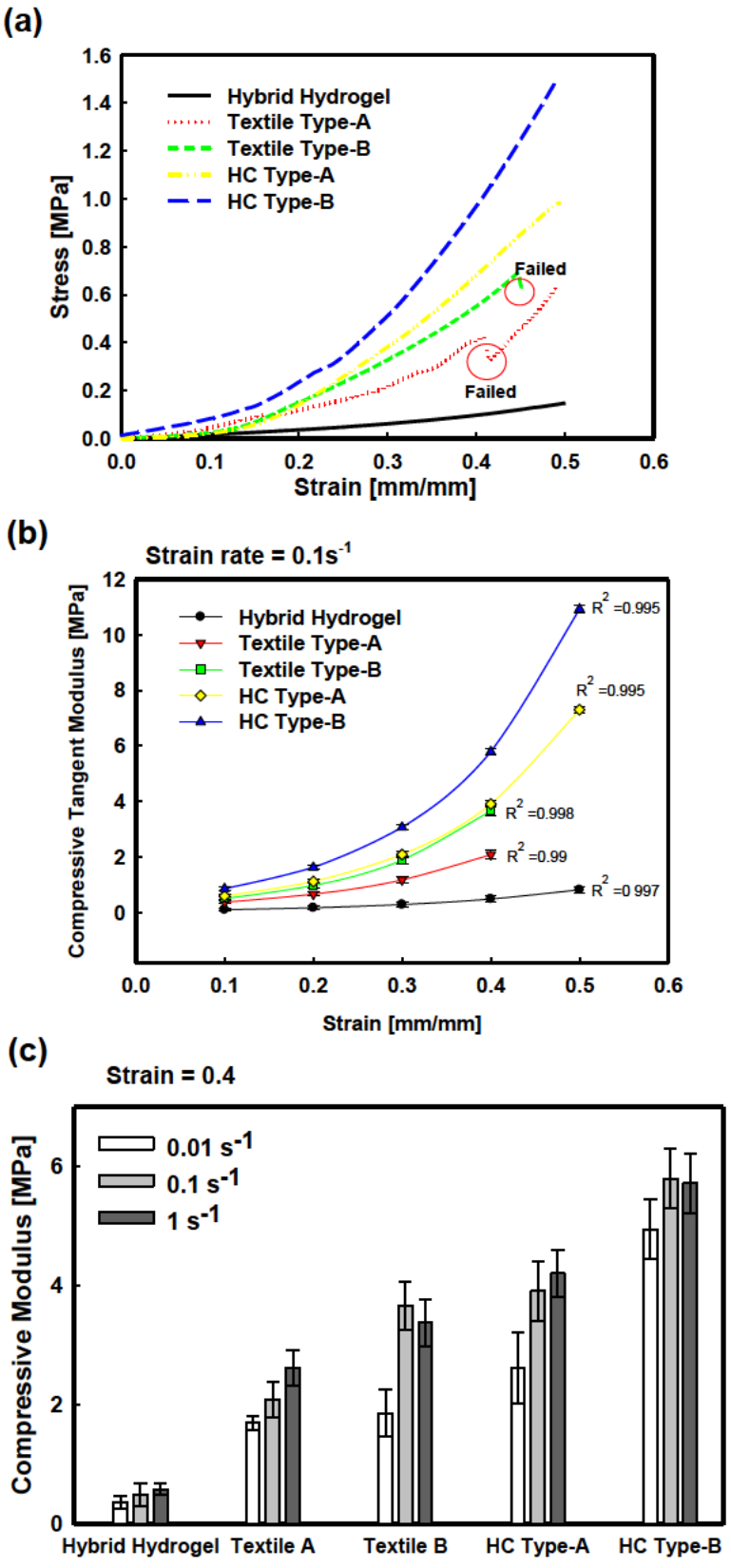

Figure 6.3 *(a) Compressive stress-strain response of HCs (mean (n=3)), and comparison with the reference hybrid hydrogel and woven textiles at a strain rate of 0.1 s^{-1}, (b) the compressive tangent moduli of all tested materials (mean (n=3) ± SD) as a function of strain magnitude under 0.1 s^{-1} rate, fitted by nonlinear regression, and (c) compressive moduli with respect to strain rates at strain = 0.4*

The correlation between the strain-rate and the compressive tangent moduli of all studied materials are illustrated in Fig. 6.3 (c) for a strain of 0.4, suggesting an increase in moduli with higher strain rates observed in almost all tested samples.

6.1.3 Stress Relaxation

The relative stress versus test time is plotted for both HC types and compared with the hybrid hydrogel as illustrated in Fig. 6.4. By keeping the strain constant, the induced stress was reduced with a sharp slope shortly after the test was initiated, followed by a gradual decrease, which formed a relatively flat line with time for both the hybrid and HC Type-A. In contrast, some fluctuations were observed in the time-dependent response of HC Type-B during steady-state stress relaxation. As mentioned in the literature, with increasing of the degree of viscoelasticity, more viscous flow is available once the stress is applied and more strain-rate dependency is achieved which is desired for a biomimetic structure [276]. Introduction of textile into hydrogel matrix would enhance the degree of viscoelasticity as observed from the stress-relaxation results shown in Fig.6.4. In fact, compared to the hybrid hydrogel, the stress relaxation response was improved by nearly 18% and 20% in HC Type-A and HC Type-B, respectively.

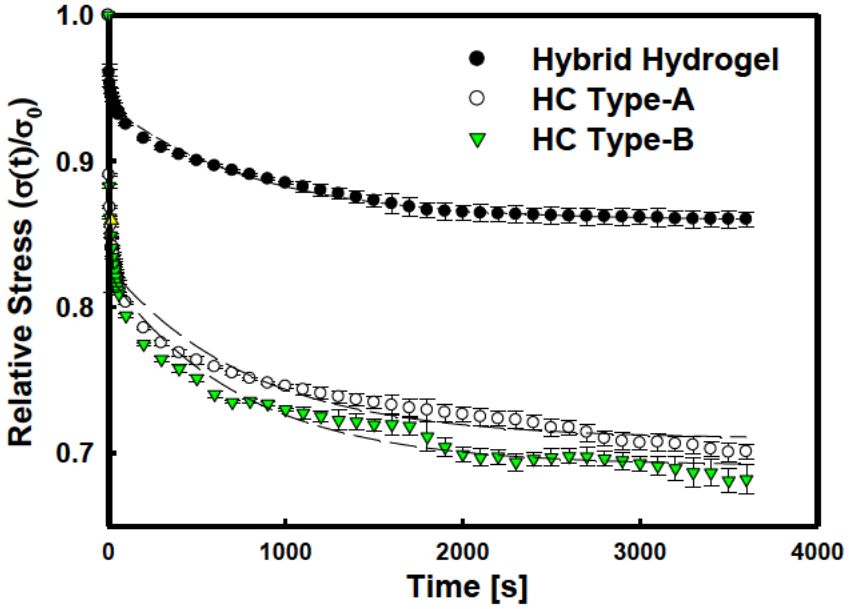

Figure 6.4 Stress relaxation behaviour of hydrogel composites in comparison to a hybrid hydrogel at 0.5 strain (mean (n=3) ±SD)

A two-term exponential decay method was utilised to fit the stress relaxation data as previously described by (3.7). The dotted lines in Fig. 6.4 represent the fitted curves for each data set, and the curve fitting parameters are tabulated in Table 6.2, as well. The viscoelastic model was applied for the prediction of relative stress at t= 7200s, while experiments were carried out for all tested materials for the same duration. A good correlation between experimental results and the mathematical model was found. Therefore, the viscoelastic model was confirmed to be capable of predicting the material behaviour at time frames beyond 3600 seconds, which was the focus of this study.

Table 6.2 Relaxation parameters for the HC and hybrid hydrogels obtained from curve fitting (Average ± SD)

Coefficient	Hybrid Hydrogel	HC Type-A	HC Type-B
σ_f/σ_0	0.8647 ± 0.0029	0.7098 ± 0.0028	0.6916 ± 0.0027
a	0.0578 ± 0.0031	0.1642 ± 0.0084	0.1706 ± 0.0088
b	0.1430 ± 0.0171	0.1376 ± 0.0153	0.1498 ± 0.0170
c	0.0751 ± 0.0027	0.1186 ± 0.0037	0.1312 ± 0.0037
d	0.0014 ± 0.0001	0.0013 ± 0.0001	0.0013 ± 0.0001

6.1.4 Friction and Wear Response

The wear volume (W) of both HCs were obtained using a stylus surface profiler (Taylor Hobson Form 50, AMETEK, PA) and were compared with the hybrid hydrogel. The effect of normal load variation on material loss under "dry" and "lubricated" conditions are illustrated in Fig. 6.5 (a) and (b), respectively. In general, under the "dry" situation, W increased with higher loads, although the rate was not similar among all studied samples. However, no similar trend was observed under the lubricated condition, in which W was flat to falling as the applied normal load increased. Nevertheless, it could be clearly seen that fibre-reinforcement has greatly affected the wear-resistance of the hydrogel matrix, regardless of external lubrication. Under the lowest load, a less visible difference was observed between the hydrogel and HCs, and as the load increased, the reinforced samples displayed better tribological performance. With no lubrication, wear of HC specimens was found on average 69% and 72.8% less than the hybrid hydrogel at 0.5 N and 0.7 N loads, respectively, while under lubrication those values were determined as 83.5% and 94.8% less, respectively, all indicating promising results.

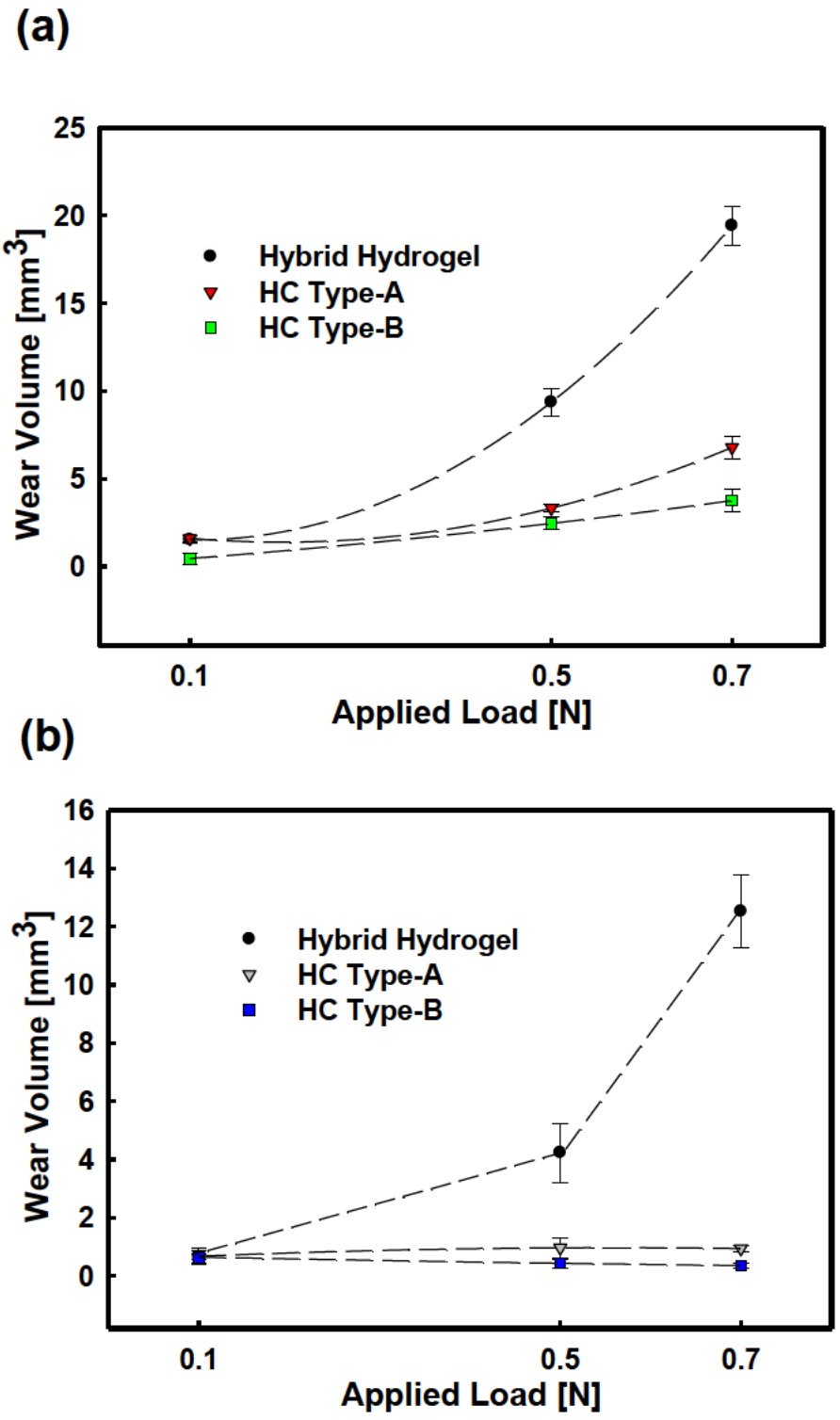

Figure 6.5 *Wear volume (mm^3) with regard to normal load for both types of HCs and the comparison with the hybrid hydrogel (mean (n=3) ±SD) under (a) "dry", (b) "lubricated" contact conditions; (v= 100 mm/s); (dashed lines were plotted using nonlinear regression except for the hybrid hydrogel in (b))*

Another factor affecting the wear rate was sliding speed, of which the results are illustrated in Fig. 6.6 (a), and (b) for “dry” and “lubricated” test conditions. Clearly a trend was observed across the range of tested materials, suggesting with the higher slip rate, W falls, especially for the hybrid hydrogel. Across the range of tested sliding velocities, HCs demonstrated significantly higher wear-resistance, compared to the unreinforced hydrogel matrix, with HC Type-B displaying a slightly lower wear rate compared to HC Type-A, specifically at lower speeds. The lowest wear volume obtained was 0.275 ± 0.12 mm^3 related to HC Type-B tested under a sliding speed of 150 mm/s in the presence of lubricant. This is approximately an order of magnitude lower than that of the hybrid hydrogel, suggesting the fibre reinforcement as an efficient wear-resistance mechanism.

Coefficient of friction over time was recorded by the tribometer during each test and the mean value was obtained by data processing. In general, under the dry test condition, CoF increased gradually with time for HC Type-B, while it decreased for HC Type-A. However, under lubrication, CoF values tended to fluctuate constantly about fixed values during the entire test duration. The variation of mean CoF versus normal loads and sliding velocities are illustrated in Fig. 6.7 (a) and (b), respectively for all studied materials in “dry” and “lubricated” contact conditions. As shown in Fig. 6.7 (a), under “dry” condition, the CoF values for HCs were lower compared to those of the hybrid hydrogel, while a trend was observed for all materials, suggesting CoF decreased with higher loads. Overall, HC Type-A demonstrated the lowest friction level under “dry” condition. However, with the application of boundary layer bovine serum at the sliding interface, friction was dramatically decreased as a result of effective asperity separation. It was found that under lubrication, for most cases, the friction values were slightly higher for the HCs compared to the hydrogel, with the highest level was observed for HC Type-

B (tested under 0.7N load) with 0.033 compared to 0.01 of the hydrogel. The lowest CoF obtained in Fig. 6.7 (a) was 0.012 for HC Type-B under 0.5N load and with lubrication.

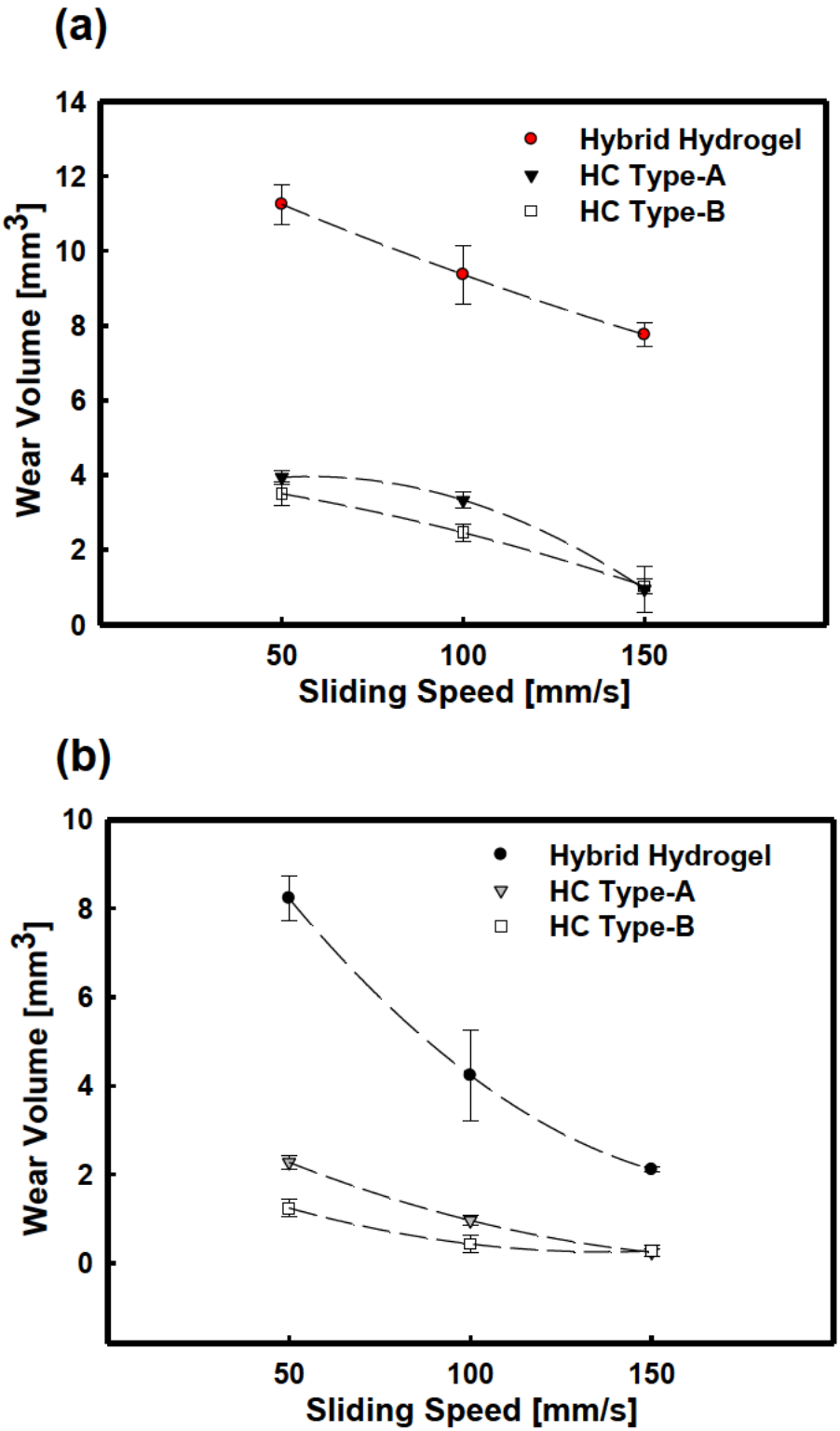

Figure 6.6 Wear volume (mm^3) with regard to varying slip rate for both types of HCs and the comparison with the hybrid hydrogel (mean (n=3) ±SD) under (a) "dry", (b) "lubricated" contact conditions; (p = 0.5N); (dashed lines were plotted using nonlinear regression)

CoF remained constant or slightly increased with the sliding speed as illustrated in Fig. 6.7 (b) during "dry" test condition, while it generally decreased during "lubricated" tests, except for HC Type-B. The lowest value of CoF was measured as 0.0046 found to be relatively close to that of articular cartilage of 0.001.

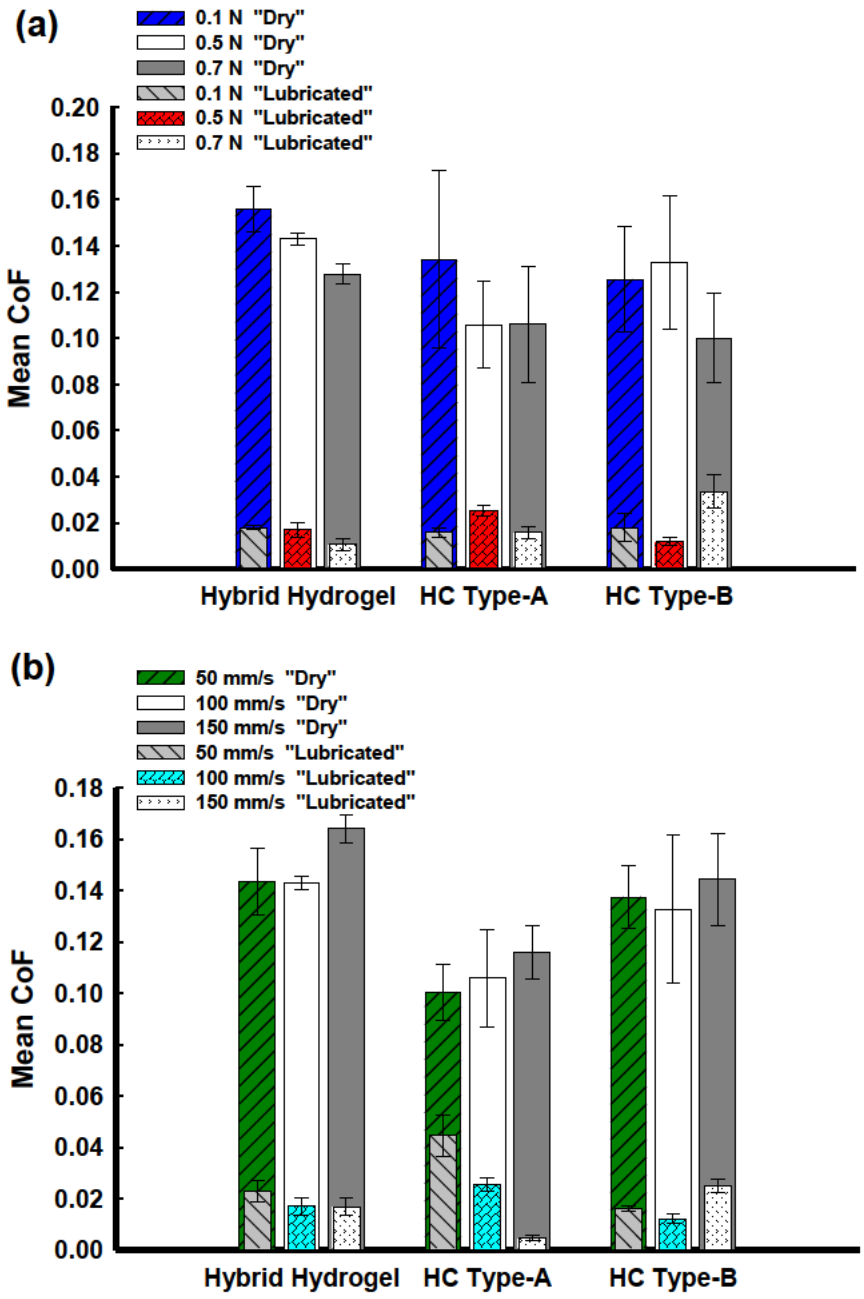

Figure 6.7 Mean CoF (n = 3 ±SD) recorded for different studied materials with/without bovine serum lubricant under (a) different normal loads (v= 100 mm/s), and (b) different sliding velocities (p = 0.5N).

The surface topography of each tested material is illustrated in Fig. 6.8 (a), obtained by the optical imaging module of the tribometer. The arithmetic roughness (R_a) was determined as an average of several lines drawn in diagonal, transverse and longitudinal directions. Comparing the R_a values revealed higher surface roughness for both HCs, compared to the hybrid hydrogel, which was also observed from the surface morphology. The optical and 3D profiles of wear tracks for each hydrated sample were captured immediately after the test and the results for the highest load and lowest sliding speed are illustrated in Fig. 6.8 (b) and (c), respectively, under "lubricated" contact condition. Significant surface deformation was generated in the hybrid hydrogel compared to the HCs, as could be seen from Fig. 6.8 (b) with a wider wear scar. It is worth mentioning that while some levels of damage were visually inspected on the surface of the hybrid hydrogel, the wear tracks on HCs were barely noticeable by the naked eye and magnification was required to detect surface deformation due to the sliding motion, as seen in Fig. 6.8 (b) and (c). In contrast, more visible surface deformations with different intensities were observed during "dry" tests, especially for those undergoing the highest load and the lowest speed. While the wear scar size was realised as larger for the hybrid hydrogel samples compared to HC as reflected in W values of Fig. 6.5 and Fig. 6.6, binder fibre pull-out and top hydrogel layer removal was observed for the reinforced HCs and less severe in the case of HC Type-B. However, no sign of woven fabric wear was found for the range of sliding distances applied in this study. The actual images of typical surface damage are illustrated in Fig. 6.9. In Fig. 6.9 (a), hydrogel removal and matrix-fibre debonding were observed as the dominant signs of damage for Type-A, while as shown in Fig. 6.9 (b), a typical wear scar comparable to those reported previously in NCH samples was observed in Type-B samples.

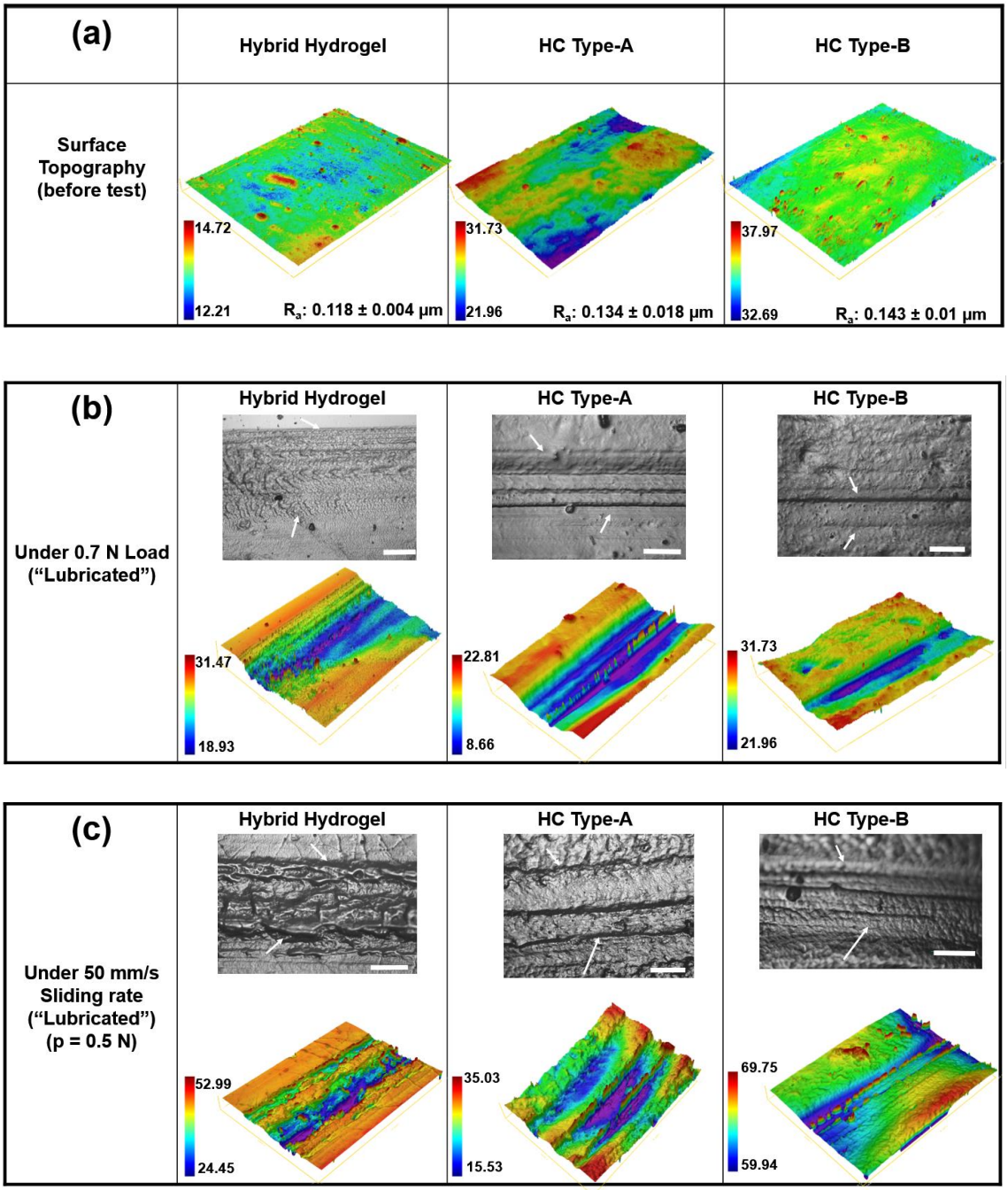

Figure 6.8 *Surface topography of the studied materials with 20X magnification (a) before wear tests and after, under (b) 0.7N load (v= 100 mm/s), and (c) 50 mm/s (p=0.5 N). The white arrows show the wear scar region. All scale bars are 100 µm.*

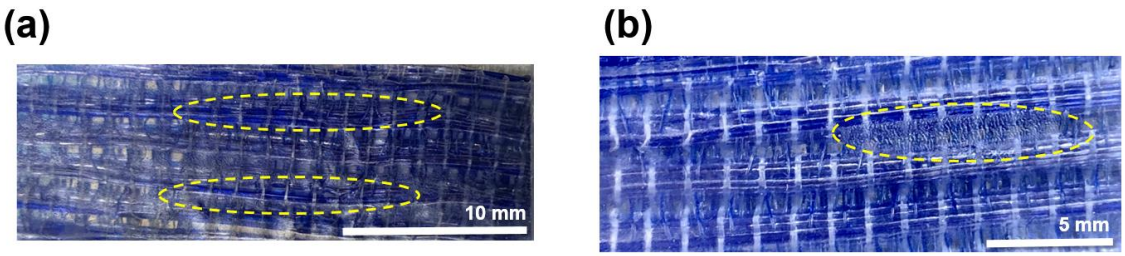

Figure 6.9 *Surface damage observed on HC samples after the sliding wear tests under "dry" contact condition, (0.7N load); (a) Type-A, (b) Type-B*

6.2 Discussion

The mechanical and tribological performance of fibre-reinforced hydrogel composites were investigated in this study to assess them as a prosthetic biomaterial for articular cartilage repair. The 3D woven textiles were produced through an innovative method, inspired by cartilage tissue, with through-the-thickness stiffness gradient allowing both resilience and strength in addition to anisotropic properties, similar to biological tissues. This anisotropy further allows a high tensile and low bending stiffness, beneficial for a biomimetic structure [156]. Two distinct woven structures were successfully produced followed by uniform infiltration of ALG-PAAm hybrid hydrogel, as previously investigated for cartilage replacement applications, resulting in a fibrous hydrogel composite. The hybrid type was preferred over single network hydrogel as a previous study has found the elastic modulus of HC would be significantly improved when the scaffold was infiltrated by the hybrid hydrogel [51].

Based on the findings, HCs demonstrated superior performance compared to un-reinforced hydrogel during indentation and compression tests. Under compression, HCs significantly outperformed the matrix and woven textile combined, suggesting a strong synergistic effect, which was also observed and investigated in a recent study [157]. The woven scaffolds failed once the compressive strain exceeded 0.4, while the HC could sustain a higher strain level with no sign of failure, thanks to the energy-dissipative mechanism of ALG hydrogel and shape-recovery feature available in PAAm component [32, 49]. These findings suggest that strong interaction exists between the fibre phase and the hydrogel matrix, also reported by a previous study [51]. Robust interfacial bonding between fibres and the matrix is essential for the load to be transferred to the matrix, resulting in matrix load-sharing and energy dissipation, in addition to a more evenly stress distribution, all leading to a more efficient mechanical response. Interestingly, even in the

case of poor fibre-matrix bonding, the fibre phase might act as an energy dissipating mechanism when pulling out of the hydrogel matrix, and this would positively affect the toughness. It was found that the HC toughness was correlated to hydrogel matrix toughness, and synergistic effect in mechanical performance could be achieved by utilising tough hydrogels and the presence of strong interfacial fibre-matrix bonding [157]. It was also discovered that the fibre-reinforcement could contribute to the improvement of strain-rate dependency, an important characteristic that enables the articular cartilage to properly function once various loads and articulation velocities exert on the joint, during physical activities [52]. The indentation study revealed the loading-unloading responses of anisotropic HCs were different to an isotropic hybrid hydrogel, with the significant improvement in mechanical response of HCs as a result of the fibre-matrix interaction. Upon the recorded force reaching zero, relatively small irreversible deformation was observed in both kinds of HCs, which could be attributed to dislocation of tows beneath the spherical indenter, leading to weave compaction. Interestingly, similar loading-unloading curves were reported in a previous study for HCs [51]. It should be noted that the same strain level used during indentation test was applied to the model developed for the prediction of the compressive modulus, resulting in fairly similar values for the moduli, therefore the model predicting the compressive behaviour was validated. The compressive modulus was found in the range of 0.59-7.3 MPa for HC Type-A and 0.86-10.93 MPa for HC Type-B comparable to that of articular cartilage of 0.4-10 MPa [66].

The time-dependent behaviour of HCs was studied and the parameters of the viscoelastic model were determined in this study. It was found that the degree of viscoelasticity could be enhanced by incorporating fibre reinforcements, while the effect of the weave pattern was less significant. Some fluctuations were observed in the long-term relative stress-time response of HCs, depending on the weave-pattern. This is

attributed to various levels of stress relaxation experienced by individual fibres in the warp, weft and binder directions, as well as distinct layers with various fibre sizes in the woven structure. The stress relaxation level also depends on the interstitial fluid flow, and more relaxation of HCs compared to un-reinforced hydrogels could be explained by a higher degree of flow mobility inside the open-celled HC compared to the micro-scale pores observed in the studied hydrogel. Submersion of the HC samples as well as the hydrogels with identical dimensions in DI water and swelling ratio comparison revealed that the HC samples could absorb higher fluid level as compared to IPN hydrogel samples. This can be attributed to the water retention capacity of the woven reinforcement. The water retained in the fibres will be released to the surrounding hydrogel, when under pressure, leading to an enhanced flow of interstitial fluid due to an increased fluid pressure gradient. Zhou and Wu [280] also observed that a higher swelling ratio correlates to larger pores exist in HC, which in turn facilitate the interstitial fluid flow once the structure is subjected to a deformation. Larger pores because of fibre reinforcement was also reported in another study carried out by Yodmuang et al [281]. Furthermore, the morphology of pores would be different near the woven fibres, due to the localised nonhomogeneity caused by the fibres. Therefore, the pore structure would be different in HCs compared to IPN hydrogels, which in turn affects the fluid flow.

It was also found that the infusion of hybrid hydrogel improved the surface roughness of the woven structure, consistent with the findings of a previous study [51], while the R_a value for HCs were slightly larger than the hydrogel. Due to anisotropy, dissimilar mechanical performance was observed in the warp direction as compared to the weft direction. Therefore, regarding the tribology tests, the HC samples were mounted such that reciprocating sliding motion was performed along the stronger warp yarns. Wear tests revealed the dependency of the wear rate to the applied load between all tested materials, while the effect of fibre reinforcement on wear-resistance boost was

significantly felt at higher loads. As for the lowest load level, it is assumed the majority of the shear force due to sliding was exerted on the hydrated layer of the hydrogel matrix at the mating interface and absorbed by it, therefore the fibre phase could not effectively contribute to the load sharing, leading to a wear rate similar to the un-reinforced hydrogel. The wear volume was decreased by increasing the sliding velocity, which could be attributed to a more efficient lubrication of the interface by the hydrated layer achieved with a higher reciprocating sliding rate, whereas the dehydration and higher level of asperity shear at the lowest speed accounted for an increase in wear rate. Wear track inspection of the samples under "dry" sliding tests, revealed different levels of surface damage, due to various levels of cross-shear caused by the reciprocal motion of the ceramic ball and the damage was larger wherever the cross-shear reached a peak value. Low CoF was observed for ALG-PAAm hydrogels sliding against a solid smooth countersurface in a previous study, attributing to a strong repulsive charge present at the interface, promoting water layer retention [268]. This phenomenon occurs more effectively at higher loads. Therefore, CoF decreased with higher applied loads as illustrated in Fig. 6.7 (a). CoF values were also decreased by increasing the sliding speed due to the hydrodynamic nature of non-adhesive hydrogels, consistent with the findings of a previous research [268]. In the presence of bovine serum lubricant, CoF values for HCs were generally found slightly higher than hybrid hydrogel. This could be attributed to the possible change in film thickness as a result of the lubricant adsorption by the relatively large-sized porous medium of woven textile incorporated in the hydrogel matrix, which could adversely affect the lubrication regime and hence increase the friction. Previously, researchers had discovered for metal-on-metal interfaces the effect of proteins in the external lubricant could be beneficial in lowering the CoF through proteins adhering to metallic surfaces and providing a boundary lubrication mechanism, whereas for ceramics, the proteins could increase friction levels by transforming the

lubrication regime from fluid film to mixed mode [282, 283]. Regarding the hydrogel materials, a lower CoF was obtained with synovial fluid containing less protein as compared to bovine serum with a higher protein content [28]. Thus, a lower friction level could be achieved once the countersurface was selected from permeable, biphasic cartilage rather than dense alumina, and the synovial fluid acting as lubricant, instead of bovine serum.

Based on the results presented here and in the previous chapter, it is worth comparing the impact of fibre reinforcement (HCs), and nano-particle addition (NCHs), on friction level and wear resistance degree of ALG-PAAm hydrogel. Clearly, the wear resistance was improved by either of reinforcement methods, as mentioned previously. Overall, higher wear resistance was achieved with fibre reinforcement, compared to nano-particle reinforcement, especially under lubrication. Concerning friction, the reported CoF values under dry sliding conditions, and with varying load and speed, were fairly close for both HCs and NCHs, with HC Type-A demonstrating the lowest friction levels. With lubrication, friction levels were reported lower for NCHs, especially at the highest load.

6.3 Conclusions

The mechanical and tribological characteristics of hydrogel composites with two distinct 3D woven reinforcement patterns were investigated and compared with an un-reinforced ALG-PAAm hybrid hydrogel for use in cartilage replacement applications. In previous studies, the same yarn size was used for weaving the whole textile. For the very first time, the woven textiles were designed and fabricated in this study in a way to benefit from a stiffness gradient along the thickness, similar to the human articular cartilage, while the 3D structure was utilised to provide damage-tolerance and delamination-resistance to the hydrogel matrix.

The findings confirmed an improved non-linear stress-strain response, anisotropy and enhanced time-dependent stress relaxation, along with a strain-rate dependency due to the incorporation of polymer weave into the hydrogel matrix. These are the requirements for biomaterials to be considered as a potential cartilage replacement candidate. Analysis of surface roughness values before wear tests revealed that infiltration of hydrogel into the woven structure contributed to achieving a much lower surface roughness, when compared with those of neat textiles. In addition, load-to-failure capacity of neat textiles were improved as a result of hydrogel infiltration. Moreover, wear-resistance of the hydrogel matrix was greatly improved under the range of applied loads and sliding velocities. These promising results can be attributed to the synergistic interaction between the fibre phase and the hydrogel matrix. Overall, the HC Type-B demonstrated the best mechanical and tribological performance among other studied materials and is therefore selected for further research. The composites developed in this study possess mechanical anisotropy and a stiffness gradient through the thickness, achieved by using different types of fibres with different diameters woven through the thickness of the textile. A future study should investigate the friction and wear behaviour of the HCs under more realistic sliding motions such as butterfly sliding and under body temperature. Moreover, fatigue and impact tests could be carried out to characterise the structural response to dynamic loading, as well as implantation into living creatures to study the synthetic cartilage interaction with the neighbouring tissue.

Chapter 7

FINITE ELEMENT ANALYSIS OF SLIDING WEAR IN 3D TEXTILE HYDROGEL COMPOSITES

7.1 FEA of 3D Woven Textile Unit Cells

The experimental results were presented and discussed in previous chapters. Numerical modelling and analysis of sliding wear of 3D textile unit cells and different types of HCs are focused in the current chapter. The mechanical properties obtained for the hydrogel matrix and polymer fibres in the previous chapters were used as an input for FE modelling. The numerical results were compared with the experimental data for model validation. Parametric studies on the validated model were then conducted to predict wear rates for the conditions that were not investigated experimentally. FEA of HC unit cells also gives an insight into the stress distributions in the textile as the dominant load bearing constituent, once the unit cell is subjected to compressive loads. These results are used for comparison between two types of weave patterns, which will be discussed in section 7.2.2.

7.1.1 Mesh Convergence Study

For the mesh convergence analysis, element size on the binder yarns contact region with blocks, was altered iteratively to study its effect on contact pressure. Accurate prediction of contact pressure is essential for the accuracy of wear depth calculated by the subroutine. The results from mesh convergence study were plotted and shown in Fig. 7.1, which indicates when the number of elements reached 19,200 with the element size of

0.0195, the calculated contact pressure will not change remarkably with finer mesh. Therefore, to reduce computational expenses without accuracy compromise, this element size was chosen for the FE model.

7.1.2 Model validation and FE results

Following the procedure described in section 3.4, the experimental data was acquired from accelerated wear tests of PET woven fabric with cobalt chromium pin as shown in Fig. 7.2 . Change in mass of immersed control sample was recorded, and was deducted from change in mass of test samples. Then, the mass loss was converted to volume loss (wear volume) using PET density, and by dividing the values by contact area, wear depth data were obtained and plotted as can be seen in Fig. 7.2 . Experimental results showed an almost linear trend in wear depth evolution as the test progressed and a wear coefficient of 6.084E-08 [mm^3/N.mm] was determined from the experiments. The test stopped after 9.45E+05 cycles as the fabric top layer worn excessively (see [48]). Wear depth computed from the FE model is plotted in Fig. 7.2 as well and a good correlation between numerical and experimental results can be observed. As illustrated in Fig. 7.2, the experimental and FEM results are showing excellent correlation at lower cycles and as the number of cycles increases, FEM tends to predict higher wear depth, however the difference is not significant. It should be noted that FE model was developed for 10 cycles only and the obtained numerical results were then extrapolated using the developed wear subroutine explained previously in section 3.4.2.

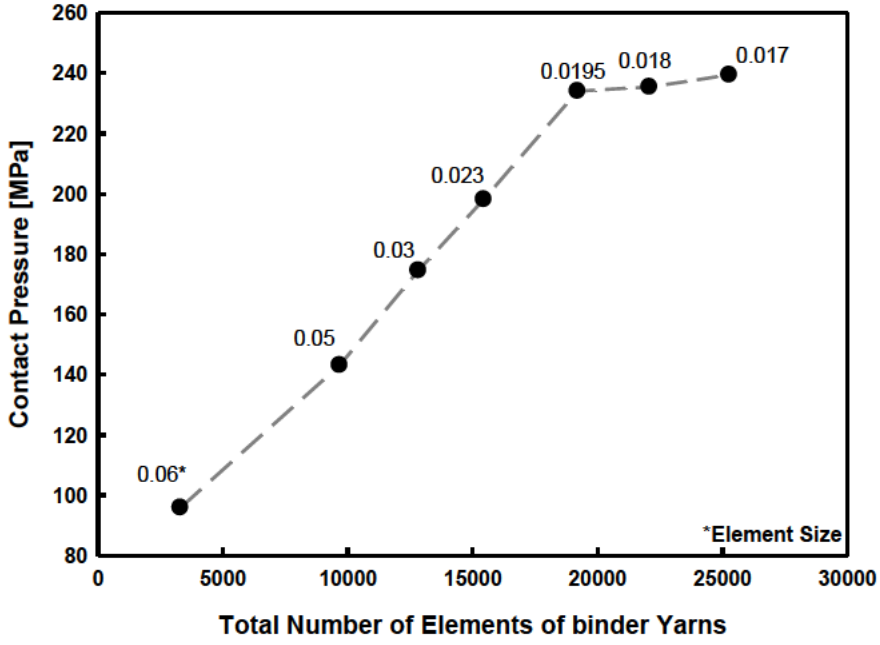

Figure 7.1 Mesh convergence study

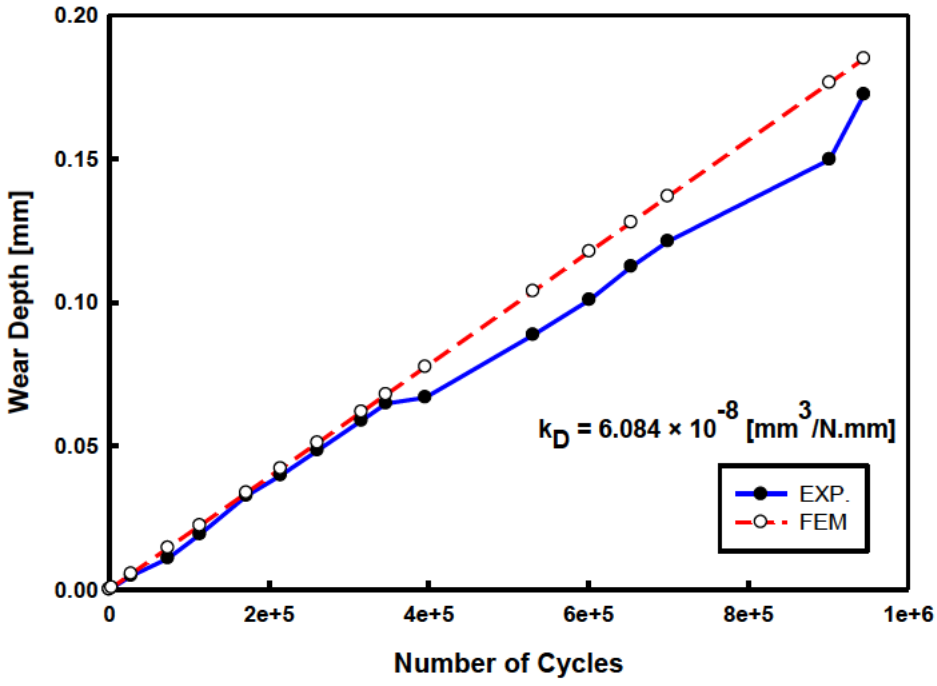

Figure 7.2 Comparison of wear depths obtained from experiments and FE simulation

Original nodal coordinates of the binder cross-section together with wear profile evolution is depicted in Fig. 7.3, which are extracted from FE simulations at different wear cycles. The figure clearly shows higher wear depths as the number of cycles

increases. At the end of the simulation, after 9.45E+05 cycles, only a minor portion of the binder was left and the majority of the cross-section was worn out.

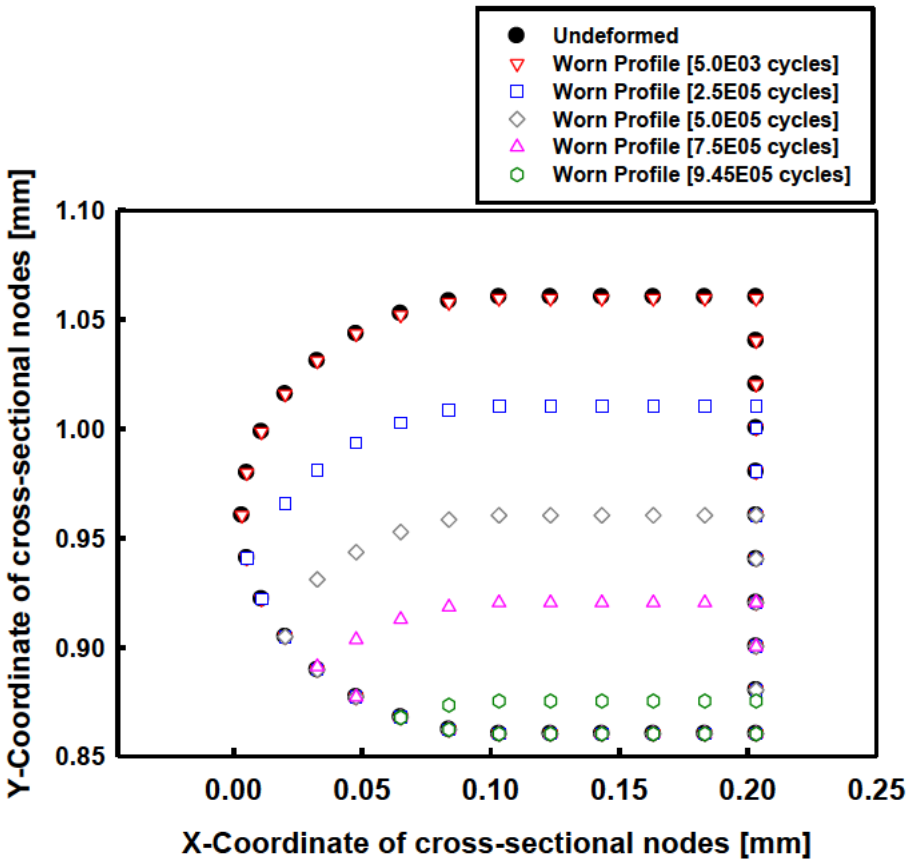

Figure 7.3 Evolution of cross-sectional profile of binder tow due to wear

Vertical nodal displacement contour of the binder yarns, together with the worn surface is visualized in Figure 7.4 (a). The coordinates of the nodes affected by sliding wear were changed based on Archard's wear law and the model was updated at every time increment by using the Fortran-based subroutine linked with the FE solver. Worn surface shown in Figure 7.5 (a) is after 3.06E+03 cycles which resulted in a wear depth of 6E-04 mm and magnification must be implemented for better visualization. As can be seen from the results, the developed FORTRAN subroutine was able to compute wear depth and perform extrapolation, which consequently, led to nodal displacement due to adaptive mesh and geometry update. The undeformed and deformed shapes of a binder yarn are depicted in Figure 7.5 (b) and Figure 7.5 (c), respectively. Contact pressure and

sliding distance were determined during the simulation for the surface nodes and the deformed shape was obtained at the end of each increment.

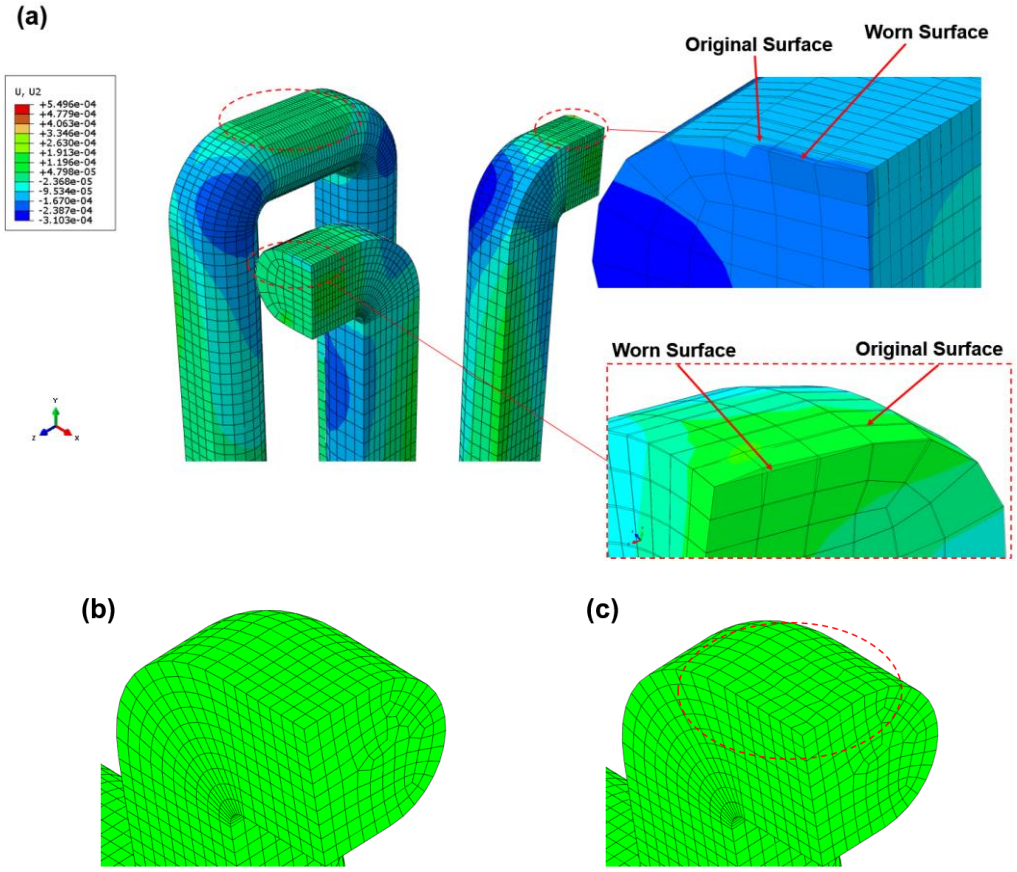

Figure 7.4 *(a) Vertical displacement contour of binder yarns with geometry updated by subroutine; overlaying of original and worn surface, (b) undeformed, and (c) deformed (worn) surface*

7.1.3 Parametric Studies

In order to explore the effect of various parameters on wear rate of 3D textile fabrics, a parametric study was conducted and the results are summarised in this section. All simulations were run for 530,000 cycles to predict wear depth. Applied pressures varied from 0.5 to 2 MPa, based on the recommended range that is tolerated by the knee joint during each gait cycle [249], and the results are shown in Figure 7.5 (a). As illustrated in the figure, wear generation is proportional to applied load and increases exponentially at higher pressures. For instance, an increase in applied pressure from 1.65

to 2 MPa (21%) leads to 70% increase in wear depth, while the same level of pressure increase from 1 to 1.2 MPa (20%), resulted in only 34% increase in wear depth.

Sliding speed is another parameter that affects the wear properties of fabrics. As illustrated in Figure 7.5 (b), wear depth increases linearly when the upper block moved against the fabric with different velocities. This can be interpreted as running might be much more detrimental for an orthopaedic implant than walking, as the sliding speed is higher in running.

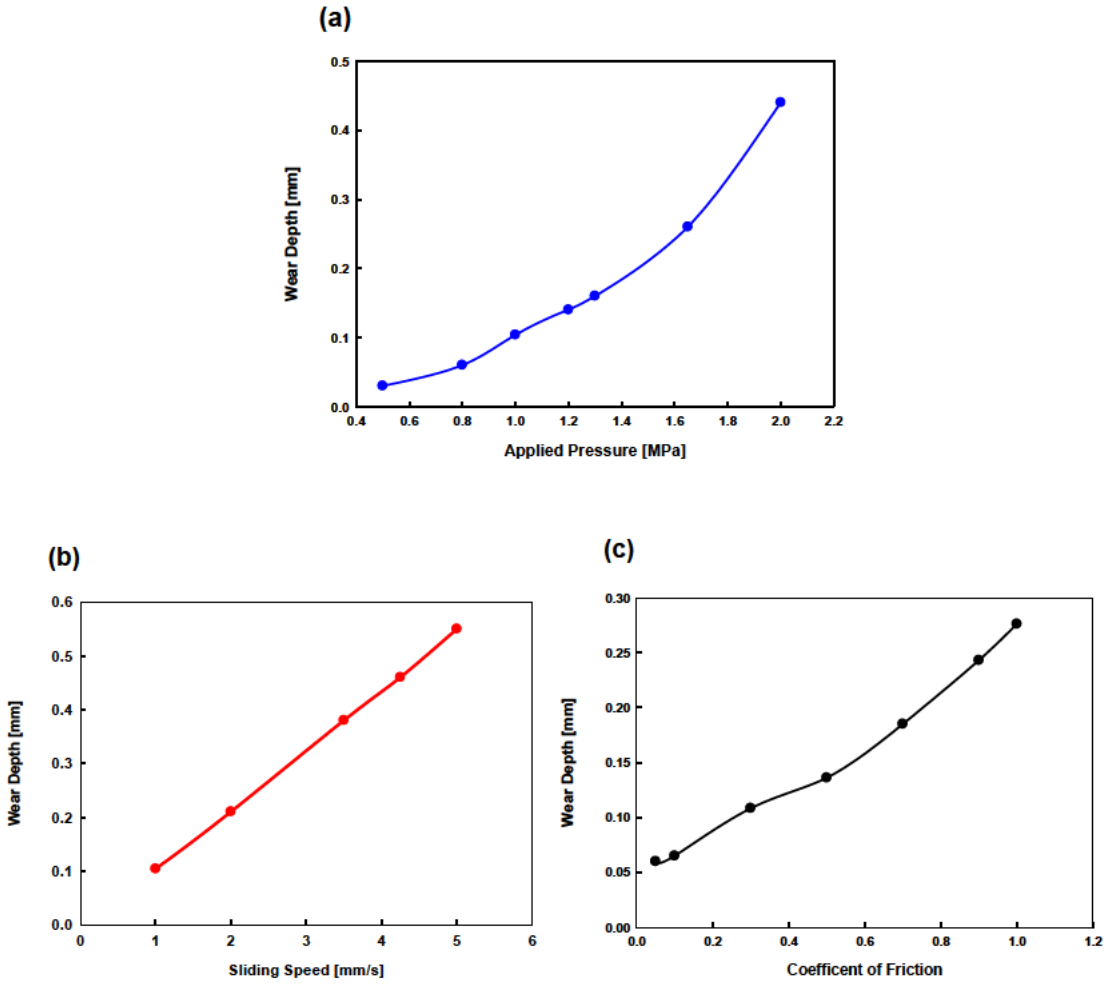

Figure 7.5 Variation of wear depth with the change in (a) applied pressure, (b) sliding speed, and (c) coefficient of friction; in each case all other parameters were fixed.

Coefficient of friction was also changed in the range of 0.05-1 to take into account the effect of lubrication and other environmental conditions that might affect the contact

condition and so the wear rate. Figure 7.5 (c), shows the similar trend in wear rate increase as observed in wear depth vs applied load plot (Figure 7.5 (a)), although applied load had a greater impact on wear depth of the textile. At higher friction coefficients, a slightly higher wear rate can be observed from the figure. This shows the significance of lubrication, which decreases the coefficient of friction by separation of asperities of contact pair.

7.2 FEA of Fibre-Reinforced Hydrogel Composites

Finite element modelling and data analysis were presented in previous sections, based on 3D woven orthogonal PET textiles and experimental set-up, proposed by Giordano and Schmid [182]. In the following sections, FE analysis of the sliding wear of unit cells associated with two patterns of the 3D woven textiles developed in this study and infused by ALG-PAAm hydrogel will be presented and discussed.

7.2.1 Mesh Sensitivity Study

Element size for the matrices of the unit cells were changed in size iteratively in an attempt to eliminate the mesh size dependency of computations. The top layer of each matrix was focused and maximum contact pressure (CPRESS) because of uniaxial compression was computed as a function of element size, as shown in Fig. 7.6. It can be seen that no significant deviation in contact pressure was occurred, when the elements were generated in the size range of 0.02~0.08 for Type-A, and 0.02~0.04 for Type-B woven fabrics. Therefore, the matrices were discretised with the aforementioned element sizes, with the finer mesh allocated to the contact regions.

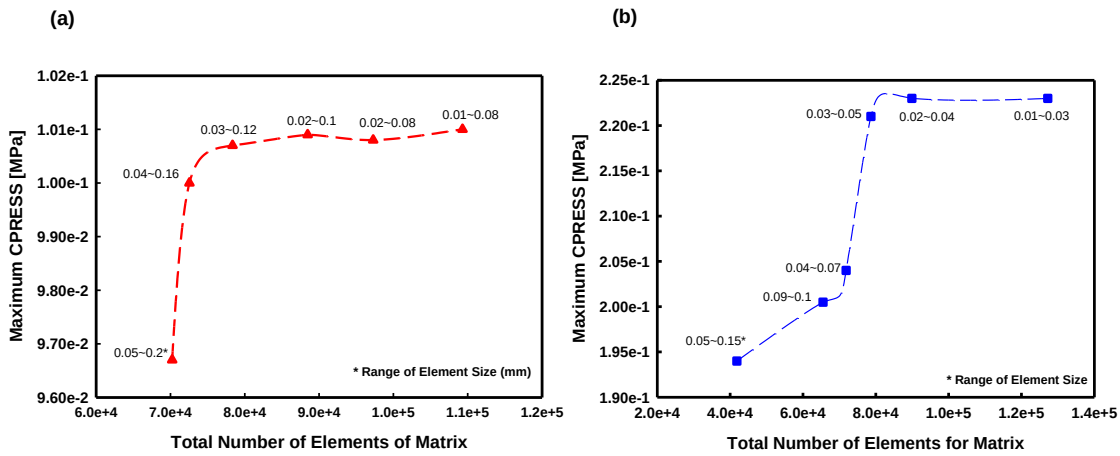

Figure 7.6 Mesh convergence study for (a) HC Type-A, (b) HC Type-B matrices

7.2.2 Comparison of FEM with Experimental Results

The wear depth values were computed from linear extrapolation of initial surface ablation after certain number of cycles were accomplished. The comparison between obtained values from experiments (EXP) and finite element method (FEM) are presented in Figs. 7.7 and 7.8 for HC Type-A, and HC Type-B unit cells, respectively. A unit cell of hydrogel matrix without reinforcement was also modelled following the same procedure described for HC unit cells, and the results are illustrated in below figures and are compared with experimental data. Overall, it was observed a fairly good correlation between experimental and numerical data, despite the assumptions and simplifications made in the FE model to conduct wear simulation successfully. The absolute mean deviation from experimental results were found as 7.19% ±21.7%, 15.33% ±29.3%, and 14.9% ±13% for HC Type-A, HC Type-B, and the hydrogel matrix (i.e. non-reinforced hydrogel) unit cells, respectively. In addition, monitoring maximum contact pressure corresponding to minimum and maximum applied loads, for both unit cells revealed these values were comparable with corresponding values measured in the experiments.

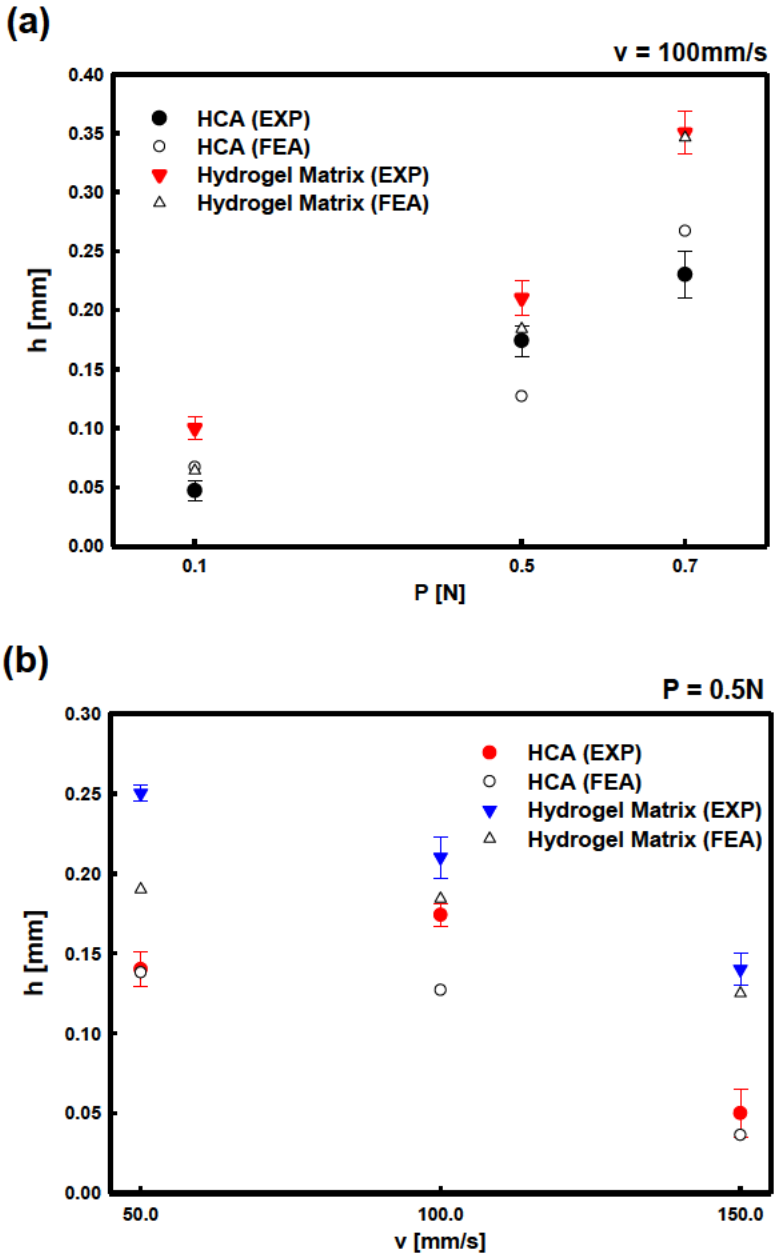

Figure 7.7 *Comparison of wear depth (h) between experimental (EXP) and numerical (FEA) (results for HC Type-A and Hydrogel unit cells with respect to (a) applied load (v= constant), (b) sliding rate (P= constant) For the experiments n=3±SD.*

Consistent with experimental observations, a trend was observed that wear depth increased at higher loads, and decreased at higher speeds among all unit cells used for FE simulations. Fibre reinforcement was found to have a positive impact on hydrogel matrix. Compared to un-reinforced hydrogel unit cell, wear depth was decreased in average by 30% and 31.4% when the matrix was reinforced with Type-A and Type-B textile unit cells, respectively. Compared to HC Type-A, slightly lower wear depth values were

obtained for HC Type-B. Moreover, the effect of load on wear rate was found more significant than changing the sliding rate across all studied unit cells.

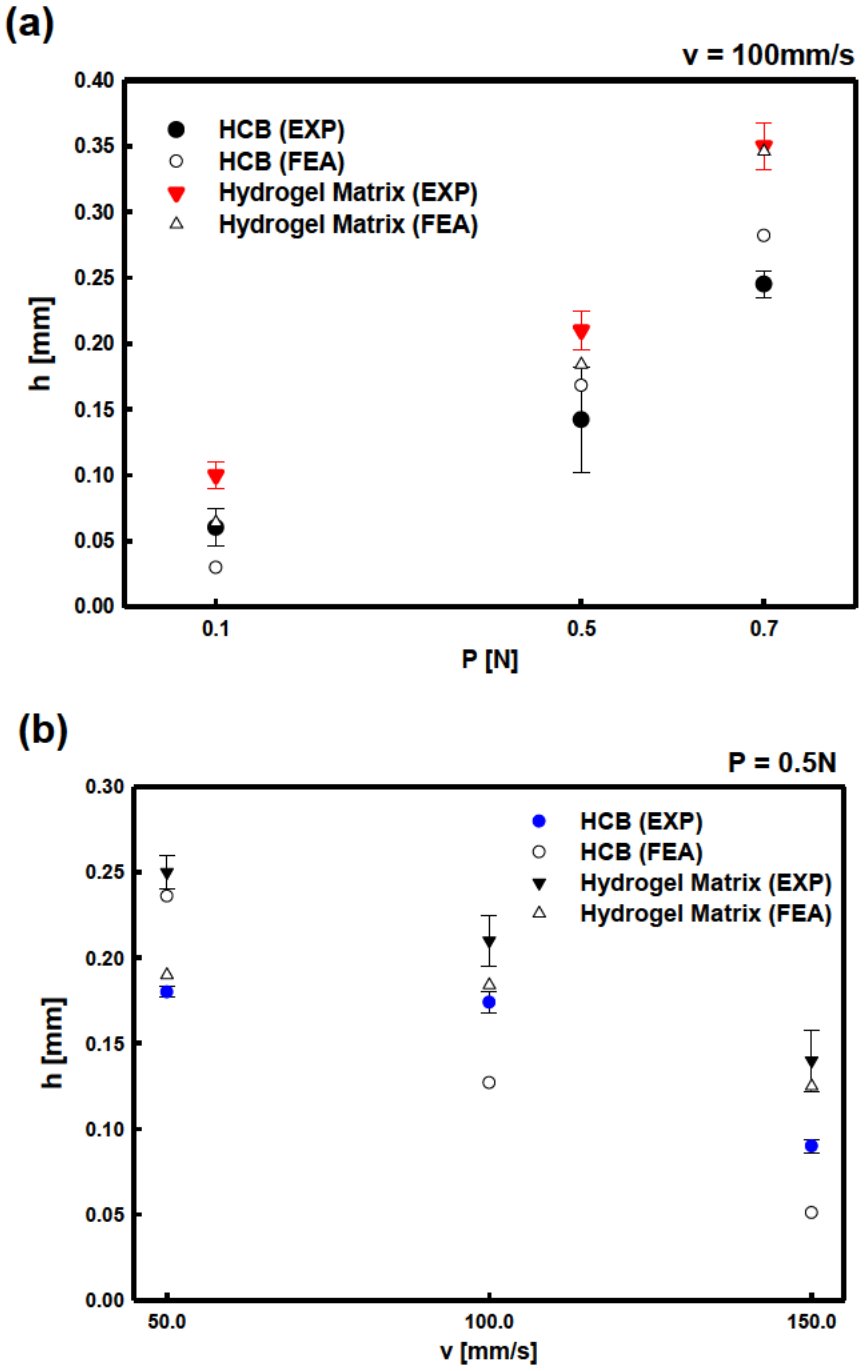

Figure 7.8 Comparison of wear depth (h) between experimental(EXP) and numerical (FEA) results for HC Type-B and hydrogel unit cells under (a) various loads (v= constant), (b) various sliding velocities (P= constant). For the experiments n=3±SD.

The hemispherical ball was made to be separated from its opposing surface at the last step of simulation, prior to node shift was taken place by the subroutine, so that

surface ablation in terms of nodal shifting could be clearly seen. Surface ablation contours due to the sliding motion of ball are illustrated in Figs. 7.9 – 7.12 corresponding to both HCs, under various load and sliding velocity conditions. U2 denotes nodal displacement in y-direction, which was found more significant compared to displacement in the remaining directions. It can be seen that higher contact area was resulted from increase in applied load in Figs. 7.9 and 7.11. Consequently, a larger region with larger number of nodes was affected, and wear depth was increased, as well.

It is worth mentioning the values seen in the colour scale bars do not represent the overall wear depth as plotted in Figs. 7.7 and 7.8, and instead indicating the nodal displacement values, corresponding to the number of sliding cycles prior to linear extrapolation to achieve accelerated wear depth data. The wear depth information could only be acquired from the data file (with .dat format) generated once simulation was successfully done. Moreover, the contact area under the highest load was found not to exceed the width of each unit cell, suggesting the dimensional difference seen in Type-A unit cell compared to Type-B unit cell would not affect the results.

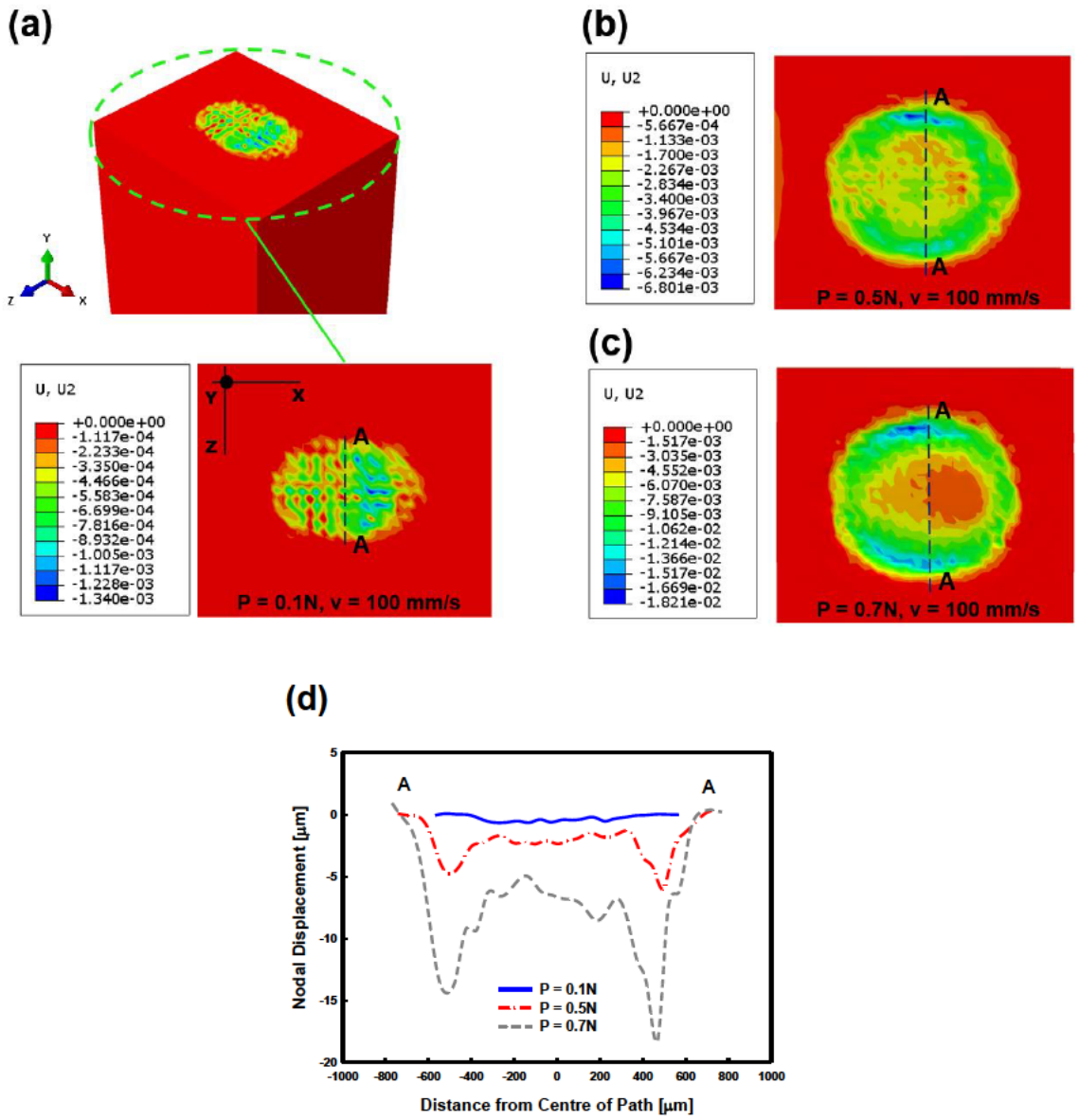

Figure 7.9 Nodal displacement was observed at the contact region of HC Type-A unit cell, after full separation of contact pair with respect to various applied load (a) P = 0.1N, (b) P = 0.5N (c) P = 0.7N, (d) plot of displacement variation as a function of load. Colour bars in mm.

Reduction of sliding velocity led to more surface ablation at the central region of the affected area as can be seen from Figs. 7.10 and 7.12. However, it was observed that change in sliding velocity had less significant impact on surface ablation as compared to change in applied load.

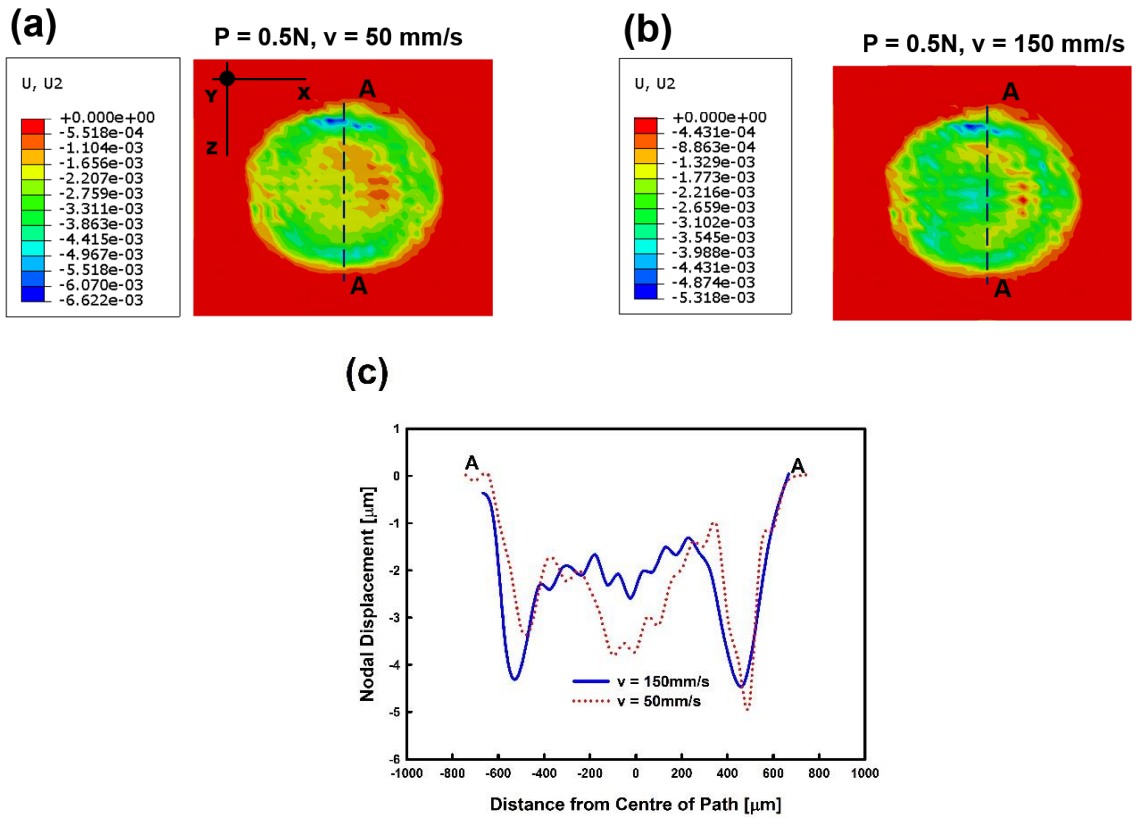

Figure 7.10 *Nodal displacement contours of HC Type-A with regard to (a) 50 mm/s, (b)150 mm/s sliding rates (c) the corresponding values are plotted. Colour bars in mm.*

The displacement values were obtained from output database files and plotted along A-A path, as can be seen in Figs. 7.9 (d), 7.10 (c), 7.11 (d) and 7.12 (c). An increase in load has had an outstanding influence on surface ablation profile of HC type-A (Fig. 7.9 (d)), as compared to HC Type-B unit cell (Fig. 7.11 (d)). Moreover, regardless of load and sliding speed magnitudes, highest level of nodal displacement was frequently observed at the edges of wear track, parallel to the sliding direction. Similar trend was observed from the wear experiments (See Fig. 7.13 (c) and (d), for instance). This could be attributed to relatively higher contact slip levels computed for those nodes, mainly due to the nonuniform contact pressure distribution experienced by the surface nodes located beneath the ball. Ball-on-flat causes nominally a point contact, and less contact pressure would be experienced by those points that are farther away from the centre of contact, suggesting more degree of mobility. The actual images of typical surface damage are

illustrated in Fig. 7.13 together with typical wear scar profiles. The dashed ovals show the wear scar on the surface of HC Type-A (Fig. 7.13 (a)) and HC Type-B (Fig.7.13 (b)).

Contact slip contours or tangential movement of surface during contact, are illustrated in Fig. 7.14 for both unit cell types, and under lowest and highest load levels. As can be seen, the corresponding slip data for central region just under the ball approaches zero, and the absolute value increases as moving farther from the centre towards the edges of contact area. Slip levels increased with load, together with a larger area developed along the contact area width. The subroutine acquires nodal contact pressure and accumulated slip values in each increment for wear geometry evolution, and therefore higher slip values resulted in higher nodal displacement at the edges of contact area.

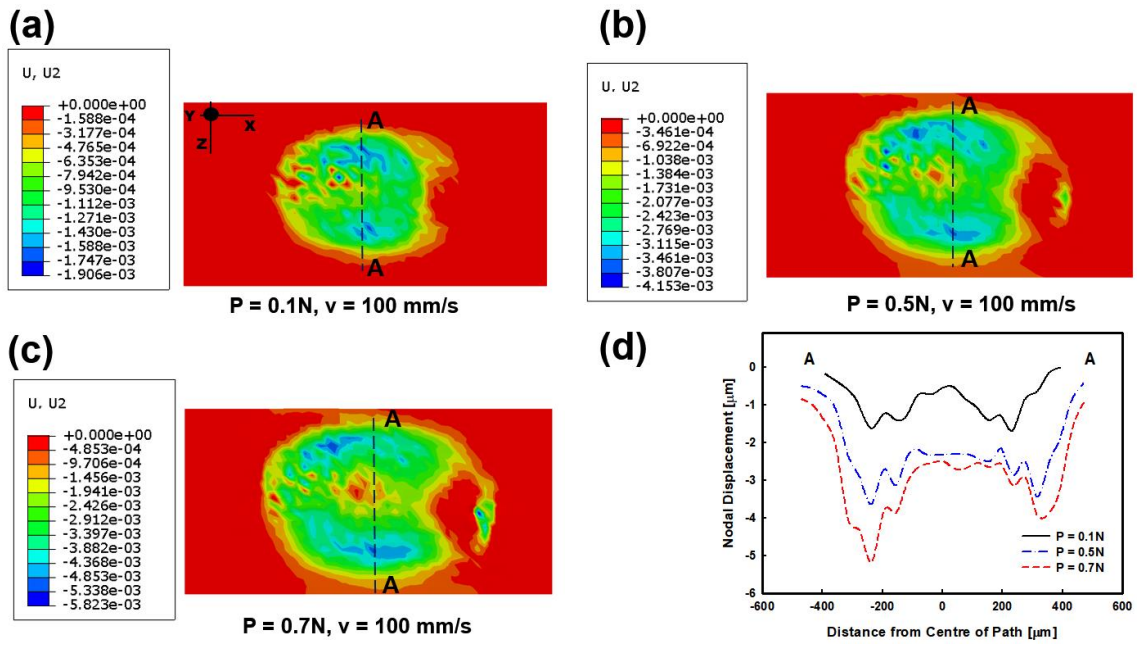

Figure 7.11 Surface ablation contours of HC Type-B at (a) P=0.1N (b) P = 0.5N, (c) P =0.7N, (d) nodal displacement graph. Colour bars in mm.

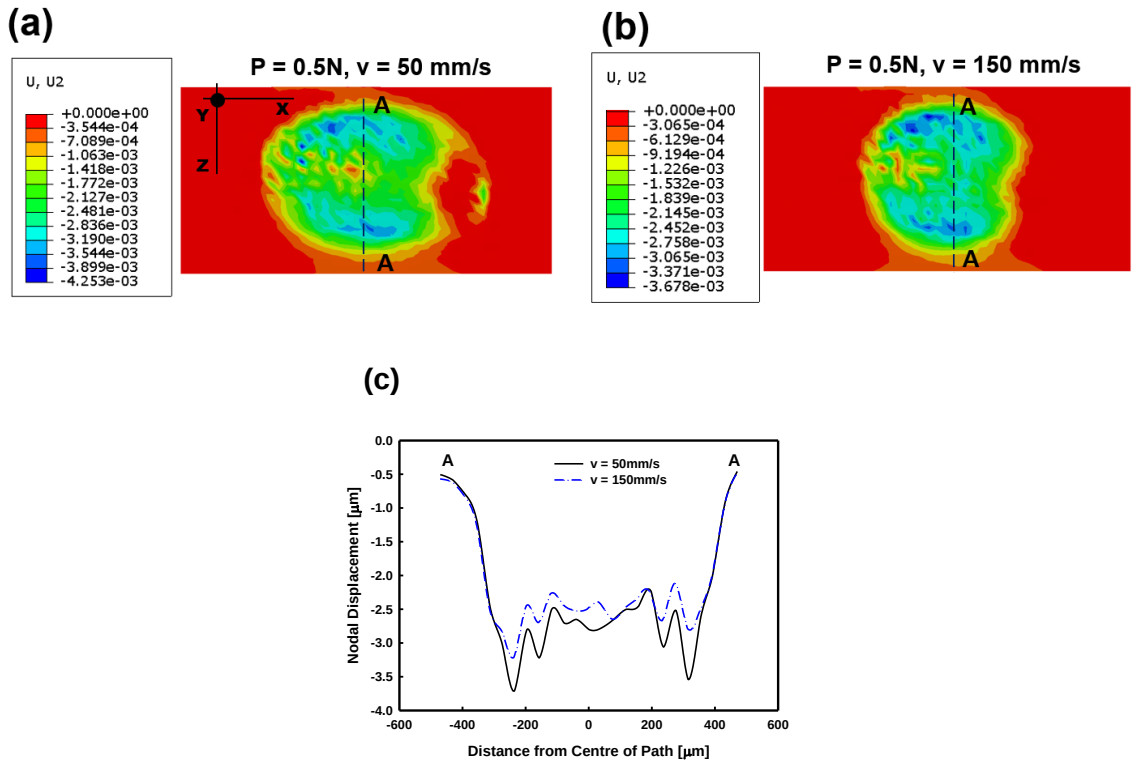

Figure 7.12 *Nodal displacement contours of HC Type-B at (a) 50 mm/s, (b) 150 mm/s sliding rates, (c) the corresponding values were plotted. Colour bars in mm.*

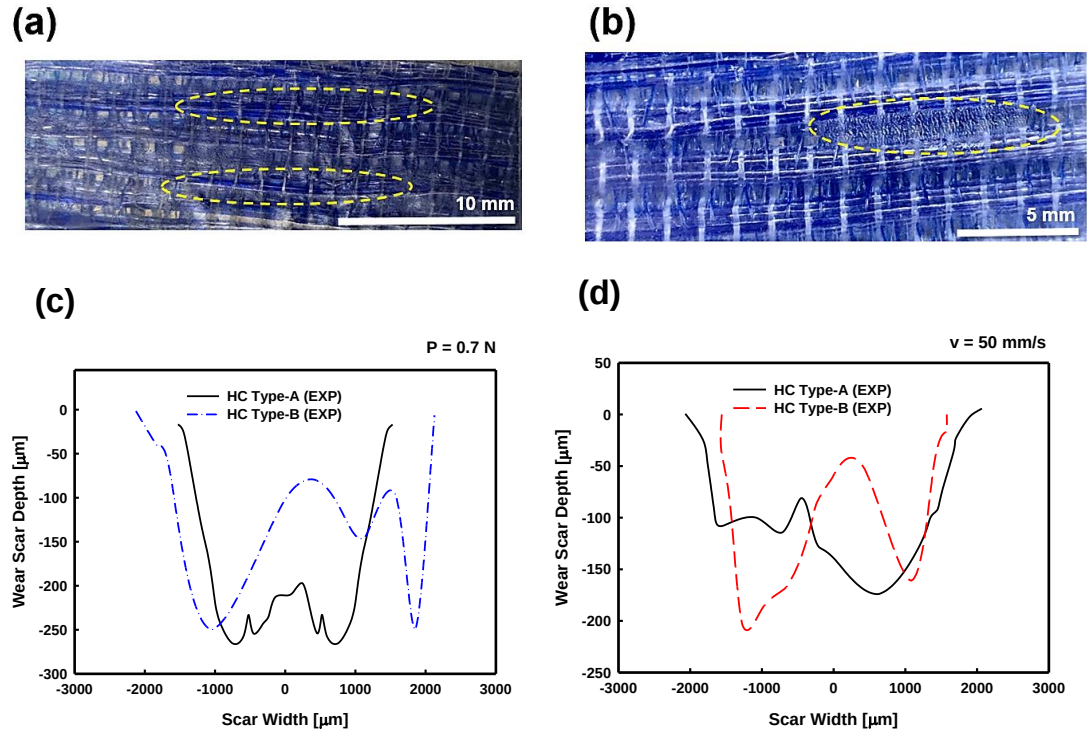

Figure 7.13 *Surface damage observed on HC samples after the sliding wear tests in the absence of external lubrication, (0.7N load); (a) Type-A, (b) Type-B. Comparison of wear scar profile along the scar width under (c) highest applied load, (d) lowest test speed (i.e. longest test duration)*

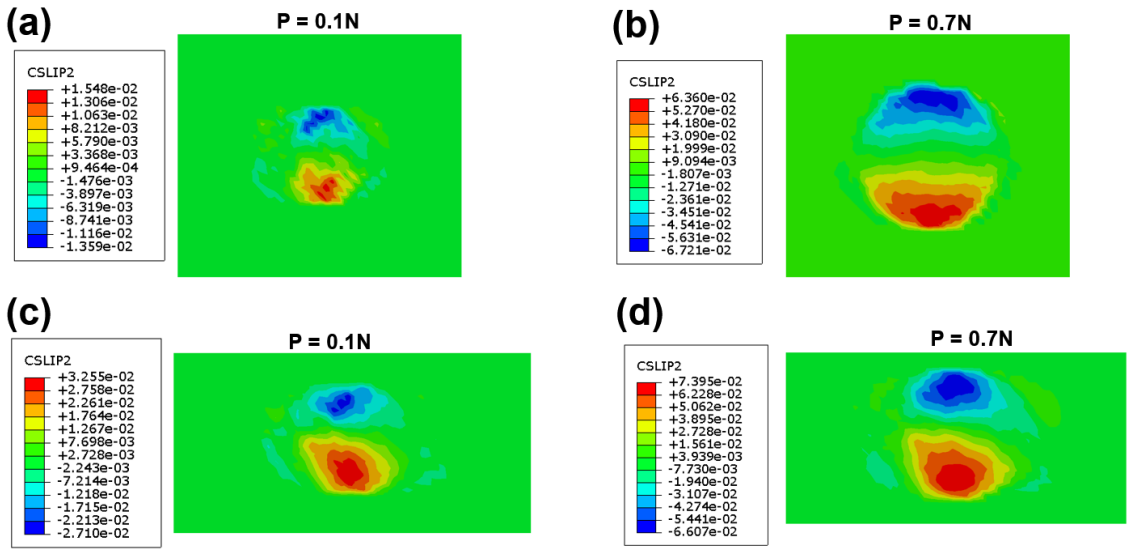

Figure 7.14 Contact slip contours of (a, b) HC Type-A, and (c, d) HC Type-B corresponding to P= 0.1N and P= 0.7N. Colour bars in mm.

The Von Mises stress contour plots of both textiles subjected to the lowest and highest load levels are shown in Fig. 7.15, for comparison. The range of applied load caused stress in the fibres, within the elastic range and caused no permanent deformation. As for Type-A, the highest stress occurred on the binder yarns in the region with the lowest cross-sectional area (see Fig. 7.15 (b)). Most of the warp and weft tows on the lower half regions of both textiles remained with almost zero stress level, suggesting the load was supported by the superficial tows, binder yarns, and the matrix. Higher stress level was observed in Type-B pattern, while stress concentration was found in the upper region of binder tow once the highest tested load was exerted on the unit cell (see Fig. 7.15 (d)). In this research, multifilament yarns were used as binder in the textiles, suggesting higher load-to-failure capacity, and therefore stress concentration could be ignored. Moreover, no binder filament rupture was reported during compression tests of composites, reassuring structural reliability for the range of applied loads.

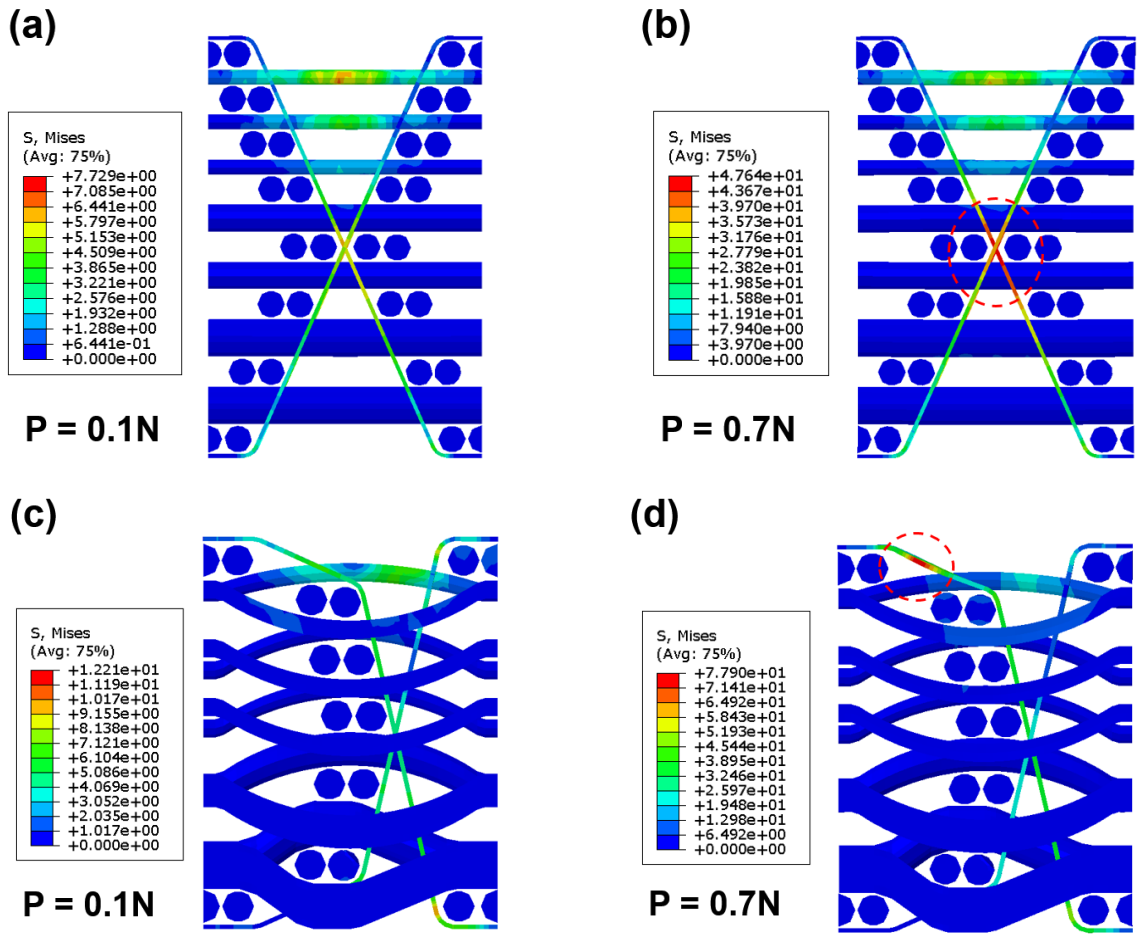

Figure 7.15 Stress distribution contours of HC Type-A (a,b), and HC Type-B (c,d), under minimum and maximum load levels, (all units in MPa).

The overall structural deflections of textile reinforcements are shown in Fig. 7.16, once each unit cell was subjected to 0.7N load, and the ball was slid to the right end of a single reciprocating cycle. Compared to Type-B, textile Type-A was considerably bent towards the right, while pattern B performed better in terms of structural stability. Similar trend was found in opposite direction, once the ball slid to the left end of the cycle. It was concluded the arc shape of warp tows in Type-B could more effectively distribute the induced stress and resist eccentric deflection, suggesting this type could potentially offer higher structural stiffness.

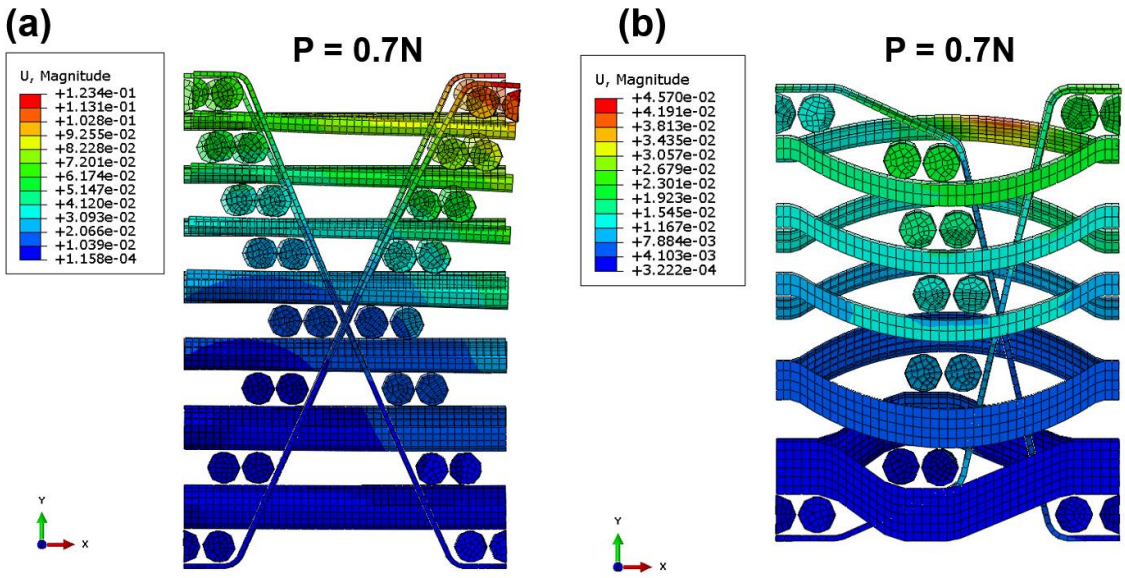

Figure 7.16 *Overall deflection of textile component under the highest applied load and when the ball reached the right end of reciprocating cycle (a) Type-A, (b) type-B. (All units in mm).*

7.3 Conclusions

In this chapter, sliding wear of a 3D orthogonal woven fabric and HCs were modelled successfully by developing a FORTRAN subroutine linked with ABAQUS. Material removal from the surface of the fabric in contact with metallic counterface, as well as a ceramic ball sliding against HC unit cell were defined by UMESHMOTION and Archard's wear law. ALE adaptive meshing method was implemented for geometry update due to surface ablation and despite some restrictions on material model selection, it was able to maintain mesh stability and distortion control. It should be noted that in the previous studies, hyperelastic material model was considered for hydrogels [284, 285]. However, the application of this model coupled with ALE technique, might lead to inaccuracies, due to the poor translation of displacement gradient state variables. Overall, the results were in good agreement with experimental data obtained from linear reciprocating wear tests. In the case of dry 3D orthogonal textiles, FE simulations tend to predict slightly higher wear rates as the pin-on-disc tests were conducted with immersed specimens, while the change in mass due to water retention capacity of fabric was not

considered in the FE model. After ensuring the efficiency of the developed wear model, a parametric study was conducted to investigate the influence of load, sliding speed and coefficient of friction on the wear rate of 3D woven fabrics. The results showed that wear rate increases by increasing these three parameters, although the effect of coefficient of friction is not as crucial as the other two factors. Based on the results, contact pressure up to 1.2 MPa, and coefficient of friction up to 0.5 were considered as safe working conditions for the 3D woven fabric's service life.

Hydrogel composite unit cells were modelled successfully, and it was demonstrated that the higher surface ablation observed at the contact surface boundaries parallel to the sliding motion arises from a higher contact slip experienced by the corresponding nodes. In average, wear resistance was improved by over 30% by introducing textile reinforcement to the hydrogel matrix. Stress analysis revealed Textile Type-B was able to distribute induced stress more effectively, and it offered better structural stiffness compared to textile Type-A, attributed to geometry of warp tows. As the numerical results were in good agreement with the experimental data, the FE model was validated, and could be utilised for wear prediction beyond the sliding distance used for experiments. Moreover, an iterative procedure could be programmed to visualize wear evolution on the FE model such that the deformed surface as a result of certain number of cycles was extracted from the output database and employed as an input for the next round of sliding wear cycles. FEM was able to provide useful information that could not be obtained directly from the experiments, such as stress analysis and contact mechanics.

Chapter 8

CONCLUSIONS

8.1 Summary

To explore an alternative method that can be used in the treatment of localised cartilage lesions, hence postponing the TJR for young patients, a functional implant inspired by the unique structure of articular cartilage was proposed. It was postulated that anisotropic, viscoelastic and inhomogeneous properties that a 3D woven textile embedded in a hydrogel matrix offers, are the requirements for a functional cartilage replacement biomaterial.

With the previous studies focused on tribology of dry woven fabrics, the mechanical and tribological performance of hydrogels, NP-reinforced nanocomposite hydrogels and fibre-reinforced hydrogel composites were all under-explored, which were studied in this research. ALG-PAAm IPN hydrogel was selected, as it exhibits promising properties as a potential load-bearing candidate. Unlike PVA, the tribological behaviour of ALG-PAAm and their reinforced forms were not studied before in detail, indicating a research must be carried out to characterise their properties, and evaluate them as cartilage replacement candidates. Mixing of polymer networks and its effect on friction and wear properties of the IPN hydrogel, along with the impact of other chemical and environmental parameters were focused as the very first attempt to assess it as synthetic cartilage. In addition, two different weave patterns were successfully produced in novel 3D architectures with through-the-thickness stiffness gradient. The hydrogels and NCHs were successfully synthesised. Hydrogel infiltration into the woven preforms was

successfully accomplished, resulting in fairly defect-free composite hydrogels. To the author's best of knowledge, FE modelling of sliding wear for the dry 3D textiles was conducted for the first time, with the aid of a user-defined subroutine based on UMESHMOTION. Moreover, the model was further developed for the simulation of the hydrogel composites' unit cells. The outcomes of current study are highlighted in the next section.

8.2 Conclusions

Based on the experimental findings for ALG-IPN hydrogels, below items can be concluded:

- The hydrogel's low friction coefficient was attributed to high water retention capacity, permeability, range of stiffness available, and presence of fluid film at the interface.
- Based on the reciprocating motion of the alumina ball as the counterface, the lowest friction coefficient obtained for ALG-PAAm hydrogel in the presence of bovine serum lubrication was 0.01, which is fairly close to that of a healthy cartilage, and lower than PVA.
- Hydrogel specimens with 0.03 X.A% showed better tribological performance in terms of a lower wear rate, and lower friction levels in the lack of bovine serum lubrication.
- Hydrogels with 0.06 X.A%, exhibited improved mechanical properties such as higher stiffness, meaning they can withstand higher loads with less deformation compared to the other types, as well as a significantly lower friction coefficient under bovine serum lubrication.

- Microscopic analysis of worn surfaces revealed adhesion as the most prevalent wear mechanism, while surface pitting as an indication of fatigue wear was observed at higher loads and lower speeds.
- Wear volume values showed a marginal increase at higher crosslinking agent concentration. Nevertheless, the higher crosslinking concentration was selected for reinforced samples, due to stronger mechanical performance and acceptable friction and wear behaviour that can be achieved.

The experiments were further carried out on NCHs, and some improvements were observed in the tribological performance as well as mechanical response, as compared to the reference ALG-PAAm IPN hydrogel. In addition:

- Ultra-low CoF, coupled with high wear-resistance, and tuneable elastic and viscoelastic behaviours, suggest these biomaterials as a promising candidate for use as a cartilage replacement.
- The improvements were attributed to the powerful interfacial bonding between the nano particles and the polymer matrix, and it is expected to achieve even more robust nanocomposite using smaller size nano particles.
- Samples with 4% concentration of Si-NP showed considerably efficient mechanical performance, high wear-resistance and fairly low CoF compared to the other samples.

Next, the mechanical and tribological characteristics of hydrogel composites with two distinct 3D woven reinforcement patterns were investigated and compared with an un-reinforced ALG-PAAm hybrid hydrogel. It was found:

- The composites developed in this study possess mechanical anisotropy and a stiffness gradient through the thickness, achieved by using different types of fibres with different diameters, woven through the thickness of the textile.

- An improved non-linear stress-strain response, anisotropy and enhanced time-dependent stress relaxation, along with a strain-rate dependency were due to the incorporation of polymer weave into the hydrogel matrix.
- Infiltration of hydrogel into the woven structure contributed to achieving a much lower surface roughness and an increase in load-to-failure capacity.
- Wear-resistance of the hydrogel matrix was greatly improved under the range of applied loads and sliding velocities.
- These promising results can be attributed to the synergistic interaction between the fibre phase and the hydrogel matrix.
- Overall, the HC Type-B demonstrated the best mechanical and tribological performance among other studied materials and is therefore selected for further research.

Sliding wear of a 3D orthogonal woven fabric was modelled successfully by developing a FORTRAN subroutine linked with ABAQUS. It could be concluded that:

- ALE adaptive meshing method was able to maintain mesh stability and distortion control despite some restrictions on material model selection.
- The results were in good agreement with experimental data obtained from pin-on-disc wear tests.
- FE simulations tend to predict slightly higher wear rates, as the pin-on-disc tests were conducted with immersed specimens, while the change in mass due to water retention capacity of fabric was not considered in the FE model.
- The parametric study showed that wear rate increases by increasing load, sliding rate and CoF, although the effect of coefficient of friction is not as crucial as the other two factors.

- A contact pressure of up to 1.2 MPa, and coefficient of friction of up to 0.5 were considered as safe working conditions for the service life of 3D woven PET fabrics.

Based on FEA of HC unit cells, the following was concluded:

- A trend was observed that wear depth increased with load, and decreased with speed among all unit cells used for FE simulations, which is in agreement with the results obtained from experiments.
- Fibre reinforcement was found to have a positive impact on hydrogel matrix, contributing to over 30% reduction in wear depth of the unit cells.
- Higher surface ablation observed at the contact surface boundaries parallel to the sliding motion arises from higher contact slip experienced by the corresponding nodes.
- Stress analysis of textile reinforcements revealed the majority of load was carried by the upper half of the textiles and the matrix, with stress concentration observed in the centre of binder yarns for Type-A textile.
- Concerning structural analysis of the reinforcements, the arc shape of warp tows in Type-B could more effectively distribute the induced stress and resist eccentric deflection, suggesting this type could potentially offer higher structural stiffness.

8.3 Future Work

This thesis covers a comprehensive preliminary study on material selection and manufacturing, mechanical and tribological testing and FE modelling for the implant proposed in section 1.2, however there are still some work to be done in the future. Regarding the implant, only the load bearing layer, comprising polymer layer within a

hydrogel matrix was studied as an initial attempt to build up systematic experimental and computational frameworks. Design and fabrication of the entire implant structure is feasible by interweaving polymer weave and metal wires and can be considered as a future research. Addition of Si-NP was shown to improve wear resistance of ALG-PAAm hydrogel. Thus, injection of pre-gel solution of ALG-PAAm, with dispersed Si-NP into a 3D woven preform could be investigated in the future studies. In addition, an optimum design could be used for animal pre-clinical research.

Tribology tests should be conducted at body temperature, and for more realistic test conditions, synovial fluid could be utilised as the lubricant, as previous studies showed that friction coefficient of hydrogels would decrease by using synovial fluid.

A future study should investigate friction and wear behaviour of the hydrogel composites under sliding patterns closer to physiological conditions such as butterfly sliding track. Moreover, fatigue and impact tests could be carried out to characterise the structural response to dynamic loading, as well as implantation into living creatures to study the synthetic cartilage interaction with the neighbouring tissue.

As previously stated, all the materials investigated in this research are biocompatible as shown in the literature. Nevertheless, an in-depth investigation on biocompatibility and toxicity of the materials should be conducted before any implantation inside human body.

Although the current FE model showed fairly good correlation with physical experiments, the material model for the hydrogel unit cell can be upgraded to biphasic model to better reflect the mechanical behaviour of hydrogel materials, which could be the subject of future studies.

REFERENCES

[1] Aumiller, W.D. and H.A. Dollahite, *Advances in total knee arthroplasty.* Journal of the American Academy of Physician Assistants, 2016. **29**(3): p. 27-31.

[2] Zagra, L., *Advances in hip arthroplasty surgery: what is justified?* EFORT open reviews, 2017. **2**(5): p. 171-178.

[3] Hui, J.H.P. and A. Marchie, *Current management of cartilage defects: a review.* International Journal of Rheumatic Diseases, 2003. **6**(2): p. 170-177.

[4] Jiang, Y.Z., et al., *Cell transplantation for articular cartilage defects: principles of past, present, and future practice.* Cell transplantation, 2011. **20**(5): p. 593-607.

[5] Bentley, G., et al., *A prospective, randomised comparison of autologous chondrocyte implantation versus mosaicplasty for osteochondral defects in the knee.* Bone & Joint Journal, 2003. **85**(2): p. 223-230.

[6] Kreuz, P., et al., *Results after microfracture of full-thickness chondral defects in different compartments in the knee.* Osteoarthritis and cartilage, 2006. **14**(11): p. 1119-1125.

[7] Clouet, J., et al., *From osteoarthritis treatments to future regenerative therapies for cartilage.* Drug discovery today, 2009. **14**(19-20): p. 913-925.

[8] Ulrich, S.D., et al., *Indications for Revision Total Hip Arthroplasty*, in *Surgical Treatment of Hip Arthritis*. 2010, Elsevier. p. 241-246.

[9] Jacobs, J.J., et al., *Wear debris in total joint replacements.* JAAOS-Journal of the American Academy of Orthopaedic Surgeons, 1994. **2**(4): p. 212-220.

[10] Saleh, K.J. and E.M. Schwarz, *Osteolysis: medical and surgical approaches.* Clinical orthopaedics and related research, 2004. **427**: p. 138-147.

[11] Huiskes, R., H. Weinans, and B. Van Rietbergen, *The relationship between stress shielding and bone resorption around total hip stems and the effects of flexible materials.* Clinical orthopaedics and related research, 1992: p. 124-134.

[12] Rodts, T.W. and S.R. Schmid. *Compression Testing of 3D Polymer Fabrics for Use as Cartilage Scaffolds*. in *ASME 2010 Summer Bioengineering Conference*. 2010. American Society of Mechanical Engineers.

[13] Kienapfel, H., et al., *Implant fixation by bone ingrowth.* The Journal of arthroplasty, 1999. **14**(3): p. 355-368.

[14] Boublik, M., F.T. Blevins, and J.R. Steadman, *Anatomy: Bony Architecture, Biomechanics, and Menisci*, in *Traumatic disorders of the knee*. 1994, Springer. p. 3-8.

[15] Engh, G.A., K.A. Dwyer, and C.K. Hanes, *Polyethylene wear of metal-backed tibial components in total and unicompartmental knee prostheses.* Bone & Joint Journal, 1992. **74**(1): p. 9-17.

[16] Saleh, M.N. and C. Soutis, *Recent advancements in mechanical characterisation of 3D woven composites.* Mechanics of Advanced Materials and Modern Processes, 2017. **3**(1): p. 12.

[17] Hunziker, E., T. Quinn, and H.-J. Häuselmann, *Quantitative structural organization of normal adult human articular cartilage.* Osteoarthritis and Cartilage, 2002. **10**(7): p. 564-572.

[18] Peppas, N.A., et al., *Hydrogels in biology and medicine: from molecular principles to bionanotechnology.* Advanced materials, 2006. **18**(11): p. 1345-1360.

[19] Slaughter, B.V., et al., *Hydrogels in regenerative medicine.* Advanced materials, 2009. **21**(32-33): p. 3307-3329.

[20] Hoare, T.R. and D.S. Kohane, *Hydrogels in drug delivery: Progress and challenges.* Polymer, 2008. **49**(8): p. 1993-2007.

[21] Lutolf, M.P., *Biomaterials: Spotlight on hydrogels.* Nature materials, 2009. **8**(6): p. 451.

[22] Salatin, S., et al., *Hydrogel nanoparticles and nanocomposites for nasal drug/vaccine delivery.* Archives of pharmacal research, 2016. **39**(9): p. 1181-1192.

[23] Yannas, I., et al., *Synthesis and characterization of a model extracellular matrix that induces partial regeneration of adult mammalian skin.* Proceedings of the National Academy of Sciences, 1989. **86**(3): p. 933-937.

[24] Drury, J.L. and D.J. Mooney, *Hydrogels for tissue engineering: scaffold design variables and applications.* Biomaterials, 2003. **24**(24): p. 4337-4351.

[25] Ko, H.-F., C. Sfeir, and P.N. Kumta, *Novel synthesis strategies for natural polymer and composite biomaterials as potential scaffolds for tissue engineering.* Philosophical Transactions of the Royal Society of London A: Mathematical, Physical and Engineering Sciences, 2010. **368**(1917): p. 1981-1997.

[26] Liu, M., et al., *Injectable hydrogels for cartilage and bone tissue engineering.* Bone research, 2017. **5**: p. 17014.

[27] Dowson, D. and J. Yao, *Elastohydrodynamic lubrication of soft-layered solids at elliptical contacts: part 2: film thickness analysis.* Proceedings of the Institution of Mechanical Engineers, Part J: Journal of Engineering Tribology, 1994. **208**(1): p. 43-52.

[28] Katta, J.K., et al., *Friction and wear behavior of poly (vinyl alcohol)/poly (vinyl pyrrolidone) hydrogels for articular cartilage replacement.* Journal of Biomedical Materials Research Part A, 2007. **83**(2): p. 471-479.

[29] Bavaresco, V., et al., *Study on the tribological properties of pHEMA hydrogels for use in artificial articular cartilage.* Wear, 2008. **265**(3-4): p. 269-277.

[30] Arakaki, K., et al., *Artificial cartilage made from a novel double-network hydrogel: In vivo effects on the normal cartilage and ex vivo evaluation of the friction property.* Journal of Biomedical Materials Research Part A, 2010. **93**(3): p. 1160-1168.

[31] Waters, D.J., et al., *Structure and mechanism of strength enhancement in interpenetrating polymer network hydrogels.* Macromolecules, 2011. **44**(14): p. 5776-5787.

[32] Sun, J.-Y., et al., *Highly stretchable and tough hydrogels.* Nature, 2012. **489**(7414): p. 133.

[33] Illeperuma, W.R., et al., *Fiber-reinforced tough hydrogels.* Extreme Mechanics Letters, 2014. **1**: p. 90-96.

[34] Skelton, S., et al., *Biomimetic adhesive containing nanocomposite hydrogel with enhanced materials properties.* Soft Matter, 2013. **9**(14): p. 3825-3833.

[35] Gaharwar, A.K., N.A. Peppas, and A. Khademhosseini, *Nanocomposite hydrogels for biomedical applications.* Biotechnology and bioengineering, 2014. **111**(3): p. 441-453.

[36] Memic, A., et al., *Hydrogels 2.0: improved properties with nanomaterial composites for biomedical applications.* Biomedical materials, 2015. **11**(1): p. 014104.

[37] Beddoes, C.M., et al., *Hydrogels as a replacement material for damaged articular hyaline cartilage.* Materials, 2016. **9**(6): p. 443.

[38] Thoniyot, P., et al., *Nanoparticle–hydrogel composites: Concept, design, and applications of these promising, multi-functional materials.* Advanced Science, 2015. **2**(1-2).

[39] Kurtz, S.M., et al., *International survey of primary and revision total knee replacement.* International orthopaedics, 2011. **35**(12): p. 1783-1789.

[40] Hooper, G., et al., *Current trends and projections in the utilisation rates of hip and knee replacement in New Zealand from 2001 to 2026.* The New Zealand Medical Journal (Online), 2014. **127**(1401): p. 82.

[41] *World Health Organization Global Burden of Health Study* 2013; Available from: http://www.who.int/healthinfo/global_burden_disease/estimates_regional/en/index1.html.

[42] Mikulak, S.A., et al., *Loosening and osteolysis with the press-fit condylar posterior-cruciate-substituting total knee replacement.* JBJS, 2001. **83**(3): p. 398-403.

[43] Maitland, P., et al., *Institute of Gender and Health: A Portrait of Innovation and Health Research Growth.* NURSING LEADERSHIP-ACADEMY OF CANADIAN EXECUTIVE NURSES-, 2006. **19**(2): p. 24.

[44] Bossley;, C.J. and K.B. Miles;. *Musculo-skeletal conditions in New Zealand, "the crippling burden"* 2009; Available from: https://nzoa.org nz//system/files/The%20Crippling%20Burden.pdf.

[45] King, D., et al., *Rugby league injuries in New Zealand: variations in injury claims and costs by ethnicity, gender, age, district, body site, injury type and occupation.* NZ J Sports Med, 2009. **36**(2): p. 48-55.

[46] Arjmandi, M. and M. Ramezani, *Finite element modelling of sliding wear in three-dimensional textile hydrogel composites.* Tribology International, 2019. **133**: p. 88-100.

[47] Arjmandi, M., et al., *Mechanical and tribological properties of a novel hydrogel composite reinforced by three-dimensional woven textiles as a functional synthetic cartilage.* Composites Part A: Applied Science and Manufacturing, 2018.

[48] Arjmandi, M., et al., *Finite element modelling of sliding wear in three-dimensional woven textiles.* Tribology International, 2017. **115**: p. 452-460.

[49] Arjmandi, M., et al., *Experimental study on friction and wear properties of interpenetrating polymer network alginate-polyacrylamide hydrogels for use in minimally-invasive joint implants.* Wear, 2018. **406**: p. 194-204.

[50] Mow, V.C., et al., *Biphasic creep and stress relaxation of articular cartilage in compression: theory and experiments.* Journal of biomechanical engineering, 1980. **102**(1): p. 73-84.

[51] Liao, I.C., et al., *Composite three-dimensional woven scaffolds with interpenetrating network hydrogels to create functional synthetic articular cartilage.* Advanced functional materials, 2013. **23**(47): p. 5833-5839.

[52] Mow, V.C. and X.E. Guo, *Mechano-electrochemical properties of articular cartilage: their inhomogeneities and anisotropies.* Annual review of biomedical engineering, 2002. **4**(1): p. 175-209.

[53] Ge, Z., et al., *Osteoarthritis and therapy.* Arthritis Care & Research, 2006. **55**(3): p. 493-500.

[54] Eyre, D.R., et al., *Covalent cross-linking of the NC1 domain of collagen type IX to collagen type II in cartilage.* Journal of Biological Chemistry, 2004. **279**(4): p. 2568-2574.

[55] Griffith, L.G. and G. Naughton, *Tissue engineering--current challenges and expanding opportunities.* science, 2002. **295**(5557): p. 1009-1014.

[56] Bedi, A., B.T. Feeley, and R.J. Williams III, *Management of articular cartilage defects of the knee.* JBJS, 2010. **92**(4): p. 994-1009.

[57] Temenoff, J.S. and A.G. Mikos, *Tissue engineering for regeneration of articular cartilage.* Biomaterials, 2000. **21**(5): p. 431-440.

[58] Hunziker, E., *Articular cartilage repair: basic science and clinical progress. A review of the current status and prospects.* Osteoarthritis and cartilage, 2002. **10**(6): p. 432-463.

[59] Khashan, M., et al., *The treatment of focal chondral lesions of the knee.* Harefuah, 2010. **149**(8): p. 542-6, 549.

[60] Benthien, J.P., M. Schwaninger, and P. Behrens, *We do not have evidence based methods for the treatment of cartilage defects in the knee.* Knee Surgery, Sports Traumatology, Arthroscopy, 2011. **19**(4): p. 543-552.

[61] Rai, V., et al., *Recent strategies in cartilage repair: a systemic review of the scaffold development and tissue engineering.* Journal of biomedical materials research Part A, 2017.

[62] Portocarrero, G., G. Collins, and T. Livingston Arinzeh, *Challenges in cartilage tissue engineering.* J Tissue Sci Eng, 2013. **4**(1): p. e120.

[63] Alsat, E., et al., *Hypoxia impairs cell fusion and differentiation process in human cytotrophoblast, in vitro.* Journal of cellular physiology, 1996. **168**(2): p. 346-353.

[64] Adkisson IV, H.D., et al., *The potential of human allogeneic juvenile chondrocytes for restoration of articular cartilage.* The American journal of sports medicine, 2010. **38**(7): p. 1324-1333.

[65] Wu, J. and W. Herzog, *Elastic anisotropy of articular cartilage is associated with the microstructures of collagen fibers and chondrocytes.* Journal of biomechanics, 2002. **35**(7): p. 931-942.

[66] Setton, L.A., D.M. Elliott, and V.C. Mow, *Altered mechanics of cartilage with osteoarthritis: human osteoarthritis and an experimental model of joint degeneration.* Osteoarthritis and Cartilage, 1999. **7**(1): p. 2-14.

[67] Schinagl, R.M., et al., *Depth-dependent confined compression modulus of full-thickness bovine articular cartilage.* Journal of Orthopaedic Research, 1997. **15**(4): p. 499-506.

[68] Wang, C.C., C.T. Hung, and V.C. Mow, *An analysis of the effects of depth-dependent aggregate modulus on articular cartilage stress-relaxation behavior in compression.* Journal of Biomechanics, 2001. **34**(1): p. 75-84.

[69] Woo, S.-Y., W. Akeson, and G. Jemmott, *Measurements of nonhomogeneous, directional mechanical properties of articular cartilage in tension.* Journal of biomechanics, 1976. **9**(12): p. 785-791.

[70] Akizuki, S., et al., *Tensile properties of human knee joint cartilage: I. Influence of ionic conditions, weight bearing, and fibrillation on the tensile modulus.* Journal of Orthopaedic Research, 1986. **4**(4): p. 379-392.

[71] Soltz, M.A. and G.A. Ateshian, *A conewise linear elasticity mixture model for the analysis of tension-compression nonlinearity in articular cartilage.* Journal of biomechanical engineering, 2000. **122**(6): p. 576-586.

[72] Ateshian, G.A., *The role of interstitial fluid pressurization in articular cartilage lubrication.* Journal of biomechanics, 2009. **42**(9): p. 1163-1176.

[73] Pierce, D.M., T. Ricken, and G.A. Holzapfel, *A hyperelastic biphasic fibre-reinforced model of articular cartilage considering distributed collagen fibre orientations: continuum basis, computational aspects and applications.* Computer methods in biomechanics and biomedical engineering, 2013. **16**(12): p. 1344-1361.

[74] Katta, J., et al., *Biotribology of articular cartilage—a review of the recent advances.* Medical Engineering and Physics, 2008. **30**(10): p. 1349-1363.

[75] Cicuttini, F., et al., *Association of cartilage defects with loss of knee cartilage in healthy, middle-age adults: A prospective study.* Arthritis & Rheumatology, 2005. **52**(7): p. 2033-2039.

[76] Ding, C., et al., *Association of prevalent and incident knee cartilage defects with loss of tibial and patellar cartilage: a longitudinal study.* Arthritis & Rheumatology, 2005. **52**(12): p. 3918-3927.

[77] Graindorge, S.L. and G.W. Stachowiak, *Changes occurring in the surface morphology of articular cartilage during wear.* Wear, 2000. **241**(2): p. 143-150.

[78] Ballantine, G.C. and G.W. Stachowiak, *The effects of lipid depletion on osteoarthritic wear.* Wear, 2002. **253**(3-4): p. 385-393.

[79] Caligaris, M. and G.A. Ateshian, *Effects of sustained interstitial fluid pressurization under migrating contact area, and boundary lubrication by synovial fluid, on cartilage friction.* Osteoarthritis and Cartilage, 2008. **16**(10): p. 1220-1227.

[80] Murakami, T., et al., *Adaptive multimode lubrication in natural synovial joints and artificial joints.* Proceedings of the Institution of Mechanical Engineers, Part H: Journal of Engineering in Medicine, 1998. **212**(1): p. 23-35.

[81] Mow, V. and G. Ateshian, *In Lubrication and Wear of Diarthrodial Joints: Basic Orthopaedic Biomechanics; Mow, VC; Hayes, WC, Eds*. 1997, Lippincott-Raven, Philadelphia.

[82] Forster, H. and J. Fisher, *The influence of loading time and lubricant on the friction of articular cartilage.* Proceedings of the Institution of Mechanical Engineers, Part H: Journal of Engineering in Medicine, 1996. **210**(2): p. 109-119.

[83] Mullen, C. and P. Roy. *Fabrication and properties description of AVCO 3D carboncarbon cylindrical composites*. in *Proceedings of the National SAMPE Symposium*. 1972.

[84] Carlson, C.H., *Preliminary scramjet design for hypersonic airbreathing missile application.* 1983.

[85] Moutos, F.T., L.E. Freed, and F. Guilak, *A biomimetic three-dimensional woven composite scaffold for functional tissue engineering of cartilage.* Nature materials, 2007. **6**(2): p. 162.

[86] Müller, J., A. Zulliger, and M. Dorn, *Economic production of composite beams with 3D fabric tapes.* Textile Month, 1994. **9**: p. 9-13.

[87] Wong, R., *Sandwich construction in the starship*, in *37th International SAMPE Symposium and Exhibition*. 1992: Anaheim, CA, USA,. p. 186-197.

[88] Redman, C., H. Bayraktar, and M. McClain, *Curved beam test behavior of 3D woven composites*. 2014.

[89] Jewell J., Kennedy R., and Menard A., *Full-scale LEAP Fan Blade-Out Rig Test Yields Outstanding Results; Advanced LEAP Fan Endurance Test Complete*, in *CFM Power Flight*. 2011.

[90] Hemrick, J.G., et al., *Woven graphite fiber structures for use in ultra-light weight heat exchangers.* Carbon, 2011. **49**(14): p. 4820-4829.

[91] Quinn, J., A. McIlhagger, and R. McIlhagger, *Examination of the failure of 3D woven composites.* Composites Part A: applied science and manufacturing, 2008. **39**(2): p. 273-283.

[92] Hosseinzadeh, R., M.M. Shokrieh, and L. Lessard, *Damage behavior of fiber reinforced composite plates subjected to drop weight impacts.* Composites science and technology, 2006. **66**(1): p. 61-68.

[93] Brandt, J., K. Drechsler, and F.-J. Arendts, *Mechanical performance of composites based on various three-dimensional woven-fibre preforms.* Composites Science and Technology, 1996. **56**(3): p. 381-386.

[94] Cox, B. and M. Dadkhah, *The macroscopic elasticity of 3D woven composites.* Journal of composite materials, 1995. **29**(6): p. 785-819.

[95] McClain, M. and J. Goering, *Overview of recent developments in 3D structures.* Albany Eng Compos, 2012: p. 1-12.

[96] Kamiya, R., et al., *Some recent advances in the fabrication and design of three-dimensional textile preforms: a review.* Composites science and technology, 2000. **60**(1): p. 33-47.

[97] Rudov-Clark, S., *Experimental investigation of the tensile properties and failure mechanisms of three-dimensional woven composites.* 2007.

[98] Tong, L., A. Mouritz, and M. Bannister, *Chapter 5 3D Woven Composites.* 3D Fibre Reinforced Composite Materials, 2002.

[99] Ji, C., et al., *Impact damage of 3D orthogonal woven composite circular plates.* Applied Composite Materials, 2007. **14**(5-6): p. 343-362.

[100] Walter, T., et al., *Monotonic and cyclic short beam shear response of 3D woven composites.* Composites Science and Technology, 2010. **70**(15): p. 2190-2197.

[101] Umer, R., et al., *The mechanical properties of 3D woven composites.* Journal of Composite Materials, 2017. **51**(12): p. 1703-1716.

[102] Cox, B., et al., *Failure mechanisms of 3D woven composites in tension, compression, and bending.* Acta metallurgica et materialia, 1994. **42**(12): p. 3967-3984.

[103] Labanieh, A.R., et al., *Influence of off-axis in-plane yarns on the mechanical properties of 3D composites.* Composites Part A: Applied Science and Manufacturing, 2017. **98**: p. 45-57.

[104] Lomov, S.V., et al. *Mechanical behaviour of non-crimp 3D woven carbon/epoxy composite under in-plane tensile loading*. in *Proc. 18th Int. Conf. on Composite Materials, Jeju Island, Republic of Korea, 21*. 2011.

[105] Behera, B.a. and B. Dash, *Mechanical behavior of 3D woven composites.* Materials & Design, 2015. **67**: p. 261-271.

[106] Mouritz, A. and B. Cox, *A mechanistic interpretation of the comparative in-plane mechanical properties of 3D woven, stitched and pinned composites.* Composites Part A: Applied Science and Manufacturing, 2010. **41**(6): p. 709-728.

[107] Naik, R.A., *Failure analysis of woven and braided fabric reinforced composites.* Journal of Composite Materials, 1995. **29**(17): p. 2334-2363.

[108] Tan, P., L. Tong, and G. Steven, *Behavior of 3D orthogonal woven CFRP composites. Part II. FEA and analytical modeling approaches.* Composites Part A: applied science and manufacturing, 2000. **31**(3): p. 273-281.

[109] Yang, Q. and B. Cox. *Predicting local strains in textile composites using the binary model formulation*. in *Proceedings of the ICCM*. 2003.

[110] El Hage, C., et al., *Analytical and numerical modeling of mechanical properties of orthogonal 3D CFRP.* Composites Science and Technology, 2009. **69**(1): p. 111-116.

[111] Yu, Y., et al., *Cell model of 3D orthogonal woven composite and its application.* Acta Mater Compos Sin, 2009. **26**(4): p. 181-185.

[112] Kuo, W.-S. and B.-J. Pon, *Elastic moduli and damage evolution of three-axis woven fabric composites.* Journal of materials science, 1997. **32**(20): p. 5445-5455.

[113] Kregers, A. and Y.G. Melbardis, *Determination of the deformability of three-dimensionally reinforced composites by the stiffness averaging method.* Polymer Mechanics, 1978. **14**(1): p. 1-5.

[114] Yang, J.-M., C.-L. Ma, and T.-W. Chou, *Fiber inclination model of three-dimensional textile structural composites.* Journal of composite Materials, 1986. **20**(5): p. 472-484.

[115] Whitney, T.J. and T.-W. Chou, *Modeling of 3-D angle-interlock textile structural composites.* Journal of composite Materials, 1989. **23**(9): p. 890-911.

[116] Xu, J., et al., *A binary model of textile composites—II. The elastic regime.* Acta metallurgica et materialia, 1995. **43**(9): p. 3511-3524.

[117] Rosiak, J.M., et al., *Radiation formation of hydrogels for biomedical purposes. Some remarks and comments.* Radiation Physics and Chemistry, 1995. **46**(2): p. 161-168.

[118] Francis, R. and D.S. Kumar, *Biomedical Applications of Polymeric Materials and Composites*. 2016: John Wiley & Sons.

[119] Shikinami, Y. and H. Kawarada, *Potential application of a triaxial three-dimensional fabric (3-DF) as an implant.* Biomaterials, 1998. **19**(7-9): p. 617-635.

[120] Zhang, M., et al., *A novel ultra high molecular weight polyethylene–hyaluronan microcomposite for use in total joint replacements. II. Mechanical and tribological property evaluation.* Journal of Biomedical Materials Research Part A, 2007. **82**(1): p. 18-26.

[121] Wintermantel, E., et al., *Tissue engineering scaffolds using superstructures.* Biomaterials, 1996. **17**(2): p. 83-91.

[122] Houis, S., et al., *Application of Polyvinylidene Fluoride (PVDF) as a Biomaterial in Medical Textiles*, in *Medical and Healthcare Textiles*. 2010, Elsevier. p. 342-352.

[123] Cooper, J.A., et al., *Fiber-based tissue-engineered scaffold for ligament replacement: design considerations and in vitro evaluation.* Biomaterials, 2005. **26**(13): p. 1523-1532.

[124] Karamuk, E., J. Mayer, and G. Raeber, *Tissue engineered composite of a woven fabric scaffold with tendon cells, response on mechanical simulation in vitro.* Composites science and technology, 2004. **64**(6): p. 885-891.

[125] Laurenti, K.C., et al., *Cartilage reconstruction using self-anchoring implant with functional gradient.* Materials Research, 2014. **17**(3): p. 638-649.

[126] Wichterle, O. and D. Lim, *Hydrophilic gels for biological use.* Nature, 1960. **185**(4706): p. 117.

[127] Syková, E., et al., *Bone marrow stem cells and polymer hydrogels—two strategies for spinal cord injury repair.* Cellular and molecular neurobiology, 2006. **26**(7-8): p. 1111-1127.

[128] Lee, K.Y. and D.J. Mooney, *Alginate: properties and biomedical applications.* Progress in polymer science, 2012. **37**(1): p. 106-126.

[129] Yang, T.-H., *Recent applications of polyacrylamide as biomaterials.* Recent Patents on Materials Science, 2008. **1**(1): p. 29-40.

[130] Lessel, R., et al. 2004: E.: EP1418188.

[131] Hennink, W.E. and C.F. van Nostrum, *Novel crosslinking methods to design hydrogels.* Advanced drug delivery reviews, 2012. **64**: p. 223-236.

[132] Hoffman, A.S., *Hydrogels for biomedical applications.* Advanced drug delivery reviews, 2012. **64**: p. 18-23.

[133] Peppas, N.A. and E.W. Merrill, *Development of semicrystalline poly (vinyl alcohol) hydrogels for biomedical applications.* Journal of Biomedical Materials Research Part A, 1977. **11**(3): p. 423-434.

[134] Kim, S., et al., *Polyacrylamide hydrogel properties for horticultural applications.* International Journal of Polymer Analysis and Characterization, 2010. **15**(5): p. 307-318.

[135] Lugao, A.B. and S.M. Malmonge, *Use of radiation in the production of hydrogels.* Nuclear Instruments and Methods in Physics Research Section B: Beam Interactions with Materials and Atoms, 2001. **185**(1-4): p. 37-42.

[136] Sperling, L.H., *Interpenetrating polymer networks: an overview*. 1994, ACS Publications.

[137] Dragan, E.S., *Design and applications of interpenetrating polymer network hydrogels. A review.* Chemical Engineering Journal, 2014. **243**: p. 572-590.

[138] Gong, J.P., et al., *Double-network hydrogels with extremely high mechanical strength.* Advanced Materials, 2003. **15**(14): p. 1155-1158.

[139] Haque, M.A., T. Kurokawa, and J.P. Gong, *Super tough double network hydrogels and their application as biomaterials.* Polymer, 2012. **53**(9): p. 1805-1822.

[140] Hoppe, A., N.S. Güldal, and A.R. Boccaccini, *A review of the biological response to ionic dissolution products from bioactive glasses and glass-ceramics.* Biomaterials, 2011. **32**(11): p. 2757-2774.

[141] Gaharwar, A.K., et al., *Highly extensible, tough, and elastomeric nanocomposite hydrogels from poly (ethylene glycol) and hydroxyapatite nanoparticles.* Biomacromolecules, 2011. **12**(5): p. 1641-1650.

[142] Gaharwar, A.K., et al., *Transparent, elastomeric and tough hydrogels from poly (ethylene glycol) and silicate nanoparticles.* Acta biomaterialia, 2011. **7**(12): p. 4139-4148.

[143] Gaharwar, A.K., et al., *Physically Crosslinked Nanocomposites from Silicate-Crosslinked PEO: Mechanical Properties and Osteogenic Differentiation of Human Mesenchymal Stem Cells.* Macromolecular bioscience, 2012. **12**(6): p. 779-793.

[144] Liu, Y., et al., *Injectable dopamine-modified poly (ethylene glycol) nanocomposite hydrogel with enhanced adhesive property and bioactivity.* ACS applied materials & interfaces, 2014. **6**(19): p. 16982-16992.

[145] Mehrasa, M., et al., *Incorporation of mesoporous silica nanoparticles into random electrospun PLGA and PLGA/gelatin nanofibrous scaffolds enhances mechanical and cell proliferation properties.* Materials Science and Engineering: C, 2016. **66**: p. 25-32.

[146] Graf, C., et al., *A general method for the controlled embedding of nanoparticles in silica colloids.* Langmuir, 2006. **22**(13): p. 5604-5610.

[147] Taboada, E., et al., *Supercritical-Fluid-Assisted One-Pot Synthesis of Biocompatible Core (γ-Fe2O3)/Shell (SiO2) Nanoparticles as High Relaxivity T2-Contrast Agents for Magnetic Resonance Imaging.* Advanced Functional Materials, 2009. **19**(14): p. 2319-2324.

[148] Mulvaney, P., et al., *Silica encapsulation of quantum dots and metal clusters.* Journal of Materials Chemistry, 2000. **10**(6): p. 1259-1270.

[149] Adibnia, V. and R.J. Hill, *Viscoelasticity of near-critical silica-polyacrylamide hydrogel nanocomposites.* Polymer, 2017. **112**: p. 457-465.

[150] Zaragoza, J., et al., *Experimental investigation of mechanical and thermal properties of silica nanoparticle-reinforced poly (acrylamide) nanocomposite hydrogels.* PloS one, 2015. **10**(8): p. e0136293.

[151] Sershen, S., et al., *Independent optically addressable nanoparticle-polymer optomechanical composites.* Applied Physics Letters, 2002. **80**(24): p. 4609-4611.

[152] Weissman, J.M., et al., *Thermally switchable periodicities and diffraction from mesoscopically ordered materials.* Science, 1996. **274**(5289): p. 959-963.

[153] Bordes, P., E. Pollet, and L. Avérous, *Nano-biocomposites: biodegradable polyester/nanoclay systems.* Progress in Polymer Science, 2009. **34**(2): p. 125-155.

[154] Wu, C.-J., et al., *Development of biomedical polymer-silicate nanocomposites: a materials science perspective.* Materials, 2010. **3**(5): p. 2986-3005.

[155] Dawson, J.I. and R.O. Oreffo, *Clay: new opportunities for tissue regeneration and biomaterial design.* Advanced Materials, 2013. **25**(30): p. 4069-4086.

[156] King, D.R., et al., *Extremely tough composites from fabric reinforced polyampholyte hydrogels.* Materials horizons, 2015. **2**(6): p. 584-591.

[157] Huang, Y., et al., *Energy-Dissipative Matrices Enable Synergistic Toughening in Fiber Reinforced Soft Composites.* Advanced functional materials, 2017. **27**(9).

[158] Ker, R.F., *The design of soft collagenous load-bearing tissues.* Journal of Experimental Biology, 1999. **202**(23): p. 3315-3324.

[159] Calvert, P., *Hydrogels for soft machines.* Advanced materials, 2009. **21**(7): p. 743-756.

[160] Oyen, M., *Mechanical characterisation of hydrogel materials.* International Materials Reviews, 2014. **59**(1): p. 44-59.

[161] Anseth, K.S., C.N. Bowman, and L. Brannon-Peppas, *Mechanical properties of hydrogels and their experimental determination.* Biomaterials, 1996. **17**(17): p. 1647-1657.

[162] Olberding, J.E. and J.F. Suh, *A dual optimization method for the material parameter identification of a biphasic poroviscoelastic hydrogel: potential application to hypercompliant soft tissues.* Journal of biomechanics, 2006. **39**(13): p. 2468-2475.

[163] Ebenstein, D. and L. Pruitt, *Nanoindentation of soft hydrated materials for application to vascular tissues.* Journal of Biomedical Materials Research Part A, 2004. **69**(2): p. 222-232.

[164] Deam, R. and S.F. Edwards, *The theory of rubber elasticity.* Phil. Trans. R. Soc. Lond. A, 1976. **280**(1296): p. 317-353.

[165] Caccavo, D. and G. Lamberti, *PoroViscoElastic model to describe hydrogels' behavior.* Materials Science and Engineering: C, 2017. **76**: p. 102-113.

[166] Mao, Y., et al., *A large deformation viscoelastic model for double-network hydrogels.* Journal of the Mechanics and Physics of Solids, 2017. **100**: p. 103-130.

[167] Stachowiak, G. and A.W. Batchelor, *Engineering tribology*. 2013: Butterworth-Heinemann.

[168] Coulomb, C., *Théorie de machines simples, Memoire de Math´emathiques et de Physique de l'Acad´emie.* Royale, 1785. **10**: p. 161-342.

[169] Bowden, F.P. and G. Rowe, *The adhesion of clean metals.* Proc. R. Soc. Lond. A, 1956. **233**(1195): p. 429-442.

[170] Blau, P.J., *Friction science and technology: from concepts to applications*. 2008: CRC press.

[171] Williams, J., *Engineering tribology*. 2005: Cambridge University Press.

[172] Archard, J. and W. Hirst, *The wear of metals under unlubricated conditions.* Proc. R. Soc. Lond. A, 1956. **236**(1206): p. 397-410.

[173] HOLM, R., *Electric contacts theory and application.* Handbook, 1967: p. 60-71.

[174] Varenberg, M., *Towards a unified classification of wear.* Friction, 2013. **1**(4): p. 333-340.

[175] Hegadekatte, V., N. Huber, and O. Kraft, *Finite element based simulation of dry sliding wear.* Modelling and Simulation in Materials Science and Engineering, 2004. **13**(1): p. 57.

[176] Bhushan, B., *Introduction to Tribology, john Wiley& sons.* New York, 2002.

[177] Tabor, D., *Junction growth in metallic friction: the role of combined stresses and surface contamination.* Proc. R. Soc. Lond. A, 1959. **251**(1266): p. 378-393.

[178] Soda, N., Y. Kimura, and A. Tanaka, *Wear of some FCC metals during unlubricated sliding Part II: Effects of normal load, sliding velocity and atmospheric pressure on wear fragments.* Wear, 1975. **35**(2): p. 331-343.

[179] Errichello, R., *Morphology of micropitting.* Gear technology, 2012. **4**: p. 74-81.

[180] Stribeck, R., *Die wesentlichen eigenschaften der gleit-und rollenlager.* Zeitschrift des Vereines Deutscher Ingenieure, 1902. **46**: p. 1341-1348, 1432-1438, 1463-1470.

[181] Hamrock, B.J., S.R. Schmid, and B.O. Jacobson, *Fundamentals of fluid film lubrication*. 2004: CRC press.

[182] Giordano, M.A., *Screening methods for woven materials as artificial cartilage*. 2011: University of Notre Dame.

[183] Giordano, M., et al., *Wear evaluation of three-dimensionally woven materials for use in a novel cartilage replacement.* Wear, 2017. **386**: p. 179-187.

[184] Giordano, M., et al., *Abrasive Wear of Polymer Fibers Investigated by Reciprocal Scratching in an Atomic Force Microscope.* Journal of Tribology, 2018. **140**(2): p. 021604.

[185] Rodts, T.W., *Welded-woven fabrics for use as synthetic, minimally invasive orthopaedic implants*. 2012.

[186] Rodts, T., et al., *Selective laser fiber welding on woven polymer fabrics for biomedical applications.* Materials Science and Engineering: C, 2019. **94**: p. 628-634.

[187] Samyn, P., *Reciprocating sliding of polyester textile fabric composites along different fabric orientations.* Journal of Composite Materials, 2017. **51**(2): p. 221-240.

[188] Han, Y., S. Schmitt, and K. Friedrich, *Microfriction studies of filled PPS/PTFE-composite blends.* Industrial Lubrication and Tribology, 2001. **53**(1): p. 32-43.

[189] Burris, D.L. and W.G. Sawyer, *Improved wear resistance in alumina-PTFE nanocomposites with irregular shaped nanoparticles.* Wear, 2006. **260**(7-8): p. 915-918.

[190] Yang, X.-B., et al., *Frictional behavior investigation on three types of PTFE composites under oil-free sliding conditions.* Industrial Lubrication and Tribology, 2009. **61**(5): p. 254-260.

[191] Rattan, R., J. Bijwe, and M. Fahim, *Influence of weave of carbon fabric on low amplitude oscillating wear performance of Polyetherimide composites.* Wear, 2007. **262**(5-6): p. 727-735.

[192] Li, H., et al., *Tribological behavior of hybrid PTFE/Kevlar fabric composites with nano-Si3N4 and submicron size WS2 fillers.* Tribology International, 2014. **80**: p. 172-178.

[193] Mathew, M., et al., *Tribological behaviour of multilayered textile composites: The effect of reciprocating sliding frequency.* Wear, 2009. **267**(1-4): p. 26-33.

[194] Freeman, M.E., et al., *Friction, wear, and lubrication of hydrogels as synthetic articular cartilage.* Wear, 2000. **241**(2): p. 129-135.

[195] Yasuda, K., et al., *Biomechanical properties of high-toughness double network hydrogels.* Biomaterials, 2005. **26**(21): p. 4468-4475.

[196] Li, F., A. Wang, and C. Wang, *Analysis of friction between articular cartilage and polyvinyl alcohol hydrogel artificial cartilage.* Journal of Materials Science: Materials in Medicine, 2016. **27**(5): p. 87.

[197] Blum, M.M. and T.C. Ovaert, *Investigation of friction and surface degradation of innovative boundary lubricant functionalized hydrogel material for use as artificial articular cartilage.* Wear, 2013. **301**(1-2): p. 201-209.

[198] Lin, P., et al., *Articular cartilage inspired bilayer tough hydrogel prepared by interfacial modulated polymerization showing excellent combination of high load-bearing and low friction performance.* ACS Macro Letters, 2016. **5**(11): p. 1191-1195.

[199] Dunn, A.C., W.G. Sawyer, and T.E. Angelini, *Gemini interfaces in aqueous lubrication with hydrogels.* Tribology Letters, 2014. **54**(1): p. 59-66.

[200] Zhang, J. and N.A. Peppas, *Synthesis and characterization of pH-and temperature-sensitive poly (methacrylic acid)/poly (N-isopropylacrylamide) interpenetrating polymeric networks.* Macromolecules, 2000. **33**(1): p. 102-107.

[201] Urueña, J.M., et al., *Mesh size control of polymer fluctuation lubrication in gemini hydrogels.* Biotribology, 2015. **1**: p. 24-29.

[202] Schmalzried, T.P., et al., *Wear is a function of use, not time.* Clinical Orthopaedics and Related Research, 2000. **381**: p. 36-46.

[203] Parkes, M., et al., *Tribology-optimised silk protein hydrogels for articular cartilage repair.* Tribology International, 2015. **89**: p. 9-18.

[204] Korres, S., et al., *Swelling, compression and tribological behaviors of bentonite-modified polyacrylate-type hydrogels.* Journal of Applied Polymer Science, 2011. **119**(2): p. 1122-1134.

[205] Wu, G., et al., *The effect of preparation methods on tribological properties of PVA-H/HA composites.* 2008.

[206] Hertz, H.R., *Ueber die Beruehrung elastischer Koerper (On Contact Between Elastic Bodies)*, in *Gesammelte Werke (Collected Works)*. 1882.

[207] Johnson, K., *Contact Mechanics, Cambridge University Press, Cambridge."*. 1985, UK.

[208] Podra, P. and S. Andersson, *Simulating sliding wear with finite element method.* Tribology international, 1999. **32**(2): p. 71-81.

[209] Matveevsky, R., *The critical temperature of oil with point and line contact machines.* Journal of Basic Engineering, 1965. **87**(3): p. 754-759.

[210] Olofsson, U., *Cyclic micro-slip under unlubricated conditions.* Tribology International, 1995. **28**(4): p. 207-217.

[211] Huq, M. and J.-P. Celis, *Expressing wear rate in sliding contacts based on dissipated energy.* Wear, 2002. **252**(5-6): p. 375-383.

[212] Söderberg, A. and S. Andersson, *Simulation of wear and contact pressure distribution at the pad-to-rotor interface in a disc brake using general purpose finite element analysis software.* Wear, 2009. **267**(12): p. 2243-2251.

[213] Rezaei, A., et al., *Adaptive finite element simulation of wear evolution in radial sliding bearings.* Wear, 2012. **296**(1-2): p. 660-671.

[214] Abaqus, V., *6.14 Documentation.* Dassault Systemes Simulia Corporation, 2014.

[215] Bortoleto, E.M., et al., *Experimental and numerical analysis of dry contact in the pin on disc test.* Wear, 2013. **301**(1-2): p. 19-26.

[216] Martinez, F., et al., *Finite element implementation and validation of wear modelling in sliding polymer–metal contacts.* Wear, 2012. **284**: p. 52-64.

[217] Kawabata, S., M. Niwa, and H. Kawai, *3—THE FINITE-DEFORMATION THEORY OF PLAIN-WEAVE FABRICS PART I: THE BIAXIAL-DEFORMATION THEORY.* Journal of the textile institute, 1973. **64**(1): p. 21-46.

[218] Boisse, P., et al., *Finite element simulations of textile composite forming including the biaxial fabric behaviour.* Composites Part B: Engineering, 1997. **28**(4): p. 453-464.

[219] Gasser, A., P. Boisse, and S. Hanklar, *Mechanical behaviour of dry fabric reinforcements. 3D simulations versus biaxial tests.* Computational materials science, 2000. **17**(1): p. 7-20.

[220] Komeili, M. and A.S. Milani, *Finite element modeling of woven fabric composites at meso-level under combined loading modes*, in *Advances in Modern Woven Fabrics Technology*. 2011, InTech.

[221] Dhiman, S., P. Potluri, and C. Silva, *Influence of binder configuration on 3D woven composites.* Composite Structures, 2015. **134**: p. 862-868.

[222] Turner, P., T. Liu, and X. Zeng, *Dynamic response of orthogonal three-dimensional woven carbon composite beams under soft impact.* Journal of applied mechanics, 2015. **82**(12): p. 121008.

[223] Lomov, S.V., et al., *Textile geometry preprocessor for meso-mechanical models of woven composites.* Composites Science and Technology, 2000. **60**(11): p. 2083-2095.

[224] Dixit, A. and H.S. Mali, *Modeling techniques for predicting the mechanical properties of woven-fabric textile composites: a review.* Mechanics of composite Materials, 2013. **49**(1): p. 1-20.

[225] Li, S. and A. Wongsto, *Unit cells for micromechanical analyses of particle-reinforced composites.* Mechanics of materials, 2004. **36**(7): p. 543-572.

[226] Badel, P., E. Vidal-Sallé, and P. Boisse, *Computational determination of in-plane shear mechanical behaviour of textile composite reinforcements.* Computational materials science, 2007. **40**(4): p. 439-448.

[227] Peng, X. and J. Cao, *A continuum mechanics-based non-orthogonal constitutive model for woven composite fabrics.* Composites part A: Applied Science and manufacturing, 2005. **36**(6): p. 859-874.

[228] Tabatabaei, S.A., et al., *Full-field strain measurements and meso-FE modelling of hybrid carbon/self-reinforced polypropylene.* Composite Structures, 2015. **132**: p. 864-873.

[229] Dixit, A., R. Misra, and H.S. Mali, *Compression modeling of plain weave textile fabric using finite elements.* Materialwissenschaft und Werkstofftechnik, 2014. **45**(7): p. 600-610.

[230] Lin, H., et al., *A finite element approach to the modelling of fabric mechanics and its application to virtual fabric design and testing.* Journal of the Textile Institute, 2012. **103**(10): p. 1063-1076.

[231] Yang, G., B. Sun, and B. Gu, *Large-scale finite element analysis of a 3D angle-interlock woven composite undergoing low-cyclic three-point bending fatigue.* The Journal of The Textile Institute, 2014. **105**(3): p. 275-293.

[232] Jiang, W.-G., S.R. Hallett, and M.R. Wisnom, *Development of domain superposition technique for the modelling of woven fabric composites*, in *Mechanical response of composites*. 2008, Springer. p. 281-291.

[233] Lin, H., L.P. Brown, and A.C. Long. *Modelling and simulating textile structures using TexGen*. in *Advanced Materials Research*. 2011. Trans Tech Publ.

[234] Dixit, A., H.S. Mali, and R. Misra, *Unit cell model of woven fabric textile composite for multiscale analysis.* Procedia Engineering, 2013. **68**: p. 352-358.

[235] Moutos, F.T., *Biomimetic composite scaffolds for the functional tissue engineering of articular cartilage*. 2009.

[236] Davis, Y.L. and T. Bolle, *Development and evaluation of a woven multilayered fabric for knee cartilage tissue engineering*. 2017: RWTH Aachen University.

[237] Shepherd, D. and B. Seedhom, *Thickness of human articular cartilage in joints of the lower limb.* Annals of the rheumatic diseases, 1999. **58**(1): p. 27-34.

[238] ASTM, D., *2256-02;"Standard test method for tensile properties of yarns by the singlestrand method".* Annual book of ASTM standards, 2005. **7**: p. 01.

[239] Standard, A., *E2546-07.* Standard Practice for Instrumented Indentation Testing, ASTM International, West Conshohocken, PA, 2007.

[240] Dimitriadis, E.K., et al., *Determination of elastic moduli of thin layers of soft material using the atomic force microscope.* Biophysical journal, 2002. **82**(5): p. 2798-2810.

[241] Long, R., et al., *Effects of gel thickness on microscopic indentation measurements of gel modulus.* Biophysical journal, 2011. **101**(3): p. 643-650.

[242] Oloyede, A., R. Flachsmann, and N.D. Broom, *The dramatic influence of loading velocity on the compressive response of articular cartilage.* Connective tissue research, 1992. **27**(4): p. 211-224.

[243] Mayne, A., et al., *An assessment of the mechanical properties of leaflets from four second-generation porcine bioprostheses with biaxial testing techniques.* The Journal of thoracic and cardiovascular surgery, 1989. **98**(2): p. 170-180.

[244] Leeson-Dietrich, J., D. Boughner, and I. Vesely, *Porcine pulmonary and aortic valves: a comparison of their tensile viscoelastic properties at physiological strain rates.* The Journal of heart valve disease, 1995. **4**(1): p. 88-94.

[245] Boughner, D., et al., *The pericardial bioprosthesis: altered tissue shear properties following glutaraldehyde fixation.* The Journal of heart valve disease, 2000. **9**(6): p. 752-760.

[246] Wan, W., et al., *Optimizing the tensile properties of polyvinyl alcohol hydrogel for the construction of a bioprosthetic heart valve stent.* Journal of Biomedical Materials Research: An Official Journal of The Society for Biomaterials, The Japanese Society for Biomaterials, and The Australian Society for Biomaterials and the Korean Society for Biomaterials, 2002. **63**(6): p. 854-861.

[247] Taeger, G., et al., *Comparison of diamond-like-carbon and alumina-oxide articulating with polyethylene in total hip arthroplasty.* Materialwissenschaft und Werkstofftechnik: Entwicklung, Fertigung, Prüfung, Eigenschaften und Anwendungen technischer Werkstoffe, 2003. **34**(12): p. 1094-1100.

[248] Yarimitsu, S., et al., *Evaluation of lubrication properties of hydrogel artificial cartilage materials for joint prosthesis.* Biosurface and Biotribology, 2016. **2**(1): p. 40-47.

[249] Covert, R.J., R. Ott, and D.N. Ku, *Friction characteristics of a potential articular cartilage biomaterial.* Wear, 2003. **255**(7-12): p. 1064-1068.

[250] Brand, R.A., *Joint contact stress: a reasonable surrogate for biological processes?* The Iowa orthopaedic journal, 2005. **25**: p. 82.

[251] Ayyappa, E., *Normal human locomotion, part 1: Basic concepts and terminology.* JPO: Journal of Prosthetics and Orthotics, 1997. **9**(1): p. 10-17.

[252] Howell, S.M., S.J. Howell, and M.L. Hull, *Assessment of the radii of the medial and lateral femoral condyles in varus and valgus knees with osteoarthritis.* JBJS, 2010. **92**(1): p. 98-104.

[253] ASTM, F., *2025-06. Standard Practice for Gravimetric Measurement of Polymeric Components for Wear Assessment.* ASTM International: West Conshohocken, PA, 2009.

[254] Peirce, F.T., *5—the geometry of cloth structure.* Journal of the Textile Institute Transactions, 1937. **28**(3): p. T45-T96.

[255] Kemp, A., *An extension of Peirce's cloth geometry to the treatment of non-circular threads.* 1958.

[256] *Mechanical properties of polyethylene terephalate*.

[257] Rubin, I.I., *Handbook of plastic materials and technology*. 1990: Wiley New York.

[258] Thambyah, A. and J. Fernandez, *Squatting-related tibiofemoral shear reaction forces and a biomechanical rationale for femoral component loosening.* The Scientific World Journal, 2014. **2014**.

[259] *Material Properties of Alumina Cermaic*. July 2018]; Available from: https://accuratus.com/alumox.html.

[260] Laiarinandrasana, L., et al., *Temperature dependent mechanical behaviour of PVDF: experiments and numerical modelling.* International Journal of Plasticity, 2009. **25**(7): p. 1301-1324.

[261] Naficy, S., et al., *Mechanical properties of interpenetrating polymer network hydrogels based on hybrid ionically and covalently crosslinked networks.* Journal of Applied Polymer Science, 2013. **130**(4): p. 2504-2513.

[262] Linn, F.C., *Lubrication of animal joints: I. The arthrotripsometer.* JBJS, 1967. **49**(6): p. 1079-1098.

[263] Li, F., et al., *Tribological properties of poly (vinyl alcohol) hydrogel in response to ceramic femoral component.* 2009.

[264] Reale, E.R. and A.C. Dunn, *Poroelasticity-driven lubrication in hydrogel interfaces.* Soft matter, 2017. **13**(2): p. 428-435.

[265] Milner, P.E., et al., *A low friction, biphasic and boundary lubricating hydrogel for cartilage replacement.* Acta biomaterialia, 2018. **65**: p. 102-111.

[266] Suciu, A.N., et al., *A study upon durability of the artificial knee joint with PVA hydrogel cartilage.* JSME International Journal Series C Mechanical Systems, Machine Elements and Manufacturing, 2004. **47**(1): p. 199-208.

[267] Urueña, J.M., et al., *Normal Load Scaling of Friction in Gemini Hydrogels.* Biotribology, 2018. **13**: p. 30-35.

[268] Gong, J.P., et al., *Synthesis of hydrogels with extremely low surface friction.* Journal of the American Chemical Society, 2001. **123**(23): p. 5582-5583.

[269] Moore, A. and D. Burris, *An analytical model to predict interstitial lubrication of cartilage in migrating contact areas.* Journal of biomechanics, 2014. **47**(1): p. 148-153.

[270] Schallamach, A., *A theory of dynamic rubber friction.* Wear, 1963. **6**(5): p. 375-382.

[271] Kim, J. and A.C. Dunn, *Soft hydrated sliding interfaces as complex fluids.* Soft matter, 2016. **12**(31): p. 6536-6546.

[272] Grover, C.N., et al., *Crosslinking and composition influence the surface properties, mechanical stiffness and cell reactivity of collagen-based films.* Acta biomaterialia, 2012. **8**(8): p. 3080-3090.

[273] Bagwe, R.P., L.R. Hilliard, and W. Tan, *Surface modification of silica nanoparticles to reduce aggregation and nonspecific binding.* Langmuir, 2006. **22**(9): p. 4357-4362.

[274] Fitzgerald, M.M., et al., *Tunable stress relaxation behavior of an alginate-polyacrylamide hydrogel: comparison with muscle tissue.* Biomacromolecules, 2015. **16**(5): p. 1497-1505.

[275] Bursać, P.M., et al., *Confined and unconfined stress relaxation of cartilage: appropriateness of a transversely isotropic analysis.* Journal of biomechanics, 1999. **32**(10): p. 1125-1130.

[276] Millon, L.E., C.J. Oates, and W. Wan, *Compression properties of polyvinyl alcohol–bacterial cellulose nanocomposite.* Journal of Biomedical Materials Research Part B: Applied Biomaterials: An Official Journal of The Society for Biomaterials, The Japanese Society for Biomaterials, and The Australian Society for Biomaterials and the Korean Society for Biomaterials, 2009. **90**(2): p. 922-929.

[277] Święszkowski, W., et al., *An elastic material for cartilage replacement in an arthritic shoulder joint.* Biomaterials, 2006. **27**(8): p. 1534-1541.

[278] Gong, J. and Y. Osada, *Gel friction: a model based on surface repulsion and adsorption.* The Journal of chemical physics, 1998. **109**(18): p. 8062-8068.

[279] Ohsedo, Y., et al., *Surface friction of hydrogels with well-defined polyelectrolyte brushes.* Langmuir, 2004. **20**(16): p. 6549-6555.

[280] Zhou, C. and Q. Wu, *A novel polyacrylamide nanocomposite hydrogel reinforced with natural chitosan nanofibers.* Colloids and Surfaces B: Biointerfaces, 2011. **84**(1): p. 155-162.

[281] Yodmuang, S., et al., *Silk microfiber-reinforced silk hydrogel composites for functional cartilage tissue repair.* Acta biomaterialia, 2015. **11**: p. 27-36.

[282] Brockett, C., et al. *Influence of bearing couple, lubricant and swing phase load conditions on the friction of 28 mm hip replacements*. in *The 52nd Annual Meeting of the Orthopaedic Research Society, Chicago, Illinois*. 2006.

[283] Gispert, M., et al., *Friction and wear mechanisms in hip prosthesis: Comparison of joint materials behaviour in several lubricants.* Wear, 2006. **260**(1-2): p. 149-158.

[284] Ding, Z., et al., *Inhomogeneous large deformation study of temperature-sensitive hydrogel.* International Journal of Solids and Structures, 2013. **50**(16-17): p. 2610-2619.

[285] Toh, W., et al., *Mechanics of inhomogeneous large deformation of photo-thermal sensitive hydrogels.* International Journal of Solids and Structures, 2014. **51**(25-26): p. 4440-4451.